

**This microfiche was
produced according to
ANSI / AIIIM Standards
and meets the
quality specifications
contained therein. A
poor blowback image
is the result of the
characteristics of the
original document.**

(NASA-TP-3212) EFFECT OF PLANFORM
AND BODY ON SUPERSONIC AERODYNAMICS
OF MULTIBODY CONFIGURATIONS (NASA)
281 p

N93-10824

Unclass

HI/02 0123613

**NASA
Technical
Paper
3212**

1982

**Effect of Planform and Body
on Supersonic Aerodynamics
of Multibody Configurations**

**S. Naomi McMillin,
Steven X. S. Bauer,
and Dorothy T. Howell
*Langley Research Center
Hampton, Virginia***



**National Aeronautics and
Space Administration
Office of Management
Scientific and Technical
Information Program**

Contents

Summary	1
Introduction	1
Symbols	2
Model Description	3
Test Description	4
Discussion	5
Outboard Panel Study	5
Experimental evaluation	6
Theoretical analysis	7
Inboard Panel Study	8
Experimental evaluation—force data	8
Experimental evaluation—flow-visualization data	10
Experimental evaluation—surface pressure coefficient data	14
Theoretical analysis	16
Side Bodies-Off Study	16
Experimental evaluation—flow-visualization data	16
Experimental evaluation—surface pressure coefficient data	17
Conclusions	19
Tables	21
Figures	28
Appendix A—Internal Duct Skin-Friction-Drag Correction	207
Appendix B—Force and Moment Data	228
Appendix C—Surface Pressure Coefficient Data	254
References	279

Summary

An experimental and theoretical investigation on the effect of the wing planform on the supersonic aerodynamics of a low-fineness-ratio, multibody configuration has been conducted in the Langley Unitary Plan Wind Tunnel at Mach numbers of 1.60, 1.80, 2.00, and 2.16. Three uncambered outboard wing panels were tested on a low-fineness-ratio, twin-body configuration equipped with an unswept and swept inboard wing panel. The outboard wing planform variations were a delta with a 65° leading-edge sweep, a trapezoidal with a 20° leading-edge sweep, and a trapezoidal with a 20° leading-edge sweep and with increased span and area. The two inboard wing variations included an unswept planform and a leading-edge planform swept 65° . Also examined was the effect of side bodies (on versus off) on the multibody configuration with the unswept inboard wing panel. Longitudinal aerodynamic force and moment data, surface-pressure data, and flow-visualization data were obtained for the eight configurations examined.

In general, the data indicated that the ratio of outboard wing area to total wing area significantly influenced the zero-lift drag coefficient with minimal influence on the lift, drag-due-to-lift, and pitching-moment characteristics. The data also indicated that increasing the sweep of the inboard wing planform can reduce zero-lift drag. The sweep of the inboard planform also influenced the drag-due-to-lift characteristics regardless of the outboard wing planform shape.

The flow-visualization data showed a complex flow-field system occurring between the side bodies. This flow field consisted of shocks, shock-induced separation, and body vortex systems. This flow field was not sensitive to outboard wing planform shape but was sensitive to inboard wing planform shape. The flow-visualization data showed that the trends in drag with changes in inboard planform shape corresponded to distinct changes in the shock-vortex system occurring between the side bodies. The variations of the shock-vortex system between the side bodies also influenced the flow field over the small-trapezoidal outboard wing. These results were reflected in the surface-pressure data on the outboard wing, especially on the most-inboard portion of the wing. Otherwise, the surface-pressure and flow-visualization data showed that the flow over the outboard wing developed as expected with changes in angle of attack and Mach number.

The bodies-off study was conducted with the unswept inboard wing panel and the delta outboard

and small-trapezoidal outboard wing panels. The flow-visualization data for the bodies-off configurations more clearly showed the existence of the bow shock from the balance housing over the inboard wing. As for the bodies on, the outboard wing planform shape had a minimal influence on the flow pattern of the inboard wing panel. The addition of the bodies affected the size of the leading-edge vortex of the delta outboard wing and the extent of shock-induced separation of the small-trapezoidal outboard wing.

Evaluation of the linear-theory prediction methods revealed their general inability to consistently predict the characteristics of these multibody configurations. The methods predicted the correct trends in the lift, drag-due-to-lift, and zero-lift drag characteristics with changes in outboard wing size and Mach number. However, the methods did not consistently predict the correct trends in drag-due-to-lift and zero-lift drag characteristics with variations in the inboard wing planform shape. The methods were not able to correctly predict the trends in longitudinal stability with changes in outboard wing size, inboard wing planform shape, or Mach number.

Introduction

The multiple-fuselage aircraft design concept is well established in aviation history (ref. 1). Since the beginning of powered flight, this design concept has continually resurfaced. Aircraft design studies (refs. 2-4) have indicated that significant performance improvements can be achieved for subsonic passenger and cargo aircraft by utilizing the novel concept of two fuselages. In general, the benefits afforded by two fuselages are an effective increase in wing aspect ratio, reduced wing structural weight as a result of a reduced wing bending moment, and reduced total fuselage weight when both single- and twin-fuselage geometries are designed for the same number of passengers or payloads. These benefits should be independent of aircraft operating speed.

The earlier studies alluded to, but did not quantify, aerodynamic interference effects associated with the multiple-fuselage design concept. Additional theoretical and experimental research on the multibody concept at supersonic speeds (refs. 5 to 10) has shown that zero-lift drag can be significantly reduced through body shaping, body positioning, or both. In a linear-theory sense, the multibody concept creates an aerodynamically thinner configuration (i.e., equivalent body with a higher fineness ratio) than the conventional single-body concept. (See fig. 9.) In a real-flow sense, pressure drag is reduced through

the management of the near-field interference effects between the aircraft components.

For uncambered configurations at supersonic speeds, the majority of zero-lift drag is a combination of wave drag and skin-friction drag. Application of the multibody concept typically increases skin-friction drag because of the increased wetted area; however, a decrease in total zero-lift drag occurs. This decrease indicates a large decrease in zero-lift wave drag. Figure 1, which is derived from reference 10, presents the results of a fundamental theoretical study that was conducted to determine the impact of configuration fineness ratio on the zero-lift drag reduction potential of the multibody concept at supersonic speeds. The figure shows the variation in zero-lift drag with fineness ratio l/d for a single-body configuration and a comparative (same volumetric efficiency, i.e., volume/ $S^{3/2}$) double-body configuration. The multibody concept provides the greatest drag reduction potential for low-fineness-ratio geometries.

To further study the supersonic aerodynamic characteristics of low-fineness-ratio, multibody configurations, an experimental and theoretical investigation was conducted on a multibody configuration with an l/d of about 12. The effect of body cross-sectional shape (ref. 10) was examined by varying the body cross-sectional shape from circular to elliptical to horizontal and vertical cuts of those bodies. This study concluded that of the various body cross-sectional shapes examined, the circular cross-sectional shape yielded the lowest zero-lift drag. The effect of outboard wing planform shape on the aerodynamic performance of a low-fineness-ratio, multibody configuration has also been examined (ref. 11). This study concluded that a low-swept, trapezoidal outboard wing can be used without a large zero-lift drag penalty, which usually occurs on single-body configurations (ref. 12). The trapezoidal wing also retained the low drag-due-to-lift characteristics common to planforms with small values of leading-edge sweep (and high aspect ratio) for single-body configurations.

In the multibody investigation (ref. 11), the outboard wing panel area comprised about 42 percent of the total wing area; therefore, the unswept inboard panel was a significant part of the total wing area. Thus, the effect of the inboard panel on the overall aerodynamics was uncertain. The present study was conducted to determine the effect of the relative inboard wing planform size (by varying the outboard trapezoidal wing planform size) and the effect of inboard wing panel shape (unswept versus swept lead-

ing edge). In addition, the effect of side bodies (on versus off) was studied for the unswept, inboard wing panel. For this study, longitudinal force and moment, pressure, and flow-visualization data were obtained from the same basic model of references 10 and 11 but with additional inboard and outboard wing panels. Oil-flow and schlieren data from reference 11 were also used in this study. All configurations were tested at Mach numbers of 1.60, 1.80, 2.00, and 2.16 in the Langley Unitary Plan Wind Tunnel. This paper reports the results of the experimental testing and supporting theoretical analysis.

Symbols

The measurements and calculations of this investigation were made in U.S. Customary Units.

A	total (wing and body) planform area, in^2
b	wing reference span, in.
C_A	corrected axial-force coefficient, Axial force/ qS
C_D	corrected drag coefficient, Drag/ qS
ΔC_D	incremental change in drag coefficient, $C_D - C_{D,0}$
$\Delta C_D/C_L^2$	drag-due-to-lift factor
$C_{D,hb}$	zero-lift drag correction due to balance-housing geometry
$C_{D,i}$	internal duct drag coefficient, Internal duct skin-friction drag/ qS
$C_{D,0}$	zero-lift drag coefficient, Zero-lift drag/ qS
$C_{D,\phi}$	zero-lift wave drag coefficient of equivalent body of revolution in a plane through the geometry at a given ϕ
C_L	lift coefficient, Lift/ qS
ΔC_L	incremental change in lift coefficient, $C_L - C_{L,C_{D,0}}$
C_{L_α}	lift-curve slope at $\alpha = 0^\circ$
C_m	pitching-moment coefficient, Pitching moment/ $qS\bar{c}$
C_N	normal-force coefficient, Normal force/ qS
C_p	surface pressure coefficient, $(p - p_\infty)/q$
C_Y	side-force coefficient, Side force/ qS
c	wing root chord, in.
\bar{c}	wing reference chord, in.

d	maximum diameter of body, in.
dC_m/dC_L	longitudinal stability parameter at $\alpha = 0^\circ$
FFWD	far-field wave drag code
L/D	lift-drag ratio
l	side-body or maximum configuration length, in.
M	free-stream Mach number
M_D	duct Mach number
M_N	Mach number normal to wing leading edge, $M \cos \Lambda_{LE} (1 + \sin^2 \alpha \tan^2 \Lambda_{LE})^{1/2}$
P_o	stagnation pressure, lb/ft ²
p	local static pressure, lb/ft ²
p_∞	free-stream static pressure, lb/ft ²
q	free-stream dynamic pressure, lb/ft ²
R	Reynolds number, ft ⁻¹
S	wing reference area, in ²
SDAS	Supersonic Design and Analysis System
s	cross-sectional area, in ²
x	longitudinal position from nose of side body, in.
x'	longitudinal position from apex of outboard wing, in.
\bar{x}	longitudinal position of wing reference chord from nose of side body, in.
y	spanwise position from centerline of configuration, in.
y'	spanwise position from root chord of outboard wing, in.
α	angle of attack, deg
α_N	angle of attack normal to leading edge, $\tan^{-1} (\tan \alpha / \cos \Lambda_{LE})$
β	angle of sideslip, deg
η	y /local semispan
Λ	sweep angle, deg
ϕ	roll angle, deg
Subscripts:	
b	base

c	balance cavity
eq	equivalent body
LE	leading edge
out	outboard wing
TE	trailing edge
unc	uncorrected
Model components:	
F	side body
I_1	unswept inboard wing
I_2	swept inboard wing
W_1	delta outboard wing
W_3	small-trapezoidal outboard wing
W_4	large-trapezoidal outboard wing

Flow structure abbreviations:

F	feeding sheet of a vortex
R	reattachment of flow to surface
S	shock
SIS	shock-induced separation
SL	separation of flow from surface
V	vortex

Flow structure subscripts:

a	apex of inboard wing
b	side body
bh	balance housing
i	inboard side-body vortex system
iw	inboard wing
n	nose of side body
o	outboard side-body vortex system
ow	outboard wing
p	primary
s	secondary
t	tip of outboard wing
T	tab of small-trapezoidal outboard wing

Model Description

Figure 2 shows a three-view sketch of the multi-body model with the delta outboard wing panel and the unswept inboard wing panel. Figure 3 identifies the eight configurations tested and the type of data obtained for each of these configurations. Details of the multibody models are presented in figure 4

and table I. Figure 5 shows the baseline multibody model (the configuration with the unswept inboard wing panel and delta outboard wing panel identified in fig. 3 as the unswept/delta configuration) with vertical tails attached, and figure 6 shows the top views of the other seven configurations tested. For the purposes of this investigation, all models were tested without the vertical tails attached. Each side body was 30 in. long and circular in cross section. The normal area distribution of the side body is presented in table II.

Figures 4(a) and 4(b) show the balance housing and duct arrangement mounted underneath the multibody models. The balance housing was located on the lower surface of the center wing panel and was bracketed by the two flow-through ducts. The design was an attempt to limit the propagation of the interference effects from the balance housing to the free-stream flow field and model geometry. To maintain supersonic flow within the duct system, the two flow-through ducts were designed with a linear area growth ratio of 1.13 to account for the boundary layer. Figure 4(b) shows lateral and longitudinal cross-sectional views through the balance-housing system. The balance-housing geometry consisted of a combined cone (balance housing) and wedge surface (diverter) with leading-edge surface slopes of 28° and 19° . These large surface slopes resulted in a significant drag penalty and a complex and nonlinear flow field (ref. 10). Corrections for this significant drag penalty due to the surface slopes of the balance housing and diverter are discussed subsequently.

Figures 4(c) and 4(d) contain details of the unswept and swept inboard wing panels. Figures 4(e), 4(f), and 4(g) contain details of the delta and two trapezoidal outboard wing panels. The small-trapezoidal outboard wing panel in figure 4(f) had a tab that assisted in the attachment of the outboard wing panel to the balance housing and duct system. Most of the tab was covered by the side body when the wing was tested with the bodies on (i.e., the line of maximum body diameter in fig. 4(f)). However, the corner of the tab slightly protruded from the side body. (See fig. 6(a).) The small-trapezoidal outboard wing panel was centered on the chord of the unswept inboard wing panel. The large-trapezoidal outboard wing panel was placed slightly farther aft, such that the trailing edge aligned with the trailing edge of the unswept inboard wing panel.

The delta and small trapezoidal wings were instrumented on the upper surface with pressure orifices, as indicated in figures 4(e) and 4(f). The orifices were distributed spanwise between 20 and 90 percent of the local span at several x/c stations.

The locations of the pressure orifices are listed in tables III and IV for the delta and small-trapezoidal outboard wing panels. The pressures were measured externally and separately from the force and moment data.

Test Description

The wind tunnel test program was conducted in test section I of the Langley Unitary Plan Wind Tunnel at Mach numbers of 1.60, 1.80, 2.00, and 2.16. The test was conducted under the following conditions:

Mach number	Stagnation pressure, lb/ft ²	Stagnation temperature, °F	Reynolds number, ft ⁻¹
1.60	1079	125	2×10^5
1.80	1154	125	2
2.00	1253	125	2
2.16	1349	125	2

The dew point was maintained sufficiently low during the force tests to prevent condensation in the tunnel. The maximum variation in Mach number was ± 0.03 . Reference 13 contains a more detailed description of the wind tunnel and operating conditions.

Boundary-layer transition strips of No. 60 sand grit were applied 0.2 in. aft of the leading edge of all airfoil surfaces, 1.2 in. aft of the nose region for the side bodies, and 0.2 in. aft of the inlet lip leading edges. The grit size and location were selected according to the method of reference 14 to ensure fully turbulent flow over the model and inside the inlet duct.

Balance cavity pressure and base pressure were measured throughout the test with a pressure transducer mounted externally to the wind tunnel test section and connected by pressure tubing to a static pressure probe located in the balance cavity at the model base. Force and moment data were corrected for free-stream static pressure at the model base and cavity.

As noted in the section entitled "Model Description," the balance-housing geometry, which consisted of a wedge surface bracketing a partially axisymmetric body of revolution, resulted in a significant zero-lift drag penalty throughout the test. A zero-lift drag correction derived in reference 10 was therefore applied to the drag data. The correction used at each Mach number was as follows:

M	$SC_{D,bb}$, in ²
1.60	1.0840
1.80	0.9611
2.00	0.9615
2.16	0.9202

The total pressure and static pressure at the exit plane of the ducts were also measured throughout the test with a pressure transducer mounted externally to the wind tunnel test section and connected by pressure tubing to a pressure probe located at the center of the duct exit plane. These measurements were then used to correct the experimental data for internal duct friction drag. This correction is more fully discussed in appendix A.

Forces and moments were measured with a six-component electrical strain-gauge balance contained within the model and connected through a supporting sting to a permanent model-actuating system in the tunnel. The pressure data were obtained separately from the force and moment data. The pressure orifices were connected by tubing to the ESP system located outside the wind tunnel test section. The following table shows the accuracy associated with the balance and the pressure transducers used in this test:

Instrumentation	Load	Coefficient
Balance:		
Normal	±3.0 lb	±0.00423
Axial	±0.3 lb	±0.00042
Side	±1.5 lb	±0.00231
Pitch	±7.5 in-lb	±0.00075
Roll	±2.0 in-lb	±0.00021
Yaw	±5.0 in-lb	±0.00050
Pressure transducer	±0.07 psi	±0.02016

The aerodynamic data were obtained at angles of attack from -4° to 20° . All angles of attack were corrected for tunnel flow angularity and for sting and balance deflections. Extensive flow-visualization tests were performed with oil-flow, schlieren, and vapor-screen flow-visualization photographs.

The data reduction used the wing reference area and wing reference chord of each configuration. The \bar{c} and \bar{x} of each configuration were calculated at the centroid of the configuration wing planform. Table I lists the values for these parameters for each configuration.

Discussion

An experimental and theoretical investigation has been conducted to determine the effect of the inboard wing planform on the supersonic aerodynamics of a low-fineness-ratio, multibody configuration. The low-fineness ratio was about 12 and was measured by determining the diameter from twice the maximum side body cross-sectional area. This investigation had three parts. The first part determined the effect of the relative inboard wing planform size. The second part examined the effect of the inboard wing planform shape on the aerodynamics of the configuration. The third part examined the effect of the side bodies (on versus off) for the configurations with the unswept inboard wing panel (referred to hereafter as the unswept-inboard configurations).

In each section of this paper, the experimental data are discussed first and then the experimental and theoretical data are compared. Force, pressure, and flow-visualization data are presented in the experimental evaluation. Appendix B contains a tabulation of the force and moment data, and appendix C contains a tabulation of the surface pressure coefficient data. Table V contains a list of the experimental data for each configuration.

The near-field interference discussed throughout this paper is the interaction of the shock systems and body vortex systems between the side bodies and over the inboard wing panel. One of the components of the near-field interference is the mechanism by which the zero-lift drag is reduced on the multibody configuration when compared with the drag of the single-body configuration. The nose shock from one side body impinges on the opposing side body, such that a pressure increase occurs on an aft-facing surface and produces a net reduction in drag. References 10 and 11 discuss three contributions to the near-field interference: effect of nose shock on opposing side body, effect of nose shock on inboard wing panel, and effect of balance-housing bow shock on flow between side bodies. These contributions are discussed in this paper as well as other contributions to the near-field interference, such as body vortices, body-wing junction shock, and shock-induced separation.

Outboard Panel Study

In this section, the effect of the relative inboard wing planform size is examined by varying the size of the outboard wing planform. Thus, the inboard to total wing panel area ratio is varied. The trapezoidal wing examined in reference 11 was used as the baseline for this study and is hereafter referred to as the

small-trapezoidal wing. (See fig. 4(f).) The small-trapezoidal wing was chosen because it had better drag-due-to-lift characteristics and did not exhibit a large increase in zero-lift drag coefficient when compared with the more highly swept wings (65° delta wing and 70°/66° arrow wing) examined in reference 11. To determine the influence the inboard wing panel has on the aerodynamics of the multibody configuration with the trapezoidal outboard wing, the size of the trapezoidal outboard wing was increased by 75 percent to hold the leading-edge sweep of 20° for the trapezoidal planform constant. The resultant wing is referred to as the large-trapezoidal wing. (See fig. 4(g).) The two outboard wings were tested with both the unswept and swept inboard wings. The outboard wing area to total wing area ratio (A_{out}/S) of the four configurations is as follows:

Inboard wing Planform	A_{out}/S for—	
	Small trapezoidal	Large trapezoidal
Unswept	0.461	0.600
Swept	0.467	0.607

Another reason for selecting the small-trapezoidal wing as the baseline configuration for this study was to minimize cost. A larger version of the trapezoidal wing planform can be attached to the existing multibody model system with no difficulty. However, a larger version of the 65° delta wing cannot be readily attached to the existing multibody system.

Experimental evaluation. Figure 7 shows the longitudinal characteristics for the unswept/small-trapezoidal configuration and the unswept/large-trapezoidal configuration at $M = 1.80$. Figure 7(a) shows the lift and pitching-moment characteristics. The experimental data for the unswept/large-trapezoidal configuration are limited to an angle of attack of 8° because of model-sting fouling. The lift and pitching-moment data show that both unswept/trapezoidal configurations have a linear variation in C_L and C_m up to $\alpha = 8^\circ$ ($C_L = 9.38$). Both configurations also have nearly equivalent lift-curve slopes, as expected for similar planform configurations. The pitching-moment data show that the unswept/large-trapezoidal configuration has a lower slope for the C_m versus α curve and lower pitching-moment coefficient than the unswept/small-trapezoidal configuration. This observation is discussed in more detail subsequently.

The drag data in figure 7(b) show that the large-trapezoidal wing has a zero-lift drag coefficient

significantly lower (≈ 10 percent) than the small-trapezoidal wing. However, the polar shapes of the two wings are similar; this similarity indicates that the two wings have similar drag-due-to-lift characteristics. This observation is expected because of similar planform shapes for the two configurations.

In figure 8, the aerodynamic characteristics at $M = 1.80$ for the two unswept/trapezoidal configurations are presented in terms of lift-to-drag ratio L/D at three different values of lift coefficient. At all three values of C_L , the unswept/large-trapezoidal configuration has a greater L/D . At $C_L = 0.1$, the unswept/large-trapezoidal configuration results in an increase in L/D of 10.7 percent, when compared with the unswept/small-trapezoidal configuration. This increase in L/D results from the lower zero-lift drag coefficient associated with the unswept/large-trapezoidal configuration, as shown in figure 7(b). At the higher lift condition of $C_L = 0.3$, the unswept/large-trapezoidal configuration increases L/D by 3.3 percent over the unswept/small-trapezoidal configuration. Because the two configurations have the same drag-due-to-lift characteristics, the change in drag at the higher lift coefficient, due solely to the lower zero-lift drag, is a smaller increment of the total drag.

The previous discussion and results were limited to a Mach number of 1.80; however, figure 9 shows the variations of the major aerodynamic parameters over the Mach number range of 1.60 to 2.16. The lift-curve-slope characteristics are represented on the left in figure 9(a). As expected for wings of similar aspect ratio, both trapezoidal configurations have similar lift-curve-slope values over the Mach number range, despite the fact that the unswept/large-trapezoidal configuration has an A_{out}/S ratio that is 43 percent greater than that of the unswept/small-trapezoidal configuration. These results indicate that the outboard wing size has little effect on the total lift characteristics.

The longitudinal stability data presented on the right in figure 9 show that the unswept/large-trapezoidal configuration is slightly more stable (i.e., lower dC_m/dC_L) than the unswept/small-trapezoidal configuration. The large-trapezoidal wing was located slightly farther aft on the configuration than the small-trapezoidal wing. While the change in wing position did not significantly affect the centroid location, it did, to a large extent, affect the aerodynamic center location. Consequently, the unswept/large-trapezoidal configuration was slightly more stable. Consistent with observations documented in reference 11, the two unswept/trapezoidal configurations have either a constant value of or a slight increase

in longitudinal stability (i.e., decrease in dC_m/dC_L) with Mach numbers up to 2.00. At Mach numbers above 2.00, the longitudinal stability decreases (i.e., increase in dC_m/dC_L). This observation is possibly the result of a change in the near-field interference between the bodies at high Mach numbers; this change then influences the aerodynamic center such that a decrease in longitudinal stability occurs. This explanation is substantiated by noting that the decrease in longitudinal stability at higher Mach numbers occurs on both unswept/trapezoidal configurations, with the decrease being less severe on the unswept/large-trapezoidal configuration. The unswept/large-trapezoidal configuration has more outboard wing area that influences the position of the aerodynamic center and thus decreases the effect that the near-field interference between the bodies supposedly has on the aerodynamic center at the high Mach numbers.

Figure 9(b) contains the drag characteristics of the two unswept/trapezoidal configurations over the Mach number range. The zero-lift drag data, on the left in figure 9(b), show that over the entire Mach number range, the unswept/large-trapezoidal configuration has a lower zero-lift drag coefficient than the unswept/small-trapezoidal wing. More importantly, the increment in $C_{D,0}$ between the two unswept/trapezoidal configurations is nearly constant over the Mach number range. The value of $C_{D,0}$ levels off at Mach numbers greater than 2.00. This trend corresponds with the previously noted decrease in longitudinal stability that is thought to be associated with a change in near-field interference between the bodies at higher Mach numbers. The drag-due-to-lift data, presented on the right in figure 9(b), show that both unswept/trapezoidal configurations have similar drag-due-to-lift values as expected for wings with similar aspect ratio and leading-edge sweep.

In summary, the comparison of the unswept/small-trapezoidal and the unswept/large-trapezoidal configurations showed that the size of the outboard wing in relation to the total wing area did not affect the lift and drag-due-to-lift characteristics for the multibody configuration. That is, the increase in outboard wing area generated an equivalent proportion of lift and drag due to lift. In contrast, the increase in outboard wing area generated a lower proportion of zero-lift drag, so the zero-lift drag coefficient for the unswept/large-trapezoidal configuration was actually lower than that for the unswept/small-trapezoidal configuration. These trends resulted in greatly improved lift-to-drag characteristics for the unswept/large-trapezoidal configuration over the

unswept/small-trapezoidal configuration. Increasing the size of the outboard wing planform caused a favorable effect on pitching moment. Similar results were also observed on the swept/trapezoidal configurations. (See figs. 10 to 12.)

The zero-lift drag is composed primarily of a skin-friction-drag component and a wave drag component. The skin-friction drag can be expected to increase proportionally to the increase in outboard wing area, such that the skin-friction-drag coefficient is equivalent for the two configurations. Figure 13 shows the skin-friction-drag coefficient as computed with the method of reference 15 and the experimental zero-lift drag coefficient. The coefficients for this plot were adjusted to account for the total planform area, which includes the wings and the bodies. This adjustment reflects the correct proportion of increased outboard wing area to total planform area. As a result, the skin-friction-drag coefficient is equivalent for the small- and large-trapezoidal configurations.

If the wave drag increased proportionally to the increase in wing area, the zero-lift drag coefficient would be equal for the two unswept/trapezoidal configurations. However, as shown in figure 13, the unswept/large-trapezoidal configuration had a lower zero-lift drag coefficient than the unswept/small-trapezoidal configuration. This result implies that the wave drag of the multibody configuration is sensitive to the size of the outboard wing. Similar results were observed on the swept/trapezoidal configurations. (See fig. 14.)

Theoretical analysis. Two supersonic aerodynamic prediction computational codes were selected to perform the theoretical analysis. These codes were an arbitrary-geometry far-field wave drag code (FFWD) (ref. 16) and the Supersonic Design and Analysis System (SDAS) (ref. 17); both codes use the linearized supersonic potential flow equations.

SDAS is an integrated system of computer programs that was developed for the design and analysis of supersonic configurations. The system includes the lift-analysis method of reference 18 and the skin-friction calculation method of reference 15. The SDAS code also includes a version of the FFWD code that uses the solution technique described in reference 19. However, because the fuselages were located off the configuration centerline, a modified version of the FFWD code was used. (See ref. 16.) The modified FFWD code and the skin-friction code were used to obtain the zero-lift drag characteristics. The lift-analysis code was used to obtain the lift, drag-due-to-lift, and pitching-moment characteristics.

The zero-lift drag theoretical model for the unswept/delta configuration is shown on the top in figure 15. This thick representation of the total configuration was used to compute the wave drag and skin friction. On the bottom in figure 15, the lift-analysis theoretical model of the same configuration is shown. This modelling was chosen based on a lifting-surface modelling study conducted on a low-fineness-ratio, single-body configuration (ref. 20). The study in reference 20 illustrated that a mean-chord-plane representation of the fuselage and wing planform yields improved results over those obtained for the wing planform alone and the wing planform with thick fuselage representation.

Figure 16 presents the experiment and theory effects of the longitudinal aerodynamic characteristics for the unswept/trapezoidal configurations. The lift-curve-slope data on the left in figure 16(a) show that the lift-analysis method predicts equivalent lift-curve slopes for the two unswept trapezoidal wings and similar trends with the Mach number. The theory overpredicts the longitudinal stability of the configurations, incorrectly predicts the variation due to change in outboard wing size, but accurately predicts the effect of Mach number up to $M = 2.00$.

The lift-curve-slope data (fig. 16(a)) show that the computed lift-curve slope agrees well with the measured results. Theoretically, for a flat wing, the drag-due-to-lift factor is inversely proportional to the lift-curve slope. However, the drag-due-to-lift data (fig. 16(b)) show that the measured and the predicted values of $\Delta C_D/C_L^2$ differ for $M < 2.00$. This disagreement probably results from near-field interference effects affecting the induced drag characteristics but not necessarily the lift characteristics.

The drag-due-to-lift data (fig. 16(b)) also indicate that the lift-analysis method sufficiently predicts the effect of outboard wing size. The $C_{D,0}$ data (fig. 16(b)) show that the theoretical codes correctly predicted that the unswept/large-trapezoidal configuration has a significantly lower $C_{D,0}$ than the unswept/small-trapezoidal configuration. This observation contrasts with that of reference 11, which concluded that the same theoretical codes did not consistently predict the correct trend of zero-lift drag coefficient with changes in outboard wing planform shape; however, the theoretical codes did predict that the changes in $C_{D,0}$ with respect to changes in outboard planform shape were small, as was found experimentally. Also, the planforms from the investigation of reference 11 had equivalent A_{out}/S values.

In a linear-theory sense, an increase in span on a single-body configuration results in a less smooth

area distribution and thus a larger zero-lift drag. The increase in span associated with the large-trapezoidal outboard wing generates a less smooth area distribution as shown in figure 17, which presents the area distributions at different ϕ -cuts. However, for the multibody configuration, the effective area distribution, and thus the zero-lift drag, is determined by both the wing planform and the bodies. Therefore, the bodies soften the effect of the increased span on the effective area distribution, such that the resultant increase in zero-lift drag is not comparable to the increase in span and reference area. As shown in figure 18, a resultant lower theoretical $C_{D,0}$ occurs for most ϕ -cuts for the large-trapezoidal outboard wing when compared with the small-trapezoidal outboard wing; thus, a reduced zero-lift drag coefficient is predicted.

These results indicate that for low-fineness-ratio, multibody configurations, linear-theory methods adequately estimated the effect of outboard wing size and Mach number on the aerodynamic characteristics. Similar results were found on the swept/trapezoidal configurations, as shown in figure 19.

Inboard Panel Study

The effect of the inboard wing planform shape is examined in this section. The unswept inboard wing examined in reference 11 was used as the baseline for this study. As previously noted, the inboard wing constituted over half the total wing area. To determine the influence the inboard wing planform shape has on the multibody aerodynamics, an inboard swept 65° wing was constructed for comparison. The area and aspect ratio of the swept inboard wing had similar values to those of the unswept inboard wing. Figure 4 and table 1 contain details of the two inboard wings. The unswept and swept inboard wings were tested with the delta outboard wing swept 65° and the small-trapezoidal outboard wing swept 20° .

Experimental evaluation—force data. Figure 20 shows the lift, pitching-moment, and drag characteristics for the unswept-inboard configurations. Figure 21 shows the lift, pitching-moment, and drag characteristics for the swept-inboard configurations. The lift data in figures 20(a) and 21(a) show that, regardless of inboard planform shape, the trapezoidal outboard wing generates a slightly higher lift-curve slope than the more highly swept delta wing. However, at angles of attack higher than 8° , both outboard wings have a decrease in lift-curve slope and a corresponding change in the pitching-moment curve. These changes in the pitching-moment and

lift curves may be due to near-field interference effects, which are subsequently discussed in this paper and in references 10 and 11.

The drag data in figures 20(b) and 21(b) show that for $C_L > 0.2$ (which corresponds to $\alpha = 4^\circ$) the trapezoidal outboard configurations have lower drag coefficient values than their corresponding delta outboard configurations. However, the trapezoidal outboard wing has a higher zero-lift drag than the delta outboard wing for both unswept-inboard and swept-inboard configurations. For the unswept/small-trapezoidal configuration the zero-lift drag coefficient is 13 percent higher than the unswept/delta configuration. This change in zero-lift drag coefficient that results from a change in outboard planform shape is significantly less than that observed for single-body configurations (ref. 11). This difference probably results from two factors: the outboard wing composing only a portion of the total wing planform and the dominance of the near-field interference between the side bodies in reducing the zero-lift drag. The change in $C_{D,0}$ due to a change in outboard planform shape for the swept inboard configurations is even smaller—about 2.9 percent.

Figure 22 shows the longitudinal aerodynamic characteristics for the delta outboard configurations. Figure 23 shows the longitudinal characteristics for the small-trapezoidal outboard configurations. The data in figures 22 and 23 show that, regardless of the outboard wing planform shape, inboard wing leading-edge sweep has little effect on the lift, pitching moment, or drag-due-to-lift characteristics. However, the drag data in figures 22(b) and 23(b) show that increasing the sweep of the inboard wing decreases the zero-lift drag coefficient. The zero-lift drag coefficient of the unswept/delta configuration is 3.6 percent higher than the swept/delta configuration. The change in $C_{D,0}$ due to a change in inboard wing leading-edge sweep for the small-trapezoidal outboard configurations is 4.8 percent.

In figure 24, the aerodynamic performance characteristics at $M = 1.80$ for the four configurations are presented as the lift-to-drag ratio at three different lift-coefficient values. The swept-inboard configurations have higher L/D values than the corresponding unswept-inboard configurations over the lift-coefficient range. This result occurs because the zero-lift drag levels are lower for the swept-inboard configurations than for the unswept-inboard configurations. The changes in L/D due to variations in outboard planform shape are similar for both unswept and swept-inboard configurations. For both these configurations, the trapezoidal outboard wing results in a lower L/D value at the lowest C_L con-

dition because the trapezoidal outboard wing has a higher zero-lift drag than the delta outboard wing. At the highest C_L condition, the trapezoidal outboard configurations have a higher L/D value than their corresponding delta outboard configurations; this condition indicates that the improved drag-due-to-lift characteristics common to high-aspect-ratio planforms overcome the small zero-lift drag penalties associated with these wing planforms on the multi-body configuration.

The previous discussion and results were limited to a Mach number of 1.80; however, figure 25 shows the variations of the major aerodynamic parameters over the Mach number range of 1.60 to 2.16. The lift-curve-slope data presented on the left in figure 25(a) indicate that no significant impact occurs for changes in inboard planform shape for either the small-trapezoidal or the delta outboard configurations investigated. The longitudinal stability data presented on the right in figure 25(a) show that all four configurations have similar stability levels; that the center of aerodynamic center location is aft of the aerodynamic center. The data also show that the unswept and swept-inboard configurations have the same trend in longitudinal stability with respect to a change in outboard planform shape.

A more significant observation is that the longitudinal stability data, for both the delta and the small-trapezoidal outboard configuration, indicate that a swept-inboard planform provides the multibody configuration with slightly more longitudinal stability. This increased stability results from a rearward shift of the aerodynamic center that is greater than the aft movement of the computed moment center location. For the delta outboard configurations, the increase in longitudinal stability due to the swept inboard wing is nearly constant across the Mach number range. At $M = 1.60$ the increase in longitudinal stability due to the swept inboard planform is greater for the trapezoidal outboard wing than for the delta outboard wing at $M = 1.60$. However, the increase in longitudinal stability for the trapezoidal outboard wing decreases as Mach number increases. This effect is probably due to increased shock-induced separation with increasing Mach number over the trapezoidal outboard wing. All configurations have a longitudinal stability that remains constant or increases as Mach number increases up to $M = 2.00$.

Figure 25(b) shows the effect of inboard planform shape on the drag characteristics of the low-finesse-ratio, multibody configuration. The zero-lift drag data, shown on the left in figure 25(b), show that the swept-inboard configurations have lower zero-lift drag coefficient values than the corresponding

unswept-inboard configurations throughout the Mach number range. This trend corresponds to existing experimental data (refs. 21 and 22), which show that increasing leading-edge sweep reduces zero-lift drag coefficient. The data in figure 25(b) also show that the unswept-inboard configurations have a more rapid decrease in $C_{D,0}$ with an increase in Mach number than do the swept-inboard configurations. Reference 21 attributes this trend to the supersonic leading-edge condition of the unswept wing. However, another explanation for both trends in the $C_{D,0}$ data could be the interference effects between the side bodies. These interference effects are the mechanism by which zero-lift drag is reduced on multibody configurations, when compared with the zero-lift drag of single-body configurations. Specifically, the shock originating from one body impinges on an aft-facing portion of the other body, where the increase in pressure due to the shock results in an incremental reduction in drag. Thus, the swept-inboard wing probably influences the flow field between the side bodies in a more favorable manner; that is, the zero-lift drag is further reduced. The changes in $C_{D,0}$ for the swept-inboard configurations, due to variations in outboard planform shape and Mach number, are similar to those for the unswept-inboard configurations.

The drag-due-to-lift data, presented on the right in figure 25(b), show that the changes in $\Delta C_D/C_L^2$ due to changes in outboard planform shape are similar for both swept- and unswept-inboard wings. The drag-due-to-lift data also show that the influence of the inboard planform shape varies with Mach number. At the lower Mach numbers of 1.60 and 1.80, the swept-inboard configurations have a lower drag-due-to-lift parameter than the corresponding unswept-inboard configurations. However, at some higher Mach number ($M \approx 1.90$ for the trapezoidal outboard configuration and $M \approx 2.05$ for the delta outboard configuration) the trend reverses itself, such that the swept-inboard configurations have higher drag-due-to-lift levels than their corresponding unswept-inboard configurations. This variation with Mach number may result because the leading edge of the swept-inboard wing approaches a supersonic leading-edge condition as Mach number increases. However, the data in reference 21 show the opposite trend with Mach number for single-body configurations. That is, for single-body configurations, an unswept wing has lower drag-due-to-lift characteristics than a swept wing with a subsonic leading-edge condition. Then, as Mach number increases and the leading edge of the swept wing becomes supersonic, the unswept wing has higher drag-due-to-lift characteristics than the swept wing.

Thus, the trends observed on the multibody configurations suggest that the changes in drag-due-to-lift characteristics with changes in inboard planform shape probably result from the influence of the inboard planform on the near-field interference effects between the side bodies.

Experimental evaluation—flow-visualization data. Data obtained from several different techniques of flow visualization are presented in this section. The flow structures in the photographs are labeled with the notation in the section entitled "Symbols." In the previous discussion, several trends of the aerodynamic parameters were associated with near-field interference effects predominantly caused by the shock and vortex systems existing between the side bodies. Figure 26 contains a summary sketch of the flow pattern over the upper surface of the unswept/small-trapezoidal configuration. The oil-flow, schlieren, and vapor-screen data in figures 27 to 31 were used to derive this sketch. The flow-field patterns in this sketch are discussed with the flow-visualization data. Figures 27 and 28 show oil-flow and schlieren photographs obtained for the unswept/small-trapezoidal configuration at $M = 1.80$ and 2.16 and $\alpha = 0^\circ, 4^\circ$, and 8° . The oil-flow photographs shown in this paper are for the upper surface. The photographs for $\alpha = 0^\circ$ show that increasing the Mach number decreases the shock cone angle of the side-body nose shock and produces a rearward shift in the location of the intersection of the nose shocks and thus in the location of the impingement of the body nose shock onto the side body. Increasing the angle of attack also produces a rearward shift in the location of the impingement of the body nose shock onto the side body. This rearward shift with increasing angle of attack is caused by the rotation and distortion of the shock cone emanating from the nose of the side body. The growth of this shock system with angle of attack is also evident in figure 29, which presents the vapor-screen photographs obtained at $x = 12.3$ in. (which corresponds to the most-forward row of pressure orifices on the small-trapezoidal outboard wing) for $M = 1.60, 1.80, 2.00$, and 2.16 at $\alpha = 4^\circ, 8^\circ, 12^\circ$, and 16° .

For both Mach numbers, the oil-flow photographs (fig. 27) also show shocks that originate from the junction of the body and inboard wing. The oil-flow photographs and the corresponding schlieren photographs (fig. 28) show that the nose shock crosses the leading edge of the inboard wing and intersects with the shock from the junction of the body and inboard wing. The result is two weakened shocks that are shown in the oil-flow photograph for $\alpha = 8^\circ$ and $M = 2.16$. The oil-flow photographs (fig. 27) also

show that this shock system strengthens as angle of attack increases. This trend is also evident in figure 30, which presents the vapor-screen photographs obtained at $x = 17.7$ in. (which corresponds to the most-aft row of pressure orifices on the small-trapezoidal outboard wing) for $M = 1.80$ and 2.16 at $\alpha = 4^\circ, 8^\circ, 12^\circ$, and 16° . The growth of the shock system down the length of the inboard wing at $\alpha = 16^\circ$ and Mach numbers of 1.80 and 2.16 is shown in figure 31, which presents the vapor-screen photographs obtained at each of the four rows of pressure orifices on the small-trapezoidal outboard wing.

Another shock structure contributing to the near-field interference effects is the detached bow shock from the cone-wedge surface of the balance housing. A review of the exact solution for cones and wedges (ref. 23) indicates that at $M = 1.60$, the balance-housing wedge angle of 19° results in shock detachment at $\alpha = 0^\circ$. For Mach numbers greater than 1.60, the shock detaches at $\alpha > 0^\circ$, with the angle at which the bow shock detaches increasing with increasing Mach number. The schlieren photographs (fig. 28) show the protrusion of the balance-housing bow shock at the leading edge of the unswept inboard wing panel for $M = 1.80$ and $\alpha = 4^\circ$ and 8° . However, the bow shock is not evident in the schlieren photographs at $M = 2.16$. The growth of this balance-housing shock with angle of attack and Mach number is also shown in the vapor-screen photographs in figure 29. The growth of the bow shock from the balance housing in the chordwise direction on the inboard wing is shown in the vapor-screen photographs in figure 31.

Another structure contributing to the near-field interference effects is the side-body vortex system. The oil-flow photographs in figure 27 show a vortex on each side of both side bodies. These body vortices are small enough that they do not appear in the vapor-screen photographs in figure 30 for $\alpha \leq 8^\circ$. At $\alpha = 8^\circ$, the oil-flow photographs (fig. 27) show that, with increasing distance from the leading edge, the secondary separation line of each inboard side-body vortex system moves away from the side body onto the inboard wing. The secondary separation line of each outboard side-body vortex system also moves away from the side body onto the outboard wing. However, the secondary separation line of each inboard side-body vortex system moves farther away from the side body than the secondary separation line of each outboard side-body vortex system. This movement is also shown in the vapor-screen photographs in figure 31. At the most-forward longitudinal location in figure 31, both inboard and outboard

side-body vortices appear to sit on the side bodies. Moving in a chordwise direction, the core of the inboard vortex moves away from the side body, while the outboard vortex remains close to the side body and moves toward the top of the side body. The movement of both outboard and inboard side-body vortex systems in the inboard direction occurs because the swept, trapezoidal outboard wing has a greater compression field than the unswept inboard wing.

The development of the inboard shock system and the side-body vortex system is similar for the unswept/delta configuration, as shown in the summary sketch (fig. 32) and in the flow-visualization data (figs. 33 to 36). Thus, the outboard planform shape does not significantly affect the inboard side-body vortex and shock systems.

The flow structures between the side bodies are affected by the shape of the inboard planform. Figure 37 is a summary sketch of the flow field over the swept/small-trapezoidal configuration. Figures 38 and 39 are oil-flow and schlieren photographs for the swept/small-trapezoidal configuration at $M = 1.80$ and 2.16 and $\alpha = 0^\circ, 4^\circ$, and 8° . The swept/small-trapezoidal configuration has two shock systems occurring over the swept inboard wing. The schlieren photographs for $M = 1.80$ (fig. 39) clearly show that the side-body nose shock impinges the opposing side body ahead of the junction of the body and inboard wing. The nose shock angle is 35.5° . For $M = 1.80$, the Mach angle of the bow shock of the swept inboard wing is about 33.75° . Because the swept inboard wing is located behind the nose shock system, the local Mach number is less than 1.80, so the bow shock angle is greater than 33.75° . The bow shock of the swept inboard wing has probably merged with the nose shocks. Therefore, the first shock system over the swept inboard wing is the reflection of the merged nose and wing bow shock off the side body ahead of the junction of the body and inboard wing. The second shock system evident in the oil-flow photographs (fig. 38) is the result of the junction of the body and inboard wing. Both shock systems strengthen as angle of attack increases; this effect is evident in both the oil-flow photographs in figure 38 and in figures 40 and 41, which present the vapor-screen photographs obtained at $x = 12.3$ in. and $x = 17.7$ in. for $M = 1.60, 1.80, 2.00$, and 2.16 at $\alpha = 4^\circ, 8^\circ, 12^\circ$, and 16° .

In contrast, at $M = 2.16$ the overall shock system for the swept/small-trapezoidal configuration has three shock systems. Instead of the nose shock and wing bow shocks merging, the nose shock crosses the leading edge of the swept inboard wing, as shown

in the schlieren photographs (fig. 39). As the nose shock crosses the inboard wing, it intersects with the other two shock systems before impinging onto the side body. The schlieren photographs (fig. 39) show the wing bow shock forming just ahead of the leading edge of the swept inboard wing. Most of the swept inboard wing is located behind the nose shock; thus, the local Mach number is lower than the free-stream Mach number of 2.16. Because a wing swept 65° develops a supersonic leading-edge condition for $M > 2.00$, the swept inboard wing probably approaches a supersonic leading-edge condition when the free-stream Mach number is 2.16. Therefore, the second shock system results because the bow shock of the inboard wing panel impinges on the body close to the body-wing junction. The third shock system is the result of the junction of the body and swept inboard wing.

As shown in the data for the unswept/small-trapezoidal multibody configuration (figs. 29 and 30), the bow shock from the balance housing detached from the leading edge of the inboard wing and rose over the inboard wing. The schlieren and vapor-screen photographs (figs. 39 and 40) show no evidence of the bow shock from the balance housing forming over the inboard wing of the swept/small-trapezoidal configuration. The swept inboard wing extends in front of the balance-housing system (fig. 4) and apparently prevents the balance-housing shock from extending over the swept inboard wing.

The side-body vortex system is shown in the vapor-screen photographs in figure 41 for $\alpha > 8^\circ$ and $M = 1.80$ and 2.16. Figures 37 and 41 show that the inboard side-body vortex system does not move as far away from the side body as it does for the unswept/small-trapezoidal configuration (figs. 27 and 30). One reason for this trend is that the swept inboard wing has a greater compression field than the unswept inboard wing. However, another possible reason is the interaction of the side-body vortex with the shock systems. The oil-flow photographs (fig. 38) show shock-induced separation occurring at the point where the first shock system impinges on the side body (junction of the body and inboard wing). This shock-induced separation is shown in the vapor-screen photographs in figure 42, which shows the development of the shock systems and side-body vortices down the length of the inboard wing for $M = 1.80$ and 2.16 at $\alpha = 16^\circ$. At the most-forward station, a series of separated flow regions occurs just inboard of the side bodies. Upon moving in a chordwise direction on the wing, the shock-induced separation grows and eventually merges with the side-body vortex system, which is pulled down from the top

of the side body. (See fig. 42.) This interaction of the shock-induced separation and the inboard side-body vortex system is possibly one reason why the inboard side-body vortex system for the swept/small-trapezoidal configuration does not move as far away from the side body as it did for the unswept/small-trapezoidal configuration.

As previously discussed, a series of separated flow regions occurs just inboard of the side bodies (fig. 42). This effect corresponds to a slightly different shock structure for the bow shock of the inboard wing panel for $\alpha = 16^\circ$ at $M = 2.16$ and 2.00. (See fig. 41.) There appears to be two shocks where there was just one at $\alpha = 8^\circ$.

The data in figures 37 and 40 to 42 show that the outboard side-body vortex system for the swept/small-trapezoidal configuration moves farther away from the body than it does for the unswept/small-trapezoidal configuration (figs. 26 and 29 to 31). The inboard side-body vortex on the swept/small-trapezoidal multibody configuration remains closer to the side body than it does for the unswept/small-trapezoidal multibody configuration. Apparently, in remaining closer to the side body, the inboard side-body vortex system forces the outboard side-body vortex system farther away from the side body than it does for the unswept/small-trapezoidal multibody configuration.

The development of the inboard shock system and inboard side-body vortex system for the swept/delta configuration is similar to that for the swept/small-trapezoidal configuration. (See the summary sketch in fig. 43 and the flow-visualization data in figs. 44 to 47.) Thus, the outboard planform shape does not significantly affect the inboard side-body vortex system and the shock system for the swept inboard wing. This trend was also observed for the unswept inboard wing.

For all four configurations, the side-body vortex system and the shock system appear to gain strength at $\alpha > 8^\circ$. These observations suggest that the break at $\alpha = 8^\circ$ in the lift and pitching-moment curves shown in figures 20(a) and 21(a) is due to the flow structures between the side bodies.

The development of the shock system between the side bodies differs with inboard planform shape. This observation corresponds to a decrease in the zero-lift drag coefficient with an increase in the leading-edge sweep of the inboard wing (fig. 25(b)). The interference effects between the side bodies are the mechanisms by which drag is reduced; thus, multibody configurations have less drag than single-body configurations. Specifically, the shock originating from

one body impinges on the other body in a region where the increase in pressure due to the shock gives a negative incremental value of drag because of the higher pressure acting upon the aft-facing slope of the body. For the unswept-inboard configurations, the nose shock impinged on the side body downstream of the junction of the body and inboard wing at both $M = 1.80$ and 2.16 (figs. 26 and 32). Because the nose shock traveled across the unswept inboard wing, the nose shock lost some strength from interacting with the compression field of the unswept inboard wing and from interacting with the shock from the junction of the body and inboard wing. However, the swept-inboard configurations had a shock that impinged on the side body ahead of this junction (figs. 37 and 43) and was, therefore, stronger than that of the unswept-inboard configurations. Because the swept-inboard configuration has a stronger shock, the increased pressure then acts over the remaining body surface, which has a longitudinal orientation mostly aftward, and a reduction in pressure drag occurs. However, the greater drag reduction of the swept-inboard configuration has probably been compromised somewhat by the pressure decrease on the body; this decrease is caused by shock-induced separation (figs. 38 and 44).

Figure 25(b) also shows that as Mach number increases the difference in the zero-lift drag coefficient between corresponding unswept- and swept-inboard configurations decreases. This observation can also be related to the development of the shock system between the side bodies. As noted previously, the shock system for the swept-inboard configurations consisted of a shock from the nose of each side body, a bow shock from the swept inboard wing, and a shock from the junction of the body and inboard wing. As Mach number increases, the bow shock of the inboard wing approaches the leading edge. (See figs. 39 and 46.) Eventually the bow shock becomes attached as the inboard wing changes to a supersonic leading-edge condition. The shock system over the inboard wing is then composed of the nose shock and the shock from the junction of the body and inboard wing. Therefore, as Mach number increases, the swept-inboard configurations approach the same type of shock system as the one on the unswept-inboard configurations.

At angle of attack, the differences in shock systems between the swept- and unswept-inboard configurations are still evident. Thus, the drag for the swept-inboard configurations at a lift condition can be expected to be lower than that of the unswept-inboard configurations. The drag-due-to-lift data in figure 25(b) show that, at the lower Mach num-

bers, the swept-inboard configurations do indeed have lower drag-due-to-lift characteristics than their corresponding unswept-inboard configurations. This trend is opposite to the one observed in reference 21, which showed that for constant aspect ratio, an unswept wing has lower drag-due-to-lift characteristics than a swept wing with a supersonic leading-edge condition. For the higher Mach numbers, the drag-due-to-lift characteristics of the swept-inboard configurations are higher than their corresponding unswept-inboard configurations. This observation corresponds to an increase in the amount of shock-induced separation occurring at the body-wing junction with an increase in Mach number. (See figs. 38 and 44.)

Another difference in the shock system between the side bodies for the unswept- and swept-inboard configurations is the presence of the bow shock from the balance housing. As previously discussed, the cone-wedge surface of the balance housing generated a detached shock for all Mach numbers at $\alpha > 0^\circ$, with the angle of attack at which the bow shock detaches determined by the Mach number. For the unswept inboard wing, this bow shock detached from the leading edge of the inboard wing and rose over the inboard wing. (See figs. 28, 29, and 31.) The swept inboard wing extends in front of the balance-housing system (fig. 4) and thus prevents the bow shock from the balance housing from rising over the inboard wing panel. (See figs. 39, 40, and 42.) The existence of this bow shock over the inboard wing probably weakens the nose shock system and thus reduces the drag reduction due to the impingement of the nose shock on the side body.

The vapor-screen photographs in figure 35 not only illustrate the flow development between the side bodies with angle of attack but also show the development of the flow field over the outboard wing of the unswept/delta configuration with angle of attack at $M = 1.60, 1.80, 2.00$, and 2.16 . These photographs show that the primary flow structure over the delta outboard wing is that of a leading-edge vortex. For a given Mach number, this vortex becomes larger as the angle of attack increases, and the core of the vortex eventually lifts off the surface of the wing. The vapor-screen photographs also show that for a given angle of attack, the leading-edge vortex becomes elongated as Mach number increases. These observations correspond with experimental observations for delta wings by Miller and Wood (ref. 24) and many others. Figure 48(a) presents the flow classification chart constructed by Miller and Wood (ref. 24) and modified by McMillin, Thomas, and Murman (ref. 25). The chart identifies six flow fields over thin, sharp-edged

delta wings based upon the angle of attack and Mach number normal to the leading edge. Figure 48(a) also shows the locations of a wing swept 65° and a wing swept 20° at the Mach numbers and angles of attack in this investigation. Figure 48(b) presents sketches of the six flow fields.

The vapor-screen photographs (fig. 46) show the development of the flow field over the outboard wing of the swept/delta configuration with angle of attack at $M = 1.60, 1.80, 2.00$, and 2.16 . A comparison of these photographs with those of the unswept/delta configuration (fig. 35) shows that the inboard planform shape does not significantly influence the development of the leading-edge vortex with angle of attack or Mach number.

To relate the small-trapezoidal outboard wing with the flow classification chart (fig. 48), vapor-screen photographs upstream of the wing tip must be used. Figure 29 shows the vapor-screen photographs from the most-forward longitudinal location on the unswept/small-trapezoidal configuration. Figure 40 contains similar photographs for the swept/small-trapezoidal configuration. Photographs are presented at $\alpha = 4^\circ, 8^\circ, 12^\circ$, and 16° and at $M = 1.60, 1.80, 2.00$, and 2.16 . The vapor-screen photographs for both small-trapezoidal outboard configurations show attached flow at the leading edge of the small-trapezoidal outboard wing at each Mach number through the angle-of-attack range. This observation corresponds to the location of a wing swept 20° on the flow classification chart in figure 48(a).

The oil-flow photographs (figs. 27 and 38) for the small-trapezoidal outboard configurations also show attached flow at the leading edge of the small-trapezoidal outboard wing. These photographs and the schlieren photographs in figures 28 and 39 show a shock occurring over the surface of the trapezoidal outboard wing. The shock appears to emanate from the junction of the body and outboard wing, where the tab of the trapezoidal wing protrudes from the side body as shown in figure 6(a). The schlieren photographs of the unswept/large-trapezoidal configuration in figure 49 also show a shock over the outboard wing. This shock emanates from the body-wing junction. Because the large trapezoidal outboard wing did not have a tab, the shock over the small-trapezoidal outboard wing is probably a result of the body-wing junction and not the tab of the trapezoidal wing.

The growth of the shock of the body and outboard wing junction in the streamwise direction for the unswept/small-trapezoidal multibody configuration at $\alpha = 16^\circ$ is shown in the vapor-screen photographs

in figure 31. Also evident is a shock emanating from the tip of the small-trapezoidal wing. This shock corresponds to the cross flow shown at the tip in the oil-flow photographs (fig. 27) and the tip vortex shown in the schlieren photographs (fig. 28). The vapor-screen photographs in figure 31 also show the formation of separation beneath the body and outboard wing junction shock. This shock-induced separation does not occur until the most-aft longitudinal station.

However, on the swept/small-trapezoidal configuration, the shock-induced separation occurs farther upstream, as shown in figure 42. Also, the angle of the body and outboard wing junction shock is slightly larger on the swept/small-trapezoidal configuration. (See figs. 27, 31, 38, and 42.) These observations imply that the body and outboard wing junction shock is stronger on the swept/small-trapezoidal configuration than on the unswept/small-trapezoidal configuration. One explanation is that the swept-inboard configuration does not have the balance-housing bow shock sitting over the inboard wing as does the unswept-inboard configuration. Another explanation is that the swept inboard wing does not reduce the upwash on the small-trapezoidal outboard wing as much as the unswept inboard wing because of the more-aft location of the intersection of the body and inboard wing on the swept-inboard configuration.

Experimental evaluation—surface pressure coefficient data. The vapor-screen photographs discussed in the previous section were obtained at the longitudinal locations at which surface-pressure data were obtained on the outboard wing. Spanwise pressure distributions were obtained on the delta outboard wing at $x' = 0.4c, 0.6c$, and $0.8c$ (where x' is measured from the apex of the outboard wing and c is the root chord of the outboard wing, as shown in fig. 4(e)), and they were obtained at 10 nominal angles of attack. Figure 50 shows the effect of angle of attack on the spanwise surface pressure coefficient distributions on the delta outboard wing for the unswept/delta configuration at $M = 1.60, 1.80, 2.00$, and 2.16 . For each Mach number, the surface pressure coefficient distributions illustrate the development of a leading-edge vortex with increasing angle of attack. (See the vapor-screen photographs in fig. 35.) The sharp change in surface pressure coefficient near $\eta = 0.5$ marks the edge of the primary vortex (i.e., the primary reattachment line).

Figure 51 shows the effect of Mach number on the surface pressure coefficient distribution for $\alpha \approx 4^\circ, 8^\circ, 12^\circ$, and 16° . The data show that as Mach number increases, the strength of the primary vortex decreases. In fact, at the higher Mach

numbers ($M \geq 2.00$), the leading-edge vortex forms at a higher angle of attack ($\alpha > 4^\circ$) than it does at the lower Mach numbers ($\alpha \leq 4^\circ$). These observations agree with those made for the vapor-screen photographs (fig. 35) and with the location of a wing swept 65° on the flow classification chart (fig. 48(a)).

Figure 52 shows the effect of inboard wing planform shape on the surface pressure coefficient distribution over the delta outboard wing. The surface pressure coefficient distributions for both unswept- and swept-inboard configurations at the $x' = 0.4c$, $0.6c$, and $0.8c$ stations on the delta outboard wing are presented at $\alpha \approx 4^\circ$, 8° , 12° , and 16° for Mach numbers of 1.60, 1.80, 2.00, and 2.16. For each Mach number, the surface pressure coefficients at the $x' = 0.4c$ station are greater (i.e., more positive) for the swept-inboard configuration. Apparently, the outboard wing at $x' = 0.4c$ station experiences a lower local flow incidence when the swept inboard wing is attached. The reduced upwash on the outboard wing for the swept/delta multibody configuration probably occurs because of the increased sweep of the inboard wing and the location of the intersection of the inboard wing and body. Also, as shown in figure 35, the inboard swept wing has shock-induced separation occurring near the junction of the body and inboard wing. This separation can possibly produce a downwash on the outboard wing that effectively lowers the local flow incidence angle on the forward portion of the outboard wing. These explanations are supported by noting that farther downstream the surface pressure distributions of the unswept- and swept-inboard configurations are similar, especially outboard toward the leading edge. This similarity indicates that farther downstream away from the location of the junction of the body and inboard wing, the unswept- and swept-inboard configurations are nearly similar local flow incidences.

However, the data in figure 52 show that for $M > 1.60$ at $x' = 0.6c$ and $0.8c$, the most-inboard surface pressure coefficients for the unswept-inboard configuration are greater (i.e., more positive) than those for the swept-inboard configuration. This observation corresponds to the outboard side-body vortex system that moves farther away from the body with an increase in inboard leading-edge sweep.

Spanwise pressure distributions were obtained on the small-trapezoidal outboard wing at $x' = 0.2c$, $0.4c$, $0.6c$, and $0.8c$ (fig. 4(f)) and at 10 nominal angles of attack. Figure 53 shows the effect of angle of attack on the spanwise surface pressure coefficient distributions on the small-trapezoidal outboard wing for the unswept/small-trapezoidal configuration at $M = 1.60$, 1.80, 2.00, and 2.16. These distributions

show attached flow at the leading edge with a nearly constant surface pressure coefficient across the span. For $\alpha > 4^\circ$, an inflection in the surface pressure coefficient distribution occurs and travels across the span with increasing longitudinal station. This inflection corresponds to the shock emanating at the junction of the body and outboard wing. The shock angles for $M = 1.80$ and 2.16 were obtained from figure 27 and are shown in figures 53(b) and 53(d).

Figure 54 shows the effect of Mach number on the surface pressure coefficient distribution over the small-trapezoidal outboard wing for $\alpha \approx 4^\circ$, 8° , 12° , and 16° . The data show that as Mach number increases the surface pressure coefficient over the top of the wing increases (becomes more positive) but the trend with angle of attack remains the same. The data in figure 54 (especially in fig. 54(c)) show that the inflection in the distribution moves inboard with increasing Mach number. This effect corresponds with the shock angle decreasing with increasing Mach number. The data in figure 54 also show that the inflection in the surface pressure coefficient distribution moves slightly inboard with increasing angle of attack. This effect is caused by the rotation and distortion of the shock cone with increasing angle of attack.

Figure 55 shows the effect of inboard planform shape on the surface pressure coefficient distribution over the small-trapezoidal outboard wing. The surface pressure coefficient distributions for both unswept- and swept-inboard configurations at the $x' = 0.2c$, $0.4c$, $0.6c$, and $0.8c$ stations on the small-trapezoidal outboard wing are presented at $\alpha \approx 4^\circ$, 8° , 12° , and 16° for Mach numbers of 1.60, 1.80, 2.00, and 2.16. As for the delta outboard configurations (fig. 52), the most-inboard surface pressure coefficients for the swept/small-trapezoidal configuration are greater (more positive) than those for the unswept/small-trapezoidal configuration at the more-forward longitudinal locations. However, this difference is probably not due to a reduced upwash from an increase in inboard leading-edge sweep because the junction of the body and inboard wing occurs farther aft than the apex of the trapezoidal outboard wing. The data in figure 55 show that this deficit propagates across the span of the wing with increasing longitudinal location. The shock angles for $M = 1.80$ and 2.16 were obtained from figure 27 and are shown in figures 55(b) and 55(d). This deficit corresponds to the shock emanating at the junction of the body and outboard wing; this relationship indicates that the shock is stronger for the swept-inboard configuration than for the unswept-inboard configuration. This explanation corresponds

to the observations made for the flow-visualization data (figs. 27, 31, 33, and 42). Resulting from an increase in leading-edge sweep, the stronger body and outboard wing junction shock due to an increase in inboard leading-edge sweep coincides with two other events. First, the junction of the body and inboard wing occurs downstream of the trapezoidal outboard wing apex such that the downwash effects on the outboard leading edge are minimized. Second, the balance-housing bow shock is not present on the swept-inboard configuration.

As for the delta-outboard multibody configurations (fig. 52) the data in figure 55 show that the most-inboard surface pressure coefficients for the unswept/small-trapezoidal configuration are greater (more positive) than those for the swept/small-trapezoidal configuration at the more-forward longitudinal locations. The fact that this trend occurs regardless of outboard wing planform shape supports the explanation that this trend is connected with the outboard side-body vortex system moving further away from the side body with an increase in inboard leading-edge sweep.

Theoretical analysis. A comparison between experiment and theory for the longitudinal aerodynamic characteristics of the unswept- and swept-inboard configurations is shown in figure 56. The lift-curve-slope data on the left in figure 56(a) show that the SDAS code predicts the correct trends with respect to variations in inboard planform shape and Mach number. On the right in figure 56(a), the longitudinal stability data show that the theory underpredicts the instability of the configurations, as for single-body configurations. Also, the experimental data show that up to $M = 2.00$, the multibody configuration has increasing stability or nearly constant stability with increasing Mach number. This trend is the opposite of that typically found on single-body aircraft at supersonic speeds and is predicted correctly by the SDAS code. The longitudinal stability data in figure 56(a) also show that up to $M = 2.00$, the theory correctly predicts the effect of inboard wing planform shape but incorrectly predicts the effect of outboard wing planform shape across the Mach number range.

The theoretical drag characteristics are compared with the experimental results in figure 56(b). The zero-lift drag coefficient data on the left in figure 56(b) show that the theory does not consistently predict that adding leading-edge sweep to the inboard wing lowers the $C_{D,0}$, as was found experimentally. The predicted increment in $C_{D,0}$ due to a change in inboard wing planform shape is constant with increasing Mach number and does not agree

with the experiment. The levels of the predicted increments in $C_{D,0}$ due to a change in inboard or outboard wing planform shape do not agree with the experiment. However, the change in $C_{D,0}$ with any change in planform shape was small, as was found experimentally.

Comparisons of the drag-due-to-lift data presented on the right in figure 56(b) show that the SDAS code closely approximates the effects of outboard wing planform shape across the Mach number range. However, the theory inconsistently predicts the effect of inboard wing planform shape on the drag-due-to-lift characteristics across the Mach number range. The theory predicts that the swept-inboard configurations have lower drag-due-to-lift values than their corresponding unswept-inboard configurations across the Mach number range. However, the experimental data show that the swept-inboard configurations have lower drag-due-to-lift values than their corresponding unswept-inboard configurations at Mach numbers less than about 2.00.

Side Bodies-Off Study

As previously discussed, the flow field between the side bodies results in near-field interference that influences the aerodynamics of the multibody configurations. This section examines the effect of removing the side bodies from the unswept-inboard configurations. (See figs. 3 and 6.) Flow-visualization and surface-pressure data were obtained on the unswept/delta wing-alone and the unswept/small-trapezoidal wing-alone configurations.

Experimental evaluation—flow-visualization data. Figure 57 is a summary sketch of the flow-field pattern on the unswept/small-trapezoidal wing-alone configuration. This sketch is based on the data in figures 58 to 61. Figure 58 shows oil-flow photographs obtained for the unswept/small-trapezoidal wing-alone configuration at $M = 1.80$ and 2.16 and $\alpha = 0^\circ, 4^\circ$, and 8° . The flow over the inboard wing is uniform at the lower angles of attack ($\alpha = 0^\circ$ and 4°). At $\alpha = 8^\circ$ and $M = 1.80$, cross flow begins to form on the forward portion of the inboard wing. This cross flow is attributed to the bow shock from the balance housing, which strengthens as angle of attack increases and spills over onto the inboard wing. The protrusion of the balance-housing shock at the leading edge of the inboard wing is shown in the schlieren photographs in figure 28 for the unswept/small-trapezoidal multibody configuration. These schlieren photographs also show that the angle of attack at which the bow shock detaches increases with increasing Mach number. This

observation explains why the cross flow on the inboard wing at $\alpha = 8^\circ$ is less prevalent at $M = 2.16$.

Vapor-screen photographs showing the development of the flow field over the unswept/small-trapezoidal wing-alone configuration with angle of attack are presented in figures 59 and 60. Figure 59 presents the vapor-screen photographs at the most-forward pressure orifice station on the unswept/small-trapezoidal wing-alone configuration for $\alpha = 4^\circ, 8^\circ, 12^\circ$, and 16° at $M = 1.60, 1.80, 2.00$, and 2.16 . The corresponding photographs at the most-aft pressure orifice station are presented in figure 60. These photographs show a symmetrical pair of shocks forming over the inboard wing at $\alpha > 8^\circ$. The shocks intersect at some point downstream of the leading edge. The development of this shock system in the chordwise direction of the inboard wing is illustrated in the vapor-screen photographs in figure 61 for $\alpha = 16^\circ$ and $M = 1.80$ and 2.16 . This shock system is probably the result of shocks emanating from the junction of the inboard wing and the tab of the outboard wing. (See fig. 6(f).) The outboard portion of this shock system is evident in the oil-flow pattern (fig. 58) on the outboard wing for $\alpha \leq 8^\circ$. The inboard portion of the shock system from the inboard wing and tab junction does not form over the inboard wing at the low angles of attack because of the expansion occurring at the leading edge of the inboard wing. However, at $\alpha > 8^\circ$ conditions, the shock from the inboard wing and tab junction strengthens enough to form over the inboard wing.

The oil-flow photographs in figure 58 and the vapor-screen photographs in figure 59 also show that the flow over the outboard wing of the unswept/small-trapezoidal wing-alone configuration is attached at the leading edge, as for the unswept/small-trapezoidal multibody configuration (figs. 27 and 29). The oil-flow data in figure 58 show two shocks occurring over the outboard wing. The first shock emanates from the junction of the inboard wing and tab, as discussed in the previous paragraph, and the second emanates from the junction of the outboard tab and wing. The vapor-screen photographs in figures 59 to 61 do not show shock-induced separation occurring on the outboard wing of the unswept/small-trapezoidal wing-alone configuration, as for the unswept/small-trapezoidal multibody configuration. (See figs. 29 to 31.) However, the vapor-screen photographs do show a vortex just inboard of the two shock systems. This vortex does not appear to be shock induced because it appears at low angles of attack and at the most-forward longitudinal station. The vortex is probably shed from the junction

of the tab and outboard wing. Figure 61 shows the growth of these shocks and the vortex in the chordwise direction on the outboard wing for $\alpha = 16^\circ$ and $M = 1.80$ and 2.16 .

The oil-flow data in figure 58 show cross flow occurring at the tip of the outboard wing of the unswept/small-trapezoidal wing-alone configuration at $\alpha = 0^\circ$ and 4° . These observations correspond to those in figure 61, which show a shock emanating from the tip of the outboard wing. This flow feature was also evident on the small-trapezoidal outboard multibody configurations.

Figure 62 shows the flow-field pattern on the unswept/delta wing-alone configuration. This sketch is based on the data in figures 63 to 65. The oil-flow photographs and vapor-screen photographs (figs. 63 to 65) show the same type of flow pattern over the inboard wing as the one for the unswept/small-trapezoidal wing-alone configuration (figs. 58 to 61). As with the side bodies on, the outboard planform shape does not appear to significantly influence the flow pattern over the inboard wing.

The oil-flow photographs in figure 63 and the vapor-screen photographs in figures 64 and 65 also show that the primary flow structure over the outboard wing of the unswept/delta wing-alone configuration is a leading-edge vortex. For the unswept/delta wing-alone configuration, for a given Mach number, the vortex on the outboard wing becomes larger with an increase in angle of attack and the core of the vortex eventually lifts off the surface of the wing. For a given angle of attack, the leading-edge vortex becomes elongated as Mach number increases. These trends were also observed with the unswept/delta multibody configuration. (See figs. 33, 35, and 36.) Thus, the presence of the side bodies does not significantly impact the formation of the leading-edge vortex over the delta outboard wing panel.

Experimental evaluation—surface pressure coefficient data. Figure 66 shows the effect of angle of attack on the spanwise surface pressure coefficient distributions on the outboard wing for the unswept/delta wing-alone configuration at $M = 1.60, 1.80, 2.00$, and 2.16 . The surface-pressure data at $x = 0.4c, 0.6c$, and $0.8c$ at 30 different angles of attack are presented. For each Mach number, the surface pressure coefficient distributions illustrate the development of a leading-edge vortex as angle of attack increases, as shown in the vapor-screen photographs in figure 64. The abrupt change in surface pressure near $\eta = 0.5$ marks the edge of the primary vortex.

Figure 67 shows the effect of Mach number on the surface pressure coefficient distribution over the outboard wing of the unswept/delta wing-alone configuration at $\alpha = 4^\circ, 8^\circ, 12^\circ$, and 16° . The data show that as Mach number increases the strength of the primary vortex decreases. In fact, at the higher Mach numbers ($M \geq 1.80$), the leading-edge vortex does not form until a higher angle of attack ($\alpha > 4^\circ$) than it formed at $M = 1.60$ ($\alpha < 4^\circ$). These observations correspond to the observations made for the vapor-screen photographs in figure 64.

These observations correspond to those made for the unswept/delta multibody configuration (fig. 50). Figure 68 shows the effect of the side bodies on the surface pressure coefficient distribution over the outboard wing of the unswept/delta wing planform. The surface pressure coefficient distributions with and without the side bodies attached on the unswept/delta wing planform are presented at $\alpha \approx 4^\circ, 8^\circ, 12^\circ$, and 16° for each Mach number and at the $x' = 0.4c, 0.6c$, and $0.8c$ stations. Overall, the surface pressure coefficient distributions between the two configurations agree. The largest differences in the distributions for the bodies-on and the bodies-off configurations occur at the $x' = 0.4c$ station. Farther downstream, the surface pressure coefficient distributions of the bodies-on and bodies-off configurations are more equivalent. Also, at $\alpha \geq 8^\circ$ the edge of the primary vortex for the bodies-off configuration is farther inboard than it is for the bodies-on configuration. One explanation for these observations is that the side bodies act as a fence impeding inboard vortex growth with increasing angle of attack and increasing x' .

Other explanations for the discrepancies between the distributions of the bodies-on and bodies-off configurations relate to the local flow conditions at the leading edge of the outboard wing. The side body can be expected to generate an upwash over the outboard wing; this upwash increases the local flow incidence angle. An increase in flow incidence angle increases the strength of the leading-edge vortex. The shock from the nose of the side body lowers the local Mach number from the free-stream conditions. A lower Mach number strengthens the vortex. The influence of these two parameters does not appear to be significant because the surface pressure coefficients between the bodies-on and bodies-off configurations were found to be equivalent near the leading edge.

Figure 69 shows the effect of angle of attack on the spanwise surface pressure coefficient distributions over the outboard wing of the unswept/small-trapezoidal wing-alone configuration at $M = 1.60, 1.80, 2.00$, and 2.16 . These distributions show at-

tached flow at the leading edge with a nearly constant surface pressure coefficient across the span. These observations correspond with the vapor-screen photographs in figures 59 to 61. For $\alpha > 4^\circ$, two inflections in the surface pressure coefficient distribution occur and travel across the span with increasing longitudinal station. The inboard inflection evident at $x' = 0.2c$ corresponds to the shock emanating at the junction of the tab and outboard wing. The second inflection corresponds to the shock from the junction of the inboard wing and tab. The tab and inboard-wing junction shock does not have as obvious an influence on the surface pressure coefficient distribution and thus must be weaker. The shock angles for $M = 1.80$ and 2.16 were obtained from figure 58 and are shown in figures 69(b) and 69(d).

Figure 70 shows the effect of Mach number on the surface pressure coefficient distribution over the outboard wing for the unswept/small-trapezoidal wing-alone configuration at $\alpha = 4^\circ, 8^\circ, 12^\circ$, and 16° . The data show that as Mach number increases the surface pressure coefficient over the top of the wing increases (becomes more positive) but the trend with angle of attack remains the same. The data in figure 70 (especially in fig. 70(c)) show that the inflection in the distribution moves inboard with increasing Mach number. This effect corresponds to the shock angle decreasing with increasing Mach number. The data in figure 70 also show that the inflection in the surface pressure coefficient distribution moves slightly inboard with increasing angle of attack. This effect is due to the rotation and distortion of the shock cone with increasing angle of attack.

The previous observations correspond to those made for the unswept/small-trapezoidal multibody configuration (figs. 63 and 67). Figure 71 shows the effect of the side body on the surface pressure coefficient distribution over the outboard wing of the unswept/small-trapezoidal wing planform. The surface pressure coefficient distributions for both the bodies-on and the bodies-off configuration at the $x' = 0.2c, 0.4c, 0.6c$, and $0.8c$ stations on the small-trapezoidal outboard wing are presented at $\alpha \approx 4^\circ, 8^\circ, 12^\circ$, and 16° for each Mach number. The data in figure 71 show two inflections in the distribution of the bodies-off configuration, whereas the bodies-on configuration has only one inflection in the surface pressure distribution. The shocks over the outboard wing are shown in figures 71(b) and 71(d). For $x' = 0.4c$, a deficit in the surface pressure distribution occurs when the inboard surface pressure coefficients for the bodies-off configuration are lower (i.e., more negative) than those for the bodies-on configuration. This deficit travels across the span of the

wing with increasing longitudinal station and corresponds to the location of the shock of the tab and outboard wing. This shock is apparently stronger for the bodies-off configuration than for the bodies-on configuration. This result probably occurs because the nose shocks reduce the local Mach number for the bodies-on configuration. However, as figures 26 and 57 show, shock-induced separation associated with the shock of the tab and outboard wing occurred on the small-trapezoidal outboard wing with the bodies on but not with the bodies off. This observation corresponds to the existence of a second shock on the outboard wing with the bodies off. At $x' = 0.2c$ the bodies-on configuration has lower (i.e., more negative) surface pressure coefficients than the bodies-off configuration at $\eta \approx 0.5$. This deficit travels across the span of the wing with increasing longitudinal station and corresponds to the location of the shock on the inboard wing and tab.

Concluding Remarks

An experimental and theoretical investigation on the effect of the wing planform on the supersonic aerodynamics of a low-fineness-ratio, multibody configuration has been conducted in the Langley Unitary Plan Wind Tunnel at Mach numbers of 1.60, 1.80, 2.00, and 2.16. Three uncambered outboard wing panels were tested on a low-fineness-ratio, twin-body configuration. The inboard wing planform variations were an unswept leading edge and a swept leading edge. The outboard wing planform variations were a delta with a 65° leading-edge sweep, a trapezoidal with a 20° leading-edge sweep, and a trapezoidal with a 20° leading-edge sweep and with increased span and area. The two inboard wing variations included an unswept planform and a planform with a 65° leading-edge sweep. Also examined was the effect of side body (on versus off) on the multibody configuration with the unswept inboard wing. Longitudinal aerodynamic force and moment data, surface-pressure data, and flow-visualization data were obtained for the eight configurations examined.

The experimental data for the small-trapezoidal and large-trapezoidal outboard configurations showed that the ratio of outboard wing area to total wing area influenced the lift-to-drag characteristics for the multibody configuration. However, the improved aerodynamic performance with the large-trapezoidal outboard configuration was due to a reduced zero-lift drag coefficient. The outboard wing to total wing area ratio had little effect on the lift and drag-due-to-lift characteristics. The large-trapezoidal outboard configuration also had slightly better pitching moment at higher Mach numbers.

The experimental data for the unswept- and swept-inboard configurations showed that adding leading-edge sweep to the inboard wing had little effect on the lift and pitching-moment characteristics. However, adding sweep to the inboard wing slightly improved the zero-lift drag; this addition resulted in a higher lift-to-drag ratio. The difference in zero-lift drag coefficient between unswept- and swept-inboard configurations decreases as Mach number increases. The comparison of drag-due-to-lift characteristics was also dependent on Mach number, with the swept-inboard configurations having lower drag due to lift than the unswept-inboard configurations at Mach numbers less than 2.00. The flow-visualization data showed that the trends in drag with changes in inboard wing planform shape corresponded to distinct changes in the shock-vortex system occurring between the side bodies.

The surface-pressure and flow-visualization data showed that the flow over the outboard wing developed as expected with changes in angle of attack and Mach number. Shock-induced separation occurred at the junction of the body and inboard wing. This shock-induced separation, the sweep of the inboard wing, and the location of the inboard wing in relation to the delta outboard wing reduced the upwash on the forward portion and effectively lowered the local flow incidence angle. The swept inboard wing also prevented the balance-housing bow shock from forming over the inboard wing. This effect corresponded to an increase in the strength of the shock emanating from the junction of the body and outboard wing of the swept/small-trapezoidal multibody configuration. The swept inboard wing also appeared to influence the position of the outboard side-body vortex.

The bodies-off study was conducted with the unswept inboard wing panel and the delta- and small-trapezoidal outboard wing panels. The flow-visualization data for the bodies-off configurations showed more clearly the existence of the bow shock from the balance housing over the inboard wing. As with the bodies on, the outboard wing planform shape had a minimal influence on the flow pattern of the inboard wing. For the delta outboard wing, the body acts as a fence impeding inboard vortex growth with increasing angle of attack and increasing longitudinal distance. The small-trapezoidal outboard wing data show the existence of a shock emanating from the junction of the tab and outboard wing whether the bodies are on or off. This shock appears to be slightly stronger with the bodies off. However, the bodies-on data show shock-induced separation occurring on the small-trapezoidal outboard wing, whereas the bodies-off data show no apparent

shock-induced separation. This effect corresponds to the existence of a second shock on the outboard wing emanating from the junction of the inboard wing and tab.

Comparisons between the experiment and linear-theory prediction methods revealed a general inability of the methods to consistently predict the characteristics of these multibody configurations. The methods did predict the correct trends in lift, drag-due-to-lift, and zero-lift drag characteristics with changes in outboard wing size and Mach number.

However, the methods did not consistently predict the correct trends in drag-due-to-lift and zero-lift drag characteristics with variations in the inboard wing planform shape. The methods were not able to correctly predict the trends in longitudinal stability with changes in outboard wing size, inboard wing planform shape, or Mach number.

NASA Langley Research Center
Hampton, VA 23661-0001
June 24, 1992

Table I. Geometric Characteristics of Multibody Model Components

Strongback:	
Length, in.	13.000
Base area, in ²	0.697
Chamber area, in ²	1.863
Capture area (total), in ²	3.000
Exit area (total), in ²	3.399
Side body (each):	
Length, in.	30.000
Area distribution, in ²	See table II
Cross-sectional shape	Circular
Unswep inboard wing panel:	
Area, in ²	104.000
Λ_{LE} , deg	0.000
Λ_{TE} , deg	0.000
Aspect ratio	0.615
Span, in.	8.000
Airfoil section	4-percent biconvex
Swept inboard wing panel:	
Area, in ²	101.240
Λ_{LE} , deg	60.900
Λ_{TE} , deg	0.000
Aspect ratio	0.632
Span, in.	8.000
Airfoil section	4-percent biconvex
Delta outboard wing panel:	
Area, in ²	78.340
Λ_{LE} , deg	65.000
Λ_{TE} , deg	0.000
Aspect ratio	1.600
Semispan, in.	5.506
Airfoil section	4-percent biconvex
Unswep/delta wing total planform:	
Area (reference), in ²	182.340
Aspect ratio	2.020
\bar{c} , in.	11.158
\bar{x} , in.	10.341
Swept/delta wing total planform:	
Area (reference), in ²	179.580
Aspect ratio	2.050
\bar{c} , in.	11.115
\bar{x} , in.	10.385

Table 1. Concluded

Small-trapezoidal outboard wing panel:	
Area, in ²	88.820
Λ_{LE} , deg	20.000
Λ_{TE} , deg	-20.000
Aspect ratio	2.000
Semispan, in.	6.810
Airfoil section	4-percent biconvex
Unswept/small-trapezoidal wing total planform:	
Area (reference), in ²	192.830
Aspect ratio	2.420
\bar{z} , in.	10.160
\bar{x} , in.	9.92
Swept/small-trapezoidal wing total planform:	
Area (reference), in ²	190.070
Aspect ratio	2.460
\bar{z} , in.	10.105
\bar{x} in.	9.956
Large-trapezoidal outboard wing panel:	
Area, in ²	156.030
Λ_{LE} , deg	20.000
Λ_{TE} , deg	-16.861
Aspect ratio	2.000
Semispan, in.	8.830
Airfoil section	4-percent biconvex
Unswept/large-trapezoidal wing total planform:	
Area (reference), in ²	260.030
Aspect ratio	2.530
\bar{z} , in.	10.697
\bar{x} , in.	10.893
Swept/large-trapezoidal wing total planform:	
Area (reference), in ²	257.266
Aspect ratio	2.559
\bar{z} , in.	10.662
\bar{x} , in.	10.117

Table II. Normal Area Distribution of Side Body

x/l	Area, in ²
0.00	0.000
0.05	0.400
0.10	0.800
0.15	1.150
0.20	1.500
0.25	1.825
0.30	2.110
0.35	2.300
0.40	2.410
0.45	2.410
0.50	2.350
0.55	2.225
0.60	2.075
0.65	1.900
0.70	1.700
0.75	1.500
0.80	1.250
0.85	0.975
0.90	0.680
0.95	0.350
1.00	0.000

Table III. Pressure Orifice Locations for Delta Outboard Wing Panel

η	y' at—		
	Station 1 $x' = 0.4c = 5.2$ in. $(b/2)_l = 2.43$ in.	Station 2 $x' = 0.6c = 7.8$ in. $(b/2)_l = 3.64$ in.	Station 3 $x' = 0.8c = 10.4$ in. $(b/2)_l = 4.85$ in.
0.2			0.97
0.3		1.09	1.46
0.4	0.97	1.46	1.94
0.5	1.22	1.82	2.43
0.6	1.46	2.18	2.91
0.7	1.70	2.55	3.40
0.8	1.94	2.91	3.88
0.9	2.19	3.28	4.37

Table IV. Pressure Orifice Locations for Small-Trapezoidal Outboard Wing Panel

η	y' at—			
	Station 1 $x' = 0.2c = 1.8$ in. $(b/2)_l = 4.95$ in.	Station 2 $x' = 0.4c = 3.6$ in. $(b/2)_l = 6.81$ in.	Station 3 $x' = 0.6c = 5.4$ in. $(b/2)_l = 6.81$ in.	Station 4 $x' = 0.8c = 7.2$ in. $(b/2)_l = 4.95$ in.
0.2		1.36	1.36	
0.3	1.49	2.04	2.04	1.49
0.4	1.98	2.72	2.72	1.98
0.5	2.48	3.41	3.41	2.48
0.6	2.97	4.09	4.09	2.97
0.7	3.47	4.77	4.77	3.47
0.8	3.96	5.45	5.45	3.96
0.9	4.46	6.13	6.13	4.46

Table V. Experimental Data Figures for Each Configuration Examined

(a) Delta outboard wing configurations

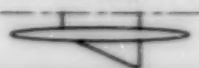


Plot	FW ₁ I ₁ 	FW ₁ I ₂ 	W ₁ I ₁ 
Drag polar	20(b), 22(b)	21(b), 22(b)	
C_L versus α , C_m versus α	20(a), 22(a)	21(a), 22(a)	
L/D at $C_L = 0.1, 0.2$, and 0.3	24	24	
$C_{D,0}$ and $\Delta C_L / \Delta C_D^2$ versus M	25(b)	25(b)	
$C_{L,0}$ and dC_m / dC_L versus M	25(a)	25(a)	
Comparison with theory: $C_{D,0}$ and $\Delta C_L / \Delta C_D^2$ versus M $C_{L,0}$ and dC_m / dC_L versus M	56(b) 56(a)	56(b) 56(a)	
Surface pressures:			
α -sweep	50		66
M -sweep	51		67
Inboard wing sweep	52	52	
Side body	68		68
Sketch of flow field patterns	32	43	62
Oil-flow photographs	33	44	63
Schlieren photographs	34	45	
Vapor screens at aft x station	35	46	64
Vapor screens at $\alpha = 16^\circ$	36	47	65

Table V. Continued

(b) Small-trapezoidal outboard wing configurations






Plot	FW ₃ I ₁ 	FW ₃ I ₂ 	W ₃ I ₁ 
Drag Polar	7(b), 20(b), 23(b)	10(b), 21(b), 23(b)	
C_L versus α , C_m versus α	7(a), 30(a), 23(a)	10(a), 21(a), 23(a)	
L/D at $C_L = 0.1, 0.2$, and 0.3	8, 24	11, 24	
$C_{D,0}$ and $\Delta C_L / \Delta C_D^2$ versus M	9(b), 25(b)	12(b), 25(b)	
$C_{L,0}$ and dC_m/dC_L versus M	9(a), 25(a)	12(a), 25(a)	
Comparison with theory:			
$C_{D,0}$ and $\Delta C_L / \Delta C_D^2$ versus M	16(b), 56(b)	16(b), 56(b)	
$C_{L,0}$ and dC_m/dC_L versus M	16(a), 56(a)	16(a), 56(a)	
Surface pressures:			
α -sweep	53		69
M -sweep	54		70
Inboard wing sweep	55	55	
Side body	71		71
Sketch of flow-field patterns	26	37	57
Oil-flow photographs	27	38	58
Schlieren photographs	28	39	
Vapor screens:			
At forward x station	29	40	59
At forward aft x station	30	41	60
At $\alpha = 16^\circ$	31	42	61

Table V. Concluded

(c) Large-trapezoidal outboard wing configurations

Plot	FW ₄ I ₁ 	FW ₄ I ₂ 
Drag Polar	7(b)	10(b)
C_L versus α , C_m versus α	7(a)	10(a)
L/D at $C_L = 0.1, 0.2$, and 0.3	8	11
$C_{D,0}$ and $\Delta C_L / \Delta C_D^2$ versus M	9(b)	12(b)
$C_{L_{\alpha}}$ and dC_m/dC_L versus M	9(a)	12(a)
Comparison with theory:		
$C_{D,0}$ and $\Delta C_L / \Delta C_D^2$ versus M	16(b)	19(b)
$C_{L_{\alpha}}$ and dC_m/dC_L versus M	16(a)	19(a)
Schlieren photographs	49	

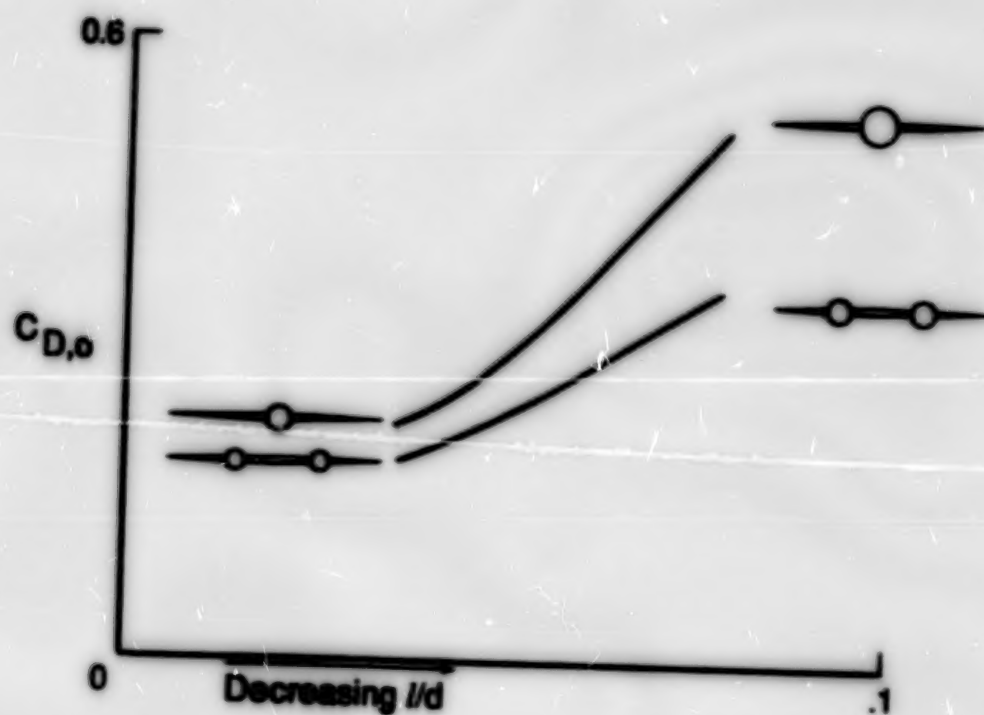


Figure 1. Effect of fineness ratio on zero-lift drag reduction potential of multibody concept. (See ref. 10.)

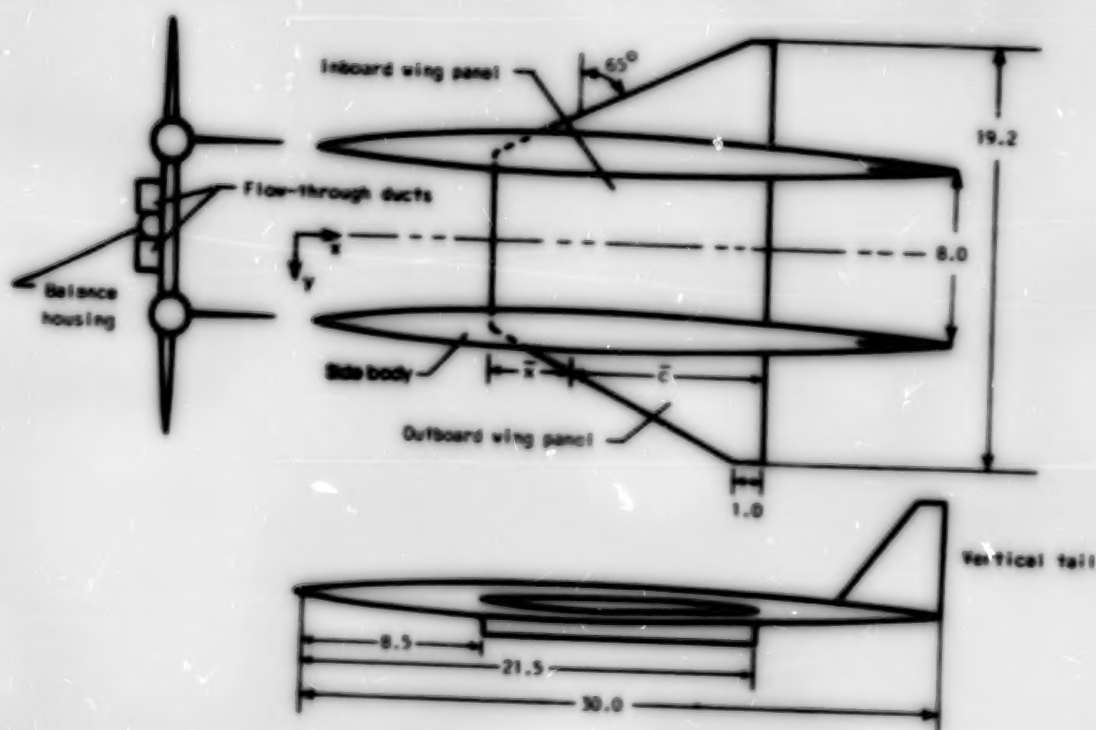
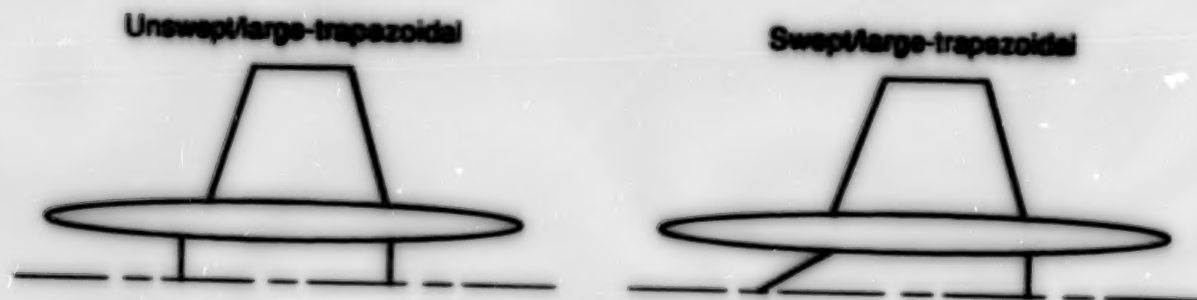


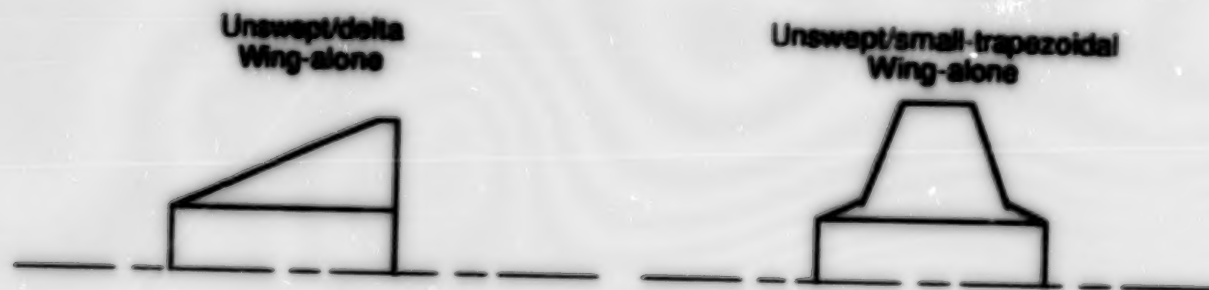
Figure 2. Three-view sketch of unswept/delta multibody research model. All linear dimensions are in inches.



(a) Longitudinal, surface-pressure, and flow-visualization data.

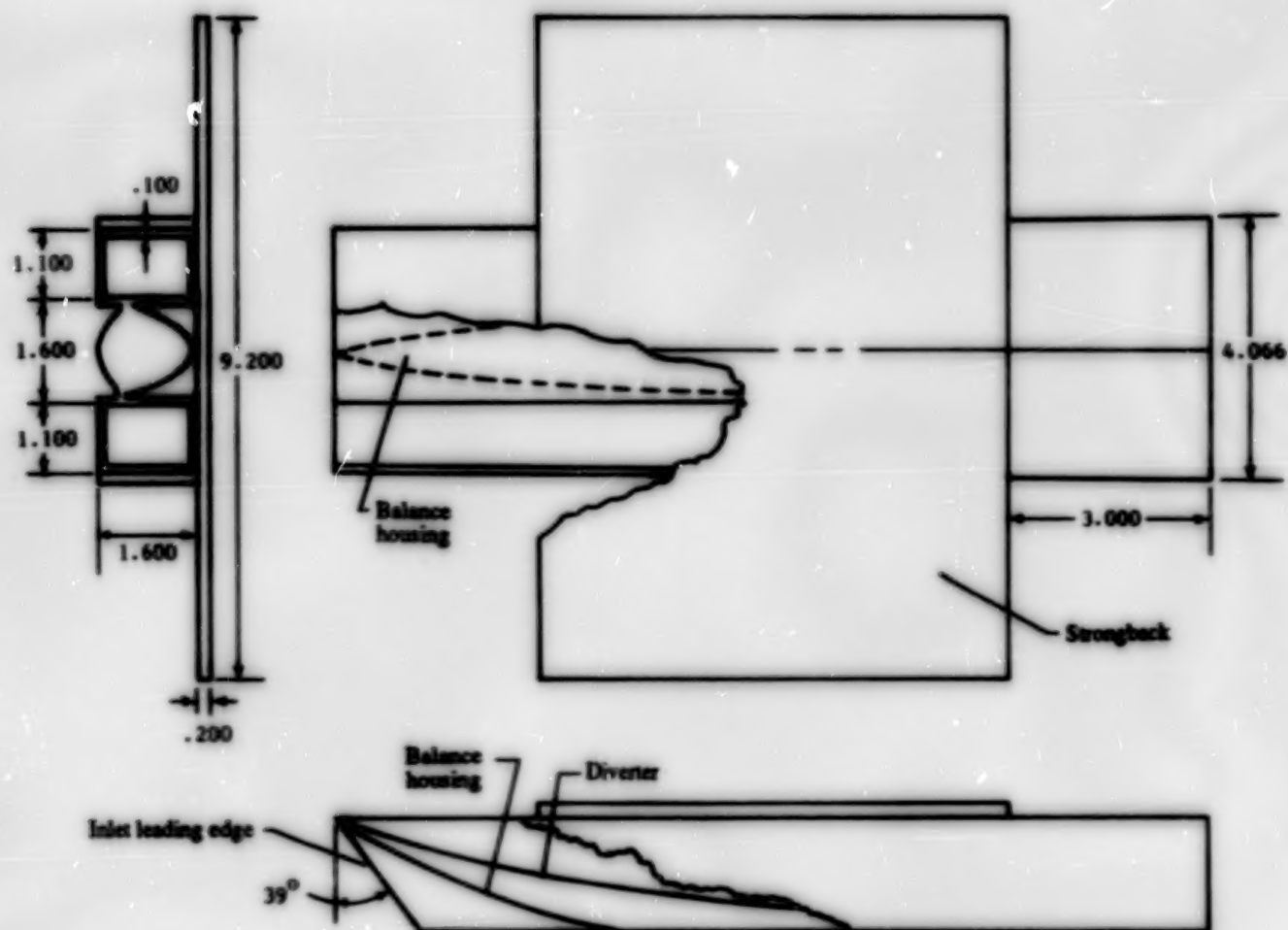


(b) Longitudinal and flow-visualization data.



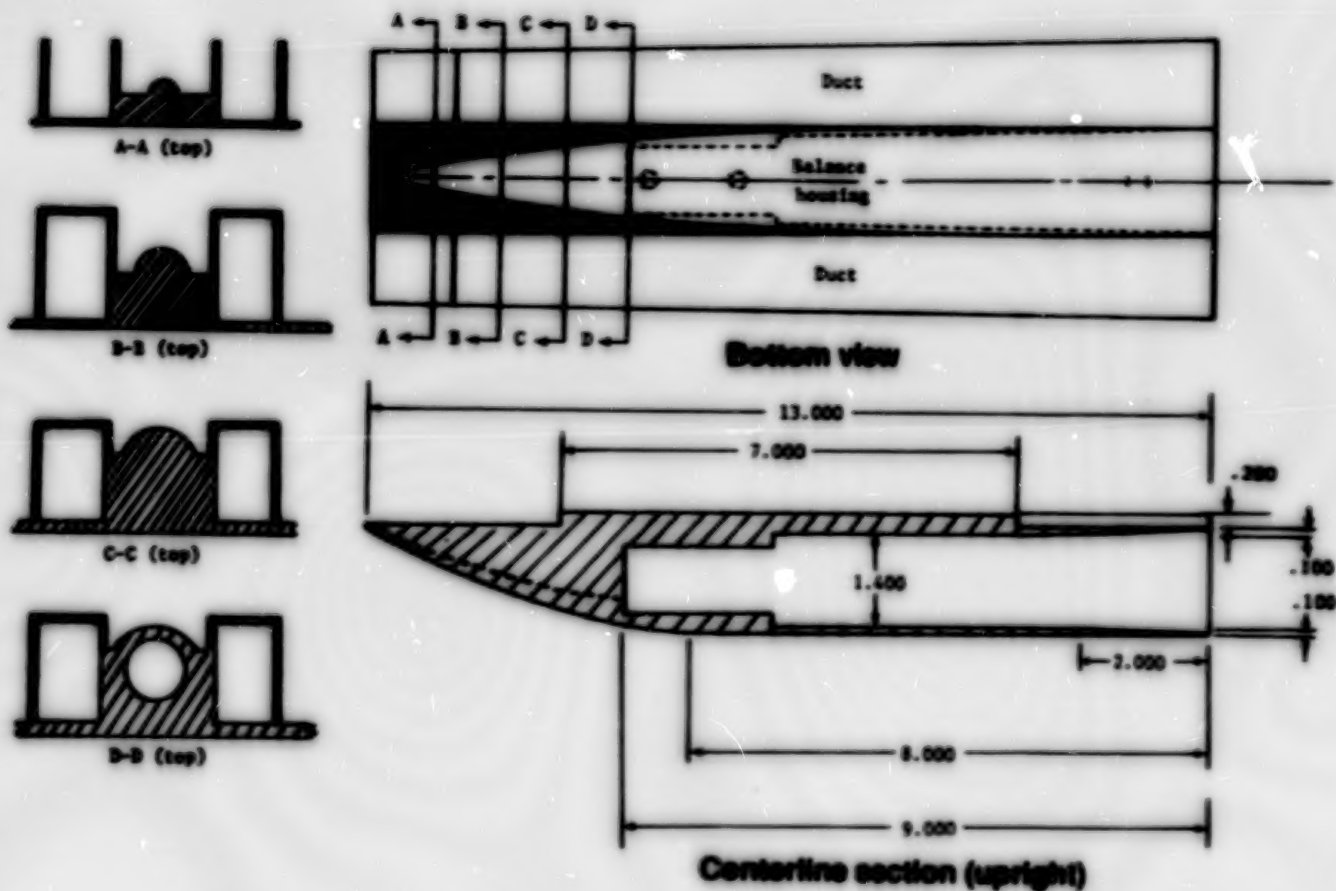
(c) Surface-pressure and flow-visualization data.

Figure 3. Wind tunnel models tested.



(a) Three-view sketch of balance housing and two rectangular flow-through ducts.

Figure 4. Details of unswept/delta multibody model. All linear dimensions are in inches.

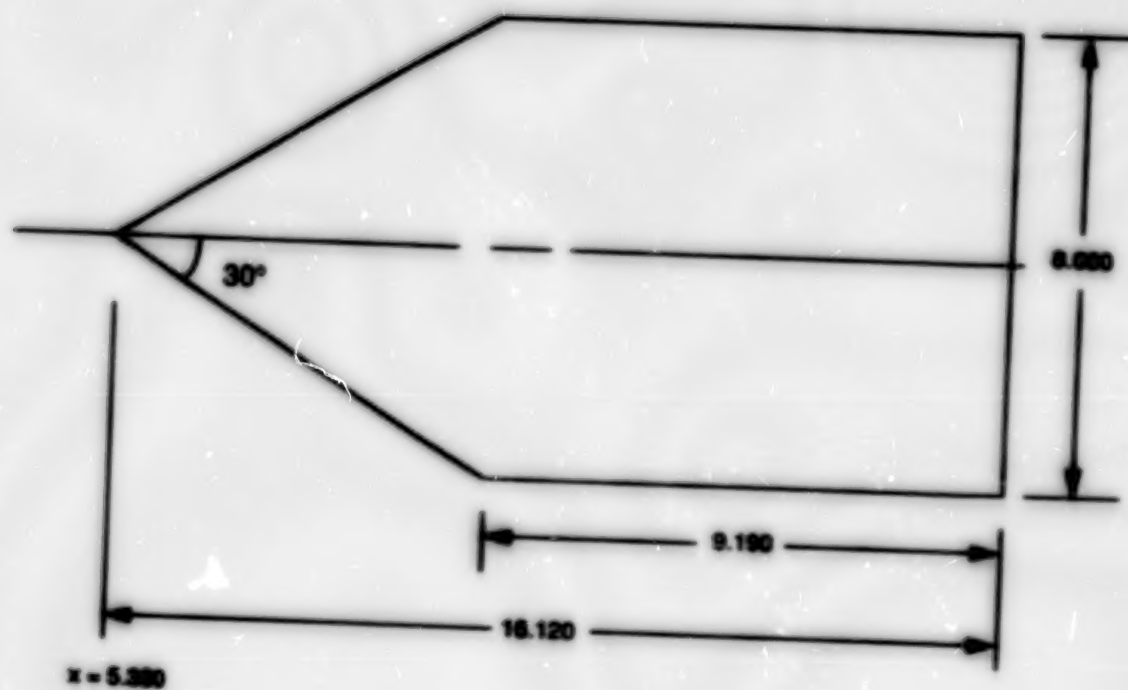


(b) Cross sections of balance housing and flow-through ducts.

Figure 4. Continued.

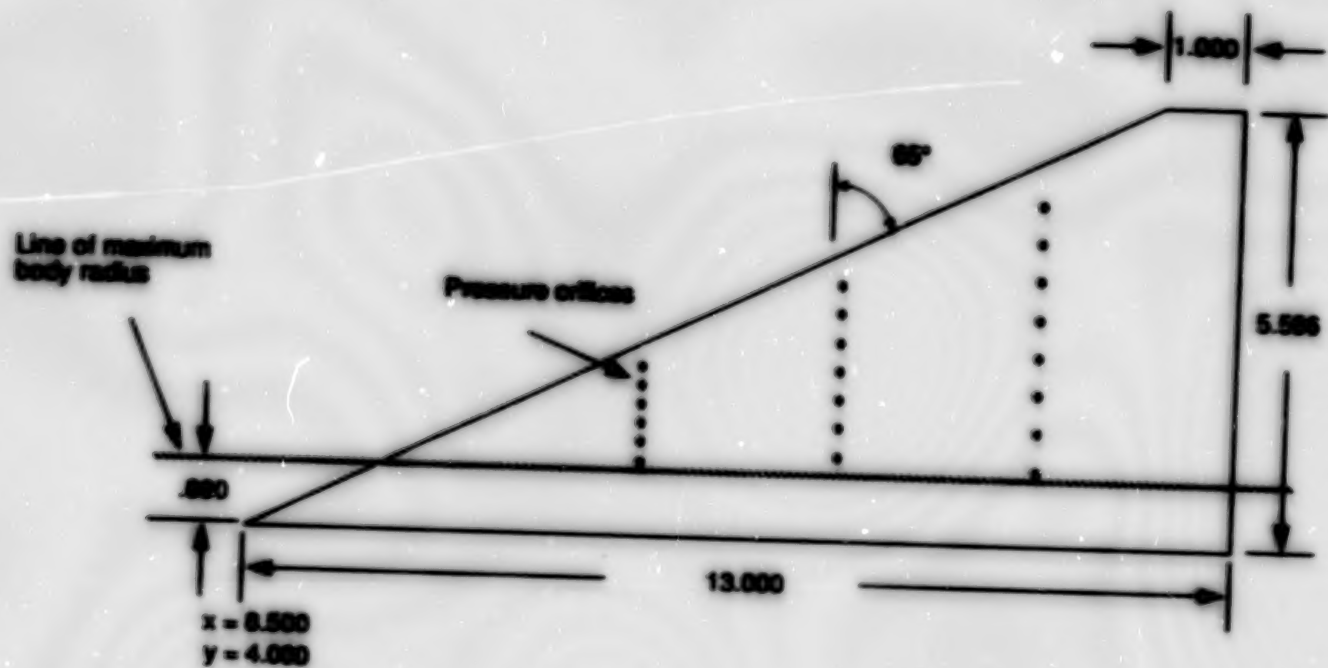


(c) Unswept inboard wing.

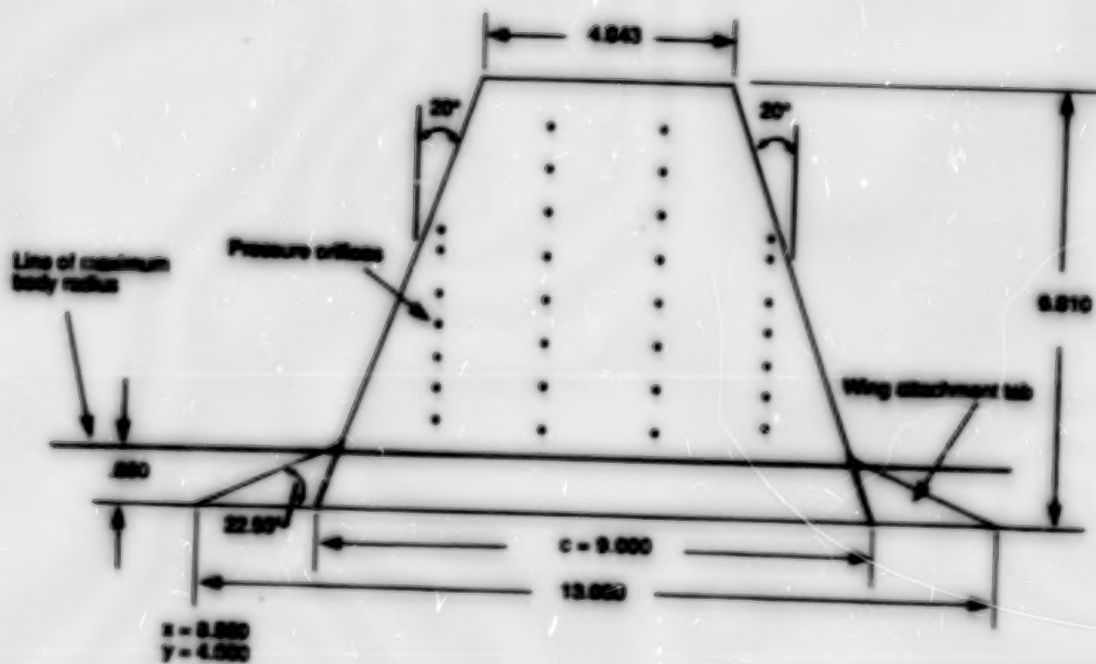


(d) Swept inboard wing.

Figure 4. Continued.

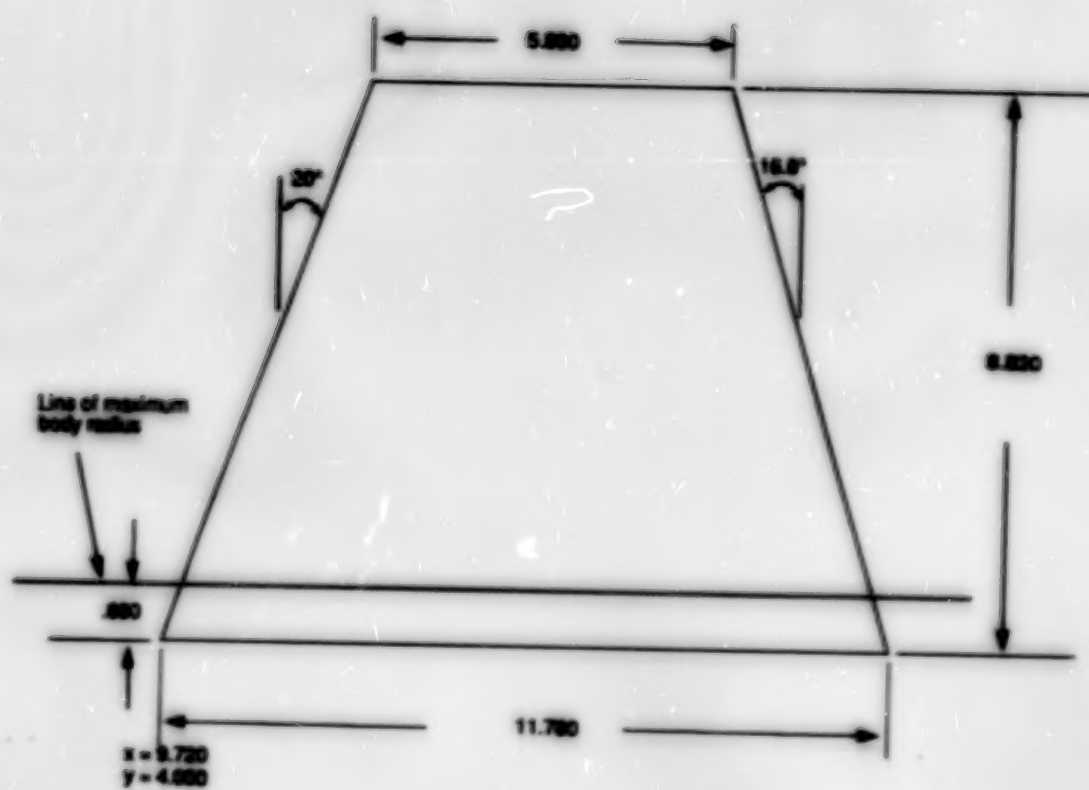


(e) Delta outboard wing.



(f) Small-trapezoidal outboard wing.

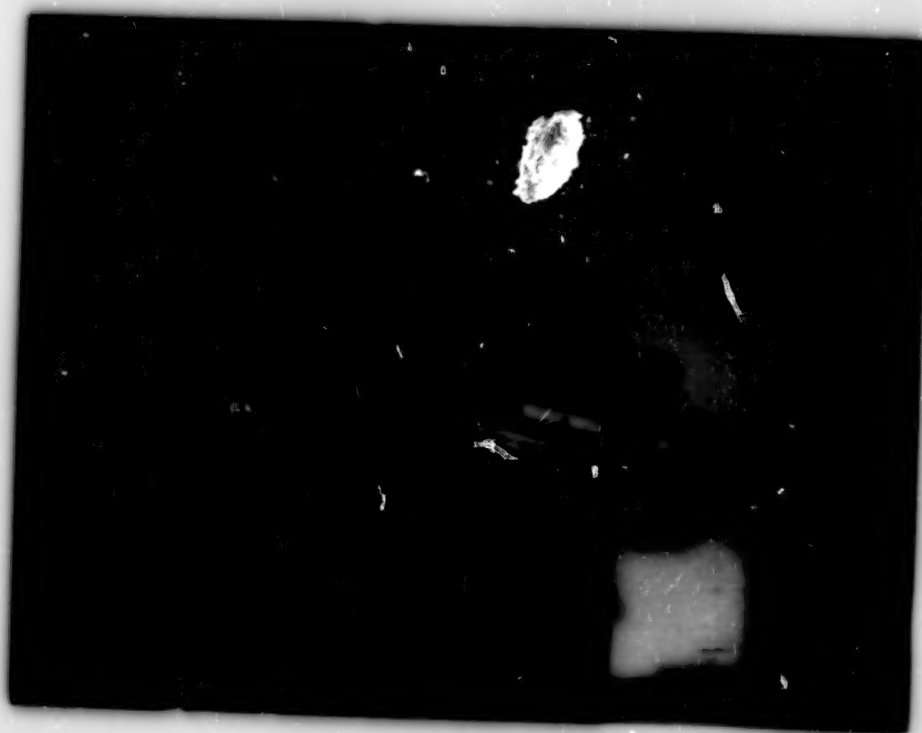
Figure 4. Continued.



(g) Large-trapezoidal outboard wing.

Figure 4. Concluded.

ORIGINAL PAGE
BLACK AND WHITE PHOTOGRAPH



(a) Upper view.

L-83-8950



(b) Lower view.

L-83-8951

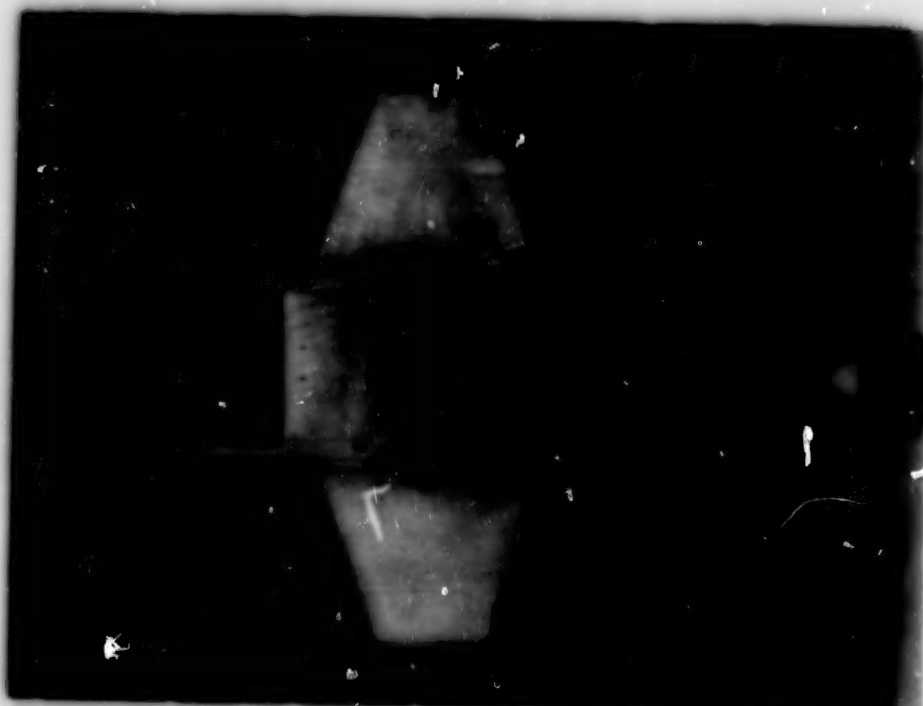
Figure 5. Multibody model with unswept inboard and delta outboard wings.

ORIGINAL PAGE
BLACK AND WHITE PHOTOGRAPH



L-85-10461

(a) Unswept/small-trapezoidal configuration.



L-87-3627

(b) Unswept/large-trapezoidal configuration.

Figure 6. Top view of seven wind tunnel models.

ORIGINAL PAGE
BLACK AND WHITE PHOTOGRAPH



(c) Swept/delta configuration.



(d) Swept/small-trapezoidal configuration.



(e) Swept/large-trapezoidal configuration.

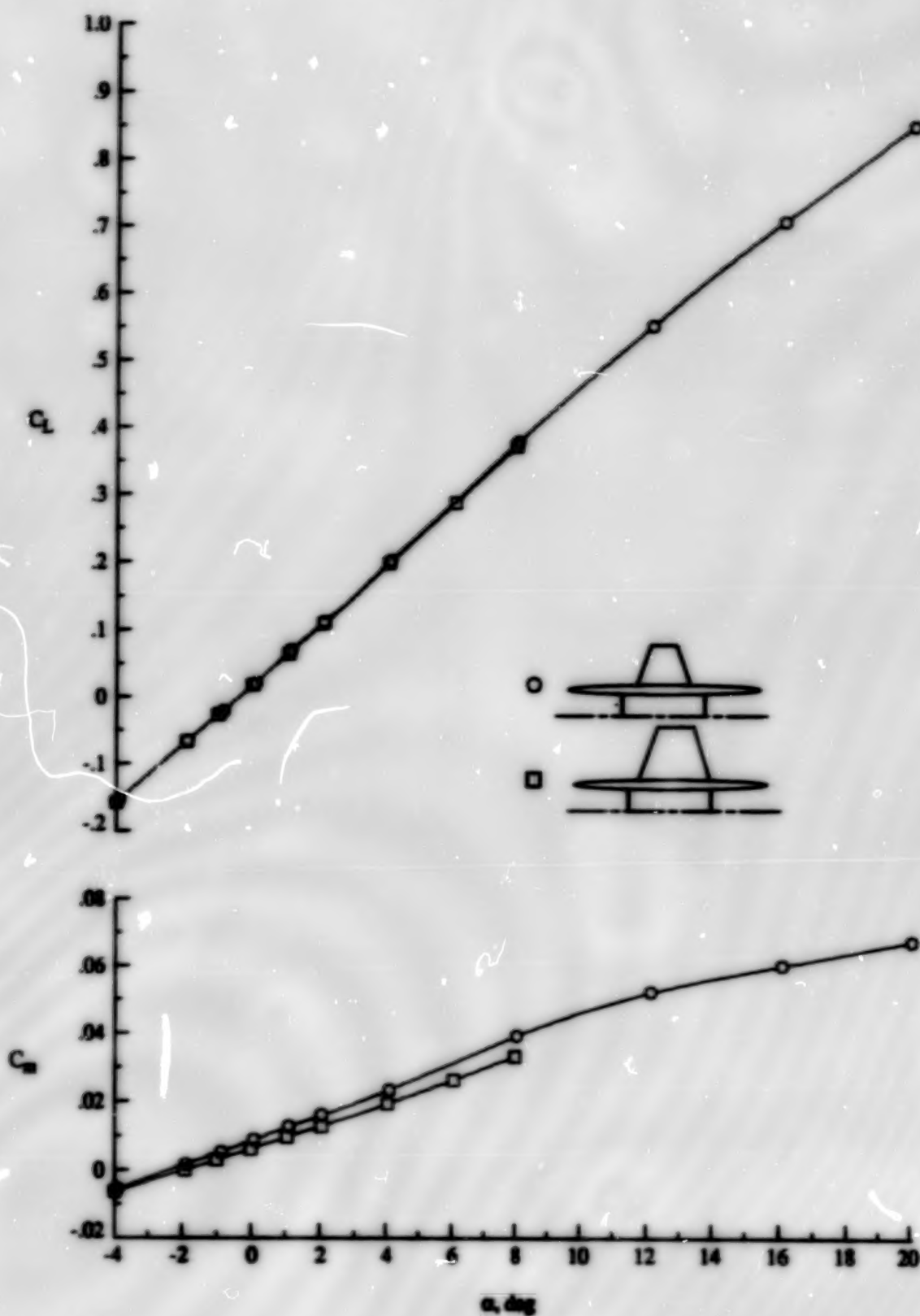


(f) Unswept/delta wing-alone configuration.



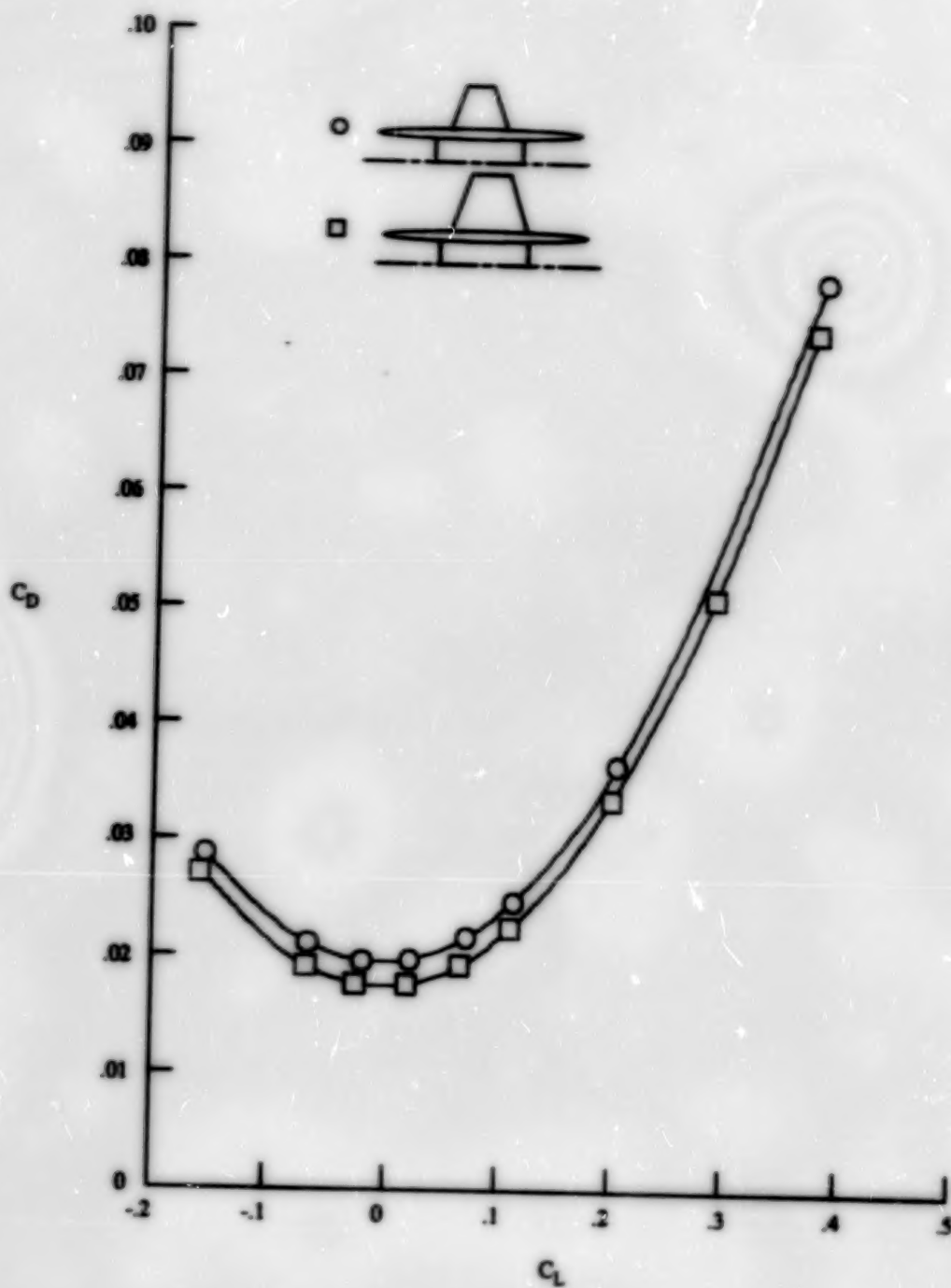
(g) Unswept/small-trapezoidal wing-alone configuration.

Figure 6. Concluded.



(a) Lift and pitching-moment characteristics.

Figure 7. Effect of outboard wing size on longitudinal aerodynamic characteristics of unswept/trapezoidal multibody configuration at $M = 1.80$.



(b) Drag characteristics.

Figure 7. Concluded.

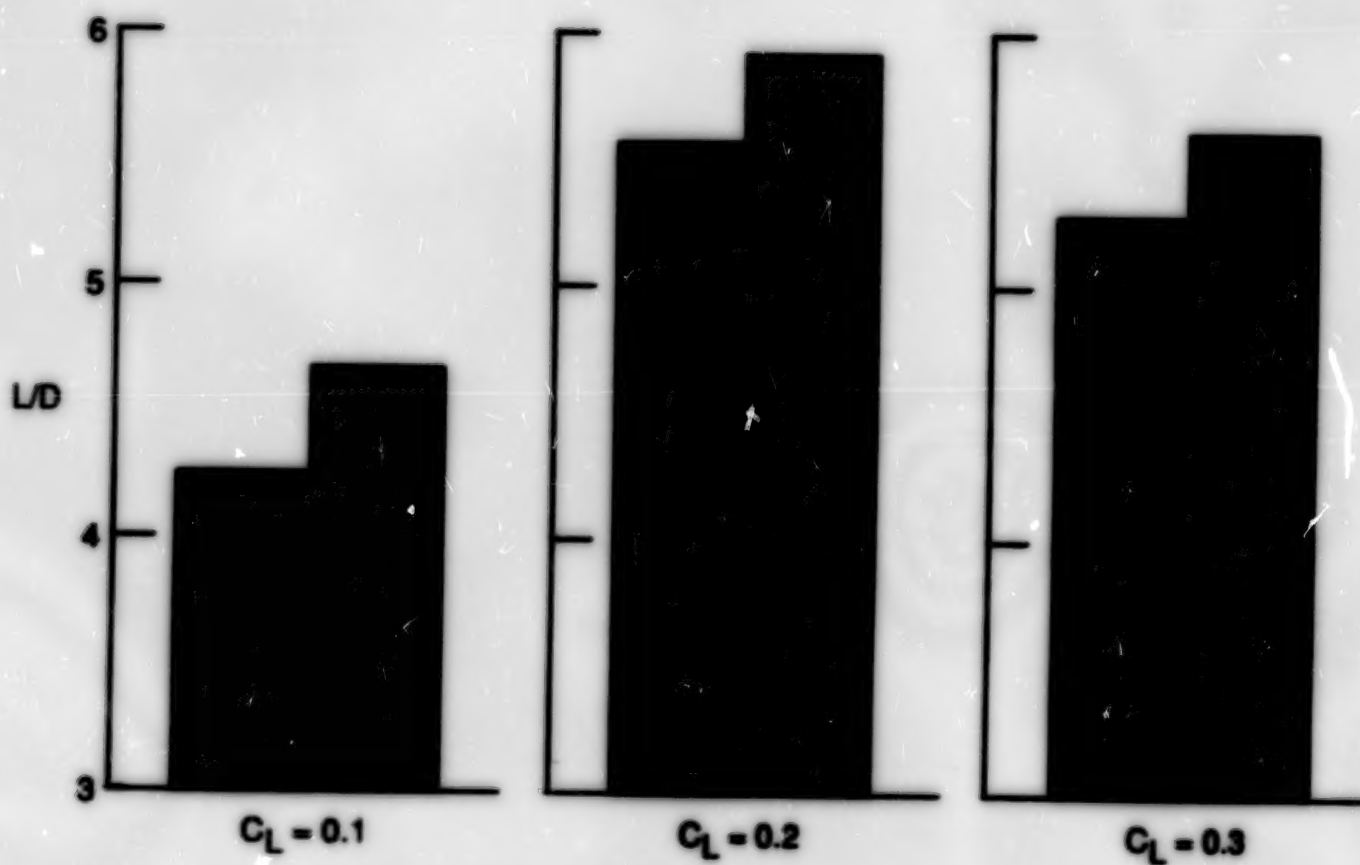
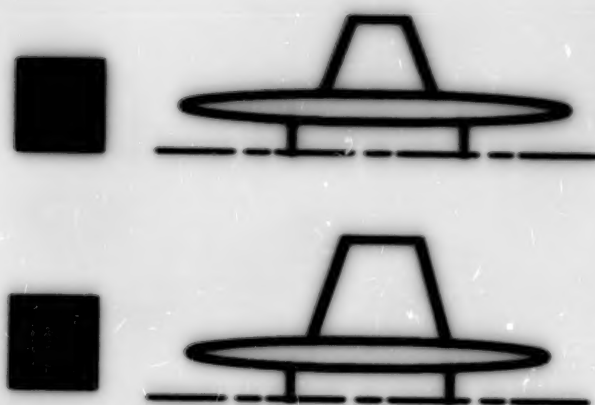
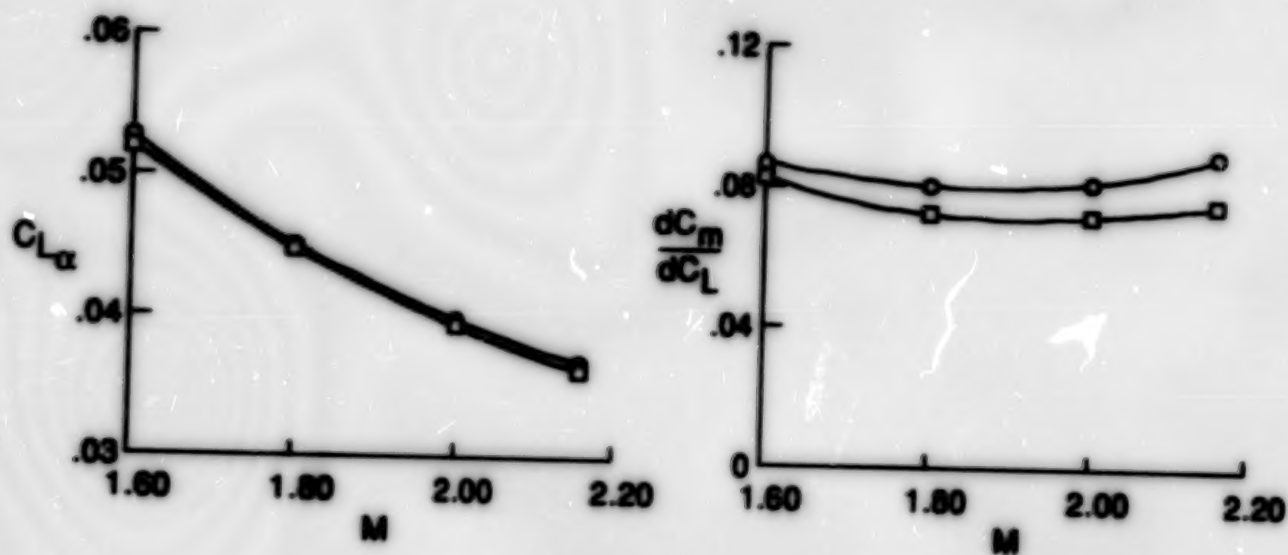
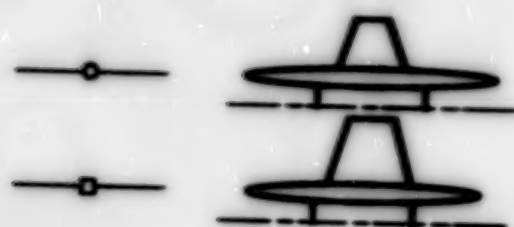
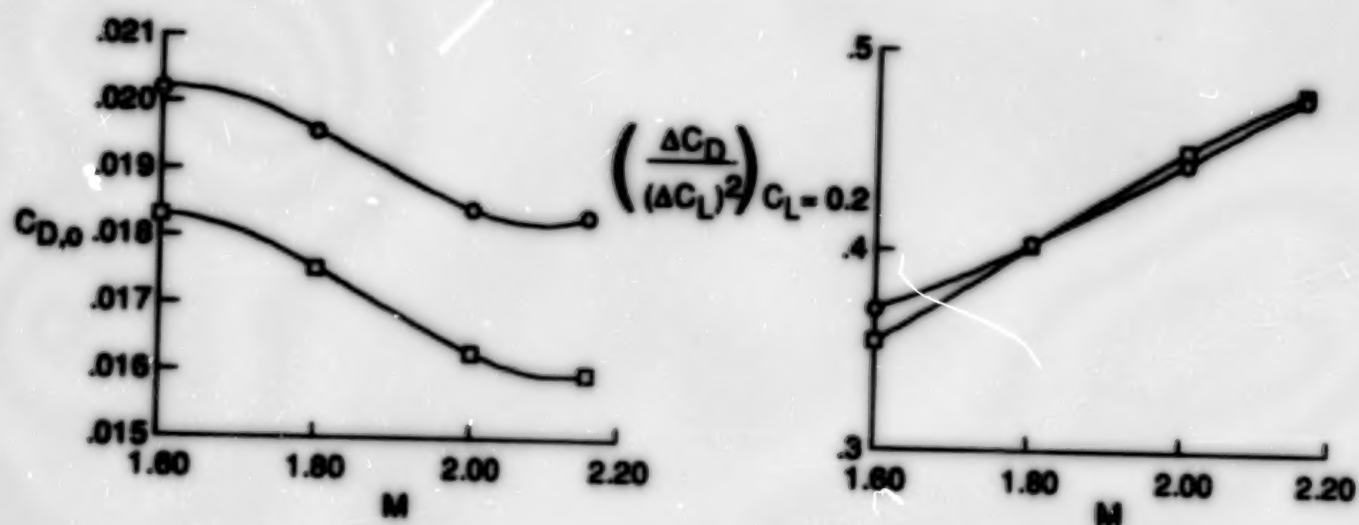


Figure 8. Effect of outboard wing size on aerodynamic performance of unswept/trapezoidal multibody configuration at $M = 1.80$ and $C_L = 0.1, 0.2$, and 0.3 .

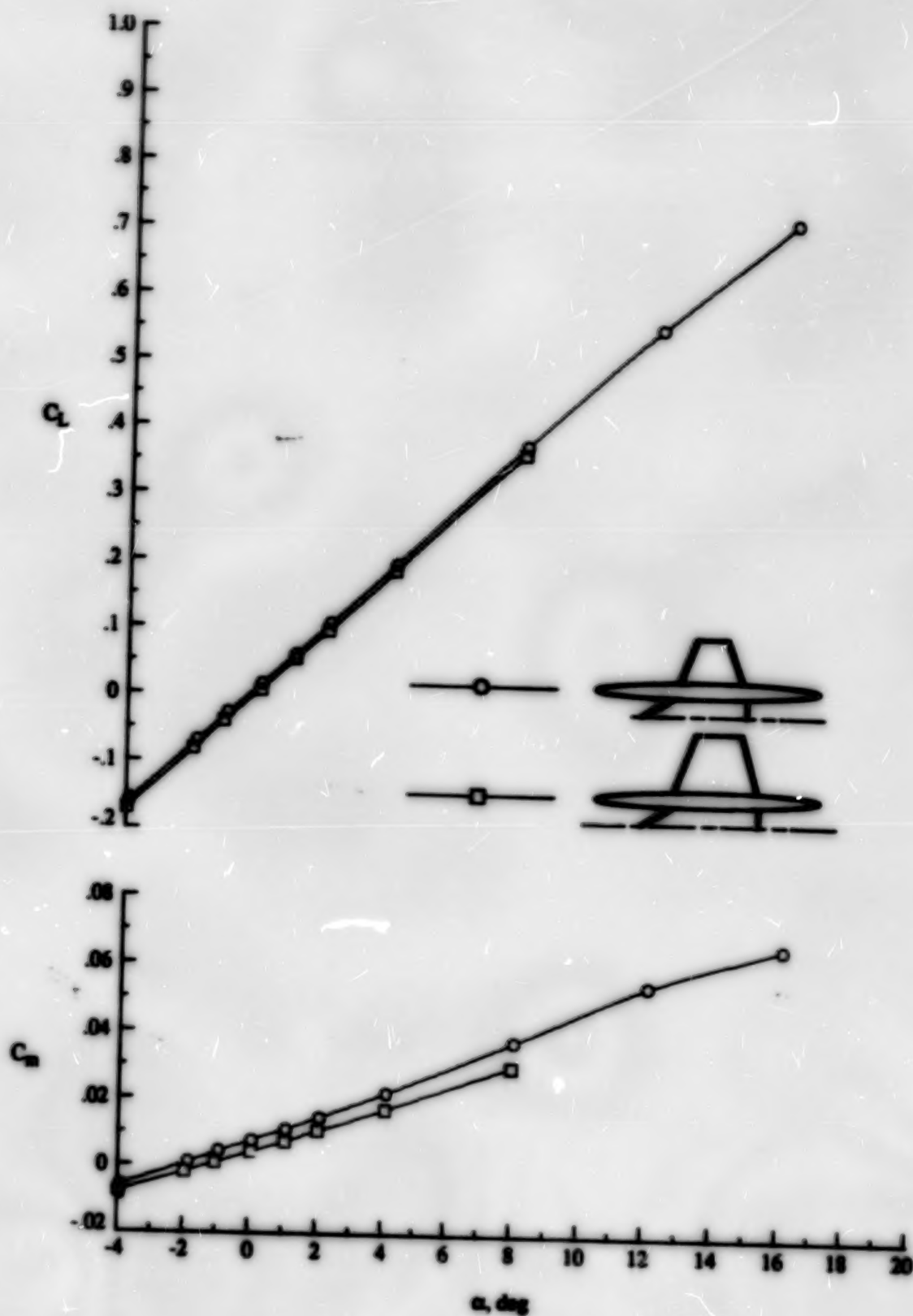


(a) Lift and pitching-moment characteristics.



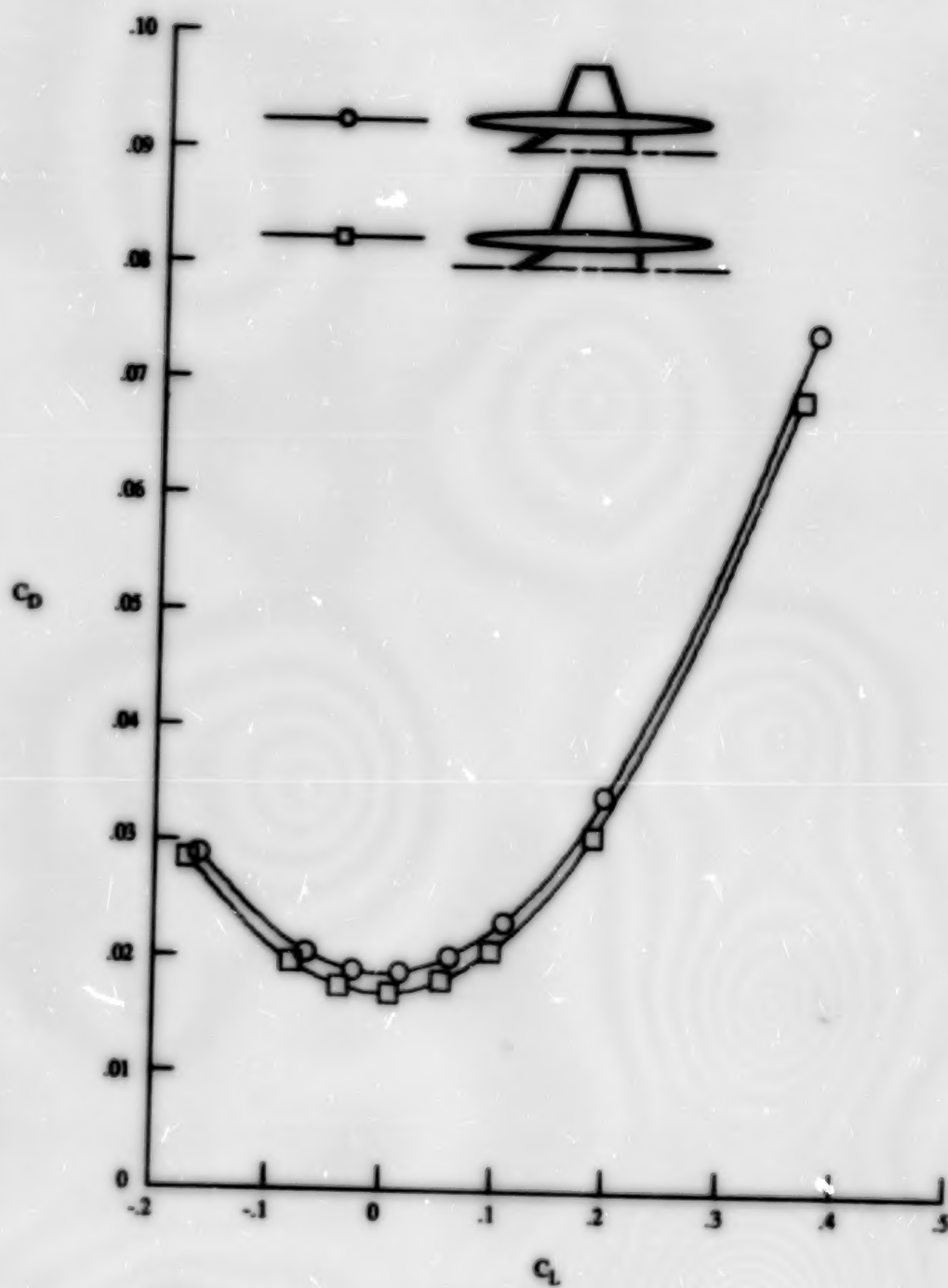
(b) Drag characteristics.

Figure 9. Effect of outboard wing size and Mach number on longitudinal aerodynamic characteristics of unswept/trapezoidal multibody configuration.



(a) Lift and pitching-moment characteristics.

Figure 10. Effect of outboard wing size on longitudinal aerodynamic characteristics of swept/trapezoidal multibody configuration at $M = 1.80$.



(b) Drag characteristics.

Figure 10. Concluded.

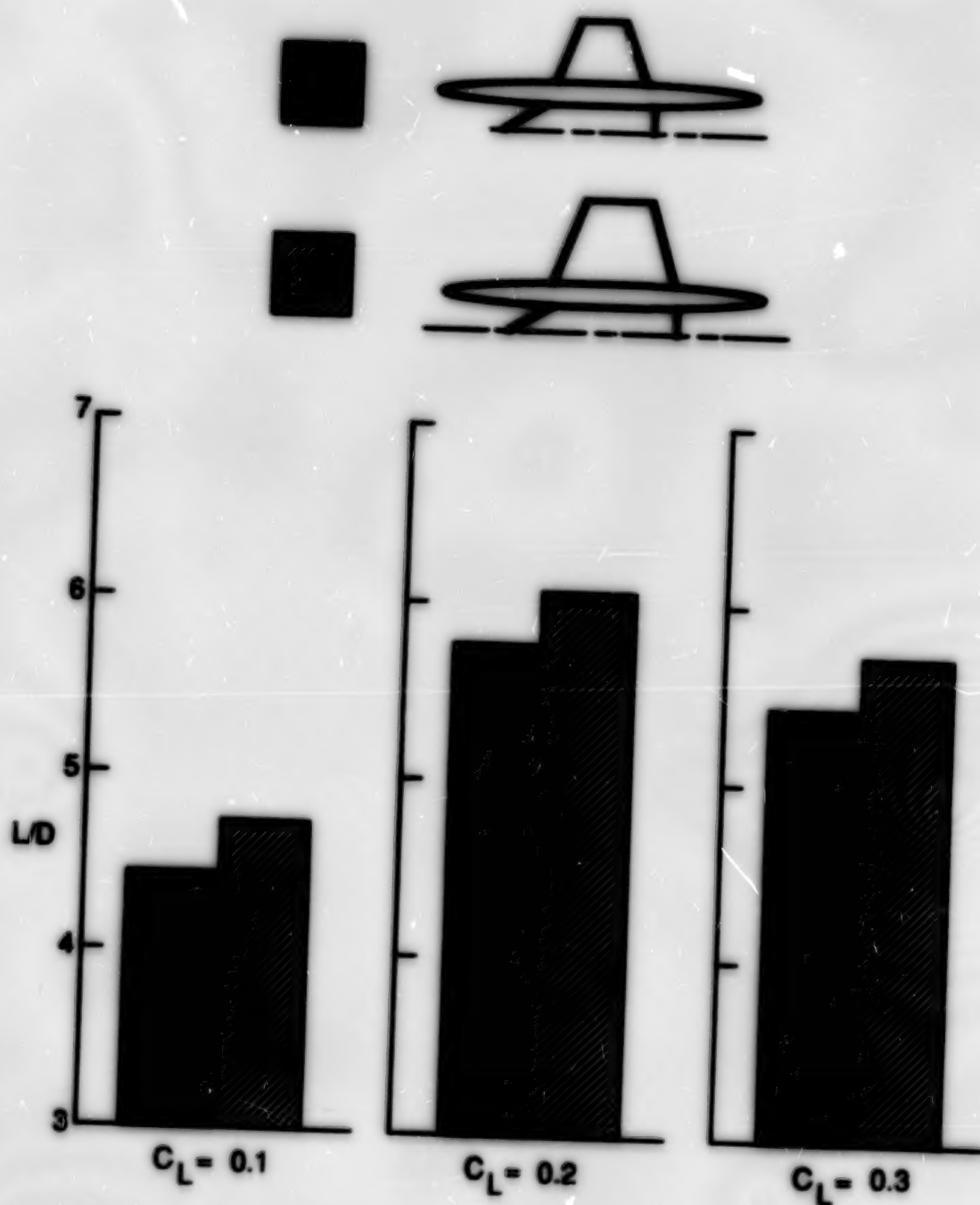
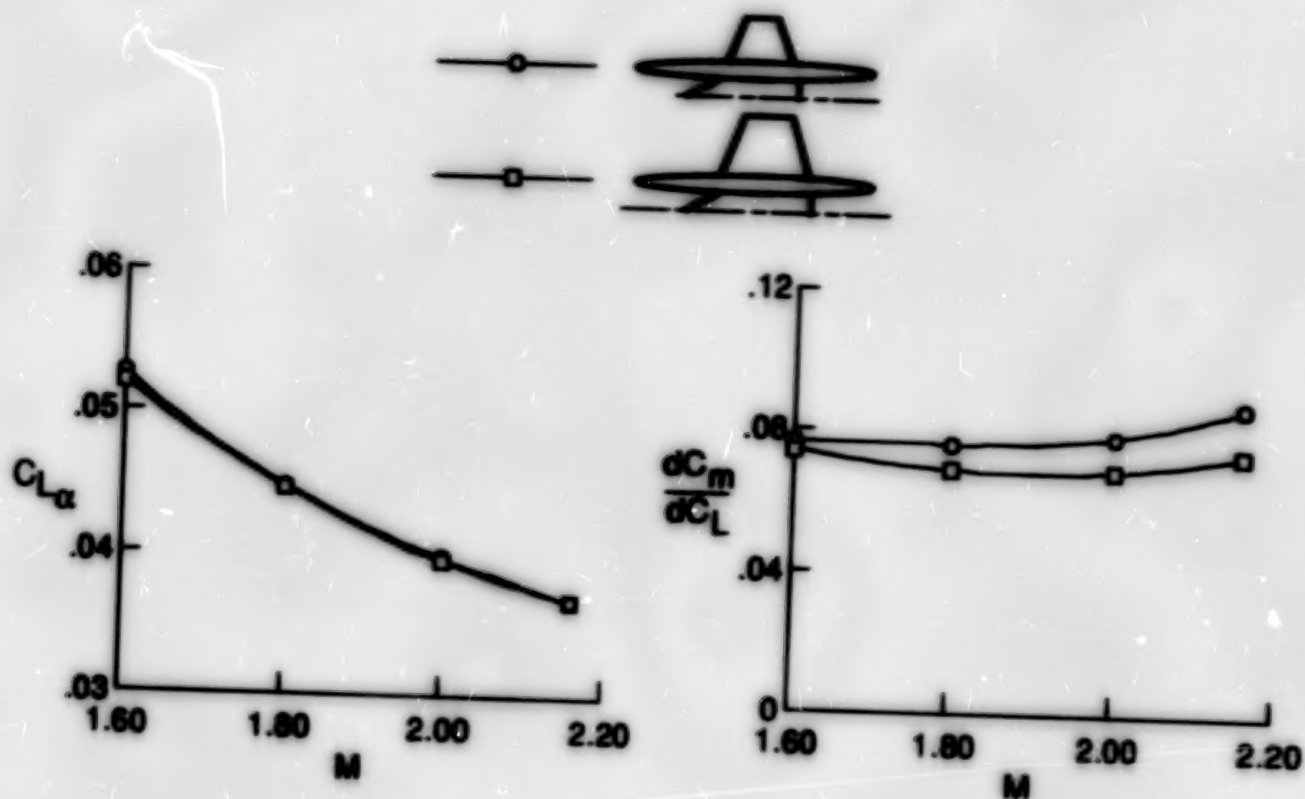
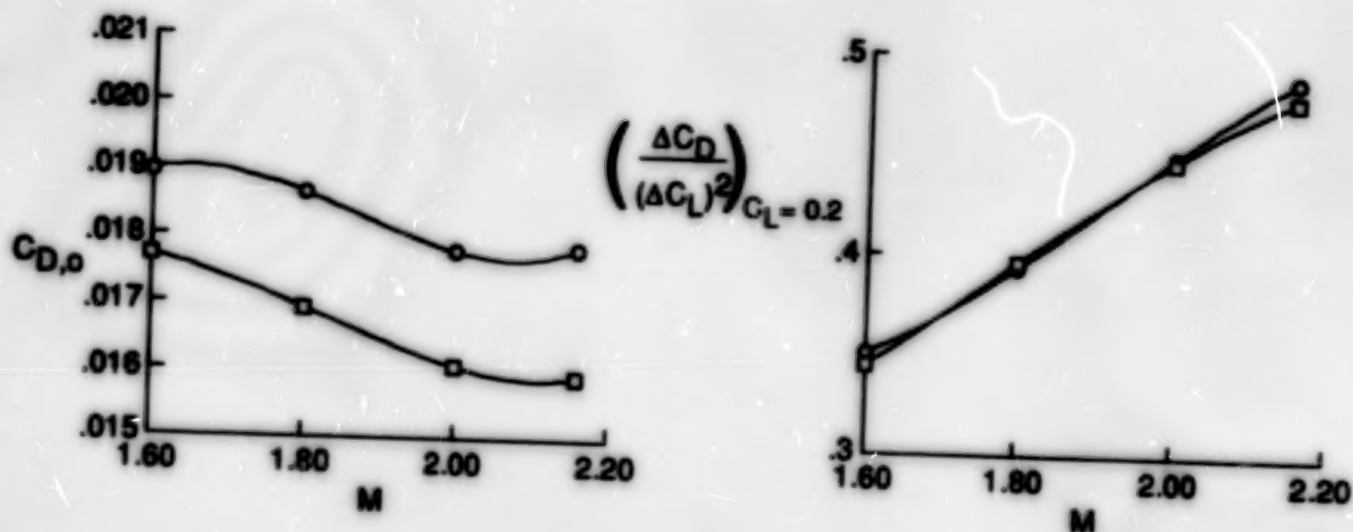


Figure 11. Effect of outboard wing size on aerodynamic performance of swept/trapezoidal multibody configuration at $M = 1.80$ and for $C_L = 0.1, 0.2$, and 0.3 .



(a) Lift and pitching-moment characteristics.



(b) Drag characteristics.

Figure 12. Effect of outboard wing size and Mach number on longitudinal aerodynamic characteristics of swept/trapezoidal multibody configuration.

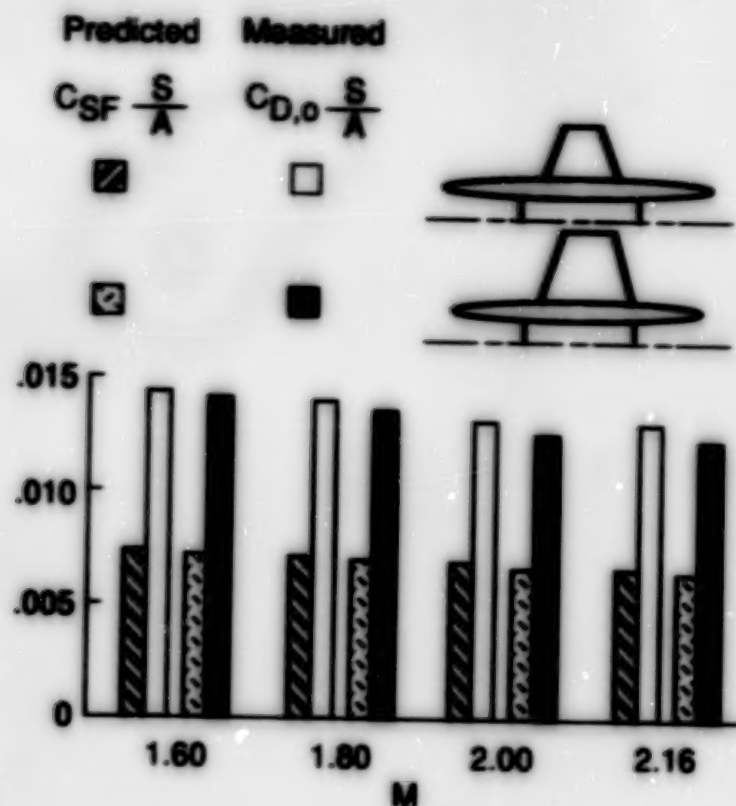


Figure 13. Predicted skin-friction-drag and measured zero-lift drag coefficients corrected for wing and body planform area for unswept/trapezoidal multibody configuration.

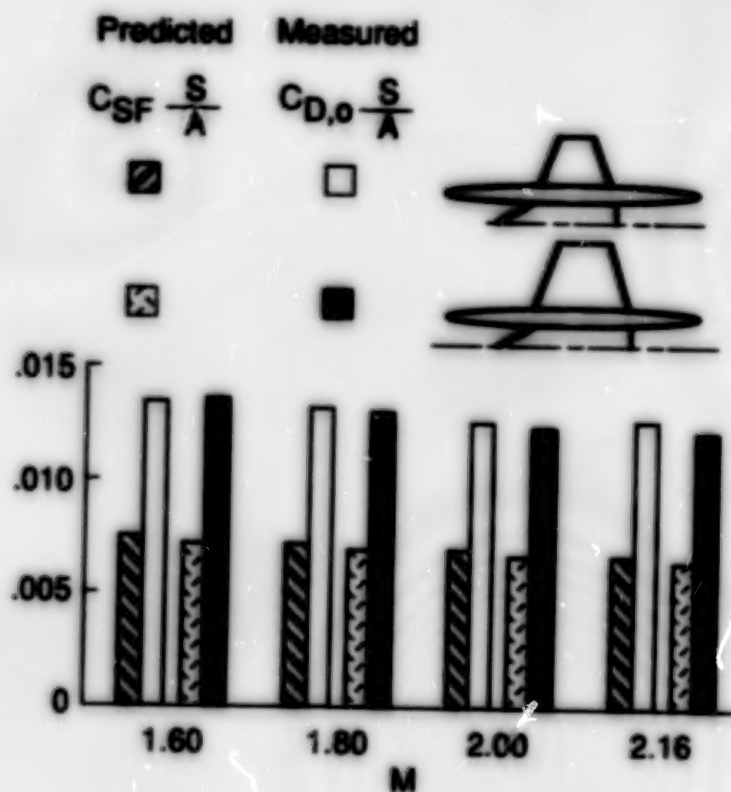
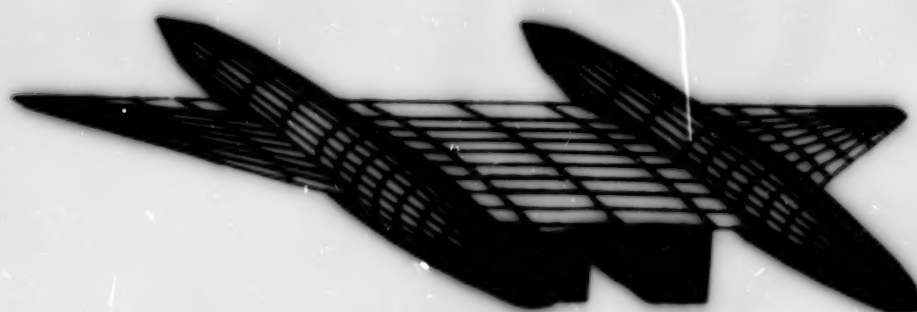


Figure 14. Predicted skin-friction-drag and measured zero-lift drag coefficients corrected for wing and body planform area for swept/trapezoidal multibody configuration.



Zero-lift drag



Lift analysis

Figure 15. Computational models of multibody configuration used in linear-theory analysis.

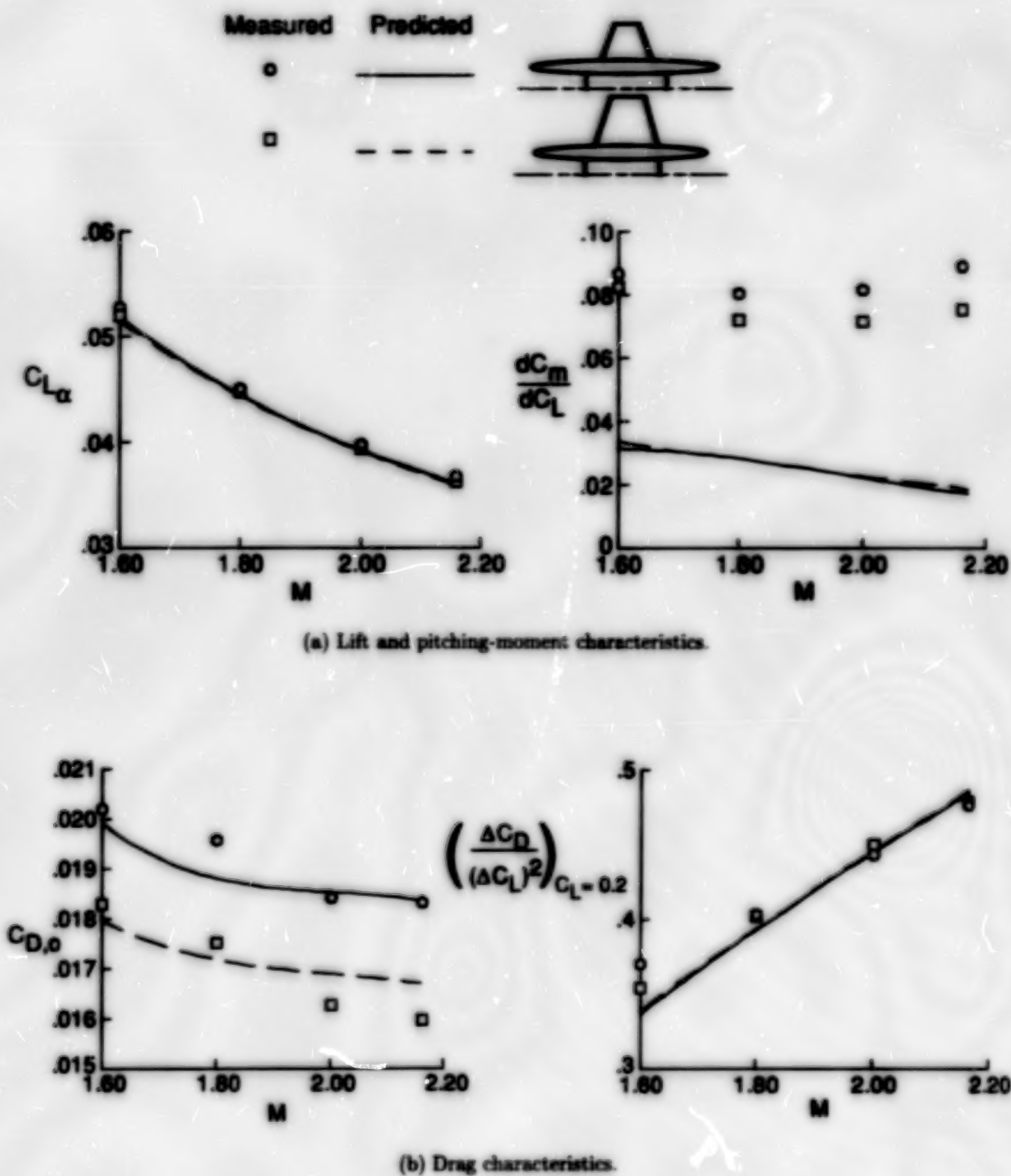


Figure 16. Predicted and measured effects of outboard wing size and Mach number on longitudinal aerodynamic characteristics for unswept/trapezoidal multibody configuration.

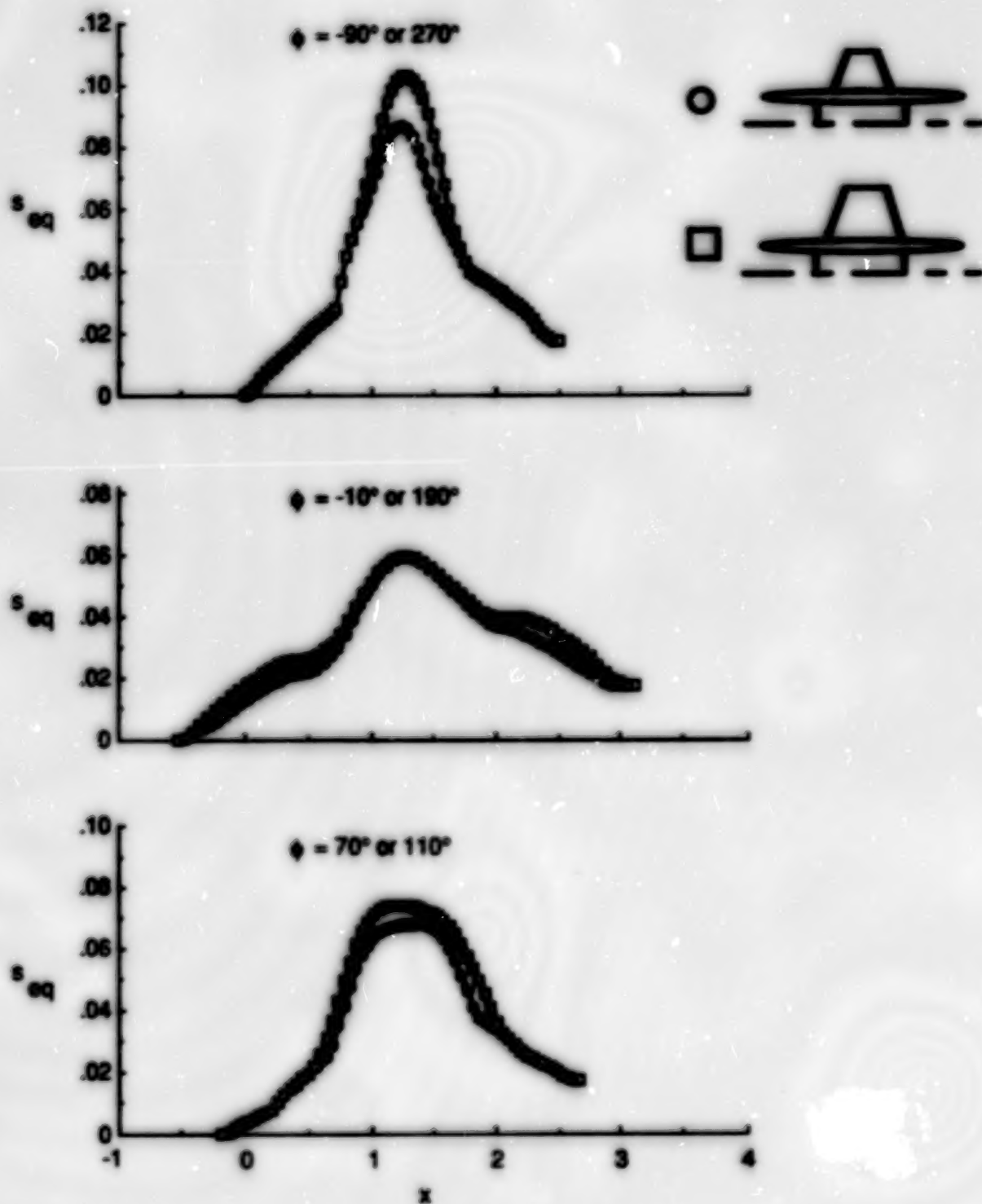


Figure 17. Area distributions of unswept/trapezoidal configurations at $M = 1.80$ from FFWD code at different ϕ -cuts.

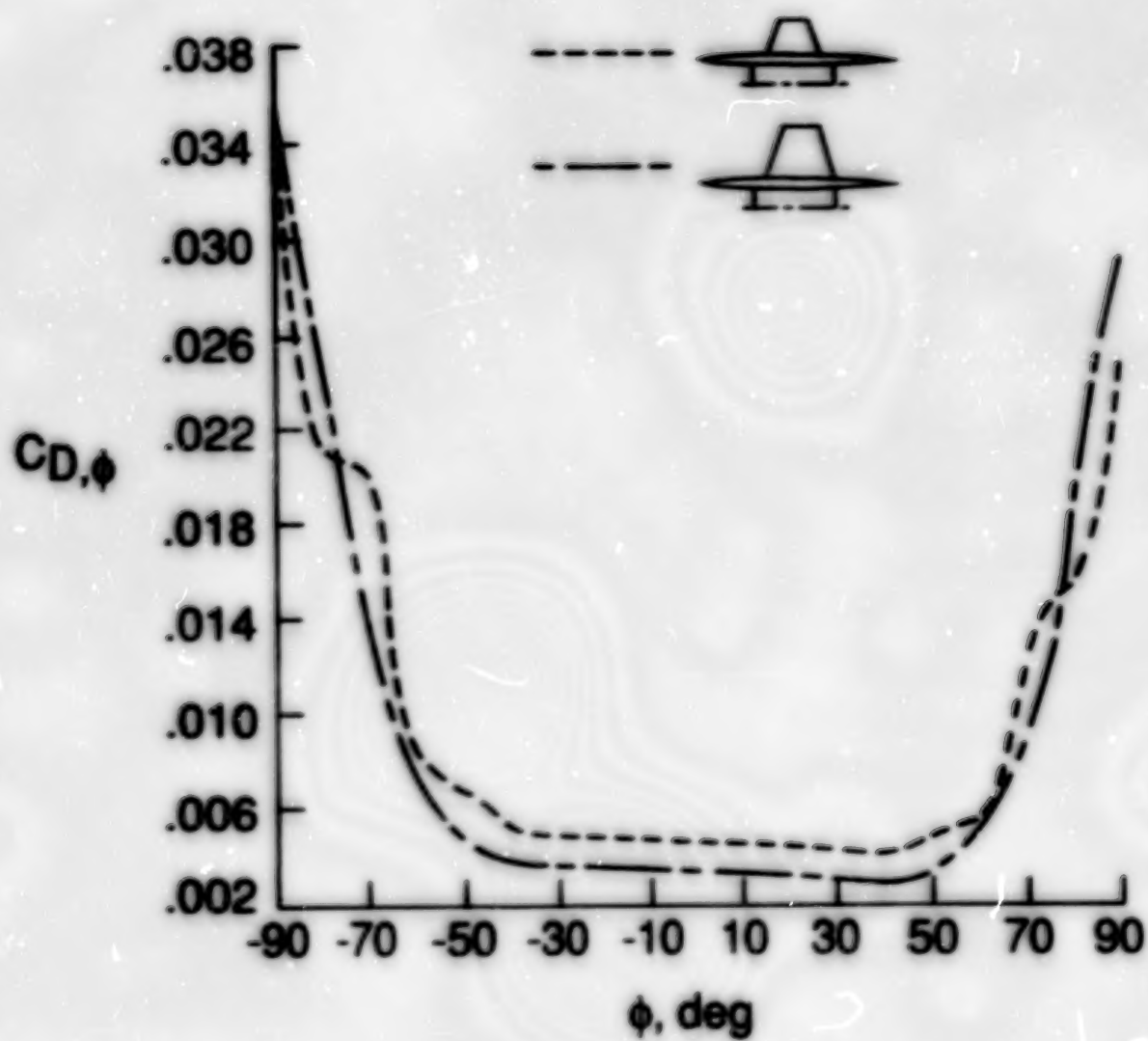
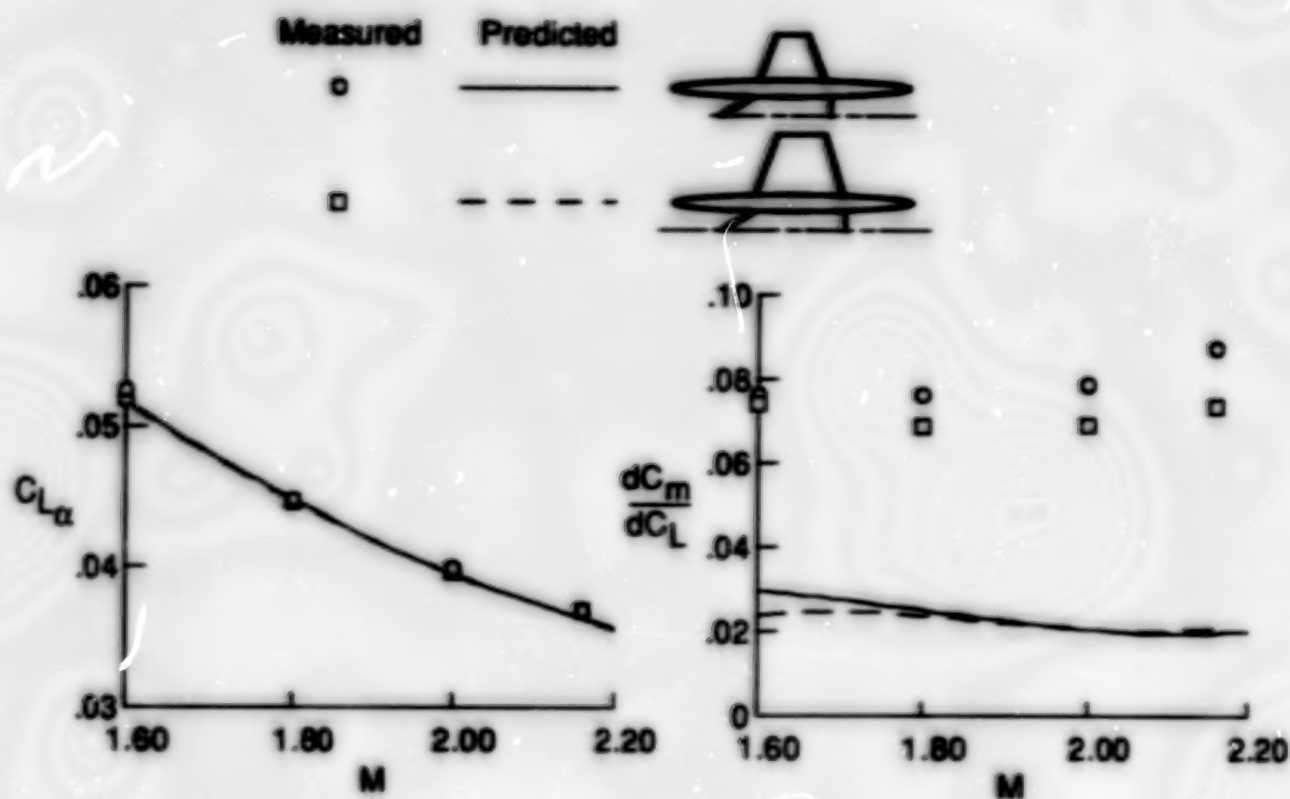
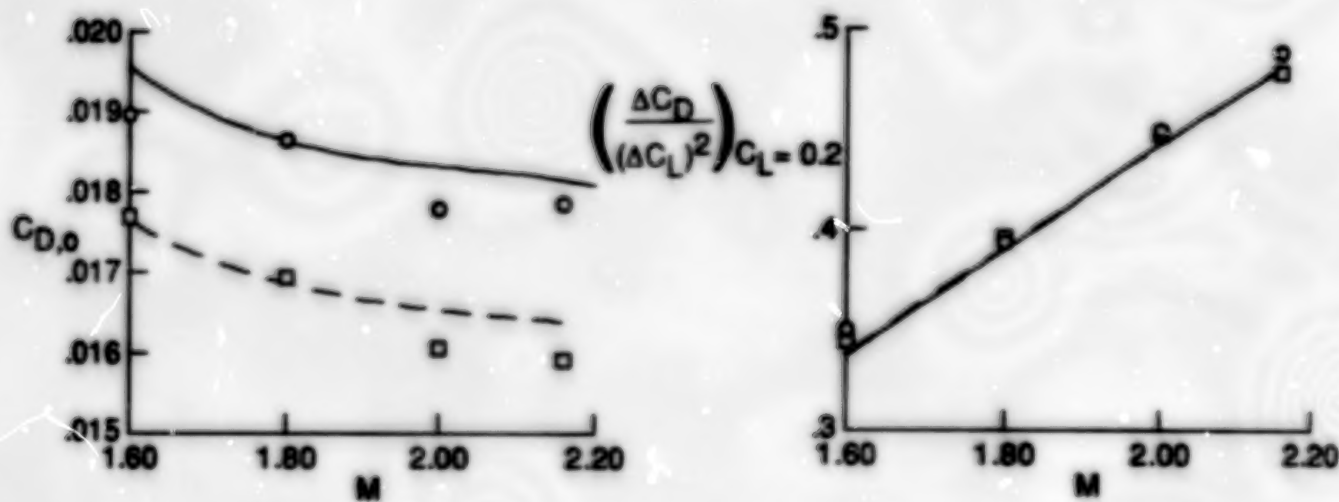


Figure 18. Variation of $C_{D,\phi}$ with ϕ for unswept/trapezoidal multibody configurations at $M = 1.80$.



(a) Lift and pitching-moment characteristics.



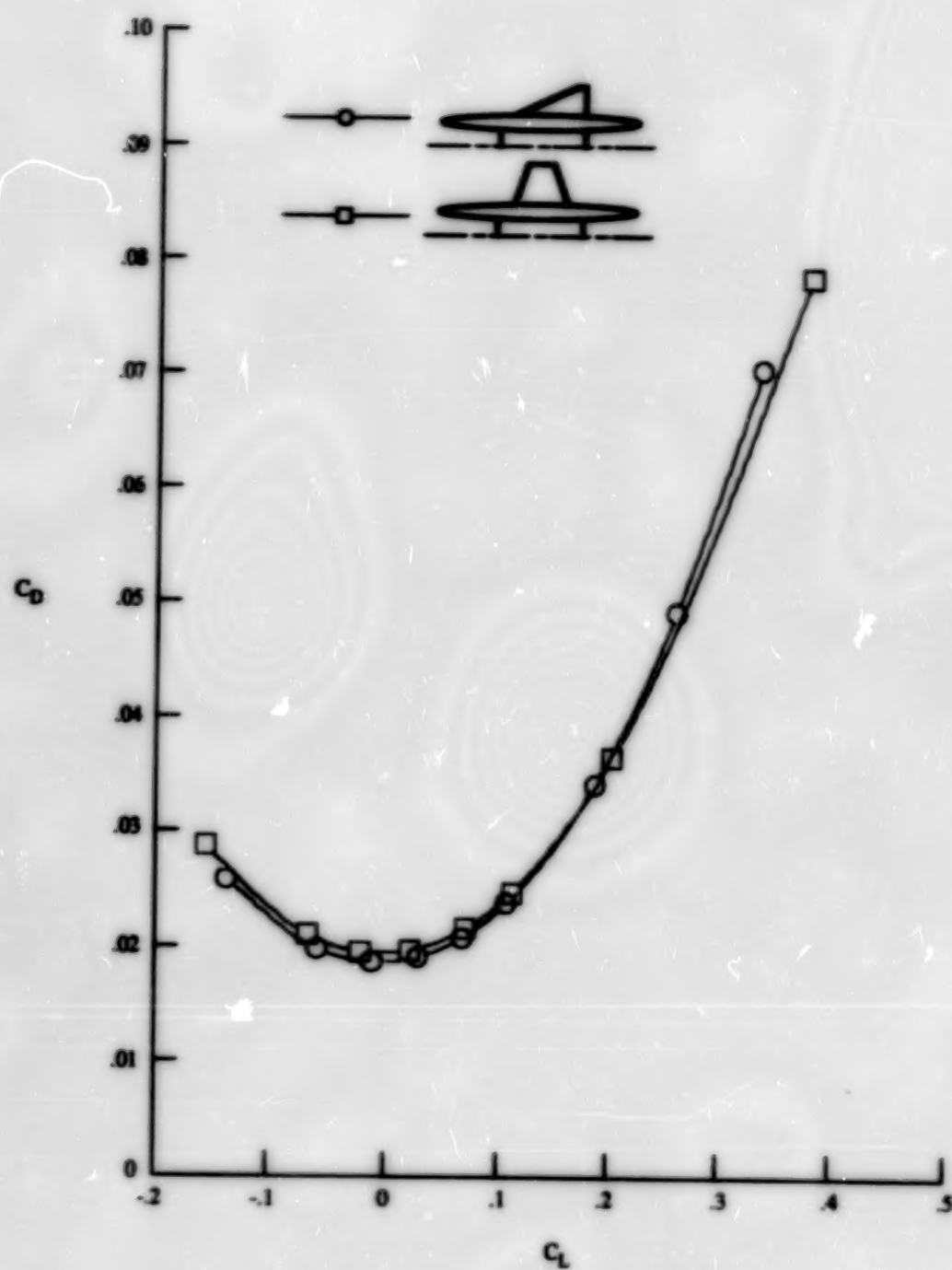
(b) Drag characteristics.

Figure 19. Predicted and measured effects of outboard wing size and Mach number on longitudinal aerodynamic characteristics of swept/trapezoidal multibody configuration.



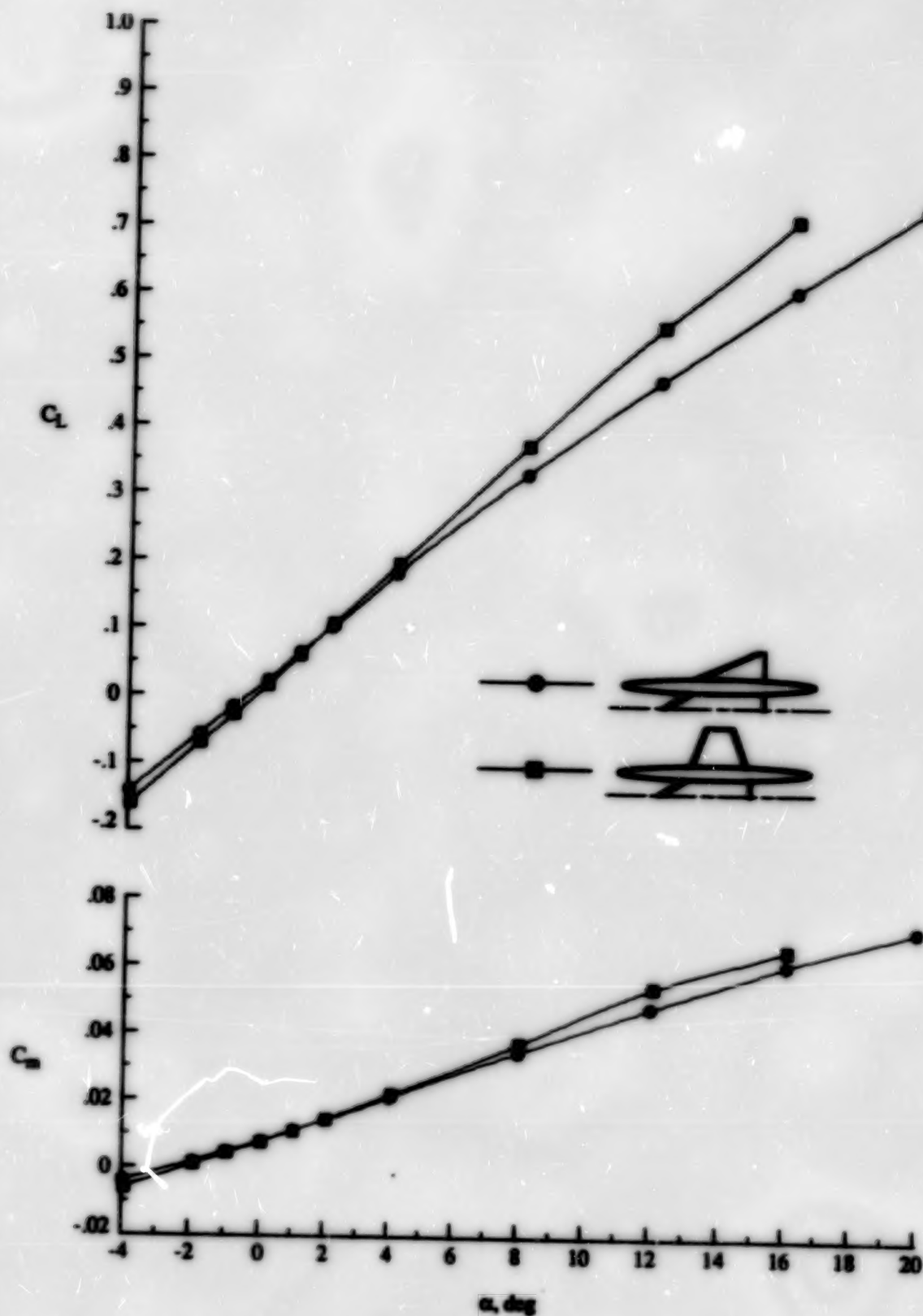
(a) Lift and pitching-moment characteristics.

Figure 20. Effect of outboard wing planform shape on longitudinal aerodynamic characteristics of unswept-inboard multibody configuration at $M = 1.80$.



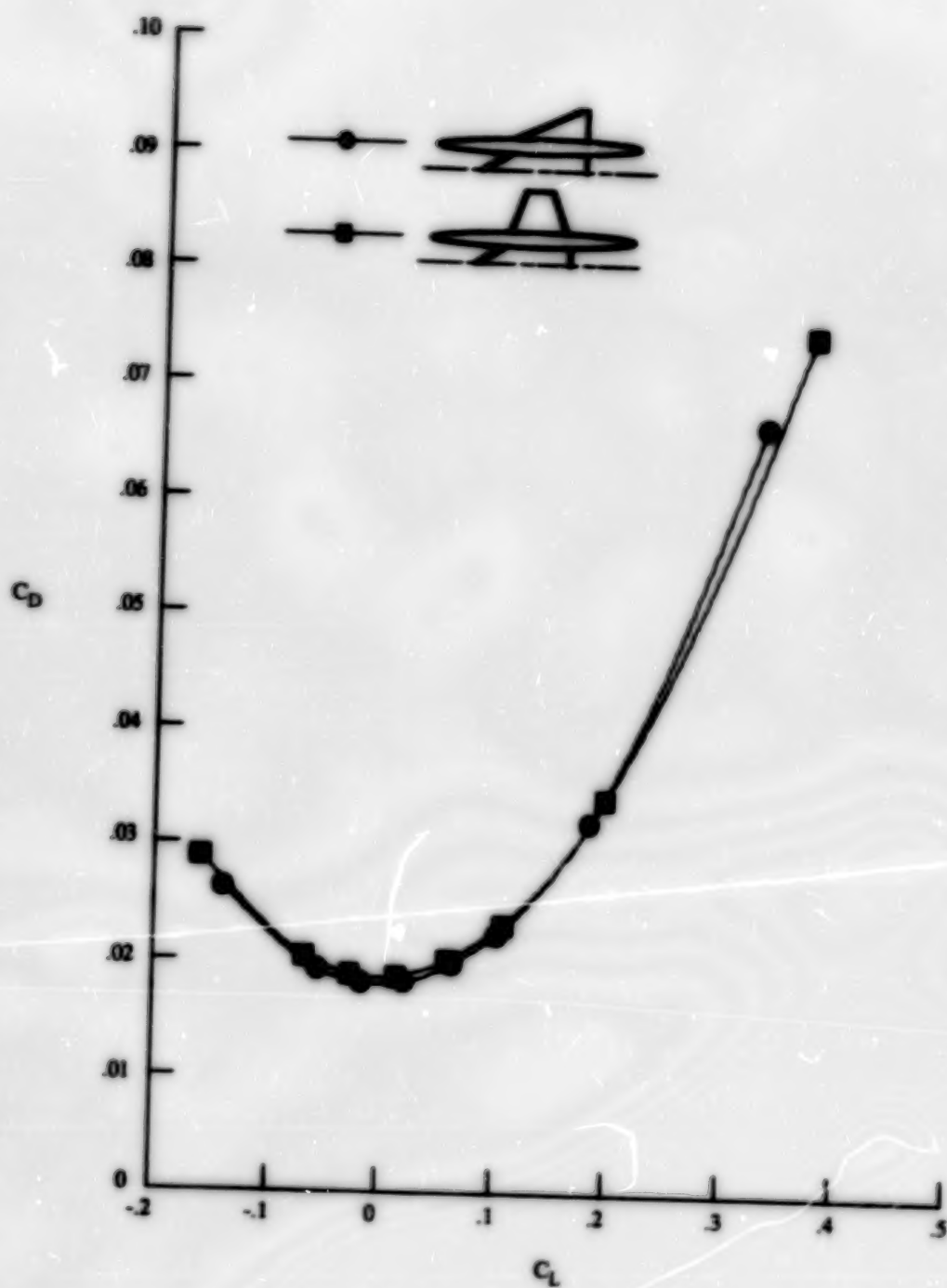
(b) Drag characteristics.

Figure 20. Concluded.



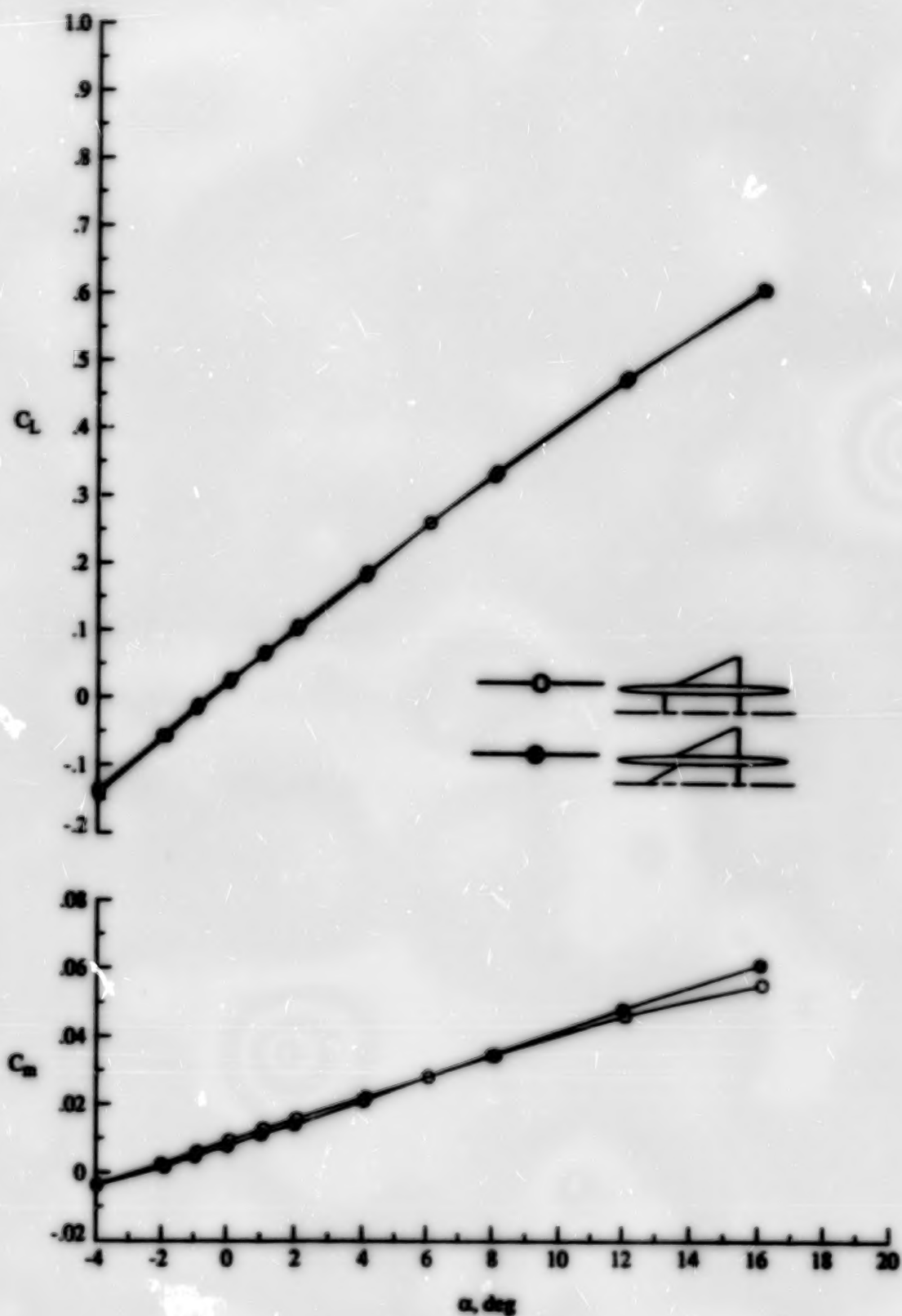
(a) Lift and pitching-moment characteristics.

Figure 21. Effect of outboard wing planform shape on longitudinal aerodynamic characteristics of swept-inboard multibody configuration at $M = 1.80$.



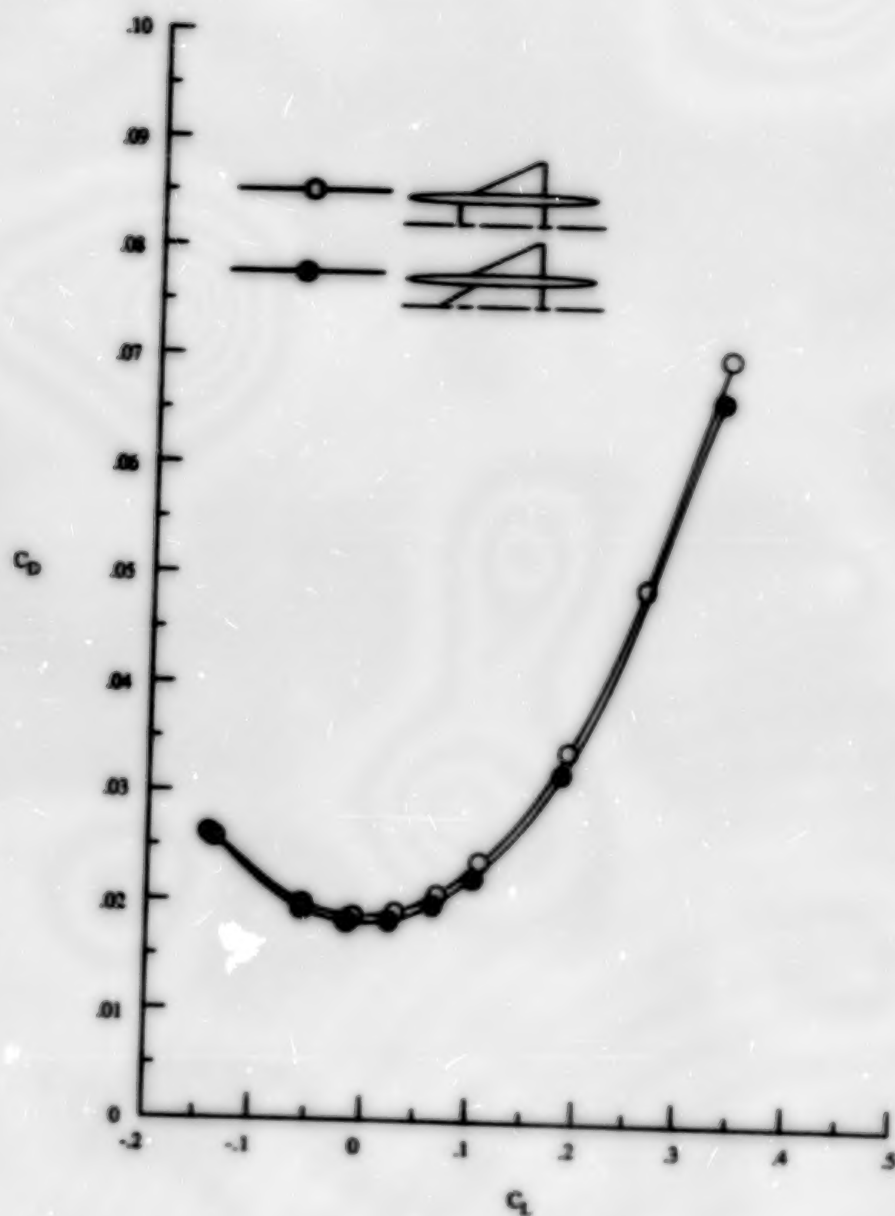
(b) Drag characteristics.

Figure 21. Concluded.



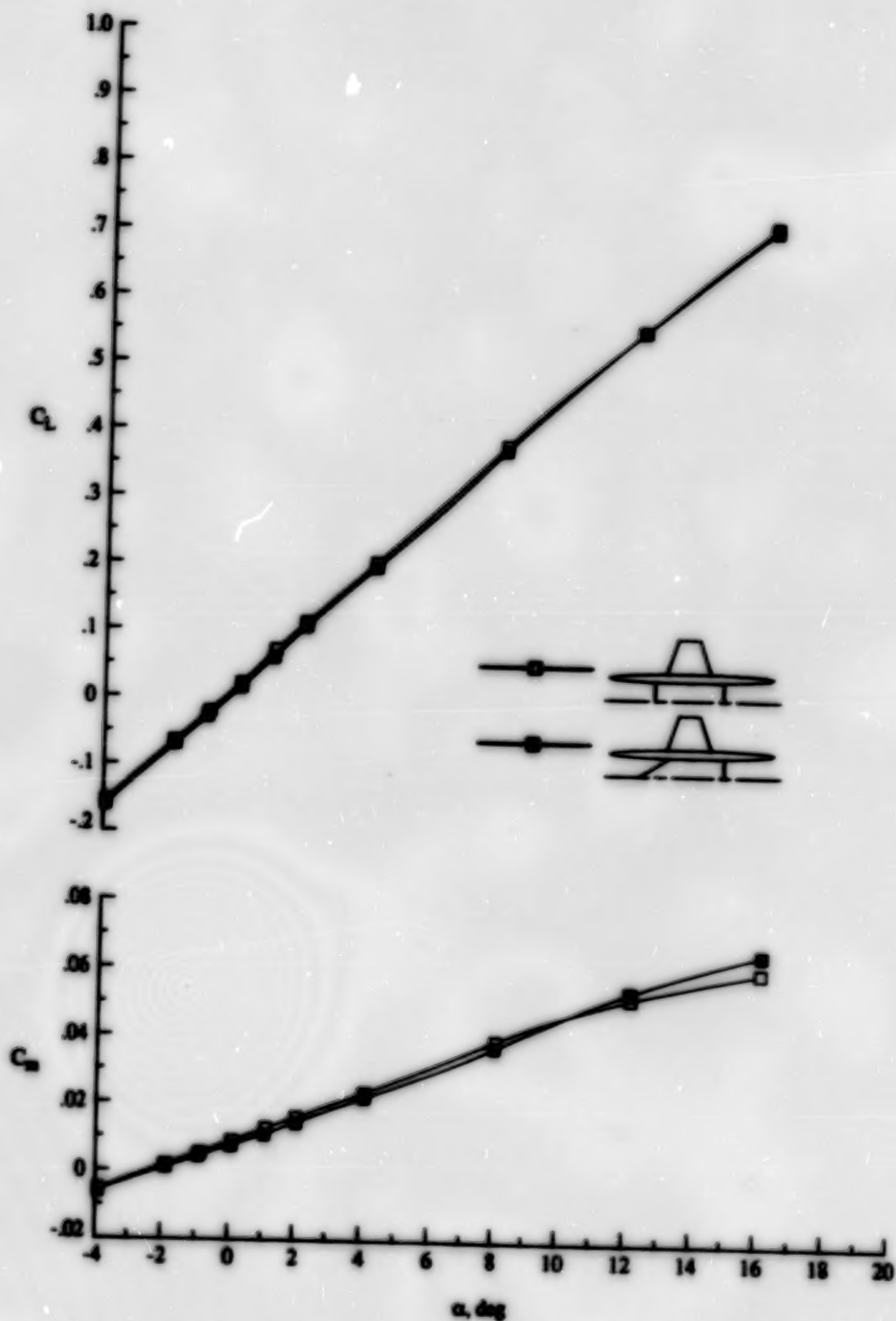
(a) Lift and pitching-moment characteristics.

Figure 22. Effect of inboard wing planform shape on longitudinal aerodynamic characteristics of delta-outboard multibody configuration at $M = 1.80$.



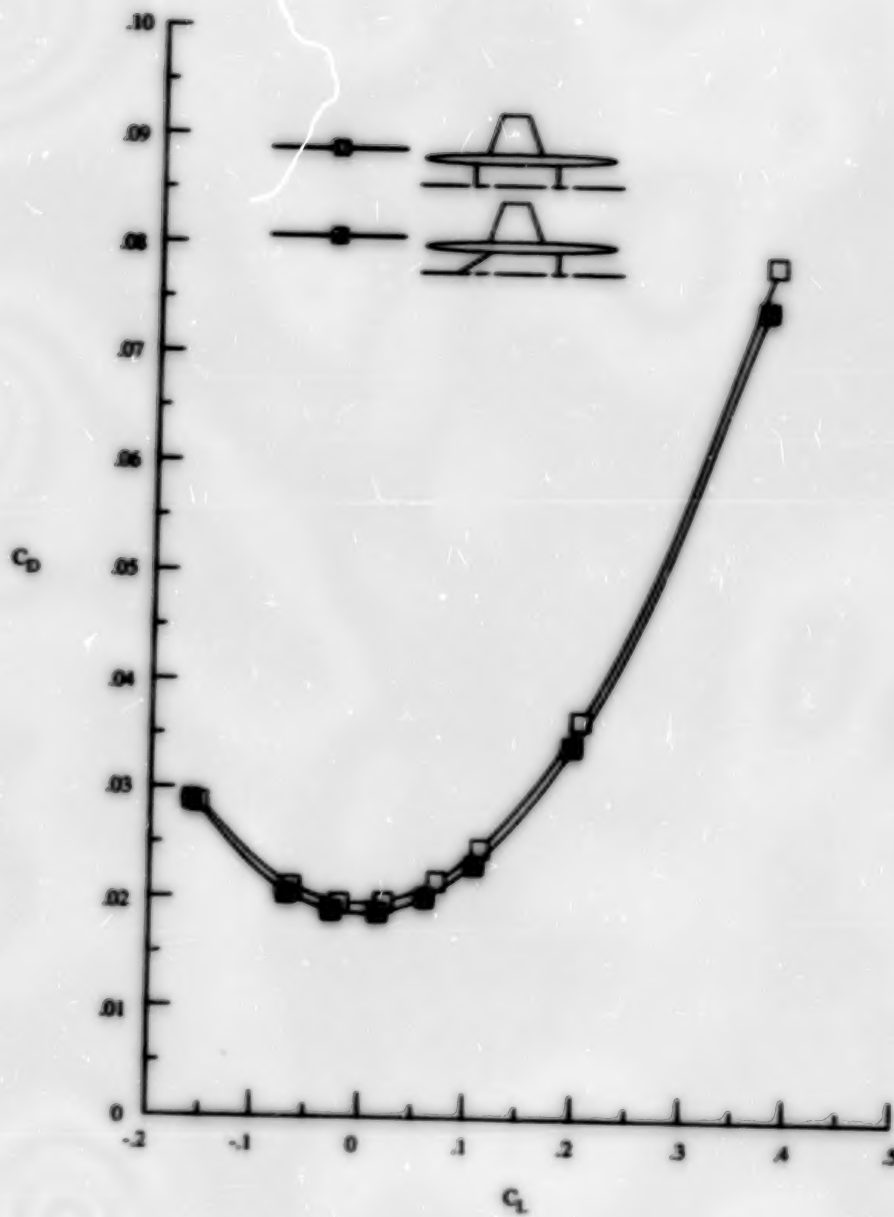
(b) Drag characteristics.

Figure 22. Concluded.



(a) Lift and pitching-moment characteristics.

Figure 23. Effect of inboard wing planform shape on longitudinal aerodynamic characteristics of small-trapezoidal outboard multibody configuration at $M = 1.80$.



(b) Drag characteristics.

Figure 23. Concluded.

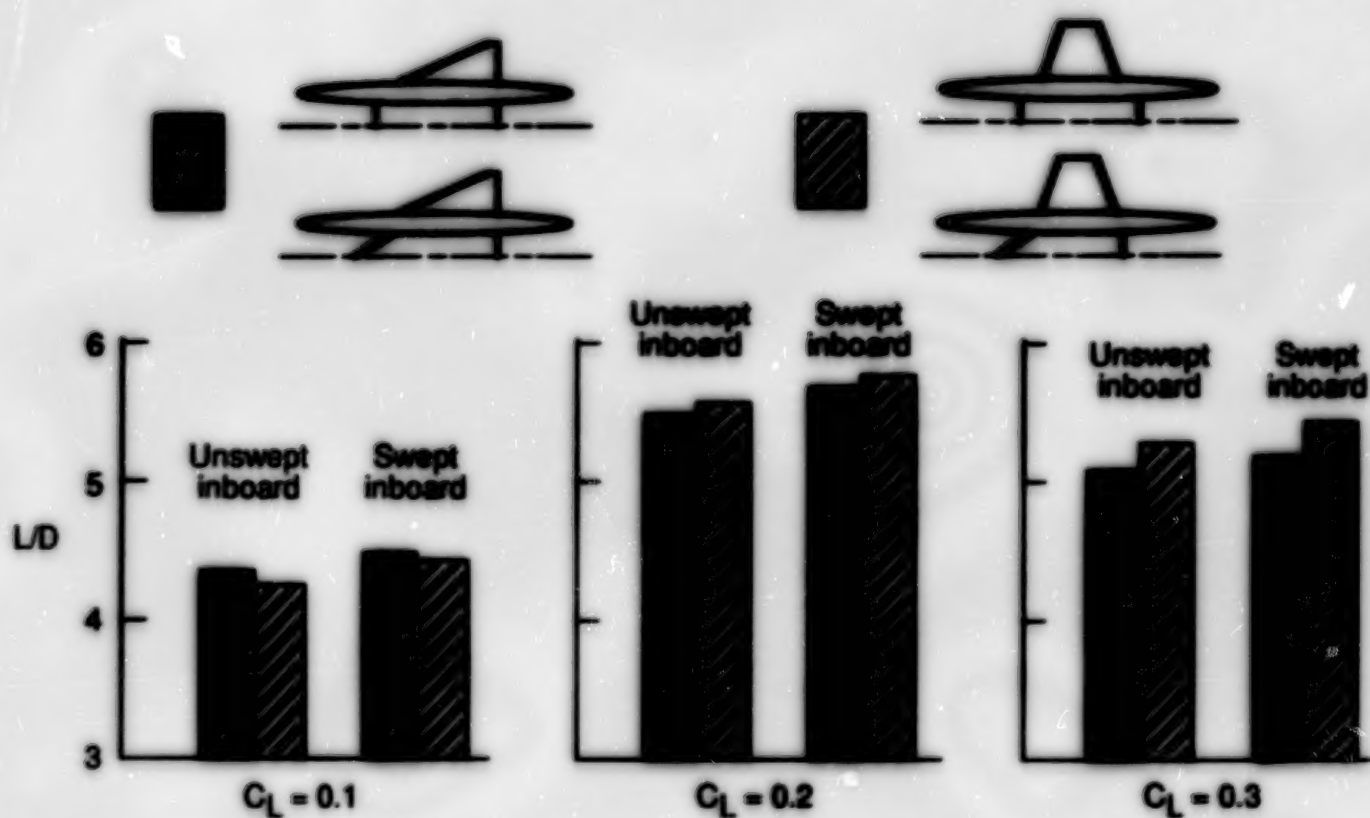
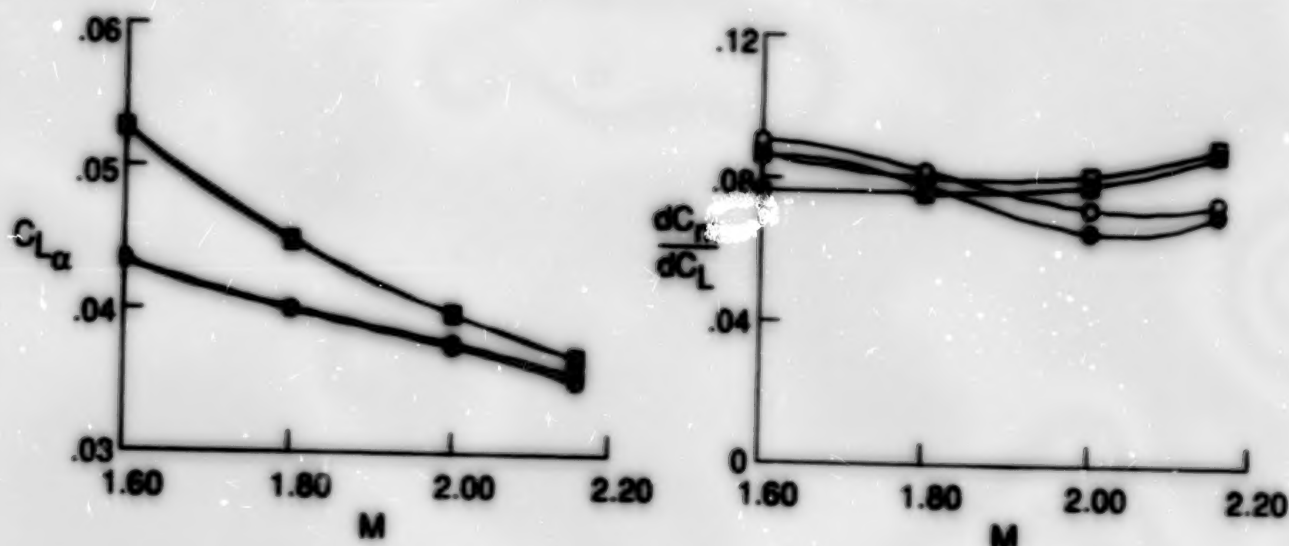
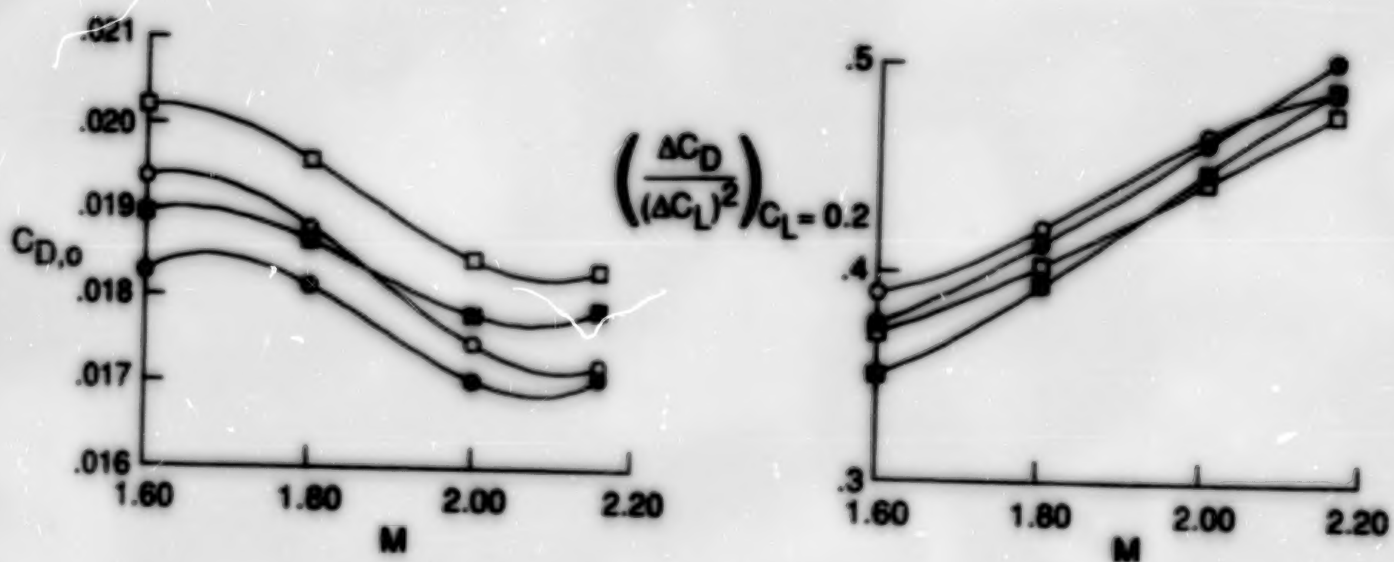


Figure 24. Effect of inboard wing planform shape on aerodynamic performance of delta and small-trapezoidal outboard multibody configurations at $M = 1.80$ and $C_L = 0.1, 0.2$, and 0.3 .

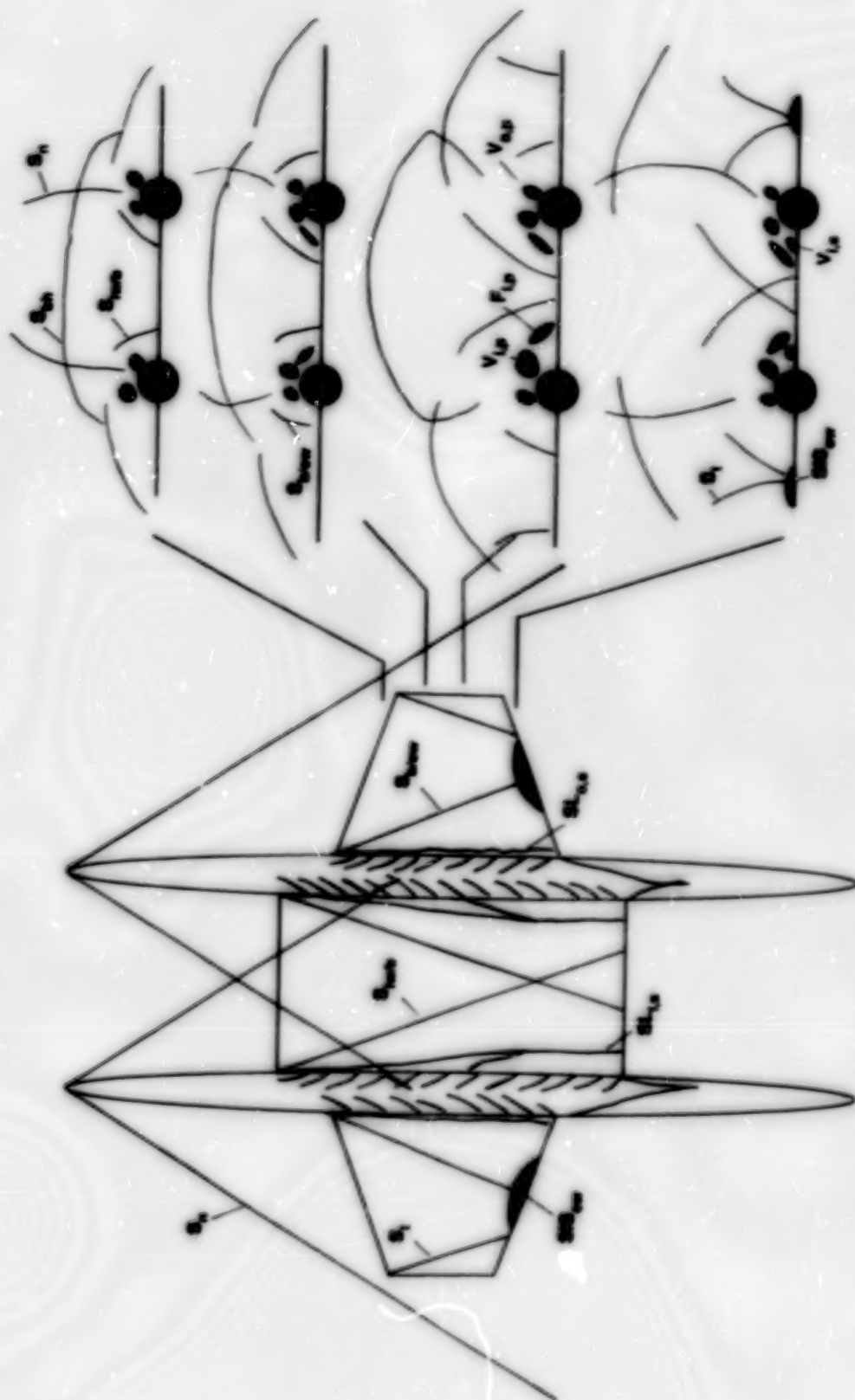


(a) Lift and pitching-moment characteristics.



(b) Drag characteristics.

Figure 25. Effect of inboard wing planform shape and Mach number on longitudinal aerodynamic characteristics of delta-outboard and small-trapezoidal outboard multibody configurations.



Top view
(See oil-flow and schlieren photographs in figs. 27 to 28.)

Spanwise cross-section cuts
(See vapor-screen photographs in figs. 29 to 31.)

Figure 26. Flow pattern over unswept/small-trapezoidal multibody configuration for $M = 2.16$ and $\alpha = 16^\circ$.

ORIGINAL PAGE
BLACK AND WHITE PHOTOGRAPH

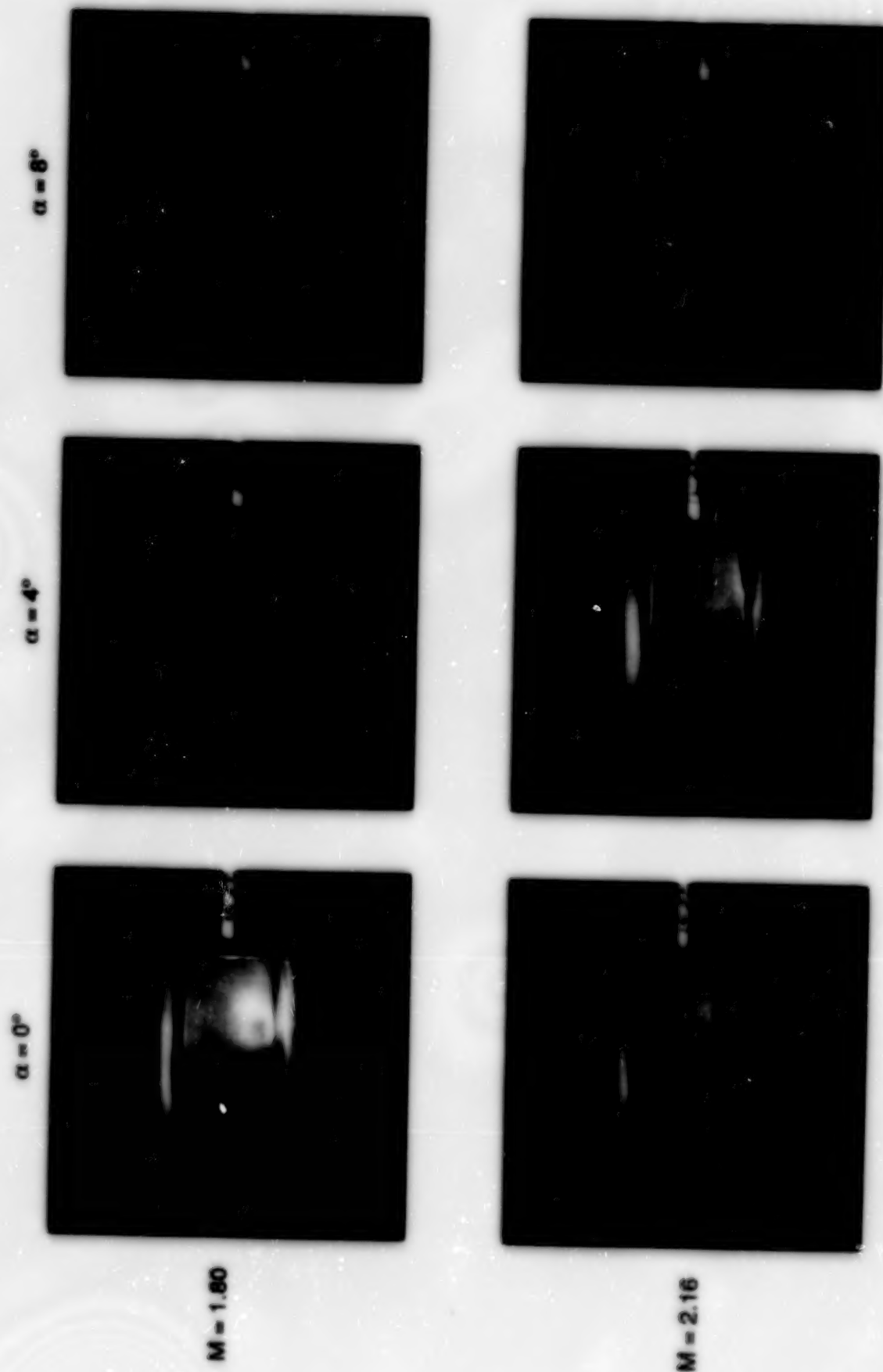


Figure 27. Oil-flow photographs for upper surface of unswept/small-trapezoidal multibody configuration at $\alpha = 0^\circ$, 4° , and 8° and $M = 1.80$ and 2.16 .

ORIGINAL PAGE
BLACK AND WHITE PHOTOGRAPH

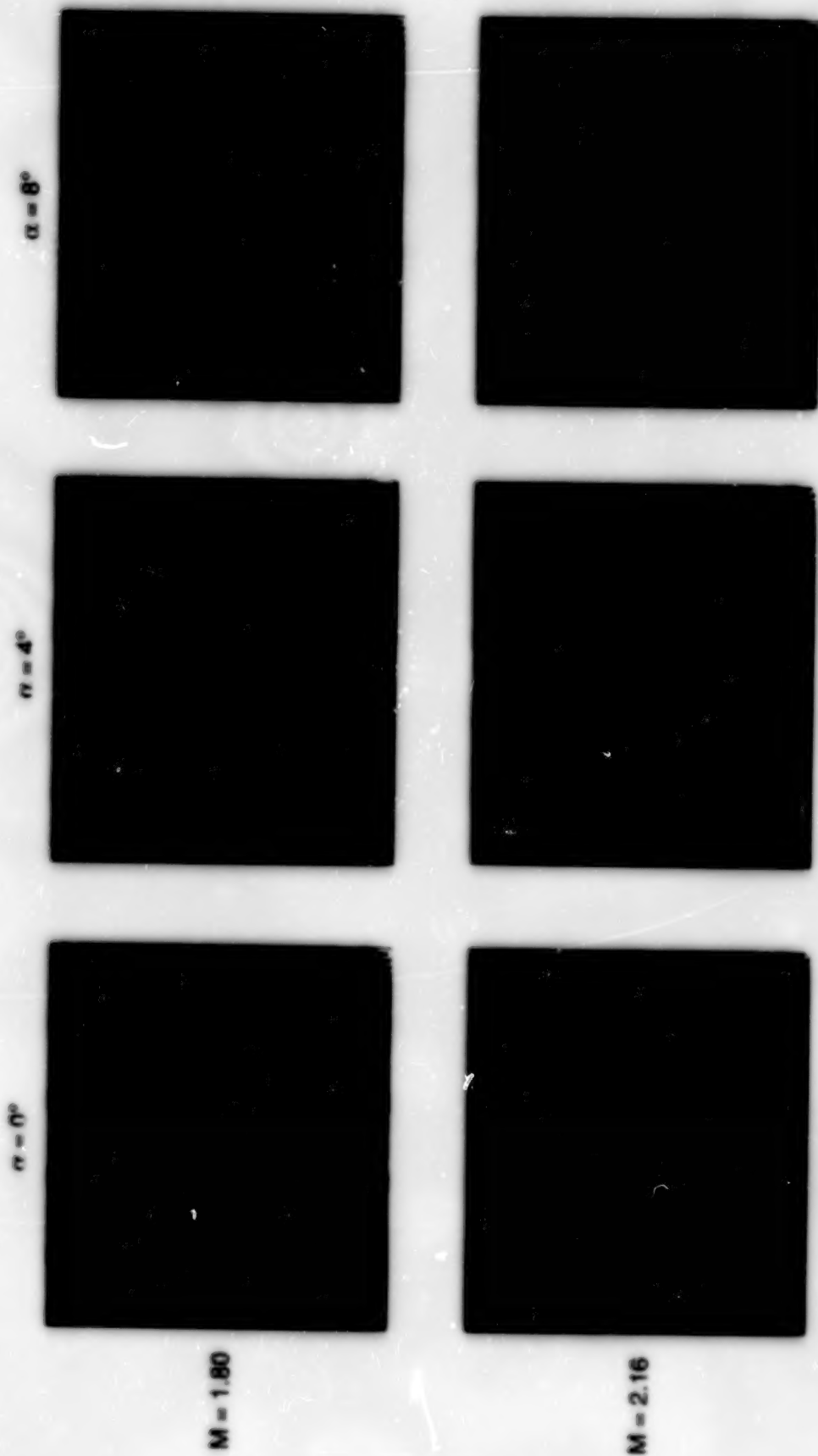


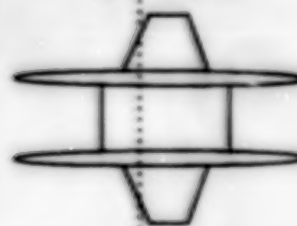
Figure 28. Schlieren photographs for unswept/small-trapezoidal multibody configuration at $\alpha = 0^\circ$, 4° , and 8° and $M = 1.80$ and 2.16 .

ORIGINAL PAGE
BLACK AND WHITE PHOTOGRAPH

$\alpha = 8^\circ$



$x = 12.3 \text{ in.}$



$\alpha = 16^\circ$



(a) $M = 1.60$.

Figure 29. Vapor-screen photographs at $x = 12.3 \text{ in.}$ for unswept/small-trapezoidal multibody configuration for various angles of attack and Mach numbers.

ORIGINAL PAGE
BLACK AND WHITE PHOTOGRAPH

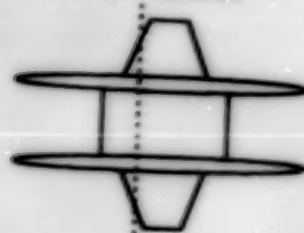
$\alpha = 4^\circ$



$\alpha = 8^\circ$



$x = 12.3 \text{ in.}$

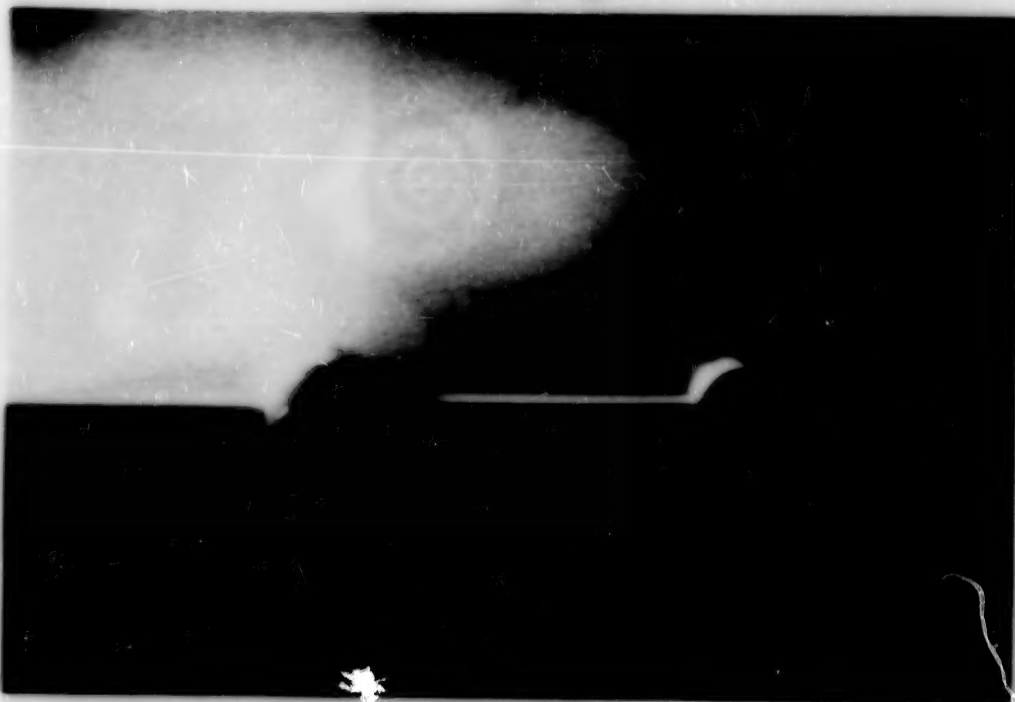


(b) $M = 1.80$.

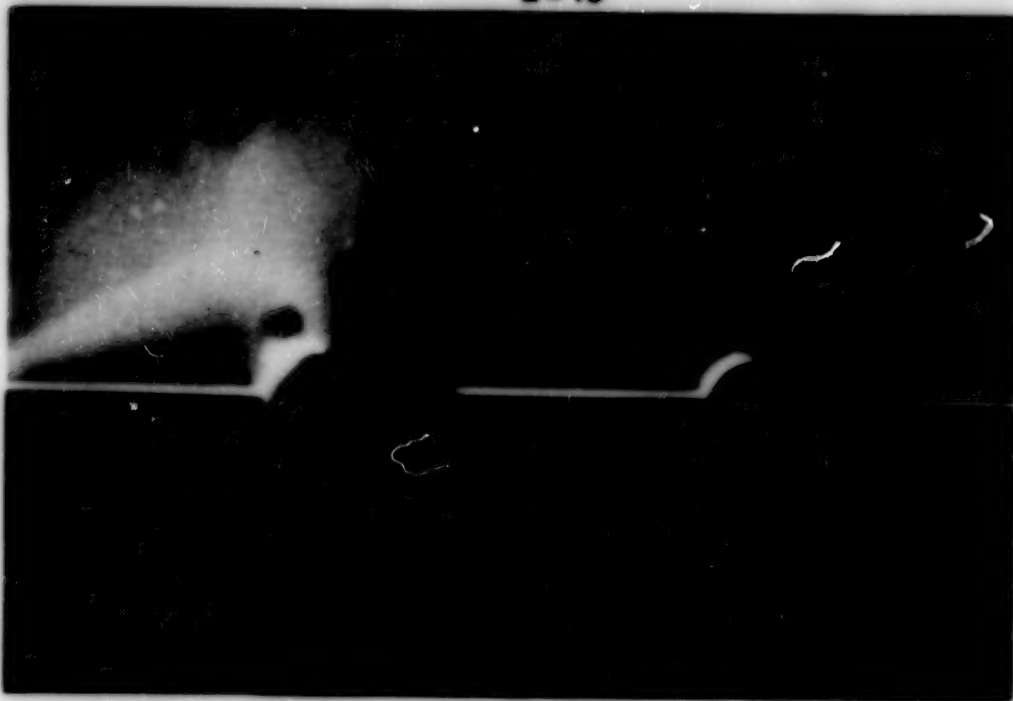
Figure 29. Continued.

ORIGINAL PAGE
BLACK AND WHITE PHOTOGRAPH

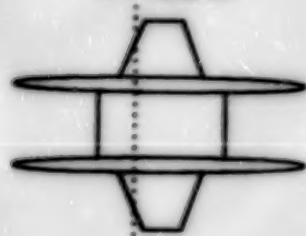
$\alpha = 12^\circ$



$\alpha = 16^\circ$



$x = 12.3 \text{ in.}$



(b) Concluded.

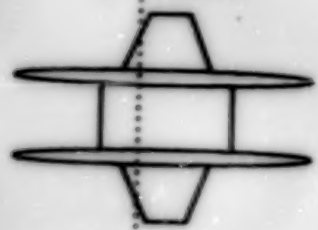
Figure 29. Continued.

ORIGINAL PAGE
BLACK AND WHITE PHOTOGRAPH

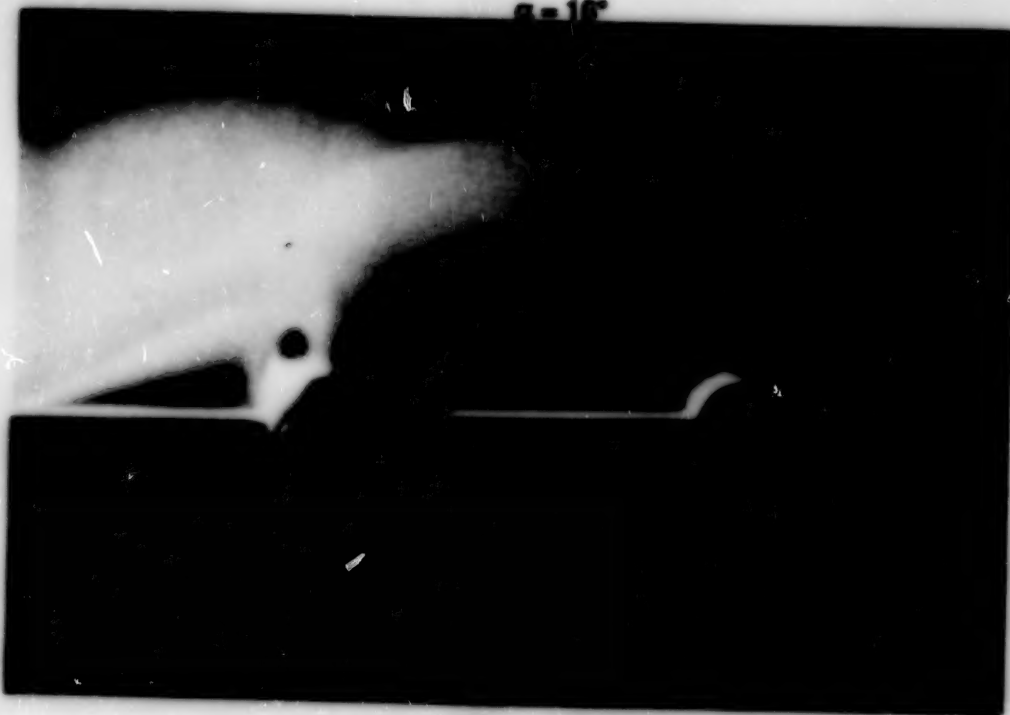
$\alpha = 8^\circ$



$x = 12.3 \text{ in.}$



$\alpha = 16^\circ$

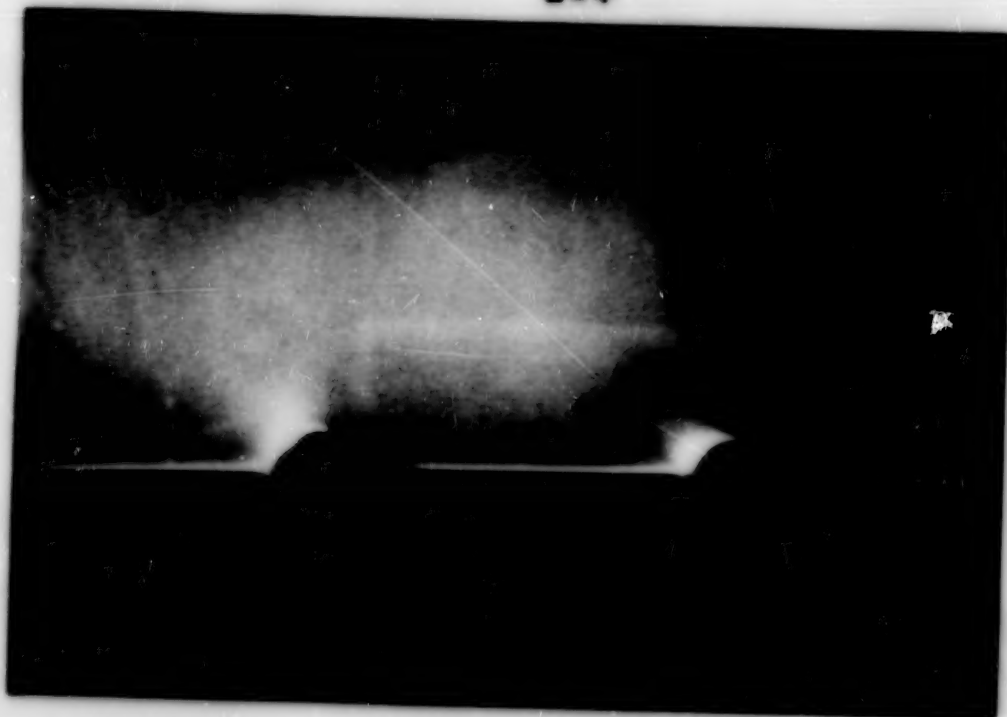


(c) $M = 2.00$.

Figure 29. Continued.

ORIGINAL PAGE
BLACK AND WHITE PHOTOGRAPH

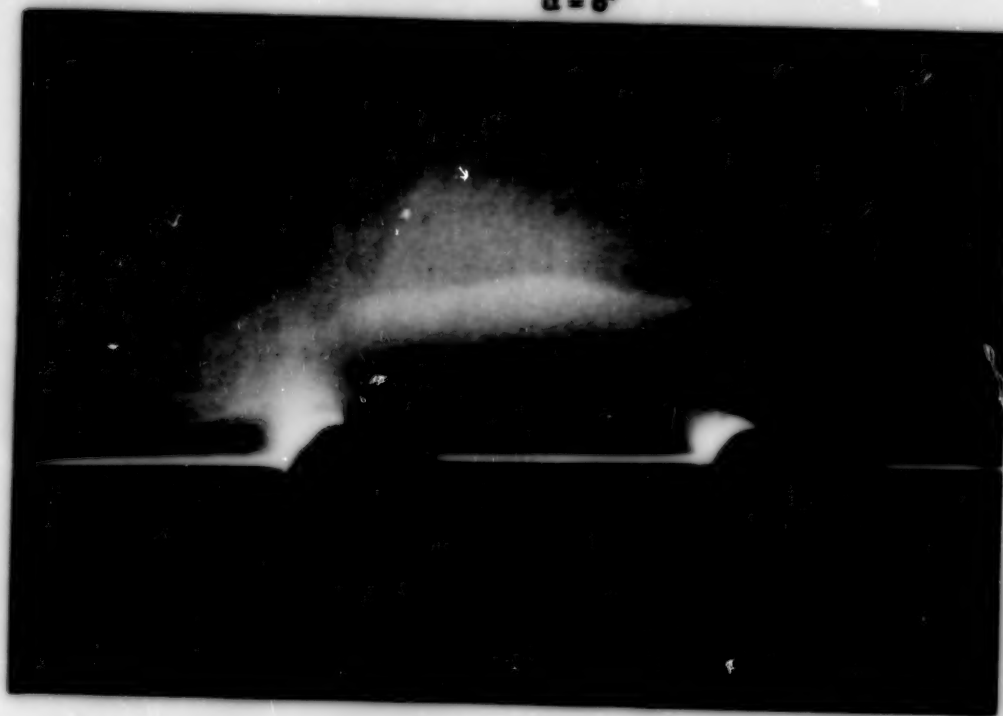
$\alpha = 4^\circ$



$x = 12.3 \text{ in.}$



$\alpha = 8^\circ$

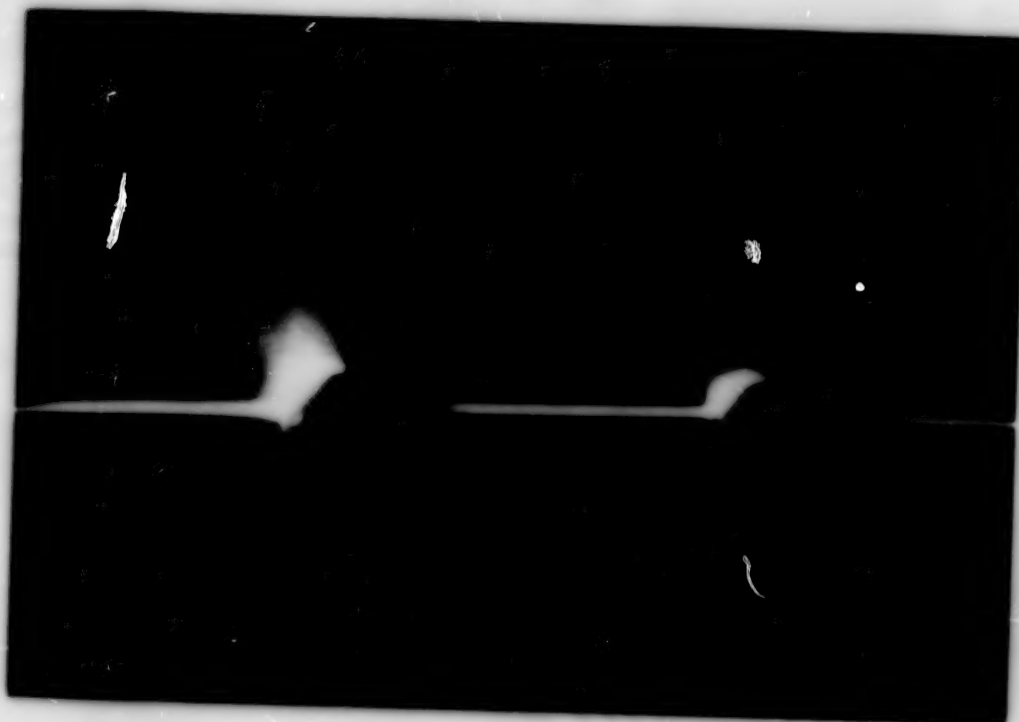


(d) $M = 2.16$.

Figure 29. Continued.

ORIGINAL PAGE
BLACK AND WHITE PHOTOGRAPH

$\alpha = 12^\circ$



$\alpha = 16^\circ$



$x = 12.3 \text{ in.}$

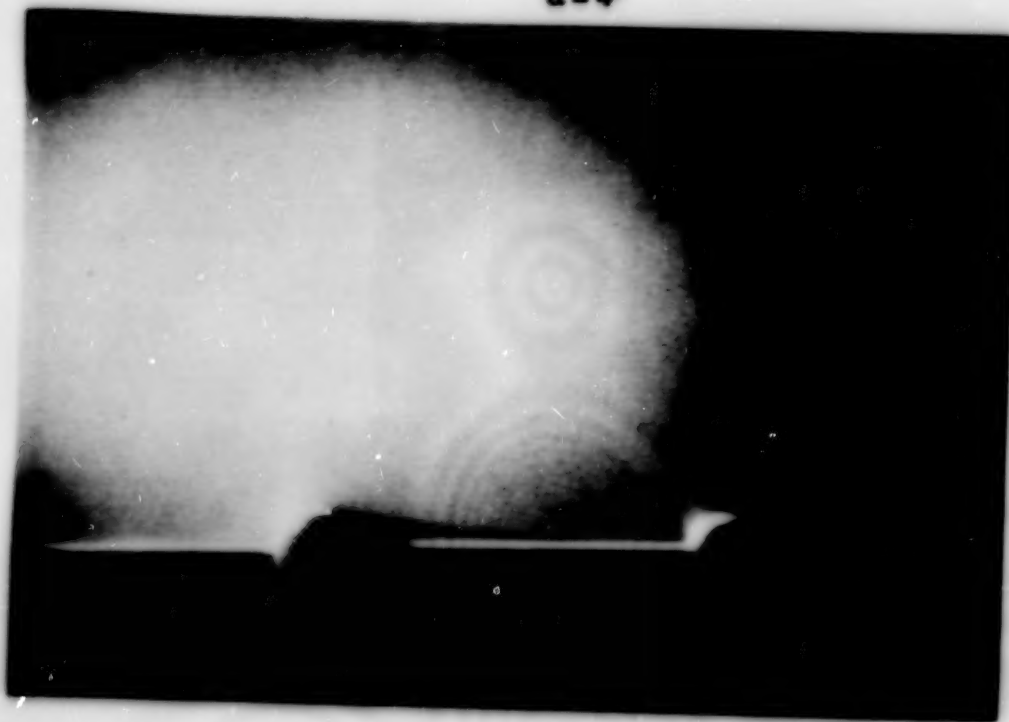


(d) Concluded.

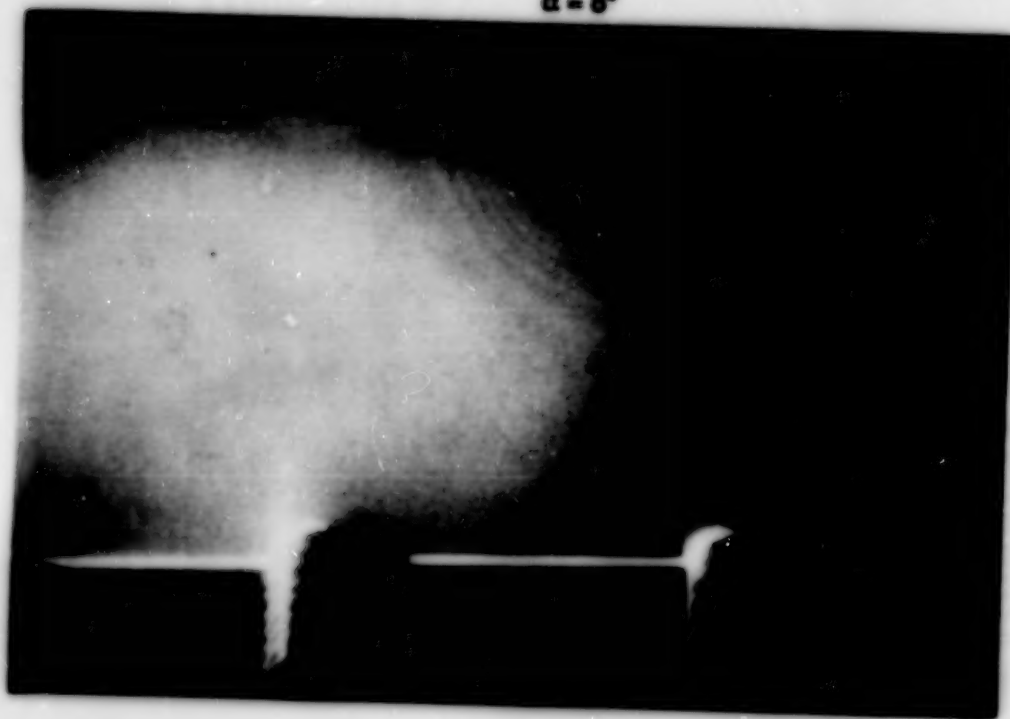
Figure 29. Concluded.

ORIGINAL PAGE
BLACK AND WHITE PHOTOGRAPH

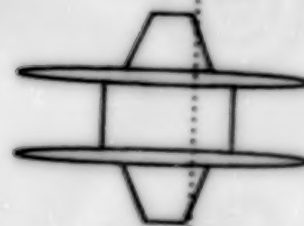
$\alpha = 4^\circ$



$\alpha = 8^\circ$



$x = 17.7 \text{ in.}$

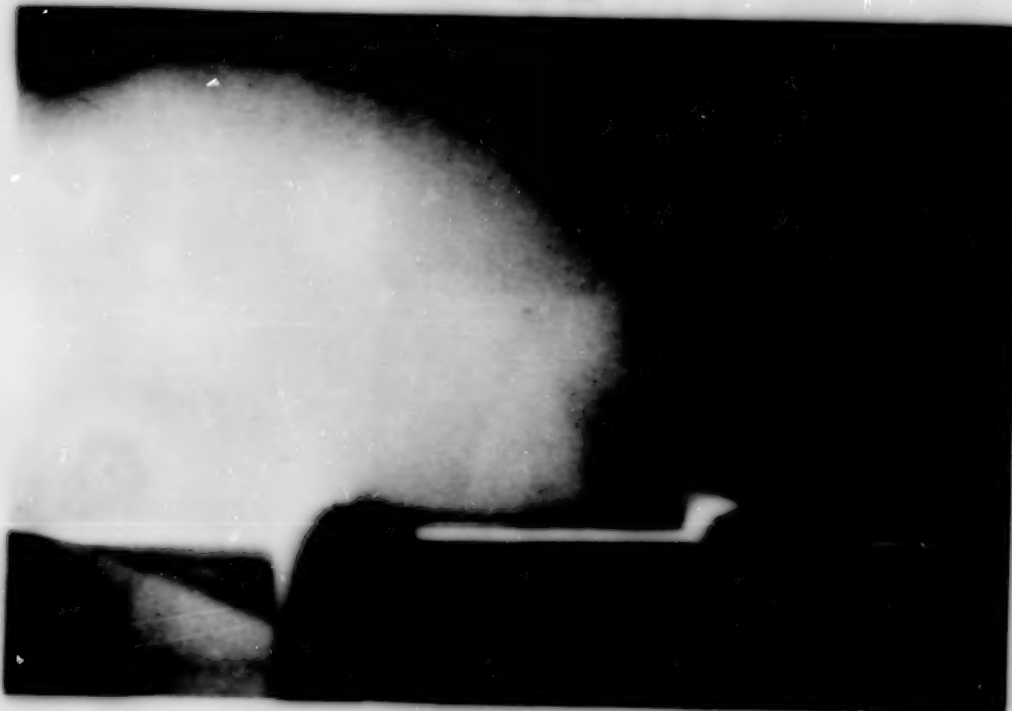


(a) $M = 1.80$.

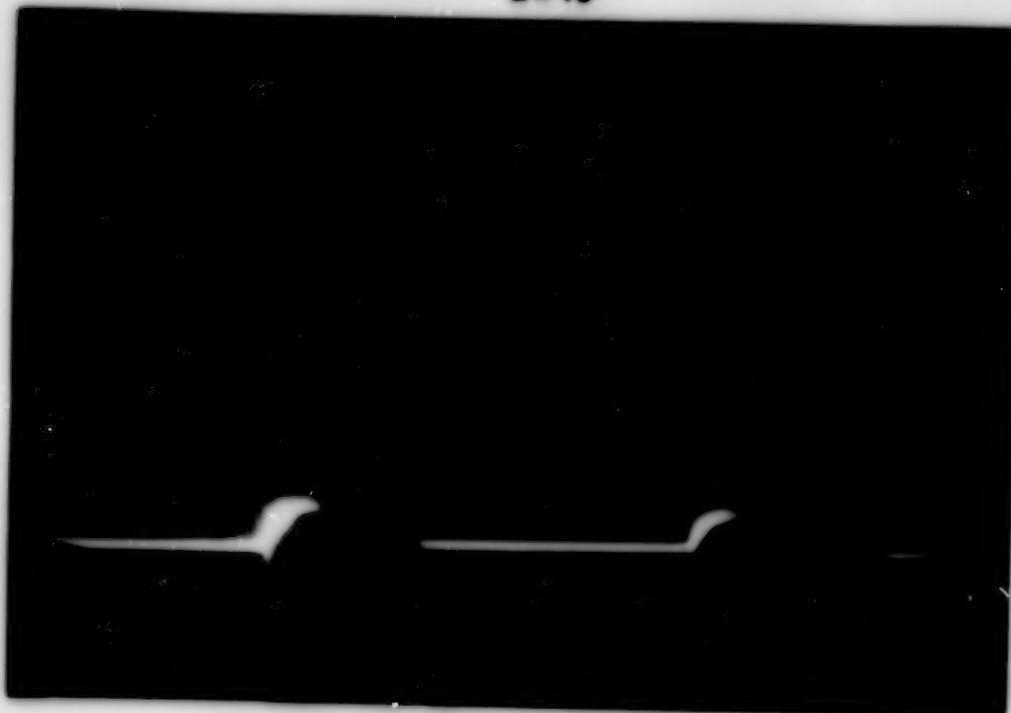
Figure 30. Vapor-screen photographs at $x = 17.7 \text{ in.}$ for unswept/small-trapezoidal multibody configuration for various angles of attack and Mach numbers.

ORIGINAL PAGE
BLACK AND WHITE PHOTOGRAPH

$\alpha = 12^\circ$



$\alpha = 16^\circ$



$x = 17.7 \text{ in.}$

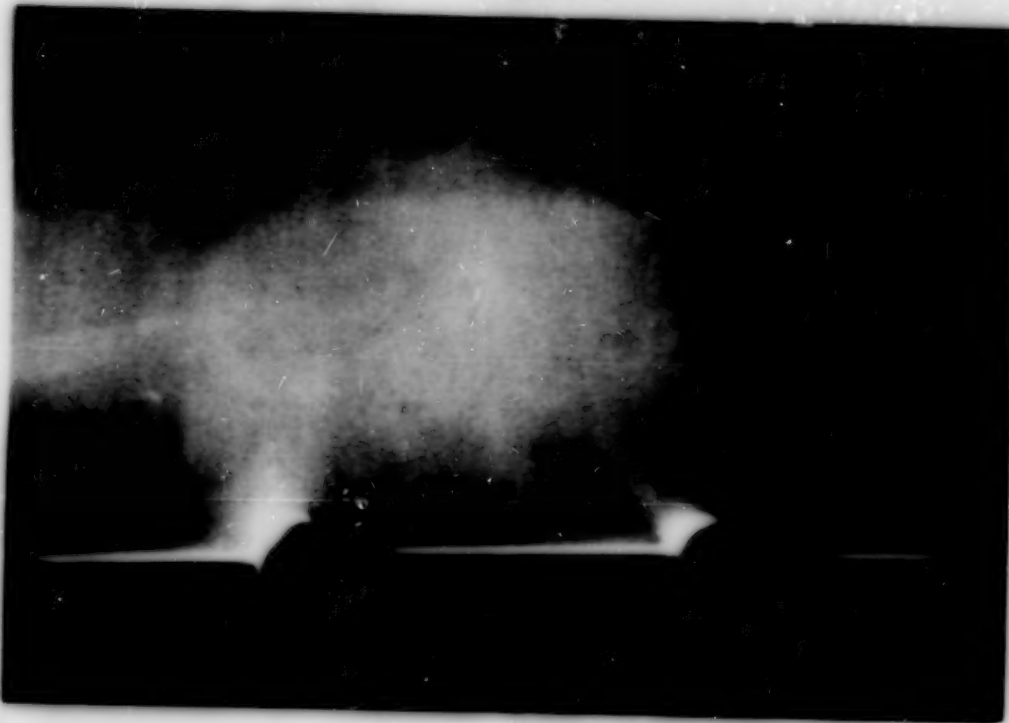


(a) Concluded.

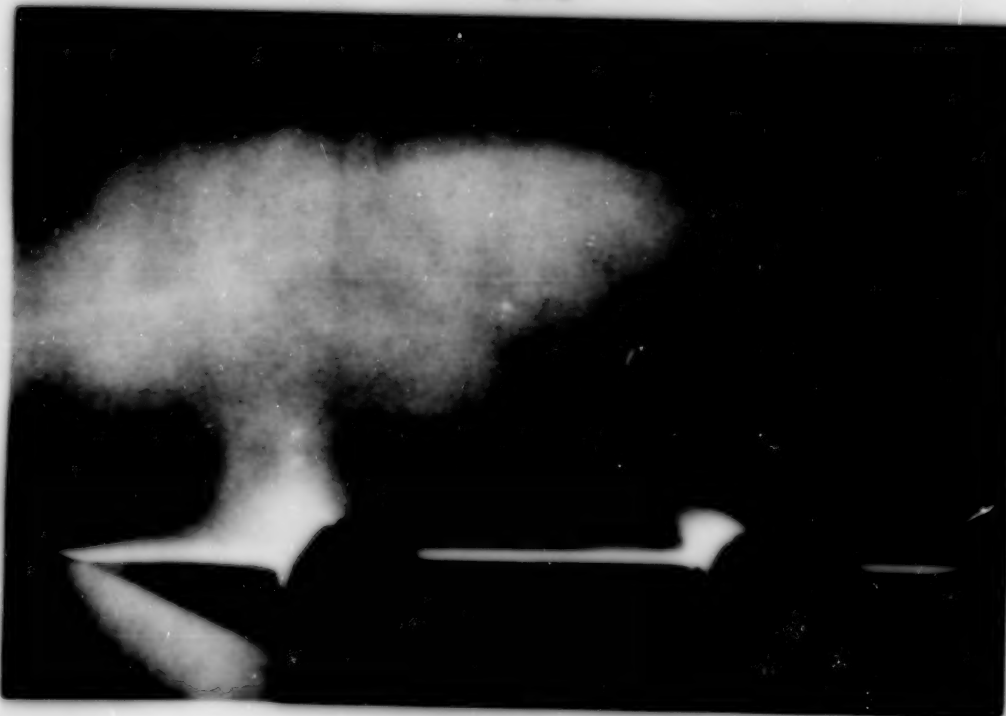
Figure 30. Continued.

ORIGINAL PAGE
BLACK AND WHITE PHOTOGRAPH

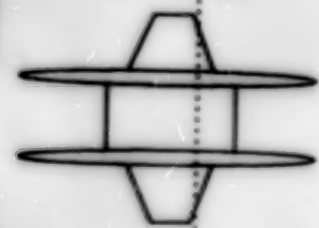
$\alpha = 4^\circ$



$\alpha = 8^\circ$



$x = 17.7 \text{ in.}$



(b) $M = 2.16$.

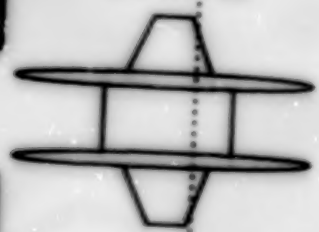
Figure 30. Continued.

ORIGINAL PAGE
BLACK AND WHITE PHOTOGRAPH

$\alpha = 12^\circ$



$x = 17.7 \text{ in.}$



$\alpha = 16^\circ$



(b) Concluded.

Figure 30. Concluded.

ORIGINAL PAGE
BLACK AND WHITE PHOTOGRAPH

$x = 12.3$ in.



$x = 14.1$ in.

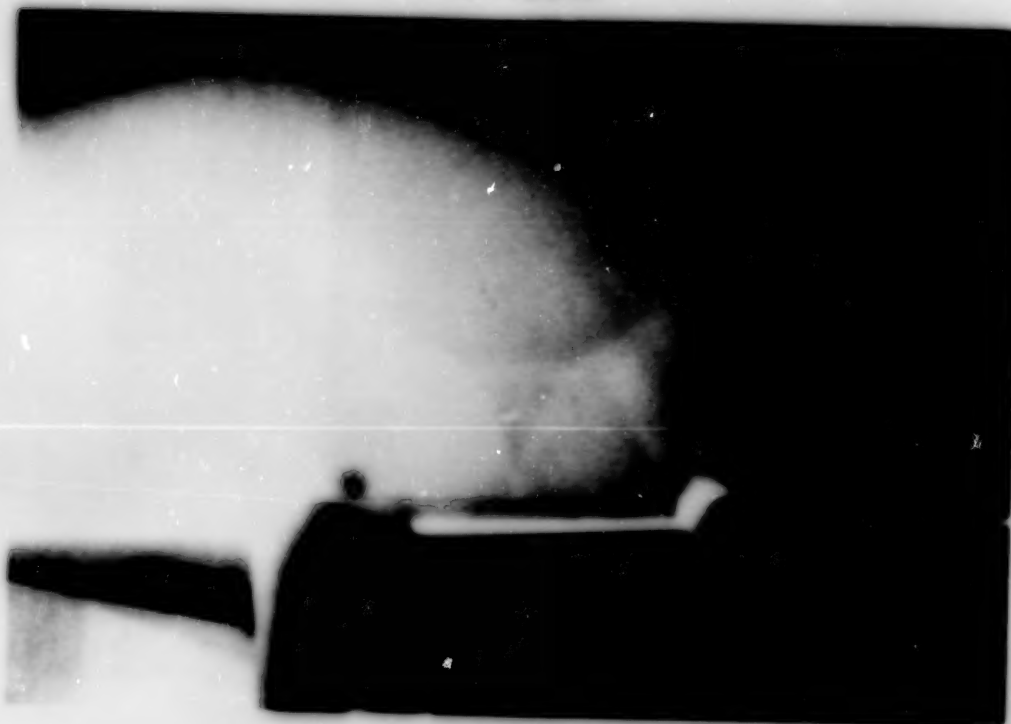


(a) $M = 1.80$.

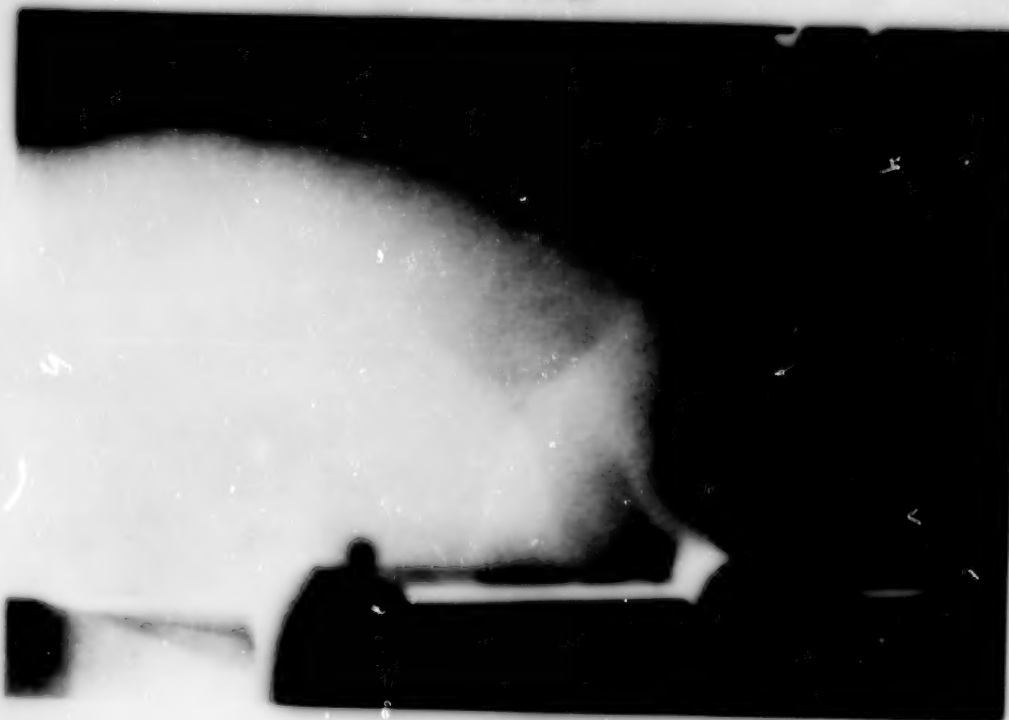
Figure 31. Vapor-screen photographs for unswept/small-trapezoidal multibody configuration at four longitudinal locations for $\alpha = 16^\circ$ and $M = 1.80$ and 2.16.

ORIGINAL PAGE
BLACK AND WHITE PHOTOGRAPH

$x = 15.9$ in.



$x = 17.7$ in.

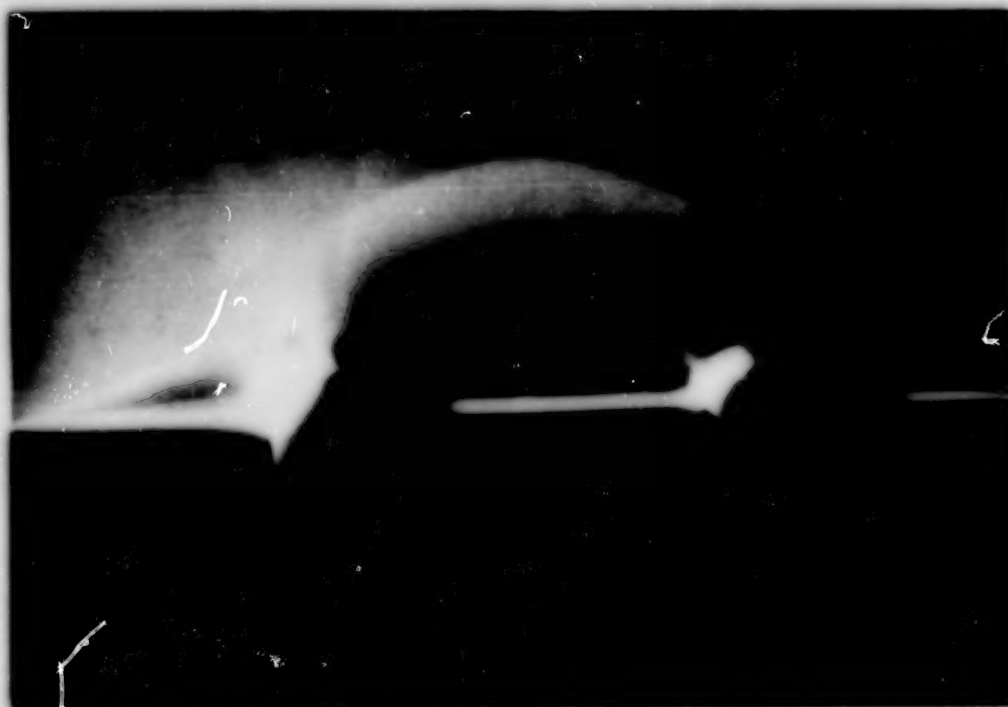


(a) Concluded.

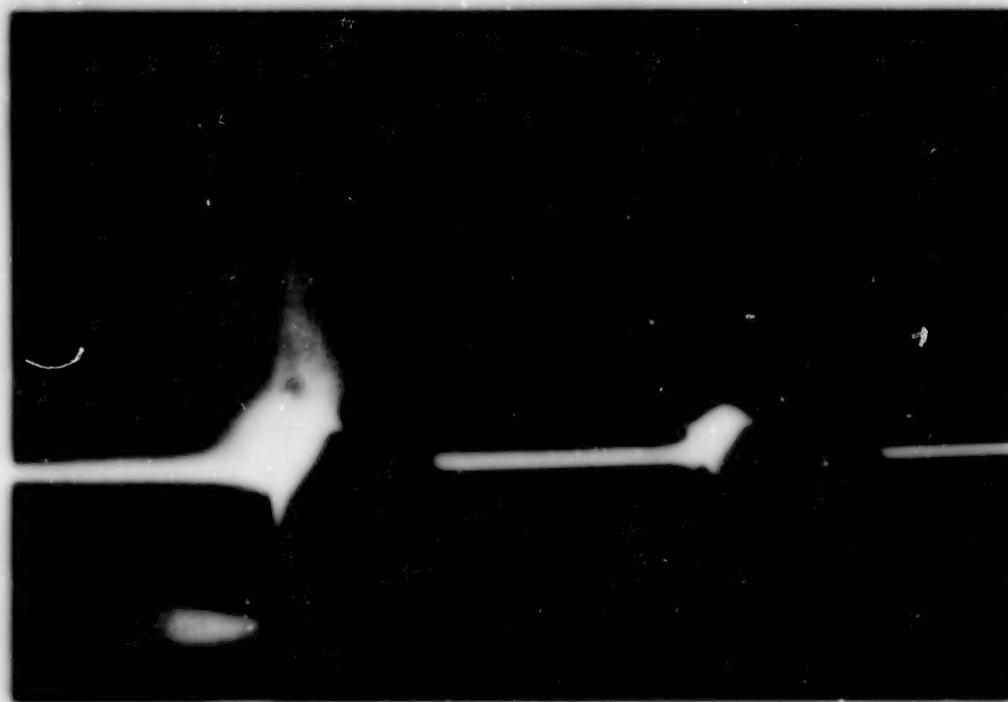
Figure 31. Continued.

ORIGINAL PAGE
BLACK AND WHITE PHOTOGRAPH

$x = 12.3$ in.

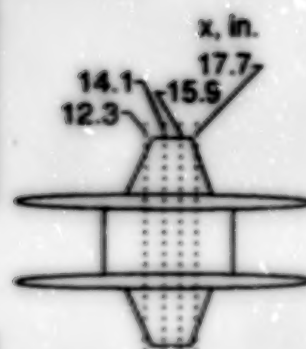


$x = 14.1$ in.



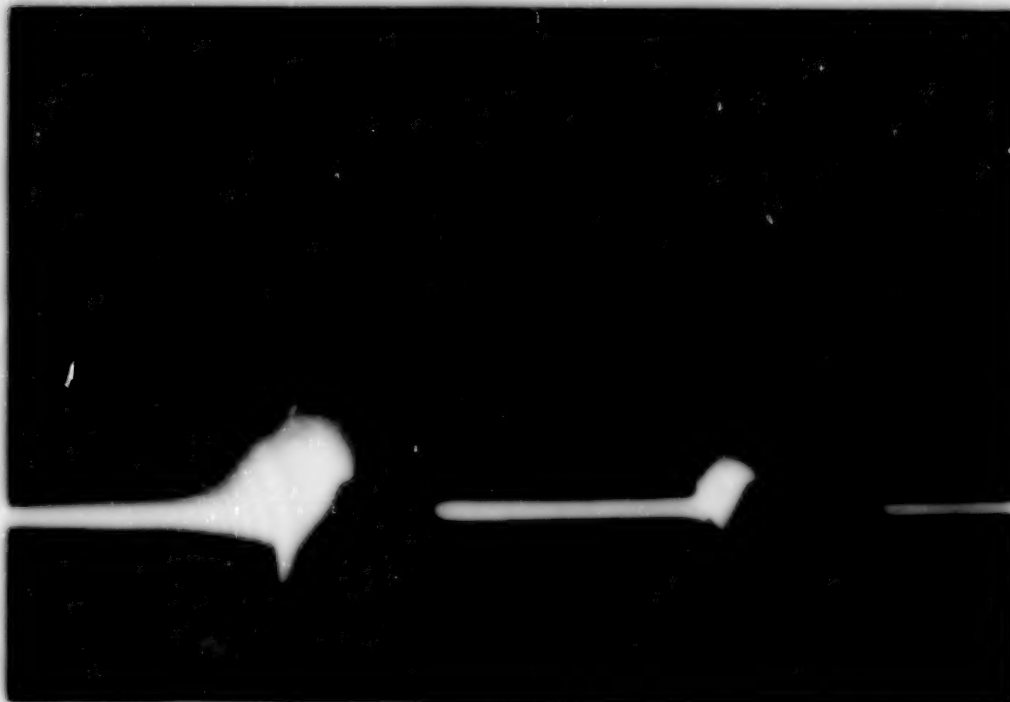
(b) $M = 2.16$.

Figure 31. Continued.

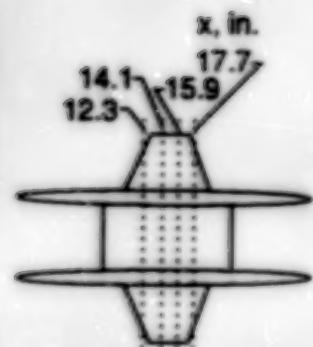
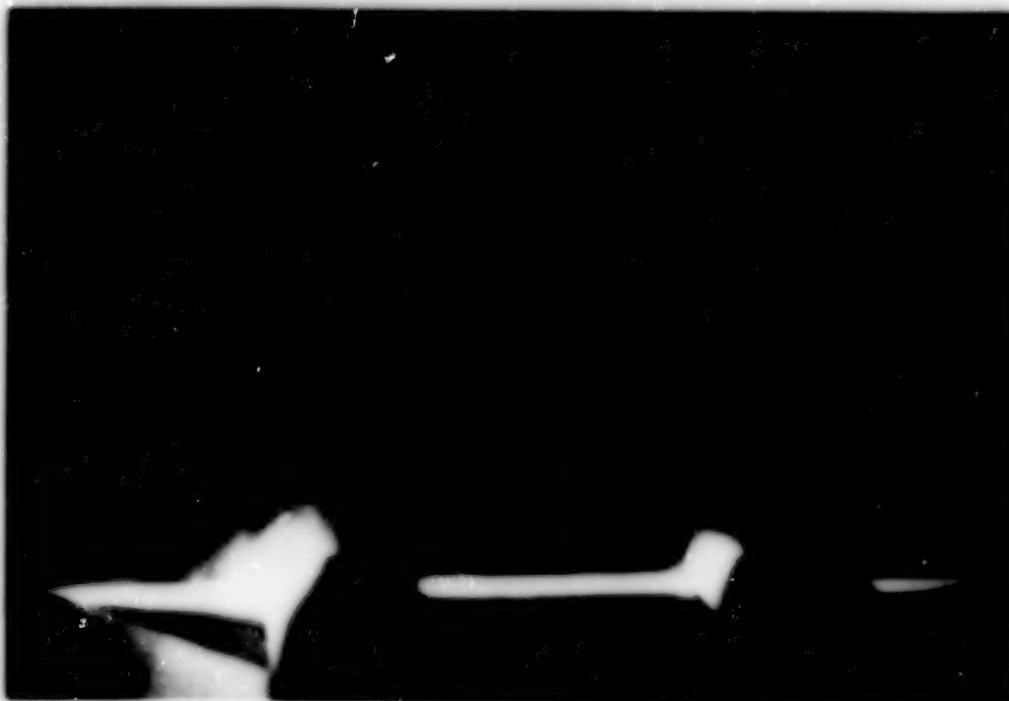


ORIGINAL PAGE
BLACK AND WHITE PHOTOGRAPH

$x = 15.9$ in.

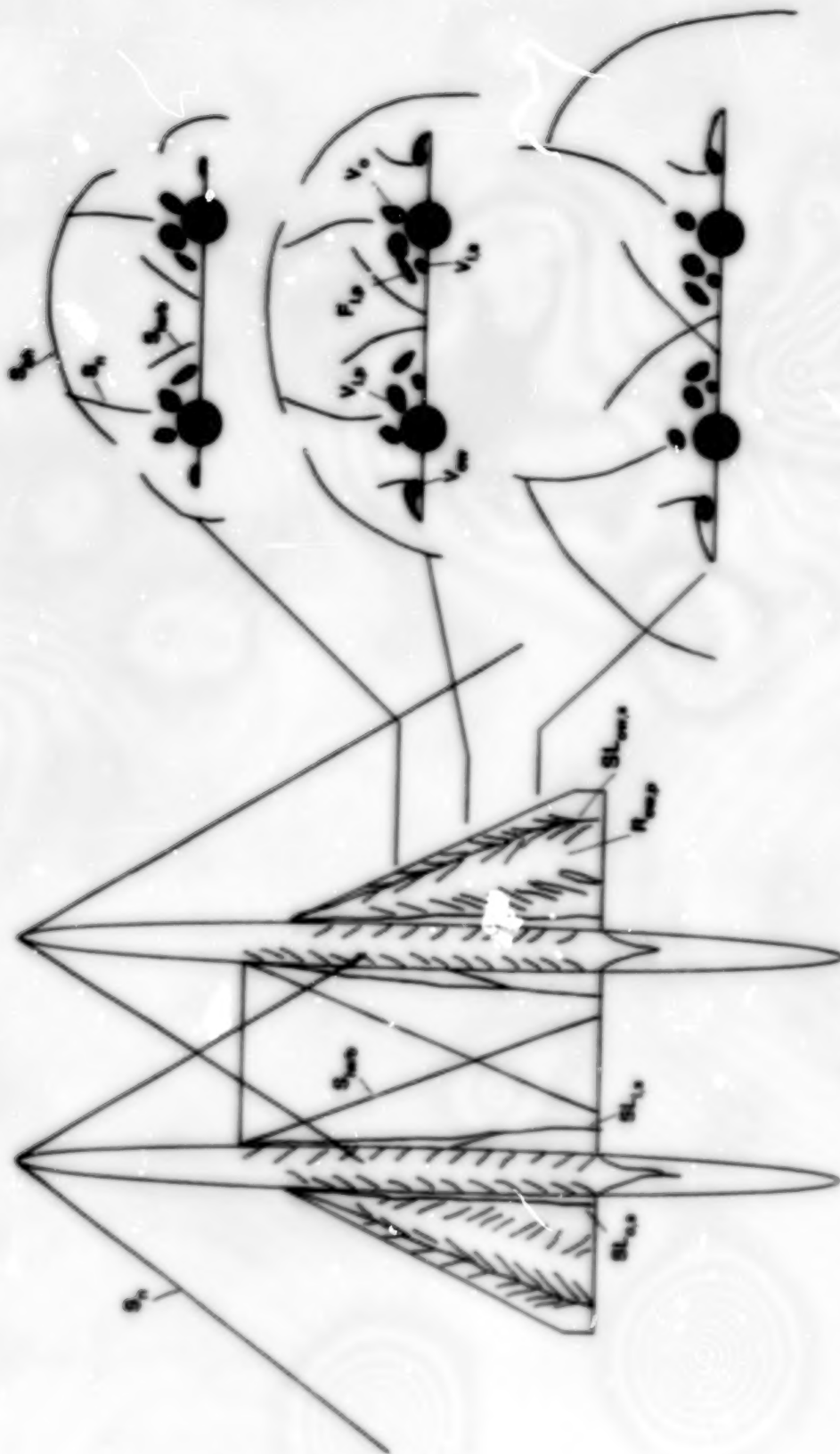


$x = 17.7$ in.



(b) Concluded.

Figure 31. Concluded.



Top view

(See oil-flow and schlieren photographs in figs. 33 to 34.)

Spanwise cross-section cuts
(See vapor-screen photographs in figs. 35 to 36.)

Figure 32. Flow pattern over unswept/delta multibody configuration for $M = 2.16$ and $\alpha = 16^\circ$.

ORIGINAL PAGE
BLACK AND WHITE PHOTOGRAPH

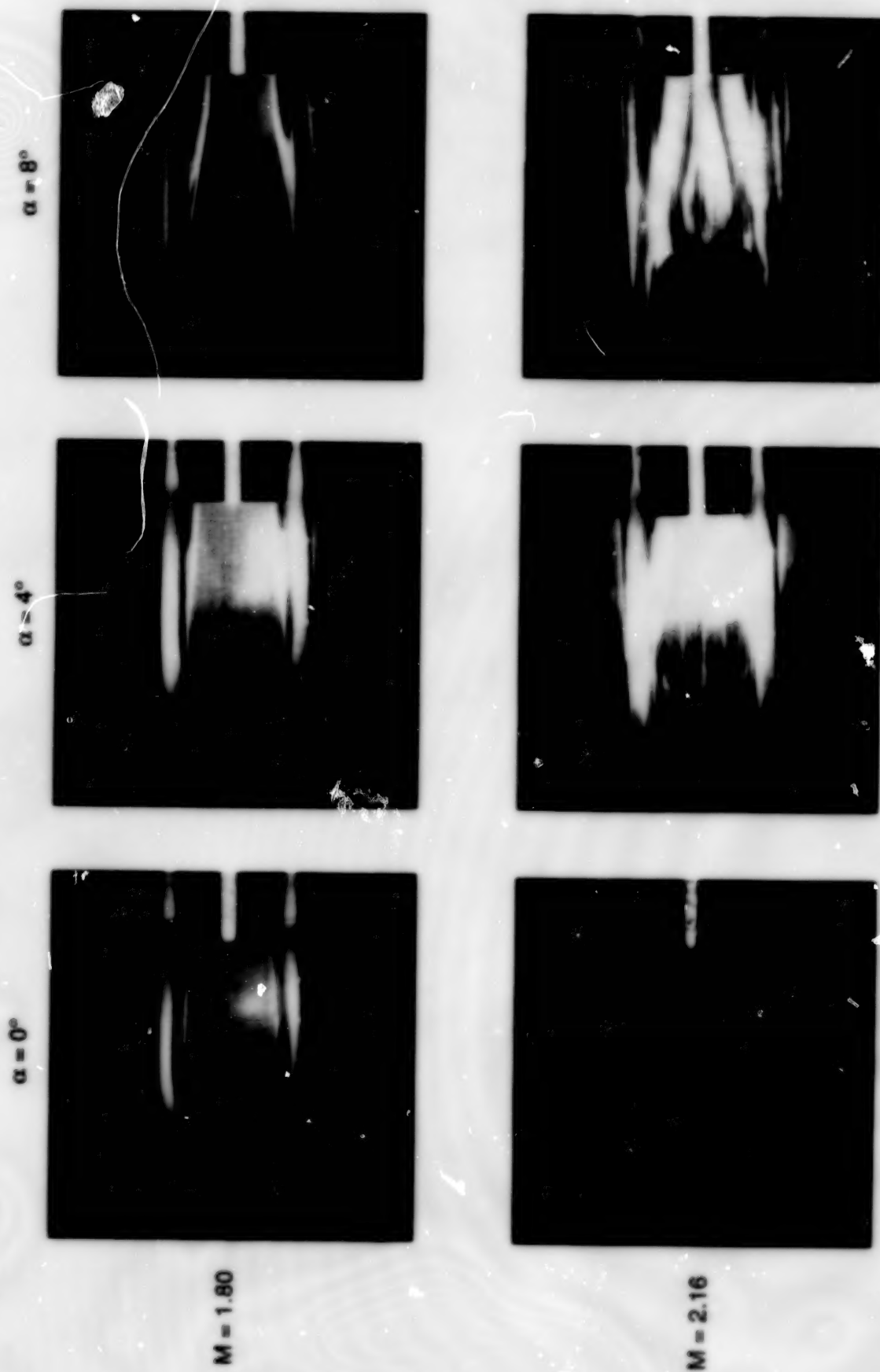


Figure 33. Oil-flow photographs for upper surface of unswept/delta multibody configuration at $\alpha = 0^\circ, 4^\circ$, and 8° and $M = 1.80$ and 2.16 .

ORIGINAL PAGE
BLACK AND WHITE PHOTOGRAPH

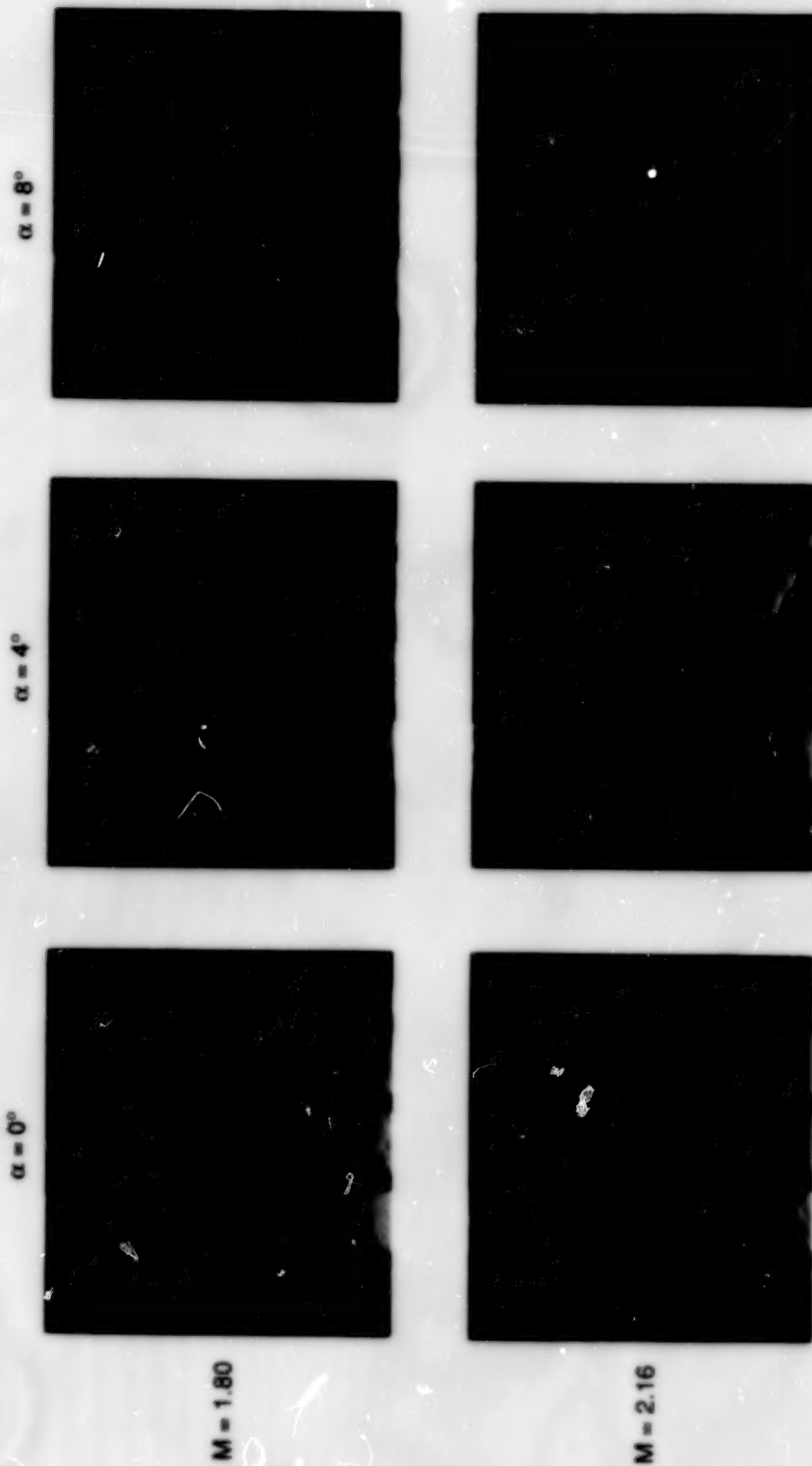
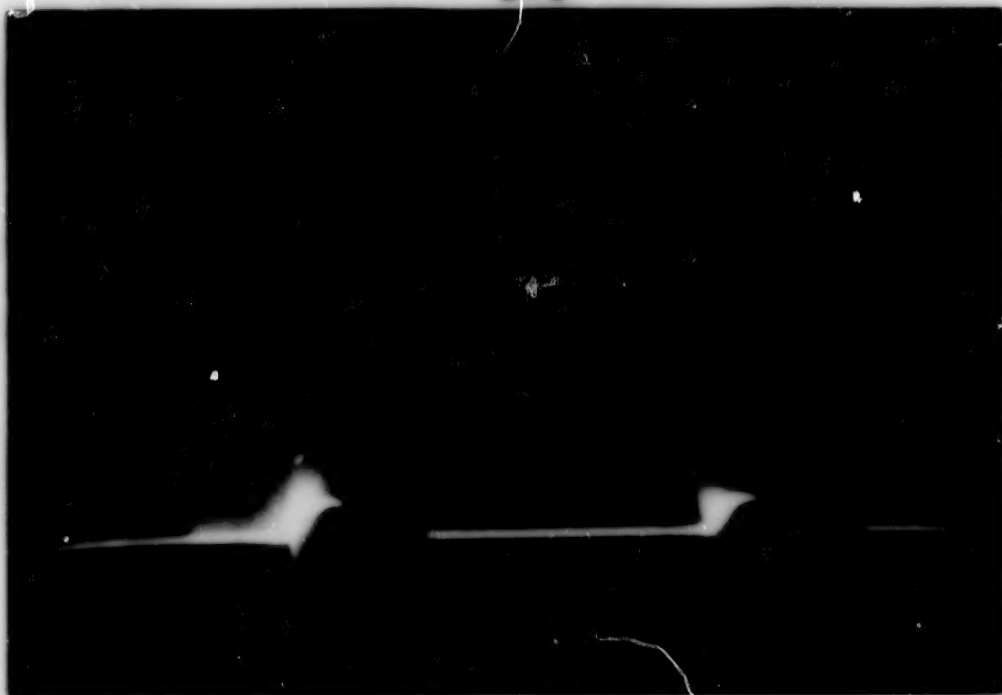
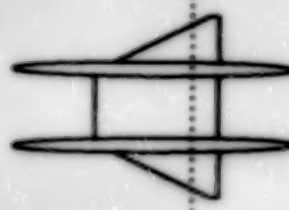


Figure 34. Schlieren photographs for unswept/delta multibody configuration at $\alpha = 0^\circ$, 4° , and 8° and $M = 1.80$ and 2.16 .

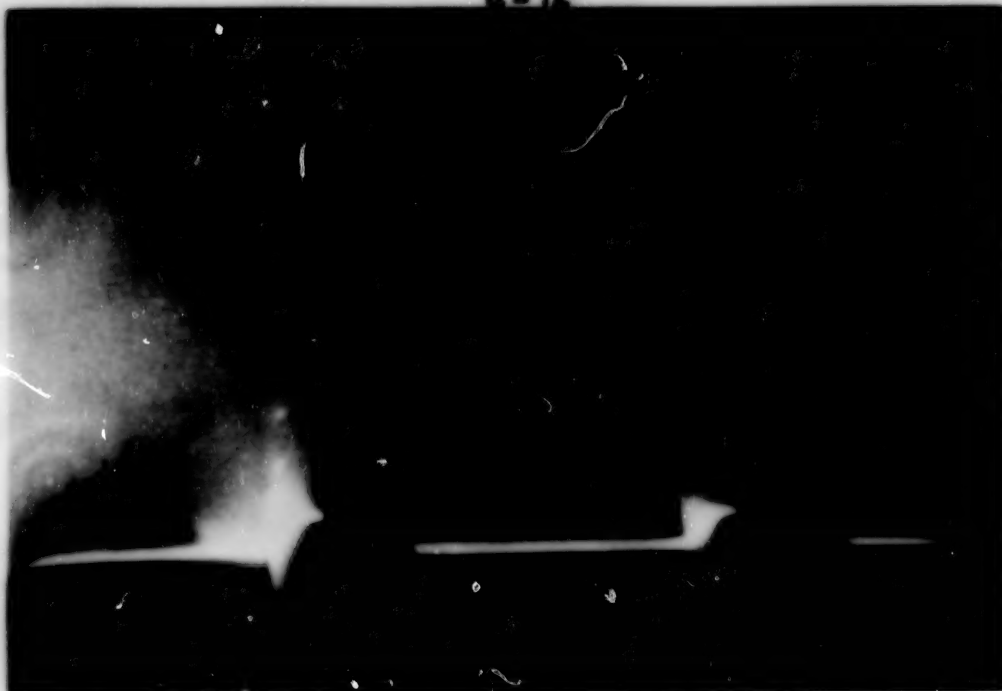
$\alpha = 8^\circ$



$x = 18.9 \text{ in.}$



$\alpha = 12^\circ$



(a) $M = 1.60$.

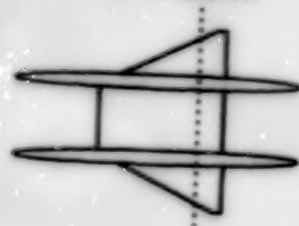
Figure 35. Vapor-screen photographs at $x = 18.9 \text{ in.}$ for unswept/delta multibody configuration for various angles of attack and Mach numbers.

ORIGINAL PAGE
BLACK AND WHITE PHOTOGRAPH

$\alpha = 4^\circ$



$x = 18.9 \text{ in.}$



$\alpha = 8^\circ$



(b) $M = 1.80$.

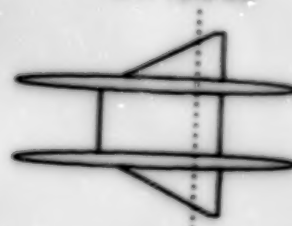
Figure 35. Continued.

ORIGINAL PAGE
BLACK AND WHITE PHOTOGRAPH

$\alpha = 12^\circ$



$x = 18.9 \text{ in.}$



$\alpha = 16^\circ$

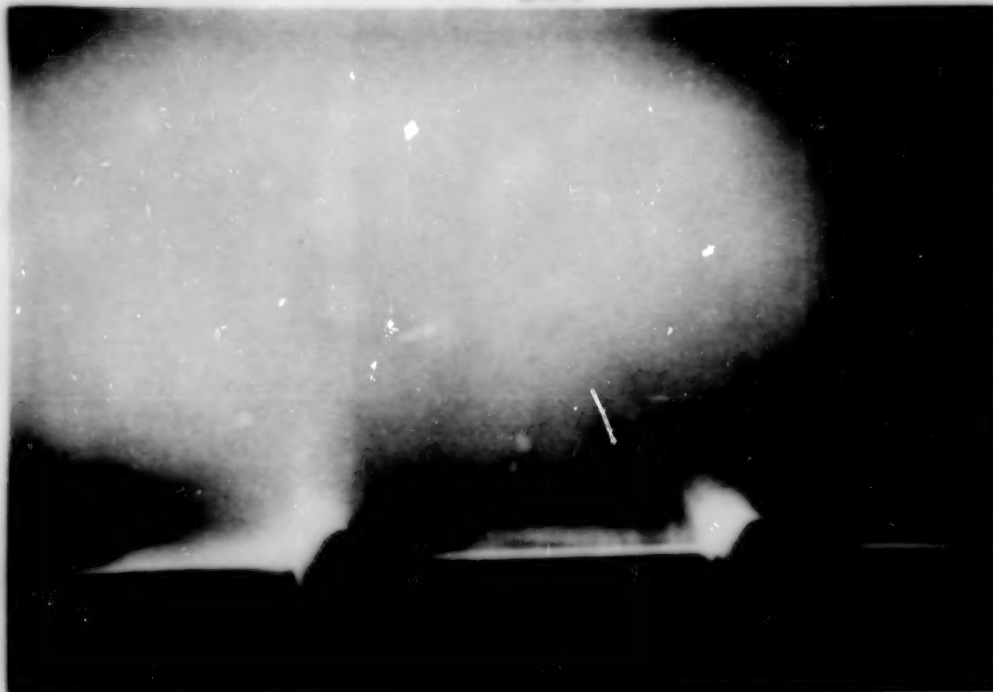


(b) Concluded.

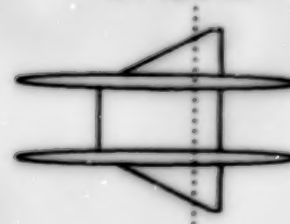
Figure 35. Continued.

ORIGINAL PAGE
BLACK AND WHITE PHOTOGRAPH

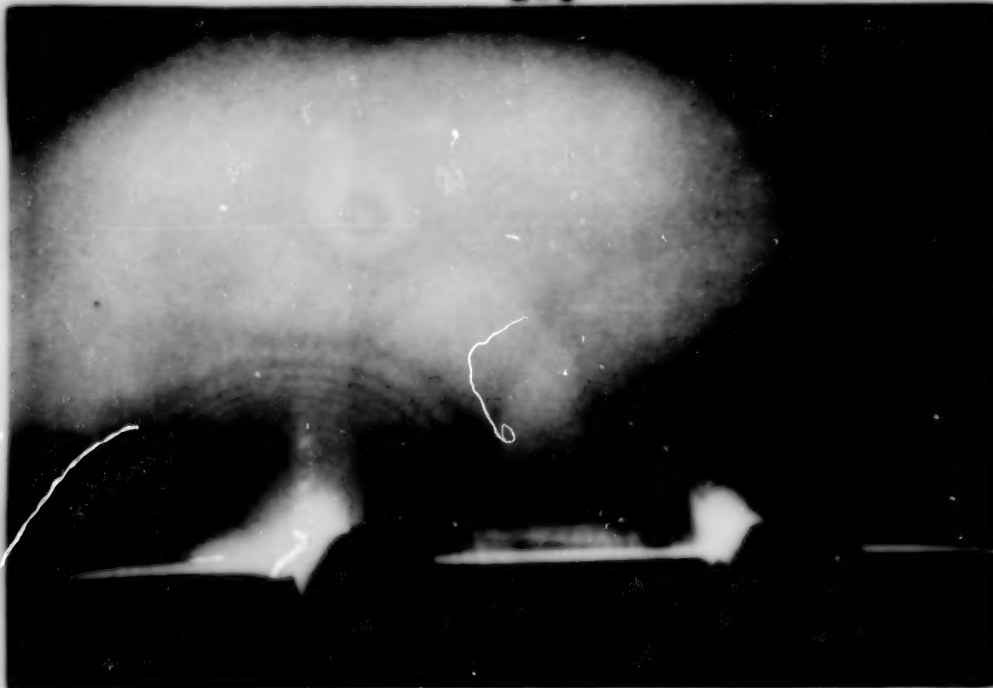
$\alpha = 4^\circ$



$x = 18.9 \text{ in.}$



$\alpha = 6^\circ$

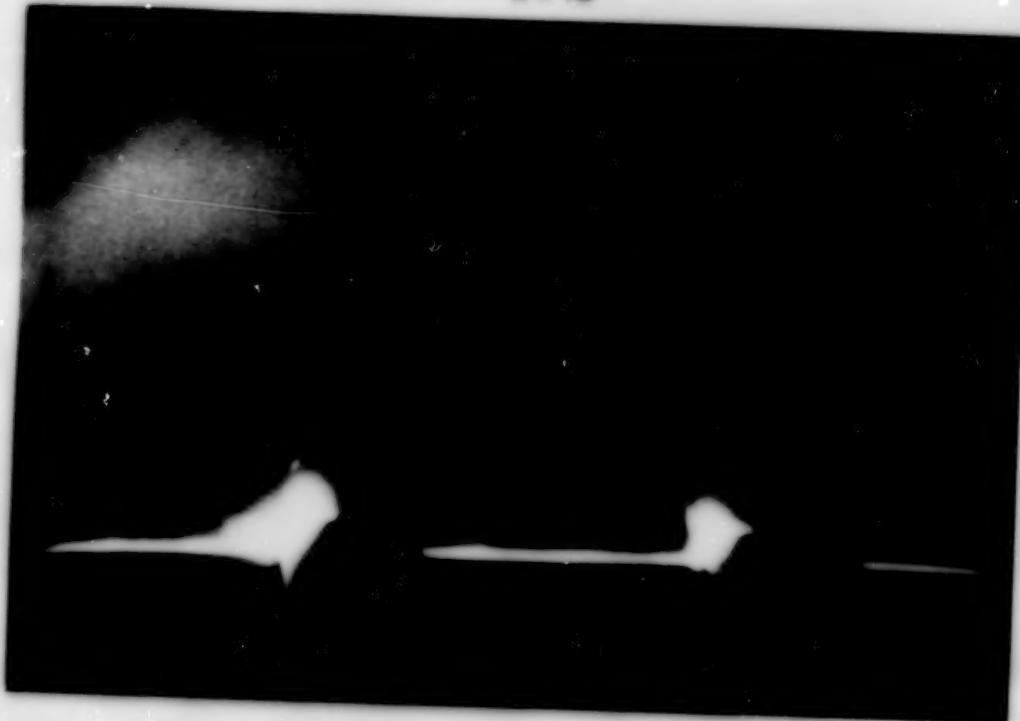


(c) $M = 2.00$.

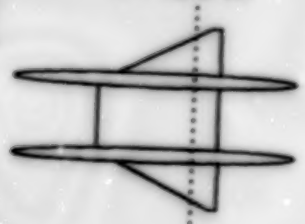
Figure 35. Continued.

ORIGINAL PAGE
BLACK AND WHITE PHOTOGRAPH

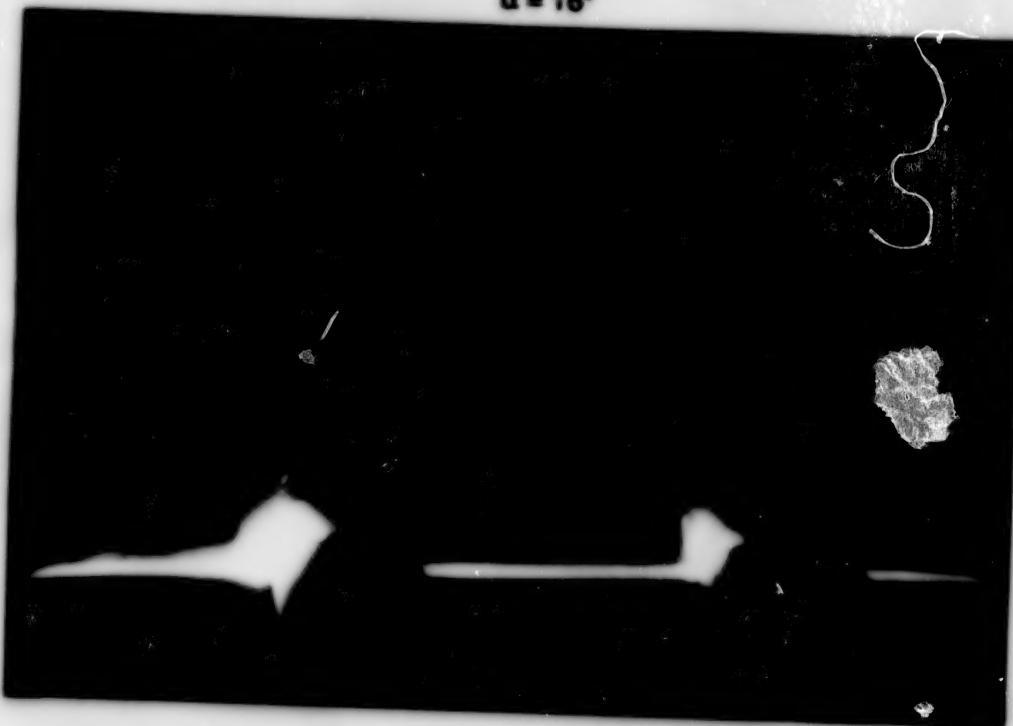
$\alpha = 12^\circ$



$x = 18.9 \text{ in.}$



$\alpha = 16^\circ$

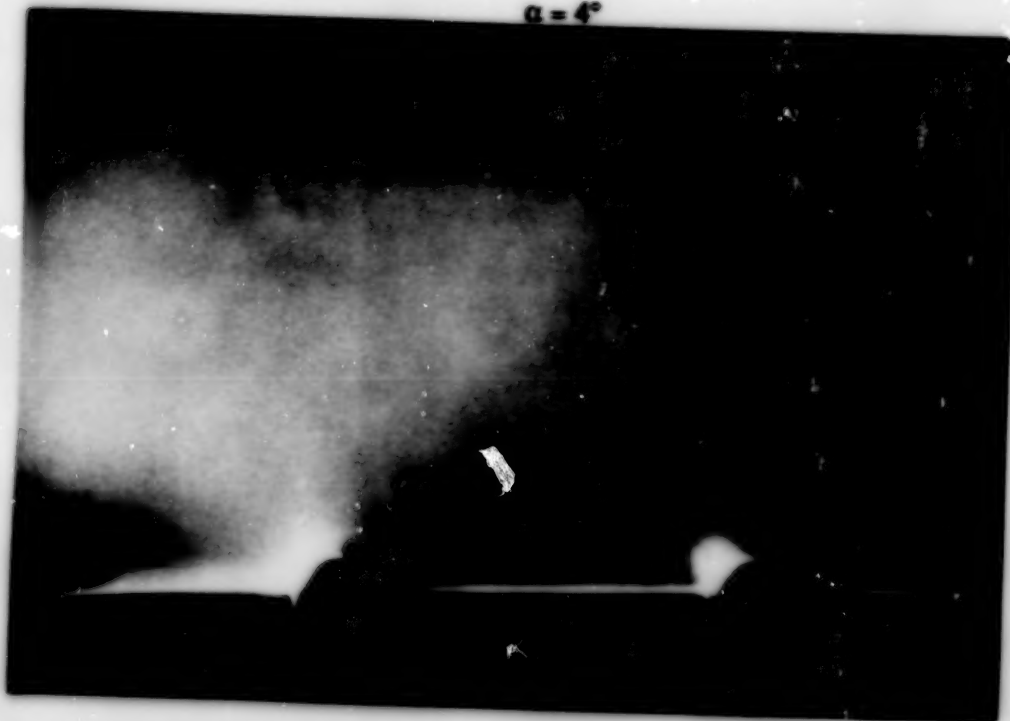


(c) Concluded.

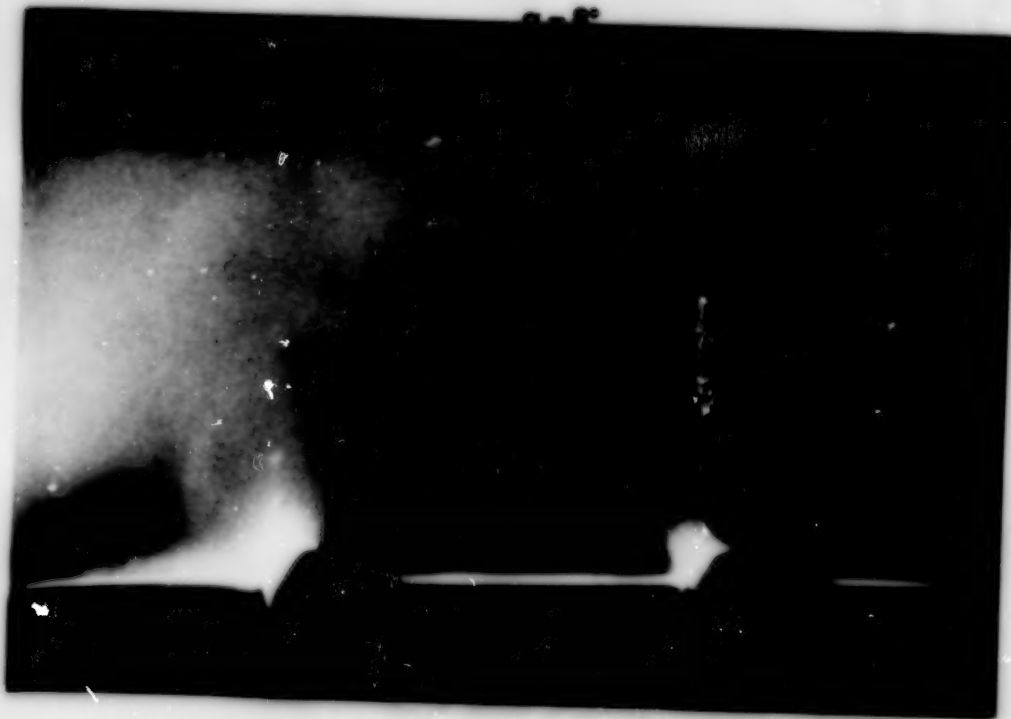
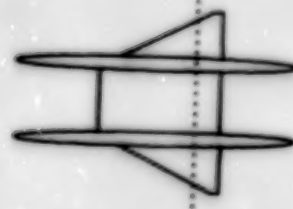
Figure 35. Continued.

ORIGINAL PAGE
BLACK AND WHITE PHOTOGRAPH

$\alpha = 4^\circ$



$x = 18.9 \text{ in.}$

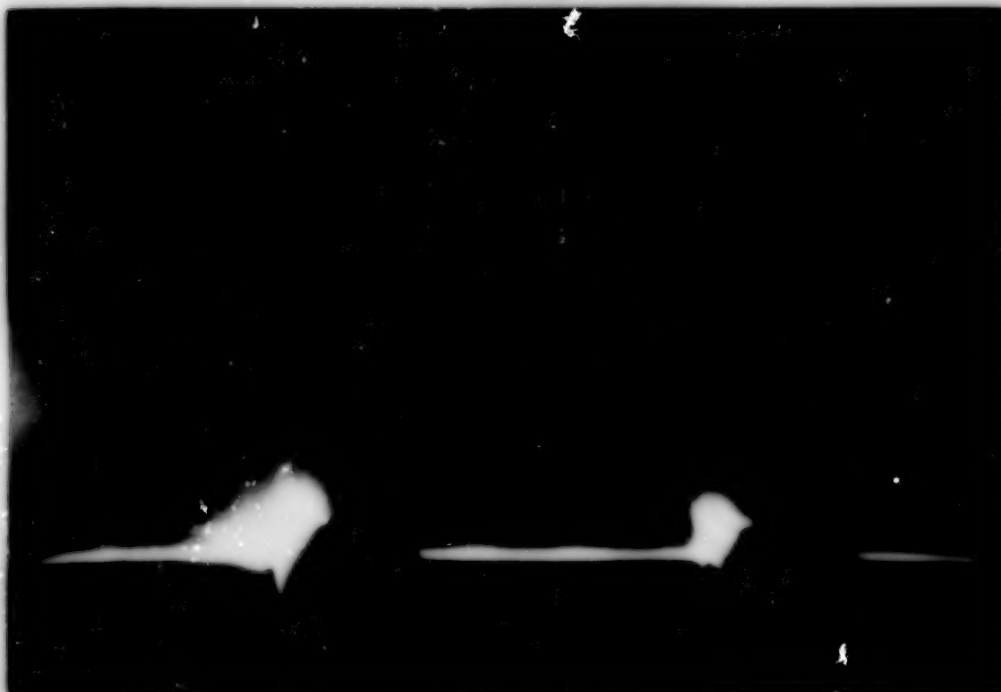


(d) $M = 2.16$.

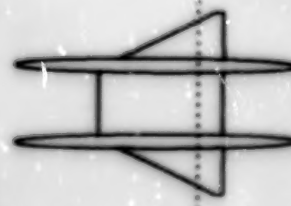
Figure 35. Continued.

ORIGINAL PAGE
BLACK AND WHITE PHOTOGRAPH

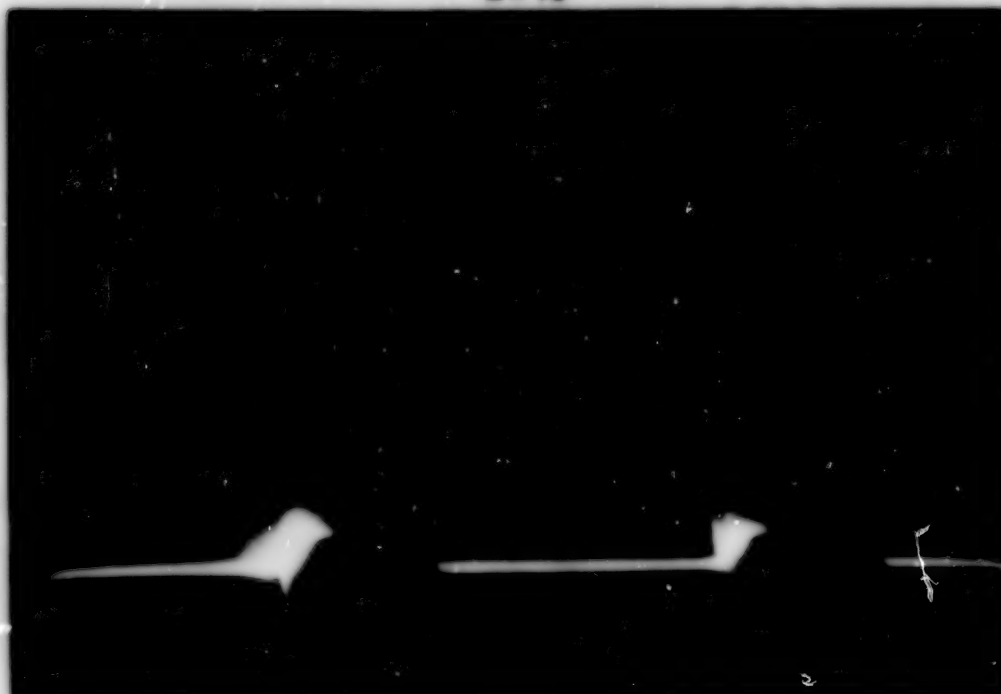
$\alpha = 12^\circ$



$x = 18.9 \text{ in.}$



$\alpha = 16^\circ$

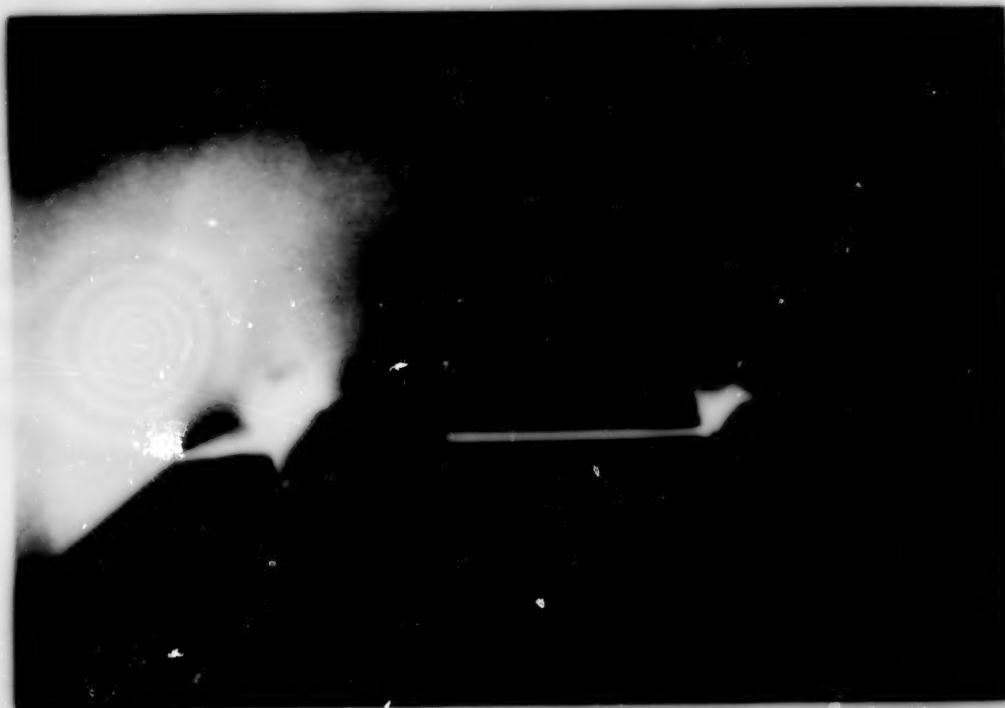


(d) Concluded.

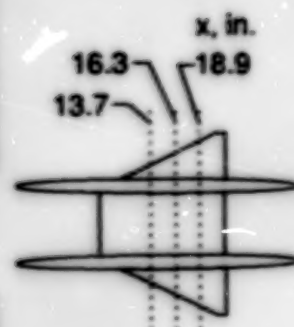
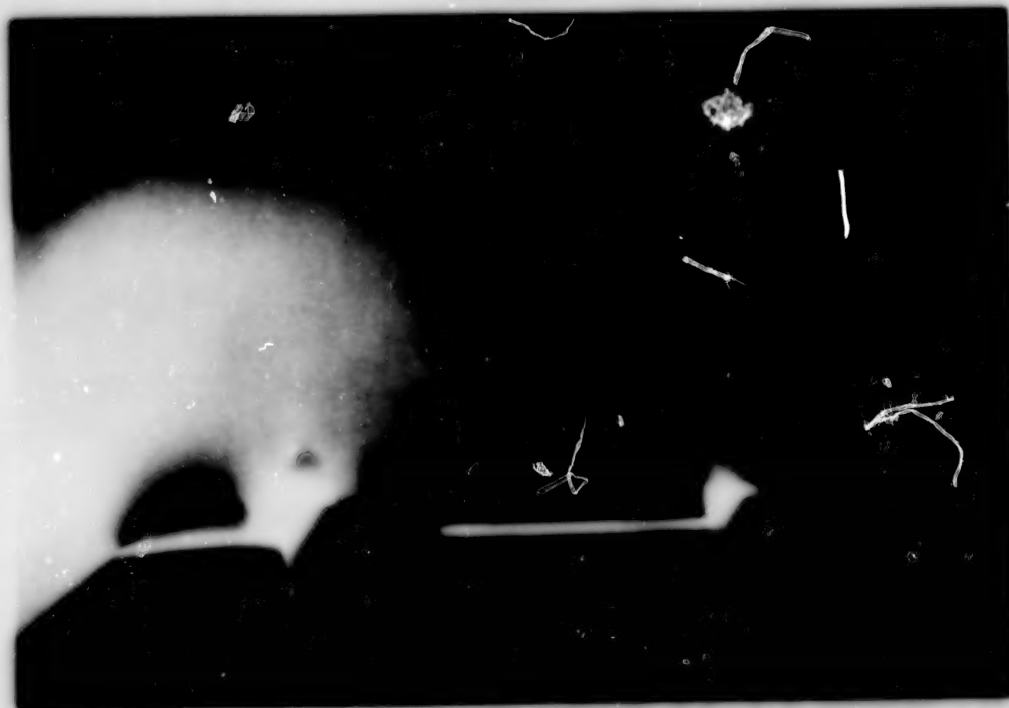
Figure 35. Concluded.

ORIGINAL PAGE
BLACK AND WHITE PHOTOGRAPH

$x = 13.7$ in.



$x = 16.3$ in.

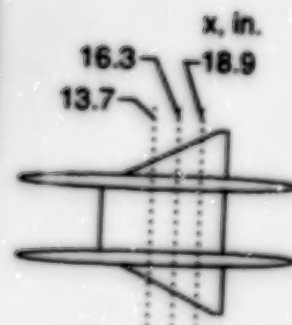


(a) $M = 1.80$.

Figure 36. Vapor-screen photographs for unswept/delta multibody configuration at three longitudinal locations for $\alpha = 16^\circ$ and $M = 1.80$ and 2.16.

ORIGINAL PAGE
BLACK AND WHITE PHOTOGRAPH

$x = 18.9$ in.

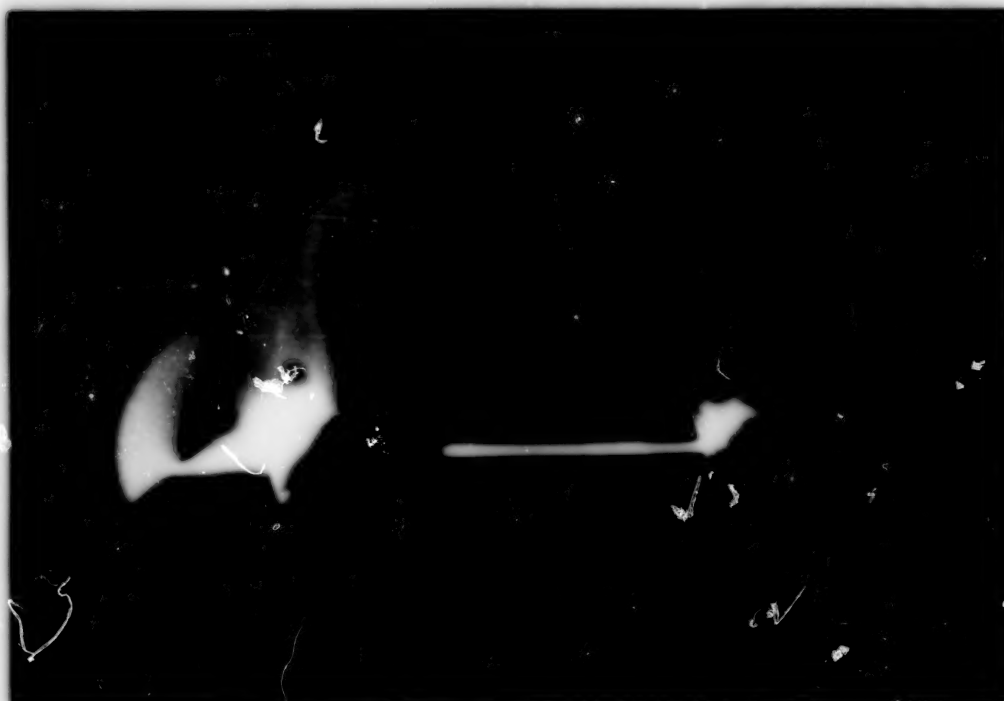


(a) Concluded.

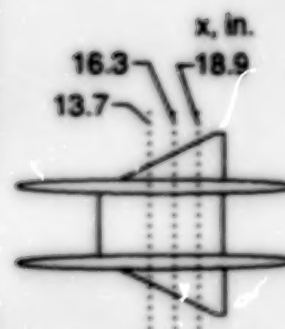
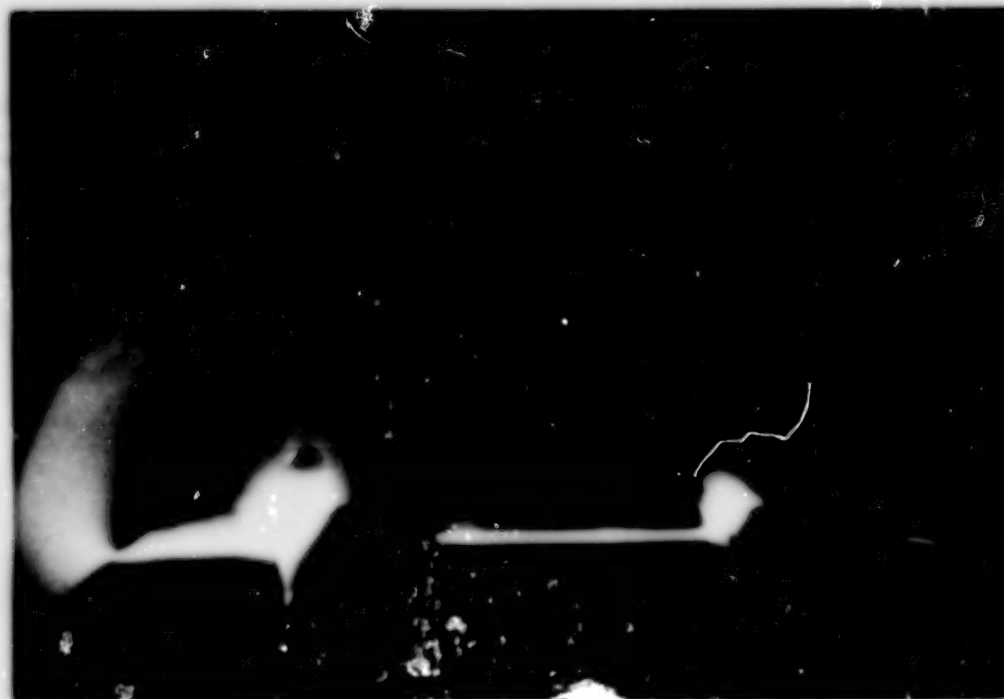
Figure 36. Continued.

ORIGINAL PAGE
BLACK AND WHITE PHOTOGRAPH

$x = 13.7$ in.



$x = 16.3$ in.

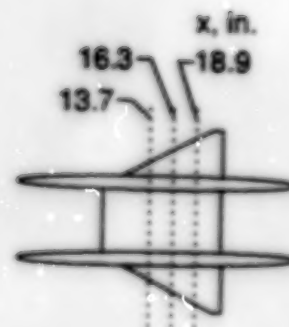
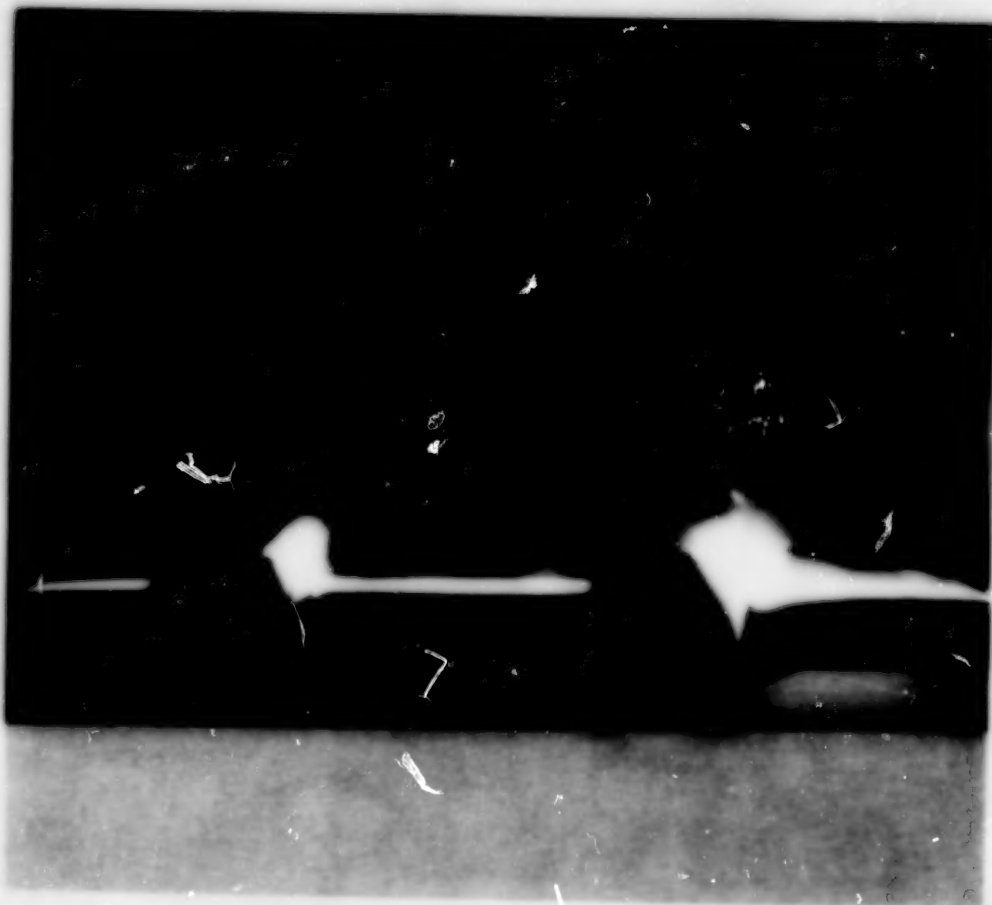


(b) $M = 2.16$.

Figure 53. Continued.

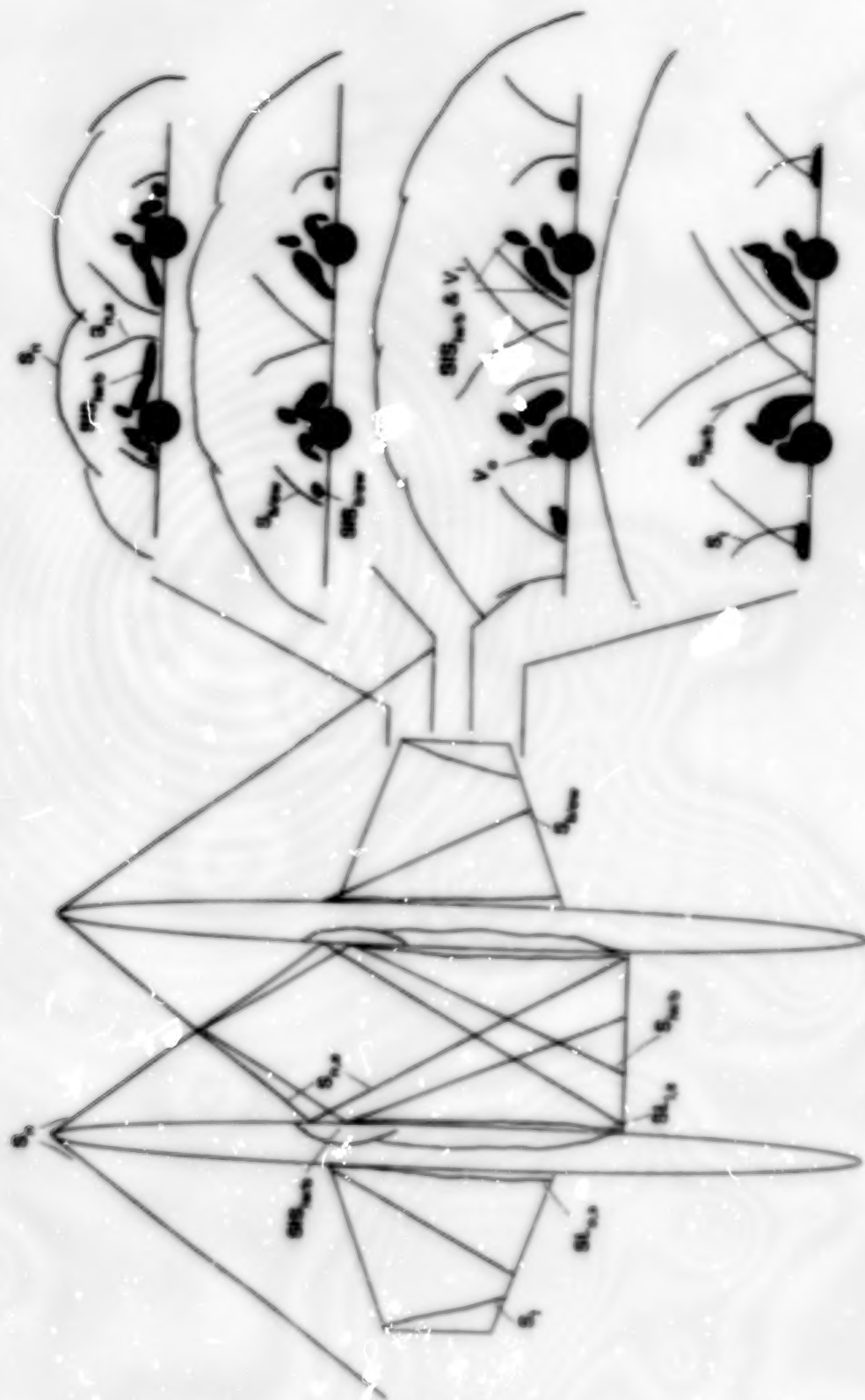
ORIGINAL PAGE
BLACK AND WHITE PHOTOGRAPH

$x = 18.9$ in.



(b) Concluded.

Figure 36. Concluded.

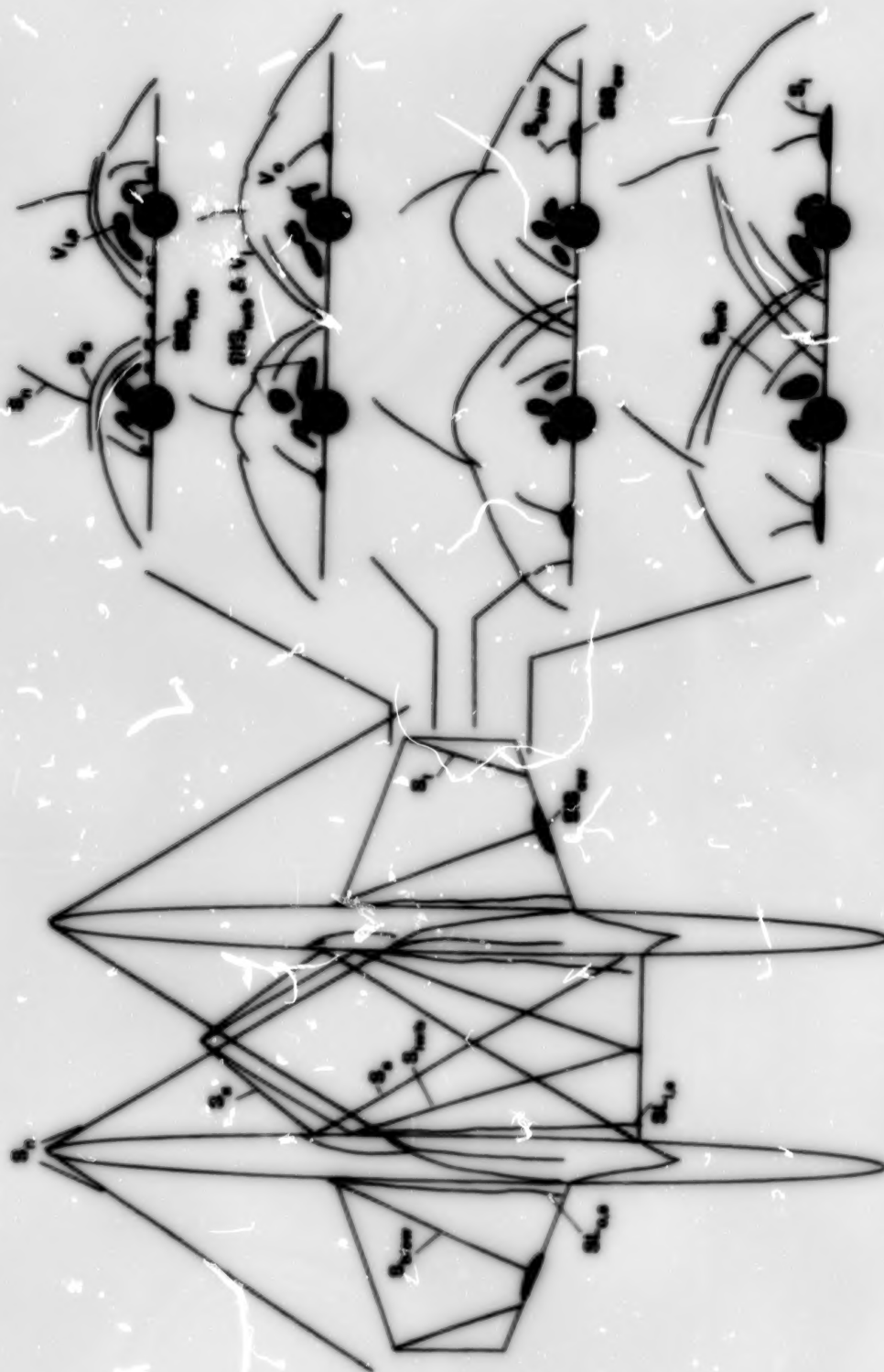


Top view; $\alpha = 8^\circ$
(See oil flow and schlieren photographs in figs. 38 to 39.)

Spanwise cross section cuts; $\alpha = 16^\circ$
(See vapor screen photographs in figs. 40 to 42.)

(a) $M = 1.80$.

Figure 37. Flow pattern over swept/small-trapezoidal multiple Δy configuration.



Top view; $\alpha = 8^\circ$
(See oil-flow and schlieren photographs in figs. 38 to 39.)

Spanwise cross-section cuts; $\alpha = 16^\circ$
(See vapor-screen photographs in figs. 40 to 42.)

(b) $M = 2.16$.

Figure 37. Concluded.

ORIGINAL PAGE
BLACK AND WHITE PHOTOGRAPH

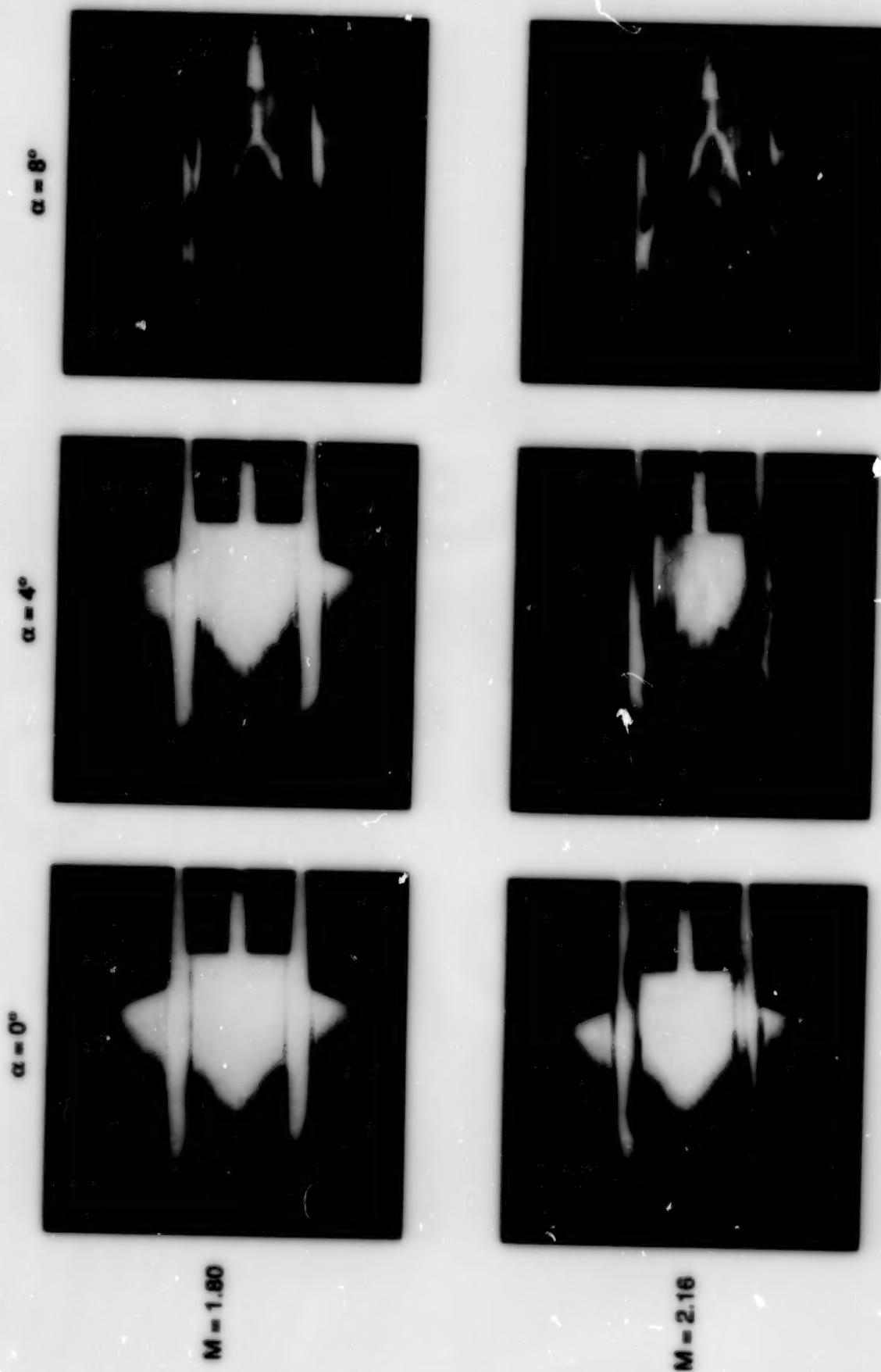


Figure 38. Oil-flow photographs for upper surface of swept/small-trapezoidal multibody configuration at $\alpha = 0^\circ$, 4° , and 8° and $M = 1.80$ and 2.16 .

ORIGINAL PAGE
BLACK AND WHITE PHOTOGRAPH

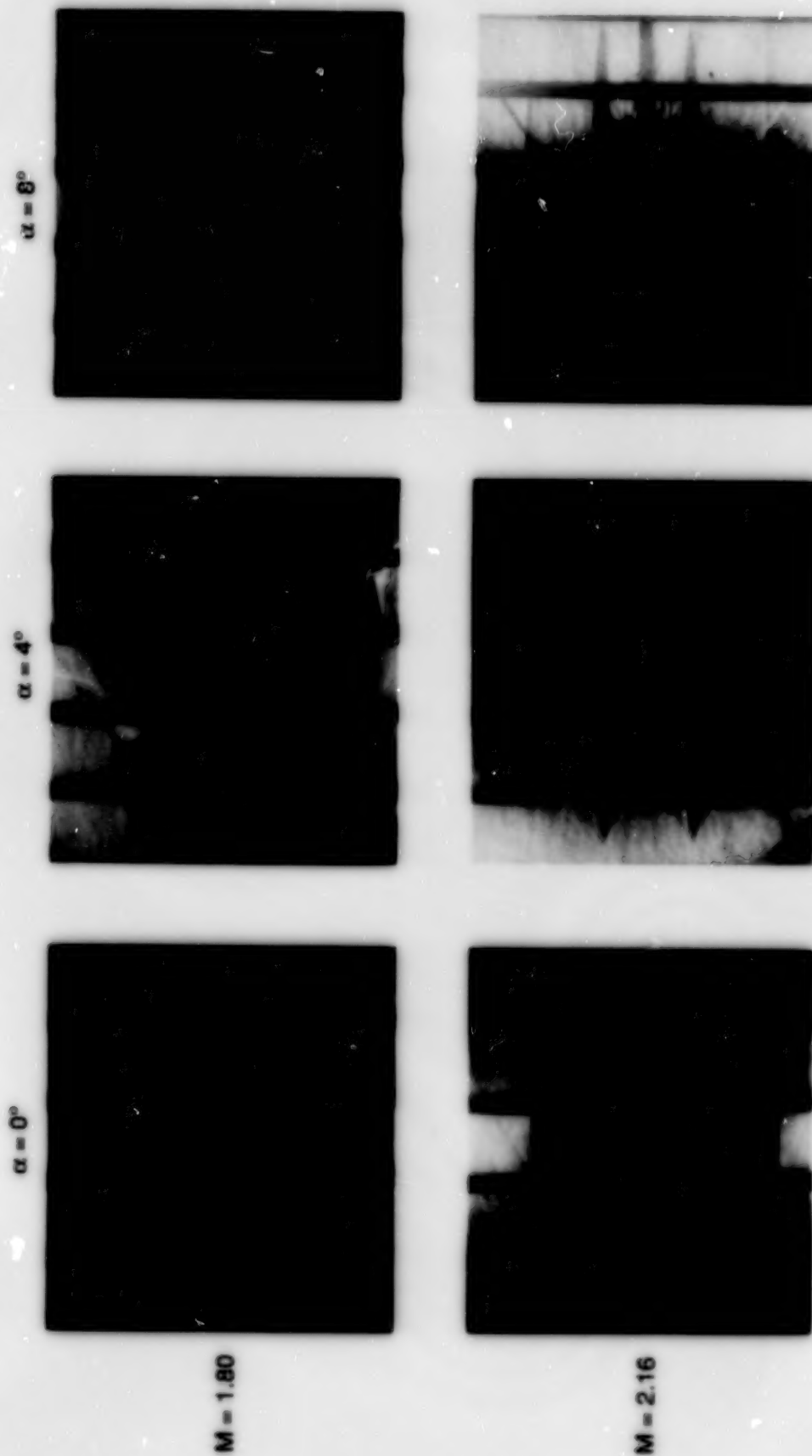


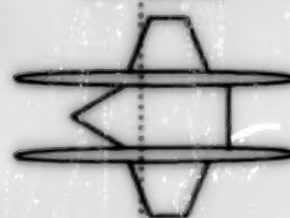
Figure 39. Schlieren photographs for swept/flat-plate configuration at $\alpha = 0^\circ$, 4° , and 8° and $M = 1.80$ and 2.16 .

ORIGINAL PAGE
BLACK AND WHITE PHOTOGRAPH

$\alpha = 8^\circ$



$x = 12.3 \text{ in.}$



$\alpha = 16^\circ$

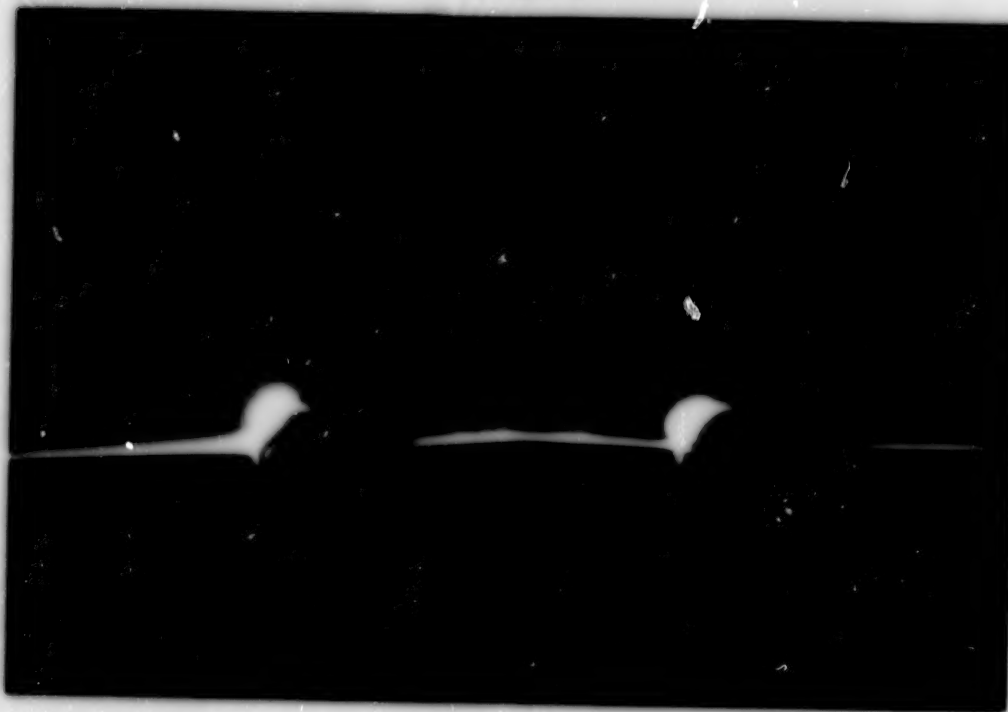


(a) $M = 1.60$.

Figure 40. Vapor-screen photographs at $x = 12.3 \text{ in.}$ for swept/small-trapezoidal multibody configuration for various angles of attack and Mach numbers.

ORIGINAL PAGE
BLACK AND WHITE PHOTOGRAPH

$\alpha = 4^\circ$



$x = 12.3 \text{ in.}$



$\alpha = 8^\circ$

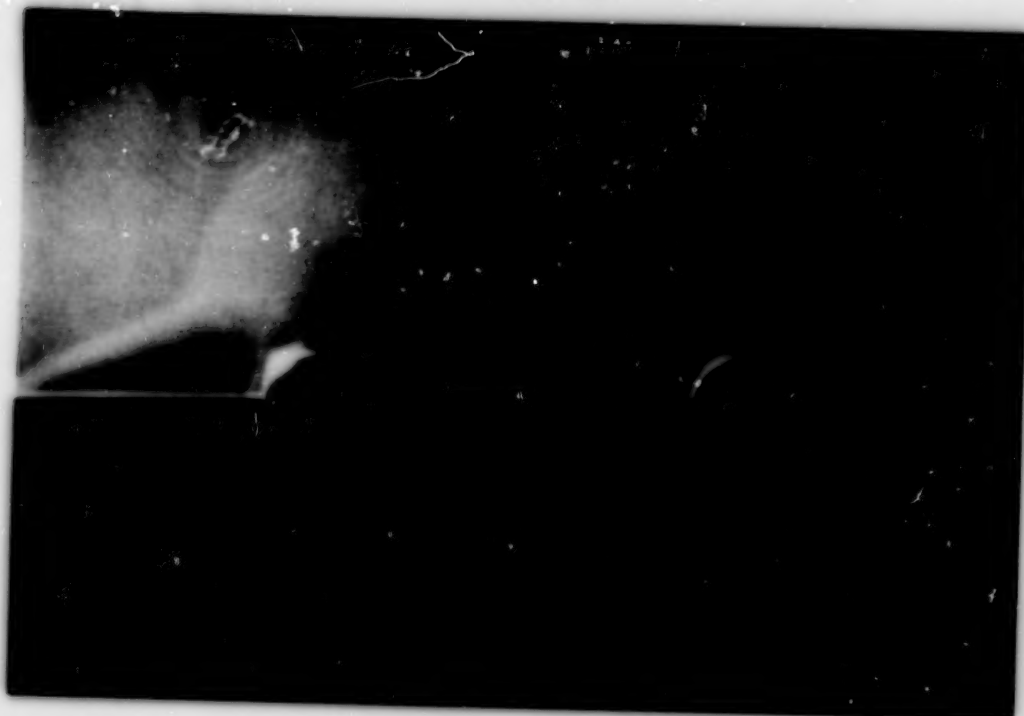


(b) $M = 1.80$.

Figure 40. Continued.

ORIGINAL PAGE
BLACK AND WHITE PHOTOGRAPH

$\alpha = 12^\circ$



$\alpha = 16^\circ$



$x = 12.3 \text{ in.}$

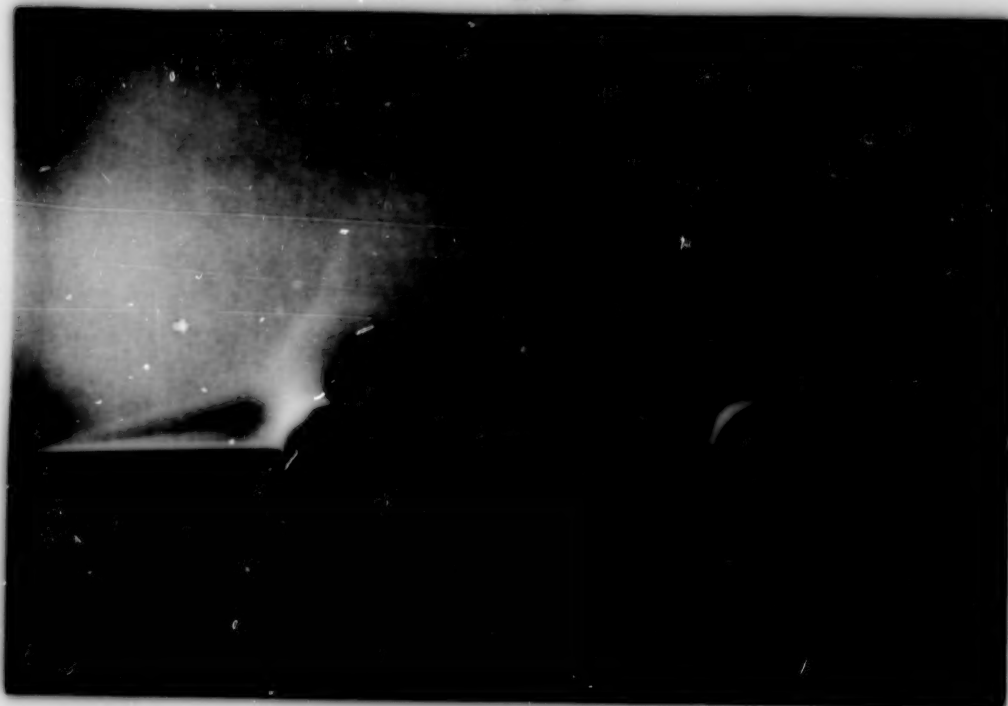


(b) Concluded.

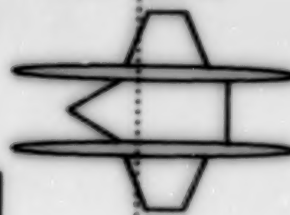
Figure 40. Continued.

ORIGINAL PAGE
BLACK AND WHITE PHOTOGRAPH

$\alpha = 8^\circ$



$x = 12.3 \text{ in.}$



$\alpha = 16^\circ$



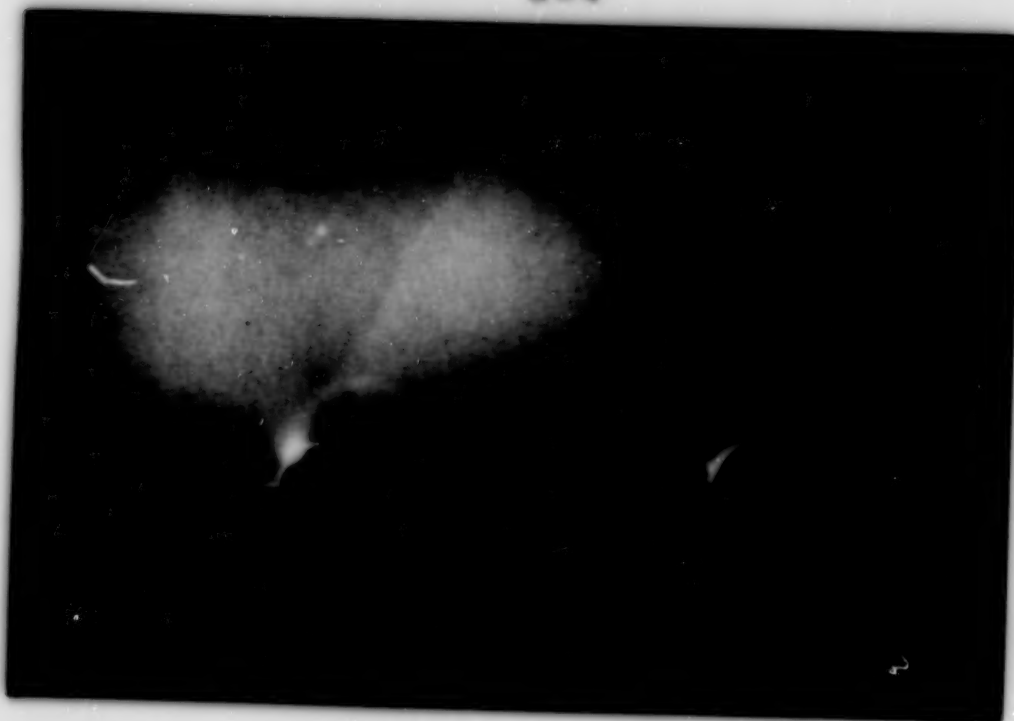
Not available

(c) $M = 2.00$.

Figure 40. Continued.

ORIGINAL PAGE
BLACK AND WHITE PHOTOGRAPH

$\alpha = 4^\circ$



$\alpha = 6^\circ$



$x = 12.3 \text{ in.}$



(d) $M = 2.16$.

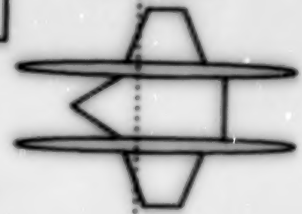
Figure 40. Continued.

$\alpha = 12^\circ$



Not available

$x = 12.3 \text{ in.}$



$\alpha = 16^\circ$

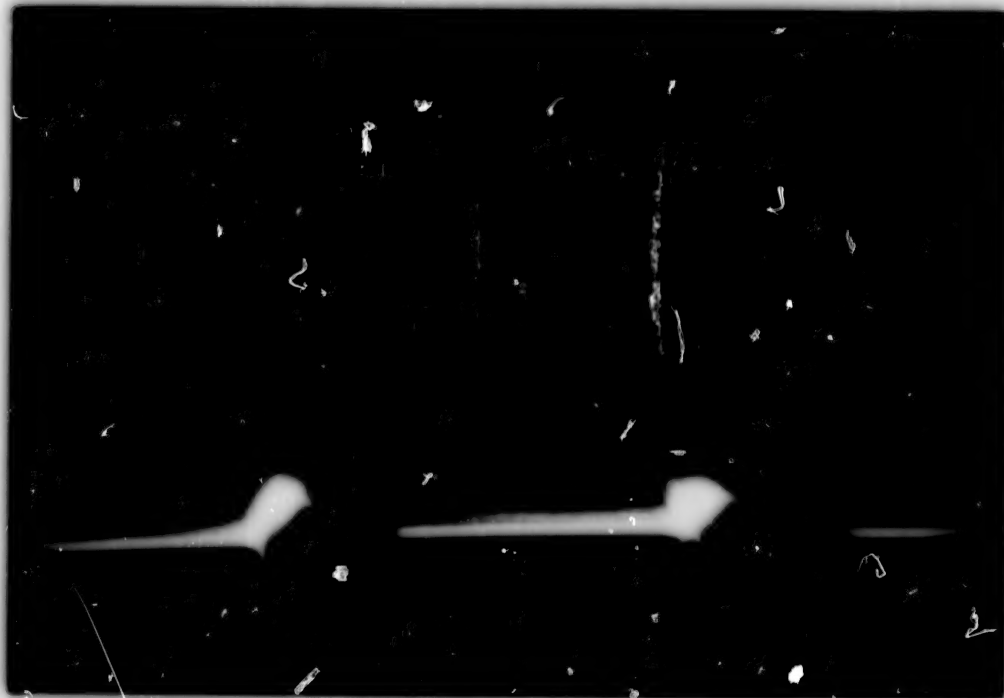


(d) Concluded.

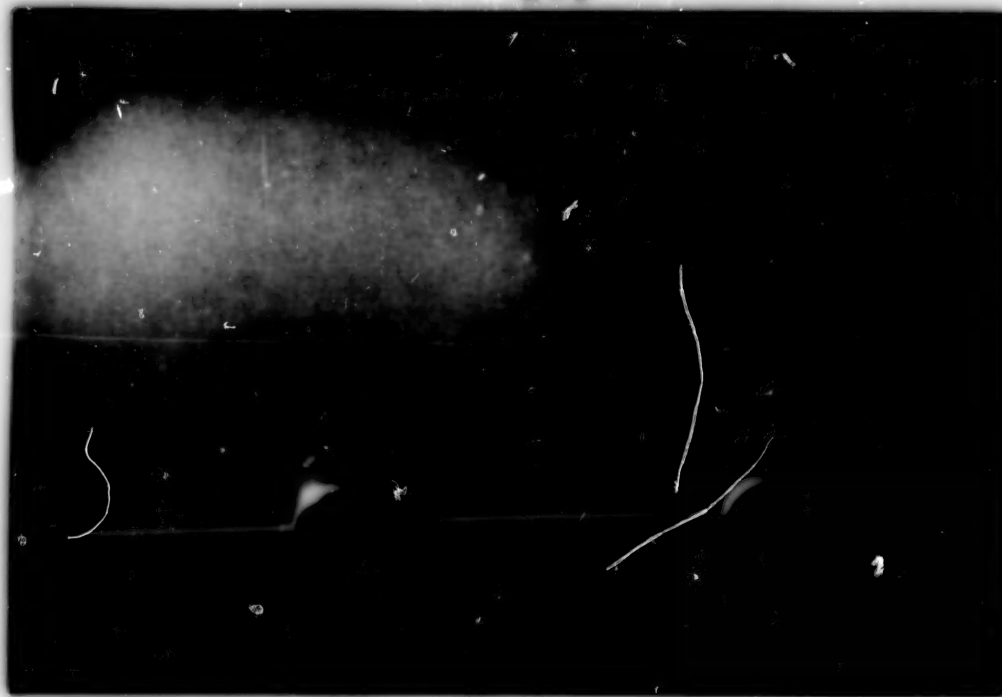
Figure 40. Concluded.

ORIGINAL PAGE
BLACK AND WHITE PHOTOGRAPH

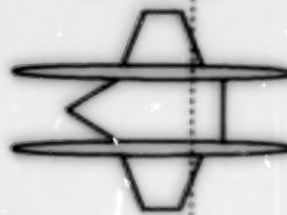
$\alpha = 4^\circ$



$\alpha = 8^\circ$



$x = 17.7 \text{ in.}$

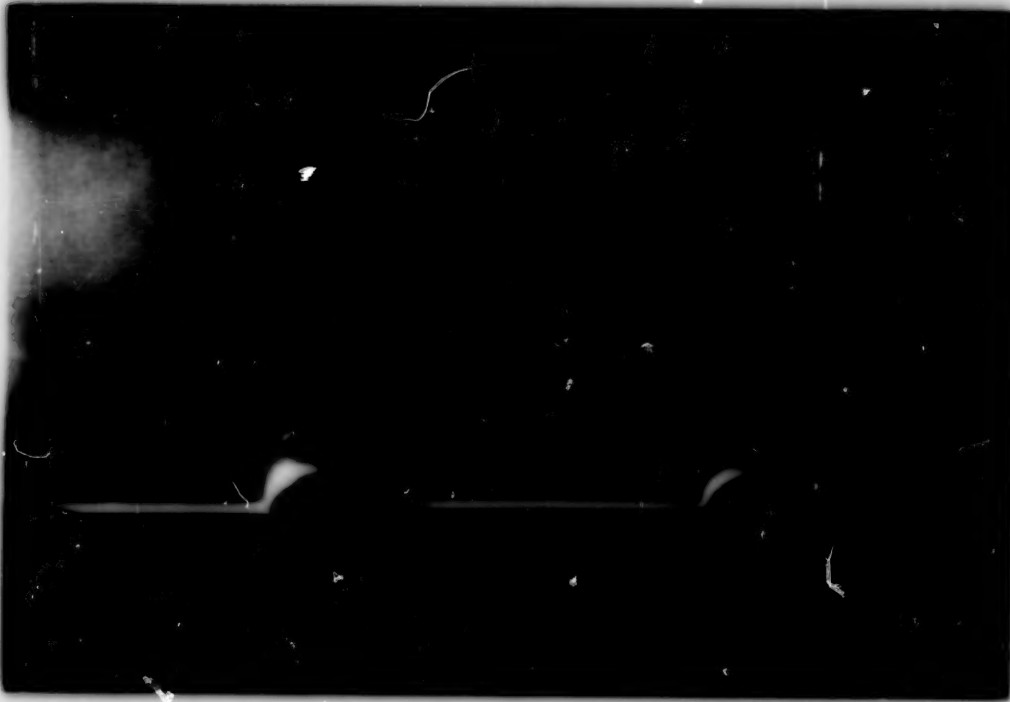


(a) $M = 1.80$.

Figure 41. Vapor-screen photographs at $x = 17.7 \text{ in.}$ for swept/small-trapezoidal multibody configuration for various angles of attack and Mach numbers.

ORIGINAL PAGE
BLACK AND WHITE PHOTOGRAPH

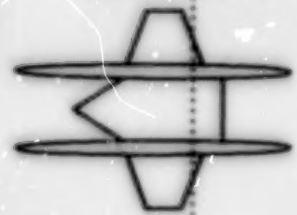
$\alpha = 12^\circ$



$\alpha = 16^\circ$



$x = 17.7 \text{ in.}$

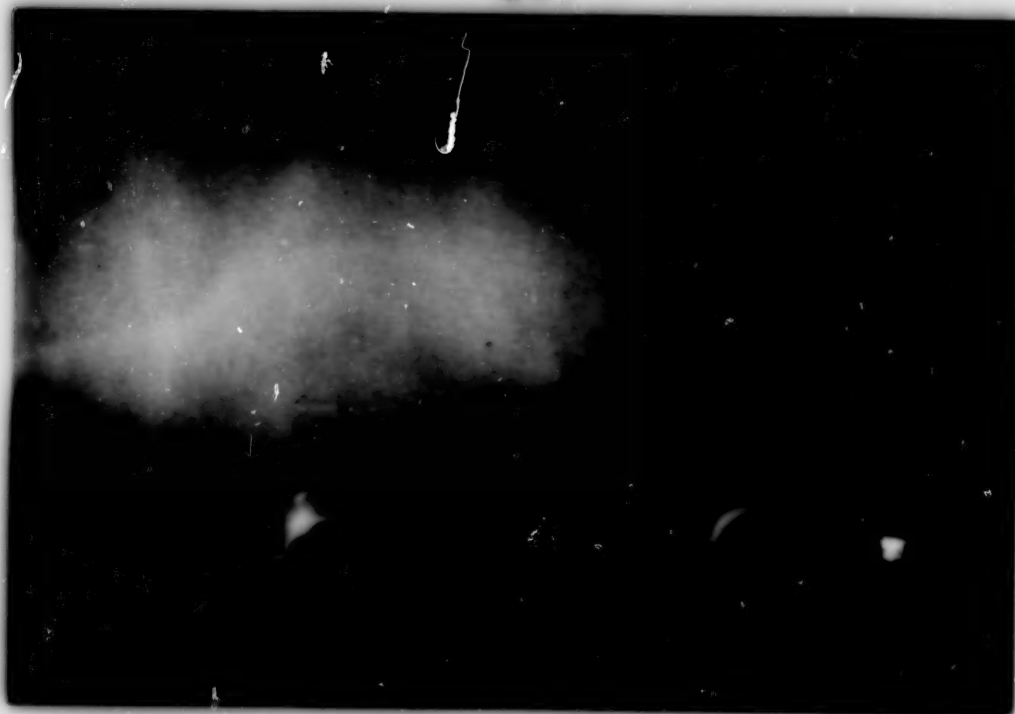


(a) Concluded.

Figure 41. Continued.

ORIGINAL PAGE
BLACK AND WHITE PHOTOGRAPH

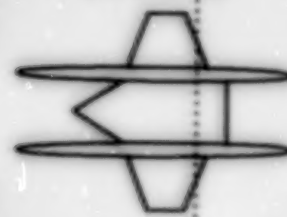
$\alpha = 4^\circ$



$\alpha = 8^\circ$



$x = 17.7 \text{ in.}$

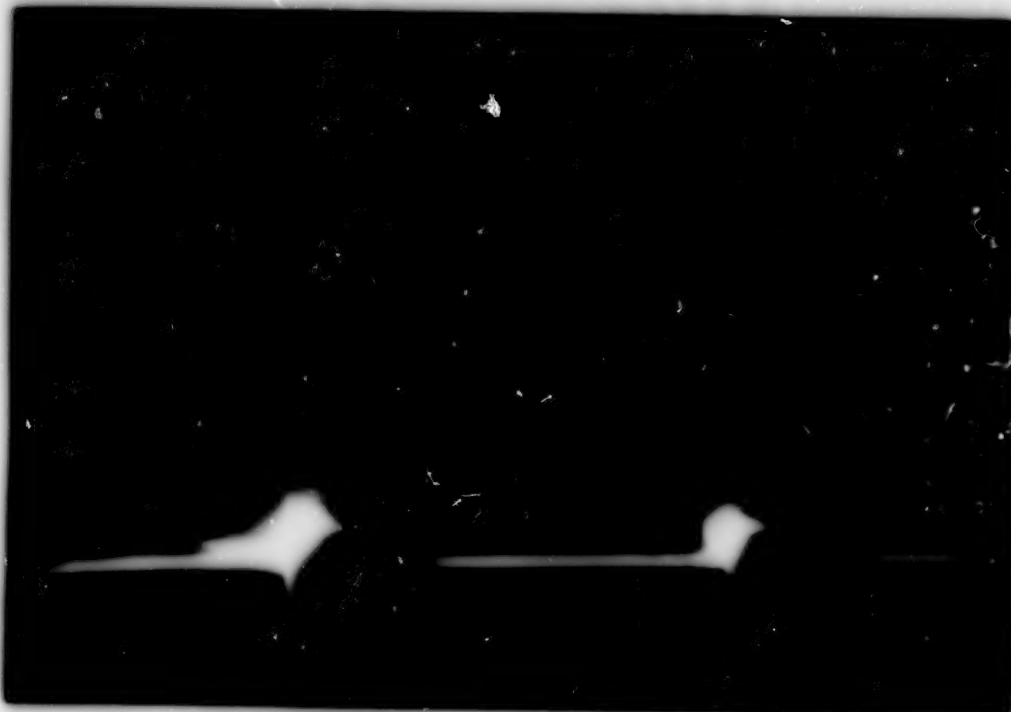


(b) $M = 2.16$

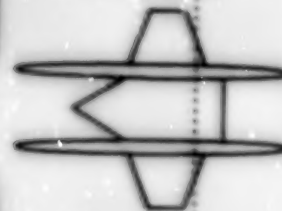
Figure 41. Continued.

ORIGINAL PAGE
BLACK AND WHITE PHOTOGRAPH

$\alpha = 12^\circ$



$x = 17.7 \text{ in.}$



$\alpha = 16^\circ$



(b) Concluded.

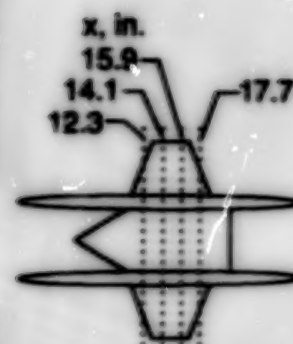
Figure 41. Concluded.

ORIGINAL PAGE
BLACK AND WHITE PHOTOGRAPH

$x = 12.3$ in.



$x = 14.1$ in.



(a) $M = 1.80$.

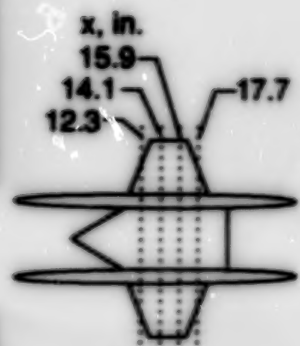
Figure 42. Vapor-screen photographs for swept/small-trapezoidal multibody configuration at four longitudinal locations for $\alpha = 16^\circ$ and $M = 1.80$ and 2.16 .

ORIGINAL PAGE
BLACK AND WHITE PHOTOGRAPH

$x = 15.9$ in.



$x = 17.7$ in.



(a) Concluded.

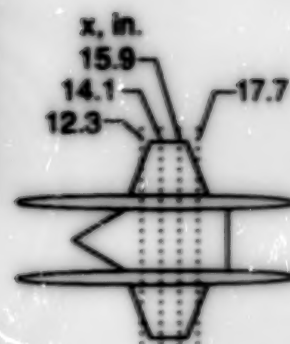
Figure 42. Continued.

ORIGINAL P. 102
BLACK AND WHITE PHOTOGRAPH

$x = 12.3$ in.



$x = 14.1$ in.

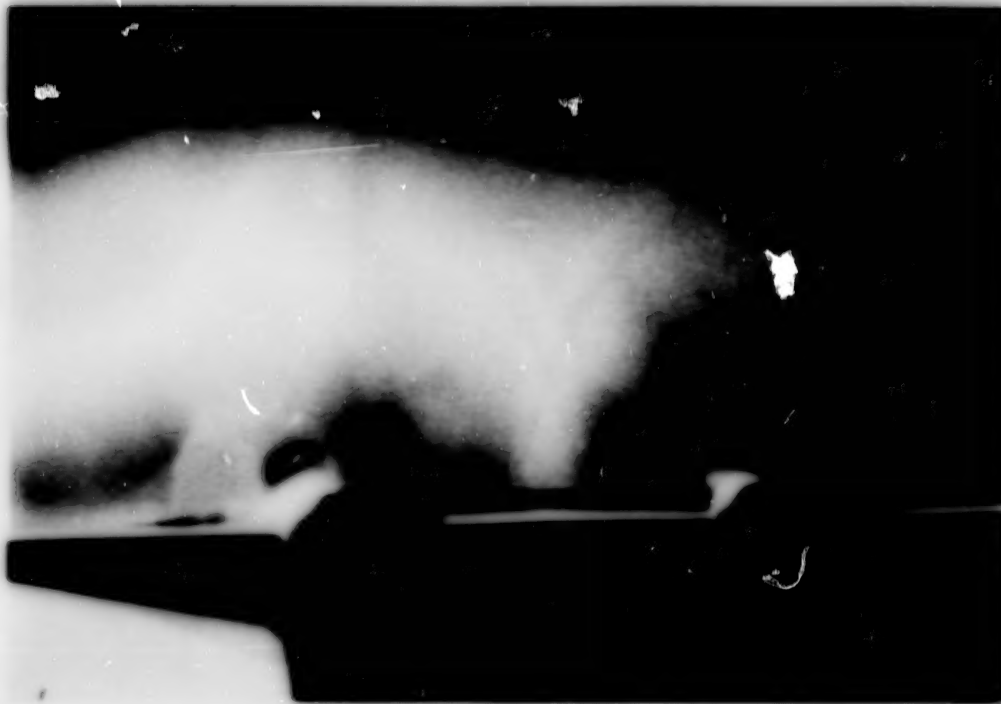


(b) $M = 2.16$.

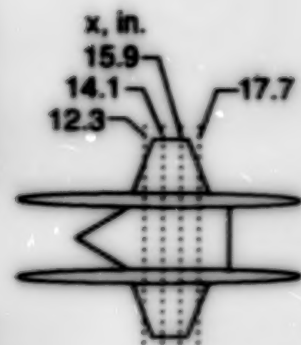
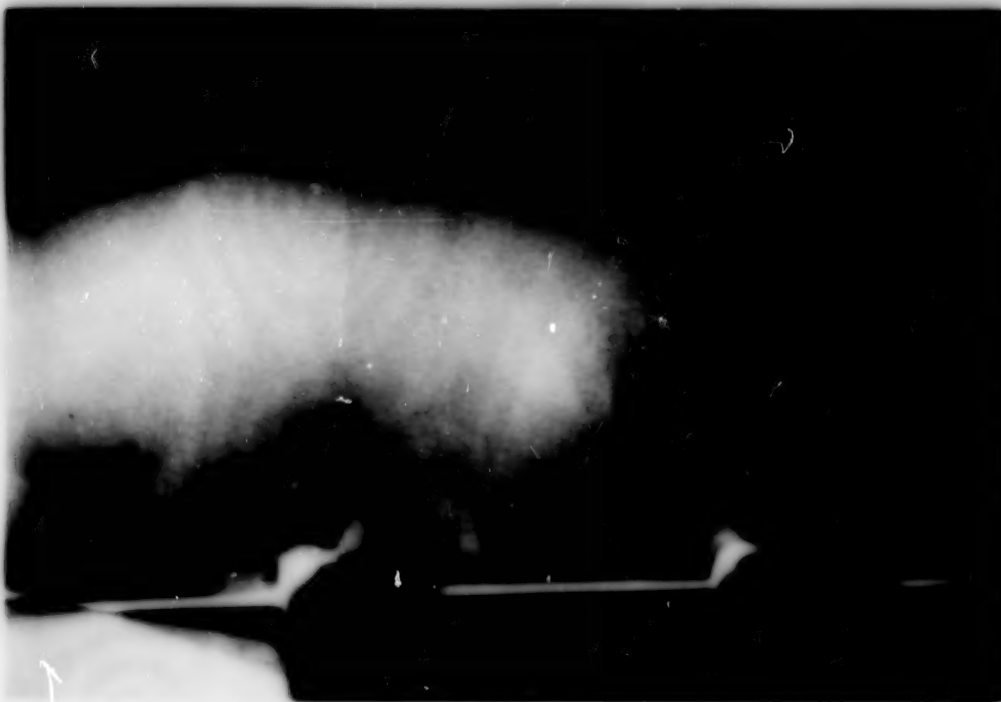
Figure 42. Continued.

ORIGINAL PAGE
BLACK AND WHITE PHOTOGRAPH

$x = 15.9$ in.

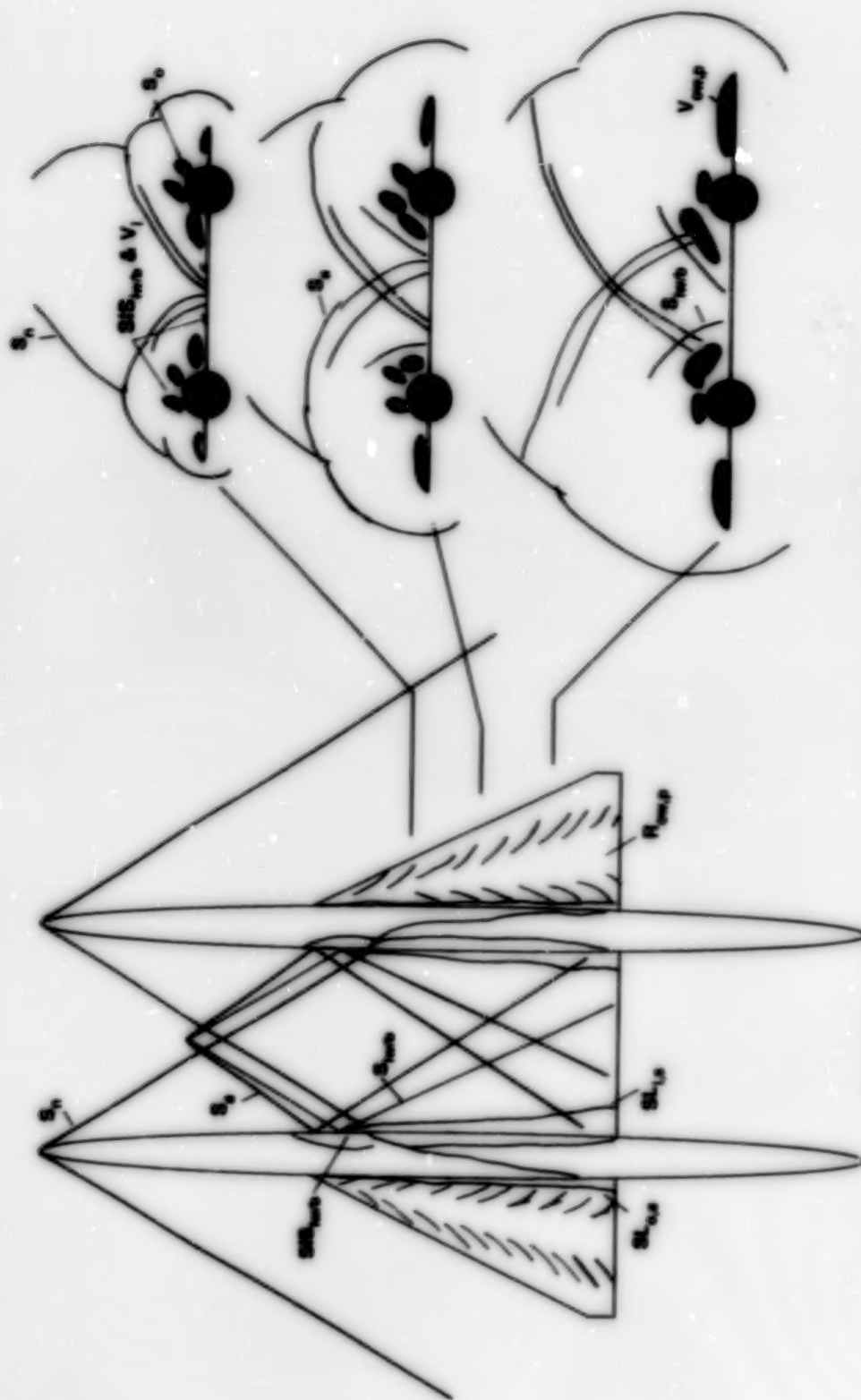


$x = 17.7$ in.



(b) Concluded.

Figure 42. Concluded.



Top view; $\alpha = 8^\circ$
(See oil-flow and schlieren photographs in figs. 44 and 45.)

Spanwise cross-section cuts; $\alpha = 16^\circ$
(See vapor-screen photographs in figs. 46 and 47.)

(b) $M = 2.16$.

Figure 43. Concluded.

ORIGINAL PAGE
BLACK AND WHITE PHOTOGRAPH

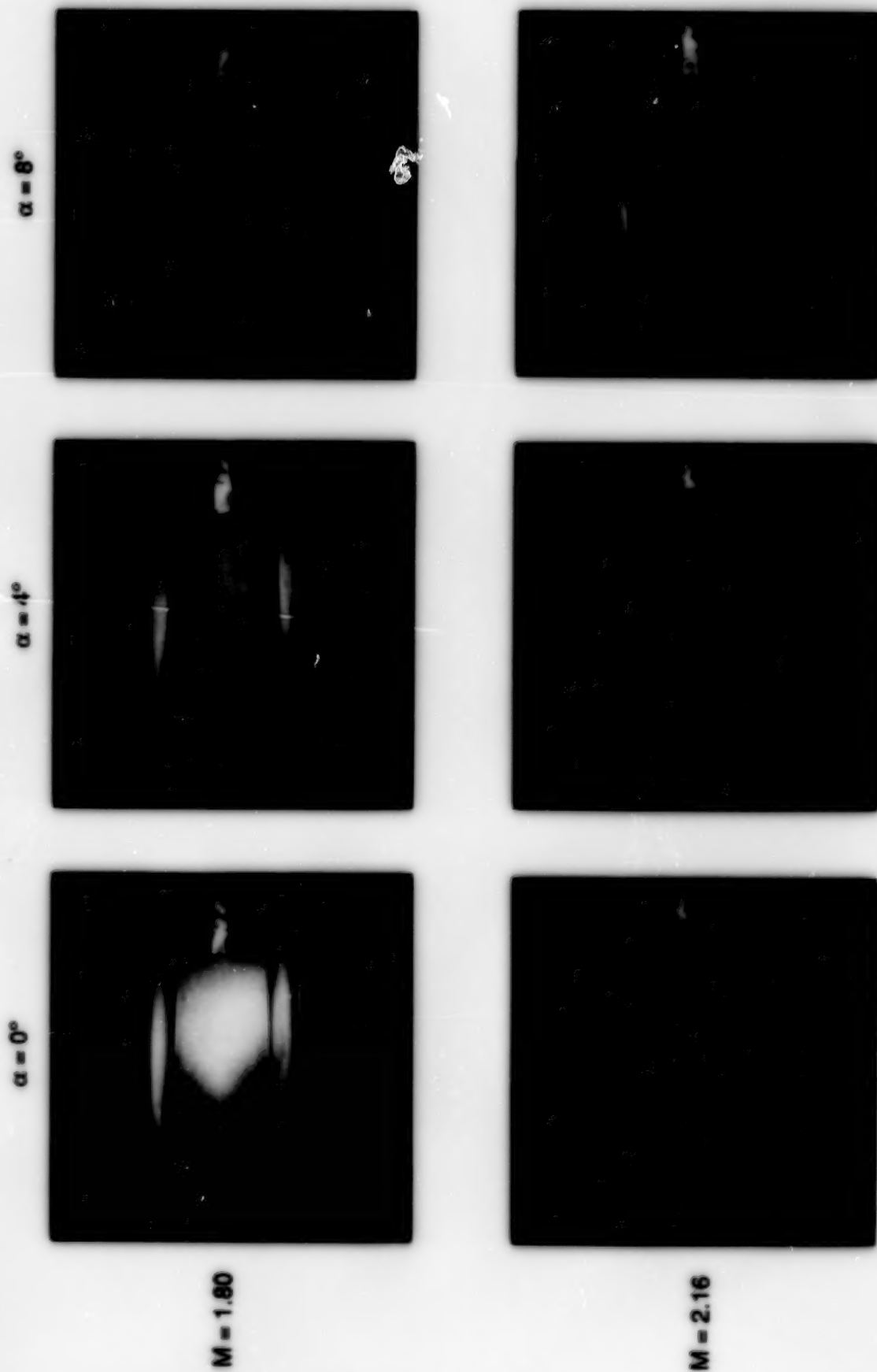


Figure 44. Oil-flow photographs for upper surface of swept/delta multibody configuration at $\alpha = 0^\circ$, 4° , and 8° and $M = 1.80$ and 2.16 .

ORIGINAL PAGE
BLACK AND WHITE PHOTOGRAPH

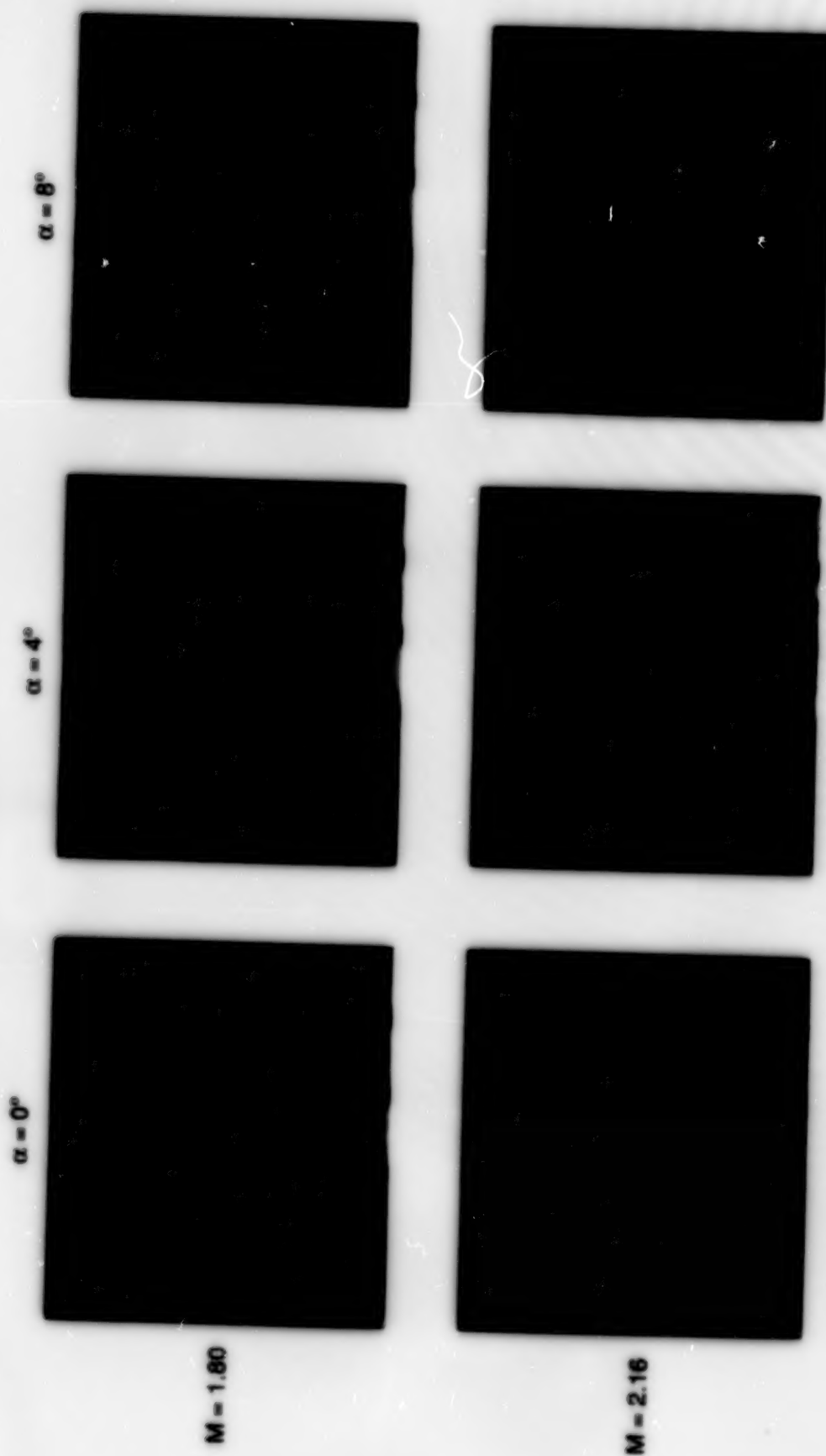


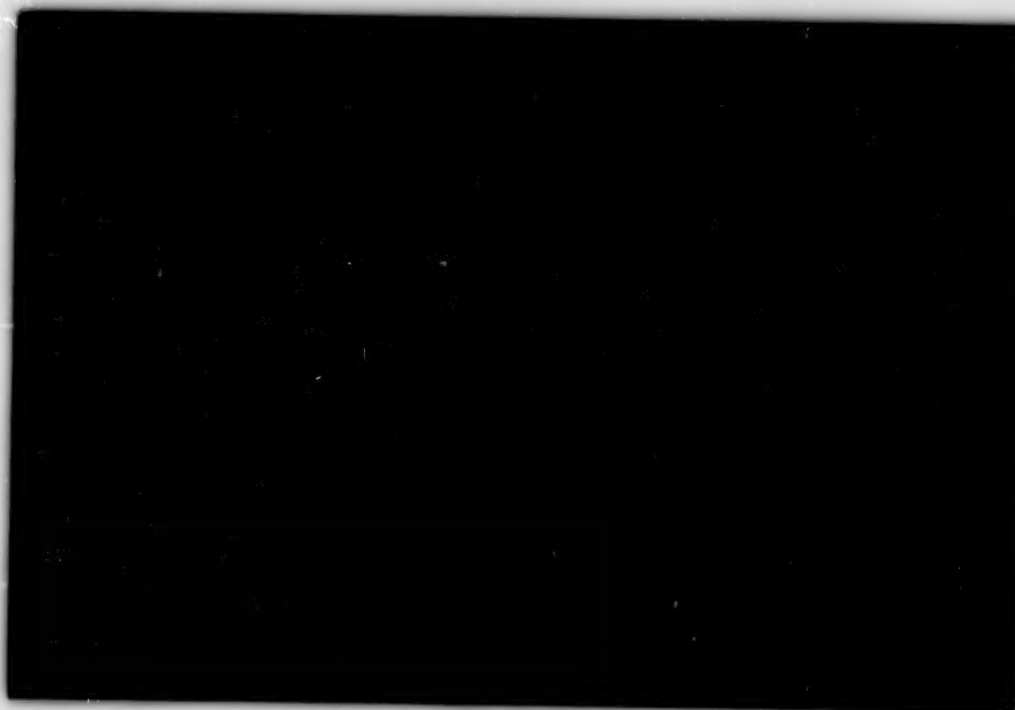
Figure 45. Schlieren photographs for swept/delta multibody configuration at $\alpha = 0^\circ$, 4° , and 8° and $M = 1.80$ and 2.16 .

ORIGINAL PAGE
BLACK AND WHITE PHOTOGRAPH

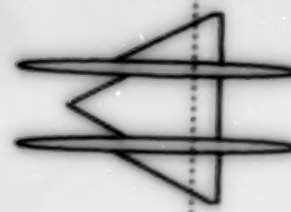
$\alpha = 4^\circ$



$\alpha = 8^\circ$



$x = 18.9 \text{ in.}$



(a) $M = 1.60$.

Figure 46. Vapor-screen photographs at $x = 18.9 \text{ in.}$ for swept/delta multibody configuration for various angles of attack and Mach numbers.

ORIGINAL PAGE
BLACK AND WHITE PHOTOGRAPH

$\alpha = 12^\circ$



$\alpha = 16^\circ$



$x = 18.9 \text{ in.}$



Not available

(a) Concluded.

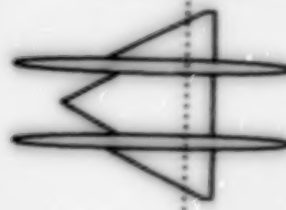
Figure 46. Continued.

ORIGINAL PAGE
BLACK AND WHITE PHOTOGRAPH

$\alpha = 4^\circ$



$x = 18.9 \text{ in.}$



$\alpha = 8^\circ$



(b) $M = 1.80$.

Figure 46. Continued.

ORIGINAL PAGE
BLACK AND WHITE PHOTOGRAPH
 $\alpha = 12^\circ$



$\alpha = 16^\circ$



$x = 18.9 \text{ in.}$



(b) Concluded.

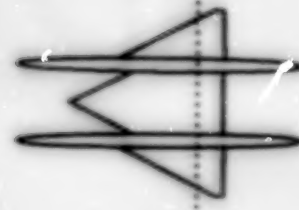
Figure 46. Continued.

ORIGINAL PAGE
BLACK AND WHITE PHOTOGRAPH

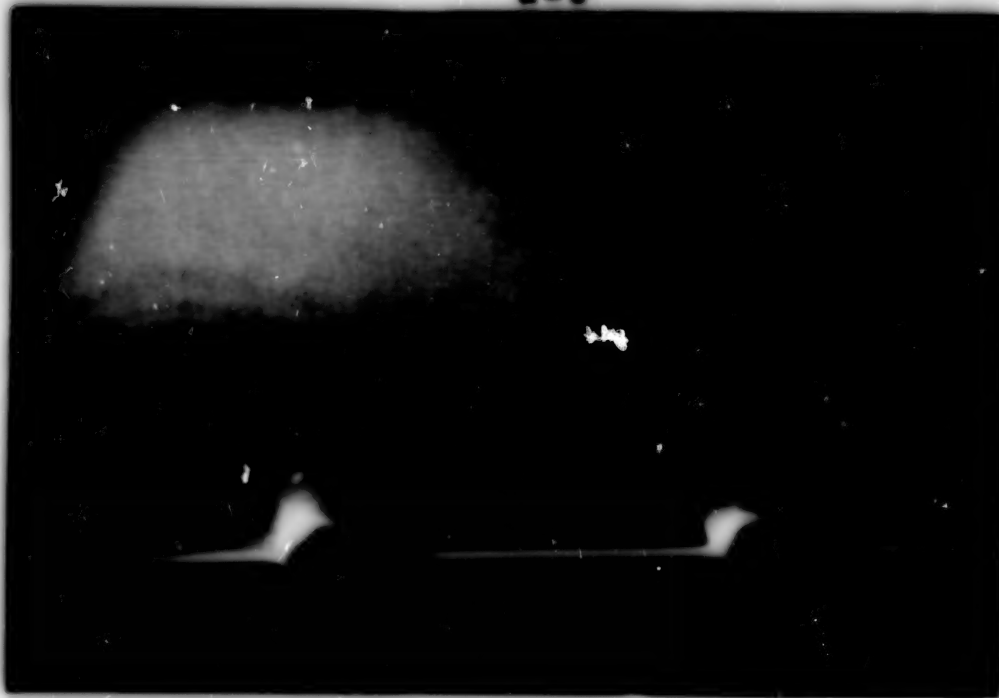
$\alpha = 4^\circ$



$x = 18.9 \text{ in.}$



$\alpha = 8^\circ$



(c) $M = 2.00$.

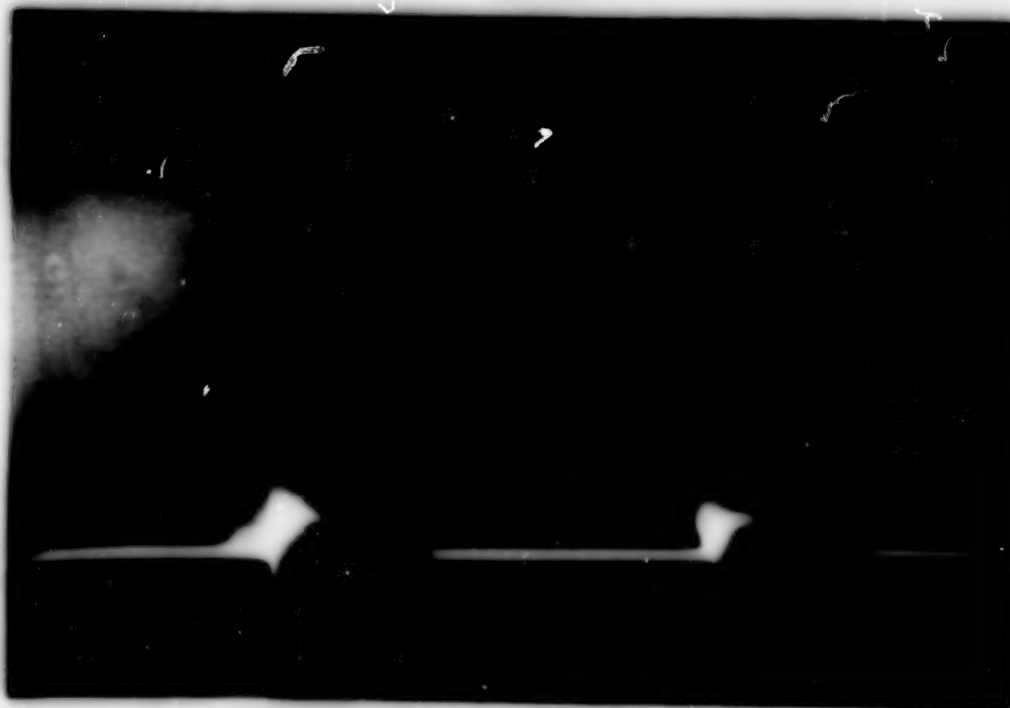
Figure 46. Continued.

ORIGINAL PAGE
BLACK AND WHITE PHOTOGRAPH

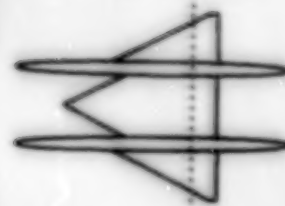
$\alpha = 12^\circ$



$\alpha = 16^\circ$



$x = 18.9 \text{ in.}$



(c) Concluded.

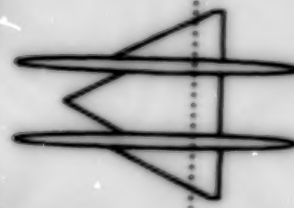
Figure 46. Continued.

ORIGINAL PAGE
BLACK AND WHITE PHOTOGRAPH

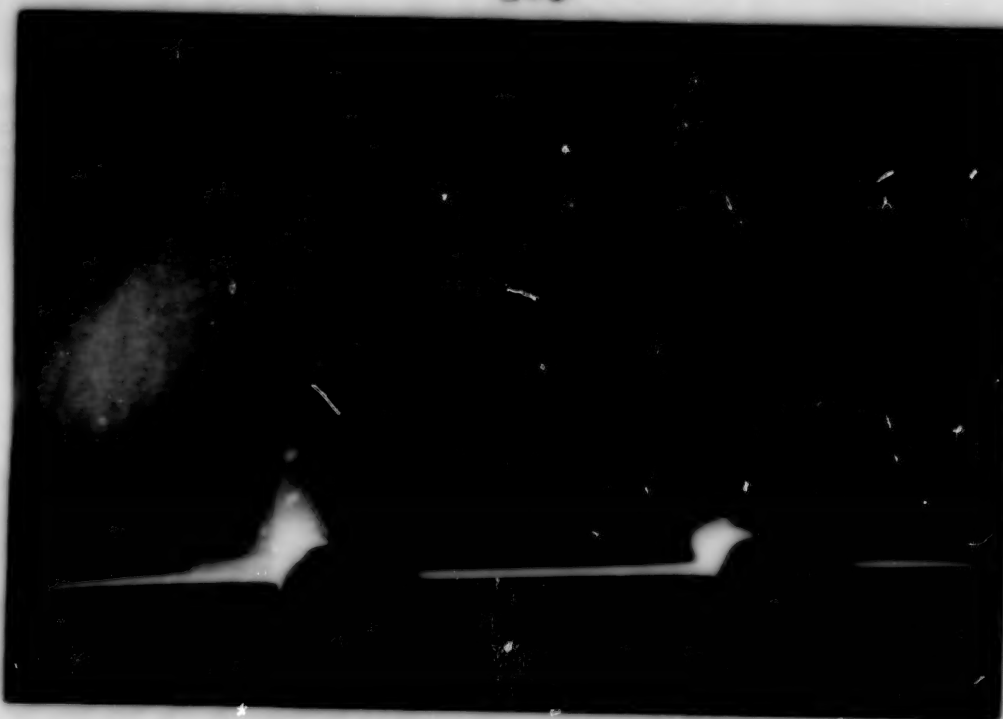
$\alpha = 4^\circ$



$x = 18.9 \text{ in.}$



$\alpha = 8^\circ$



(d) $M = 2.16$.

Figure 46. Continued.

ORIGINAL PAGE
BLACK AND WHITE PHOTOGRAPH

$\alpha = 12^\circ$



$x = 18.9 \text{ in.}$



$\alpha = 16^\circ$

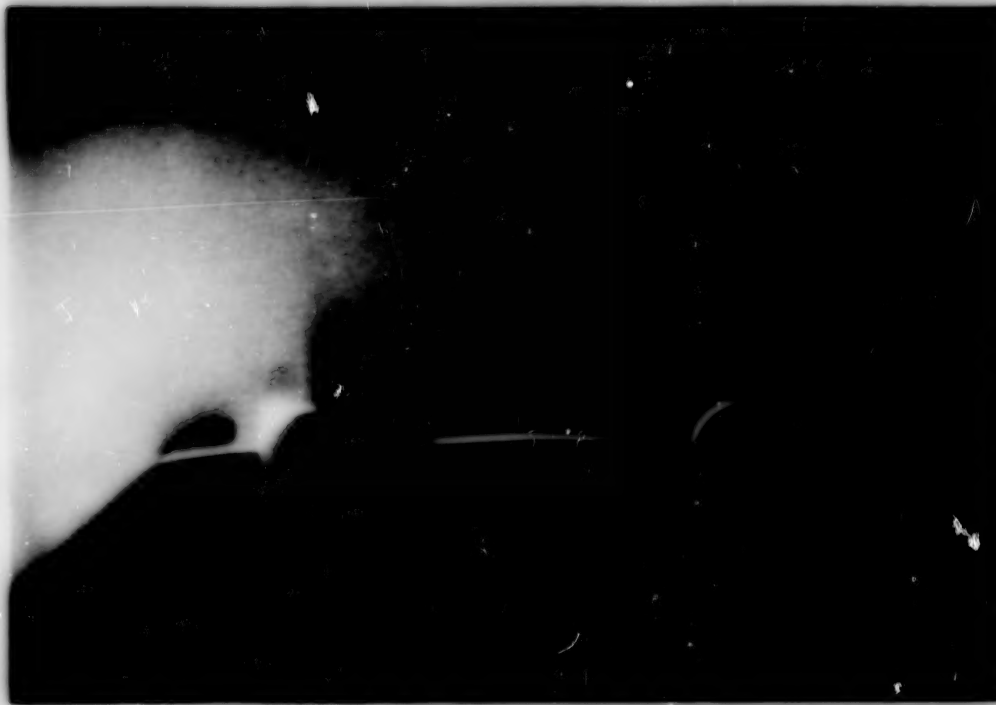


(d) Concluded.

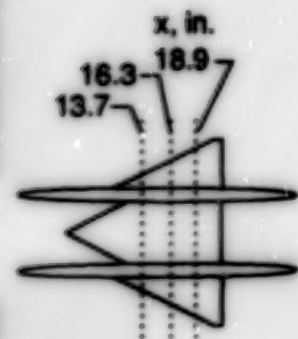
Figure 46. Concluded.

ORIGINAL PAGE
BLACK AND WHITE PHOTOGRAPH

$x = 13.7$ in.



$x = 16.3$ in.

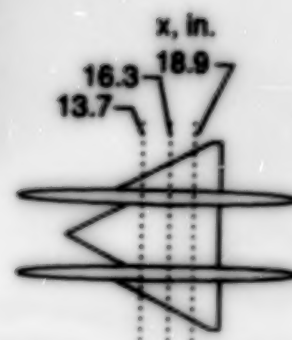


(a) $M = 1.80$.

Figure 47. Vapor-screen photographs for swept/delta multibody configuration at three longitudinal locations for $\alpha = 16^\circ$ and $M = 1.80$ and 2.16 .

ORIGINAL PAGE
BLACK AND WHITE PHOTOGRAPH

$x = 18.9$ in.



(a) Concluded.

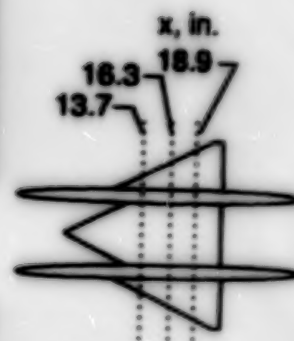
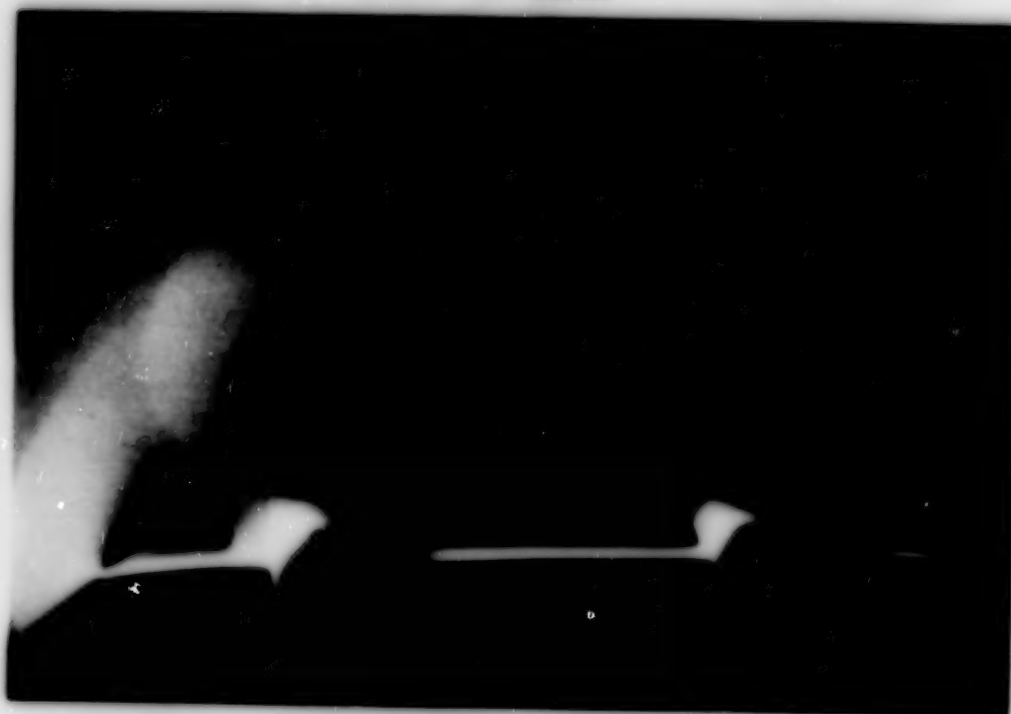
Figure 47. Continued.

ORIGINAL PAGE
BLACK AND WHITE PHOTOGRAPH

$x = 13.7$ in.



$x = 16.3$ in.

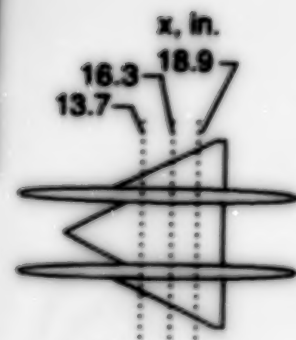


(b) $M = 2.16$.

Figure 47. Continued.

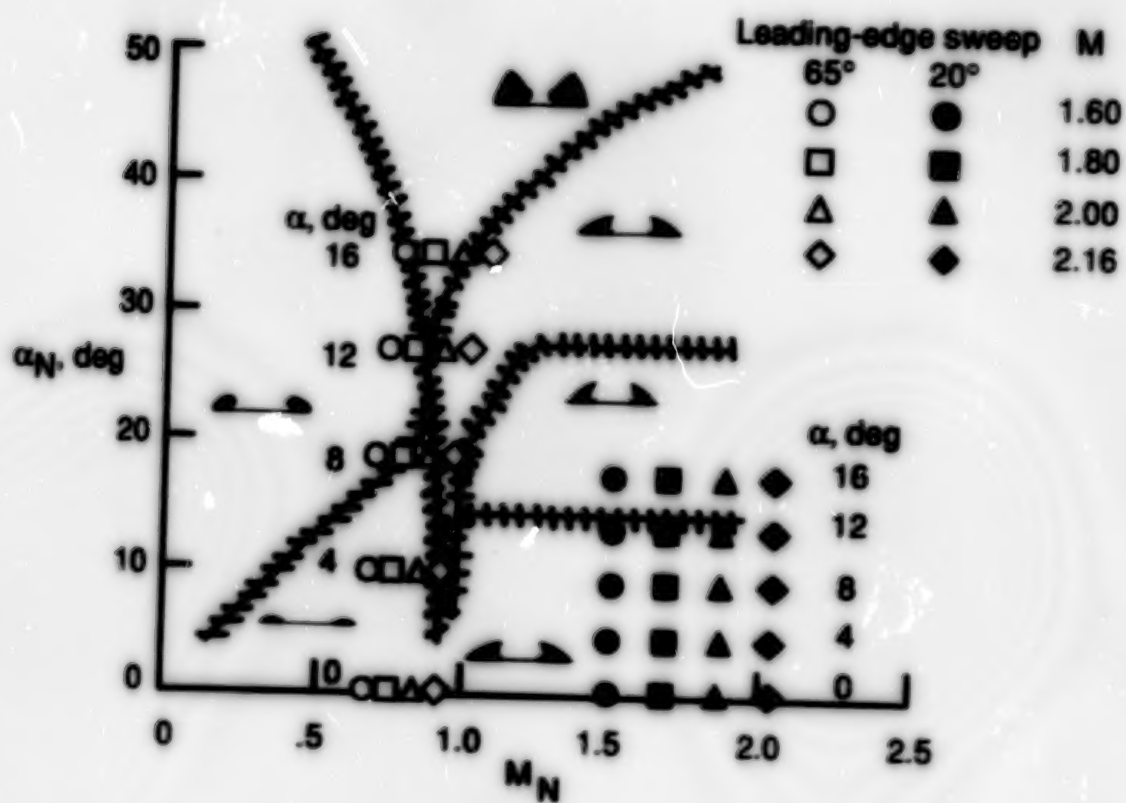
ORIGINAL PAGE
BLACK AND WHITE PHOTOGRAPH

$x = 18.9$ in.

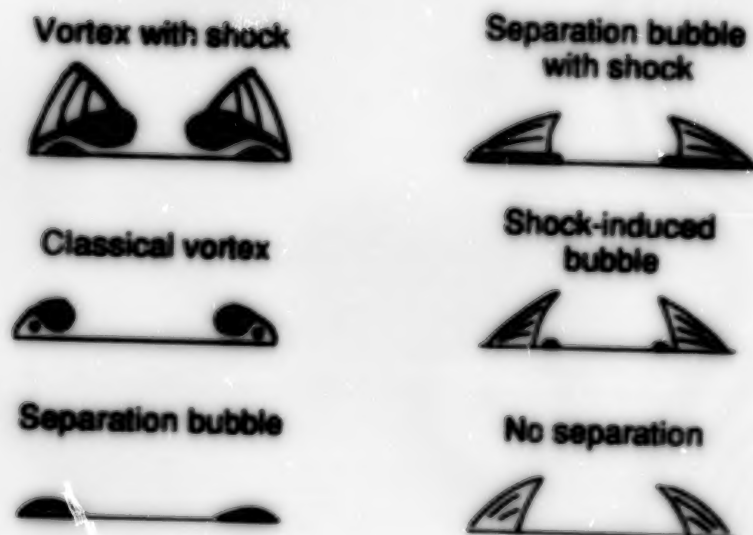


(b) Concluded.

Figure 47. Concluded.



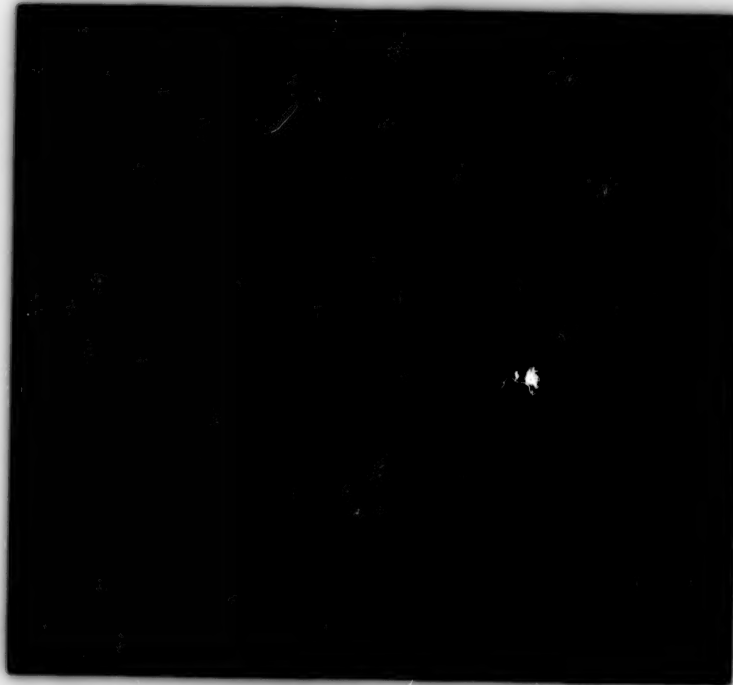
(a) Flow classification chart.



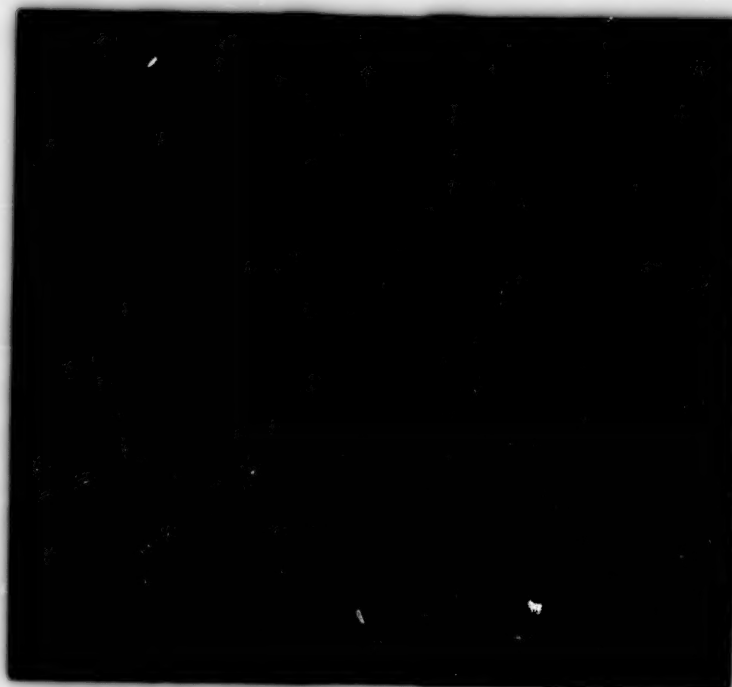
(b) Sketches of flow classifications.

Figure 48. Flow classification chart with locations of wings swept 65° and 20° at angles of attack.

ORIGINAL PAGE
BLACK AND WHITE PHOTOGRAPH

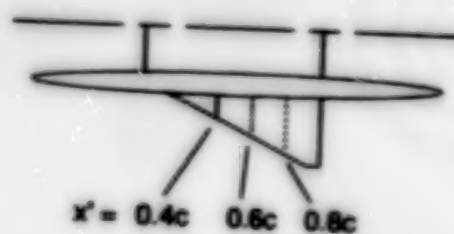
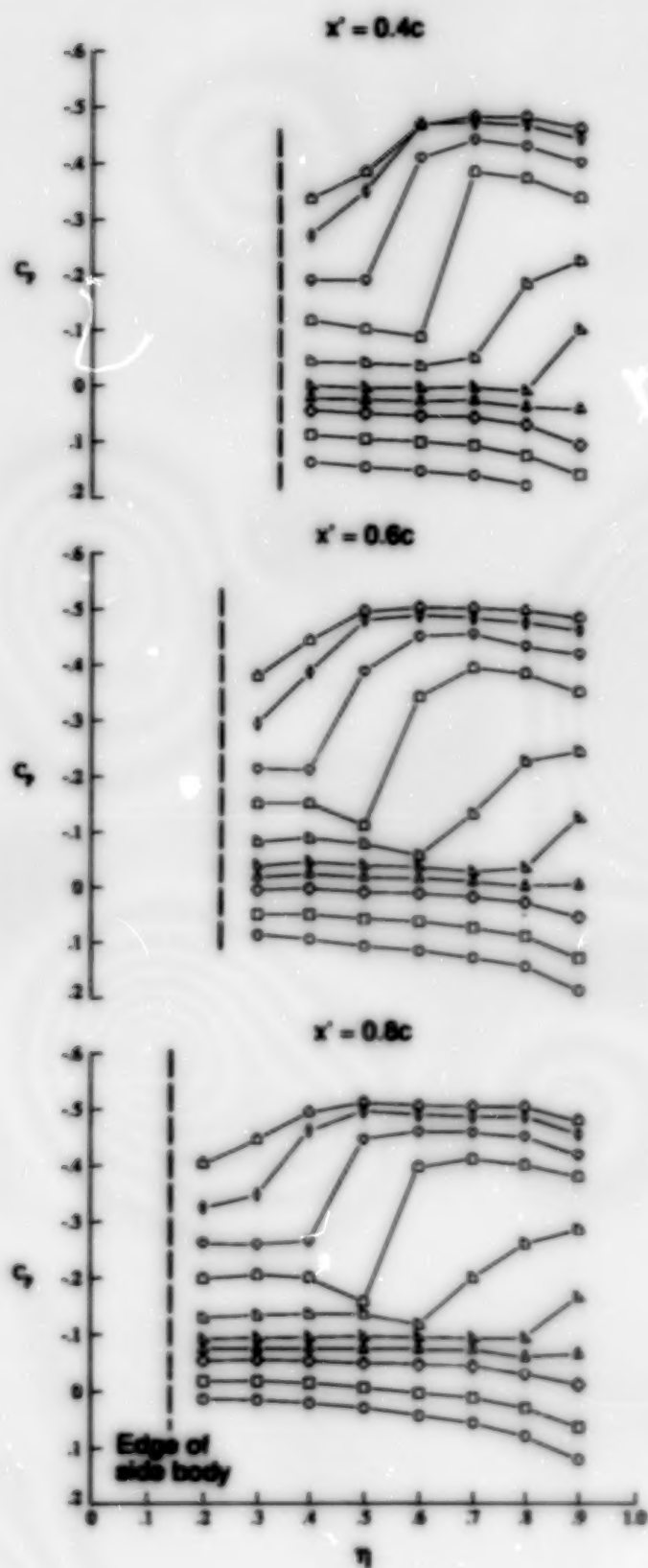


(a) $M = 1.80$.



(b) $M = 2.16$.

Figure 49. Schlieren photographs for unswept/large-trapezoidal configuration at $\alpha = 0^\circ$ and $M = 1.80$ and 2.16 .

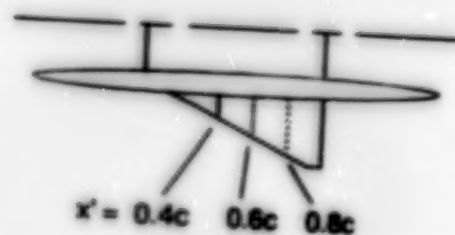
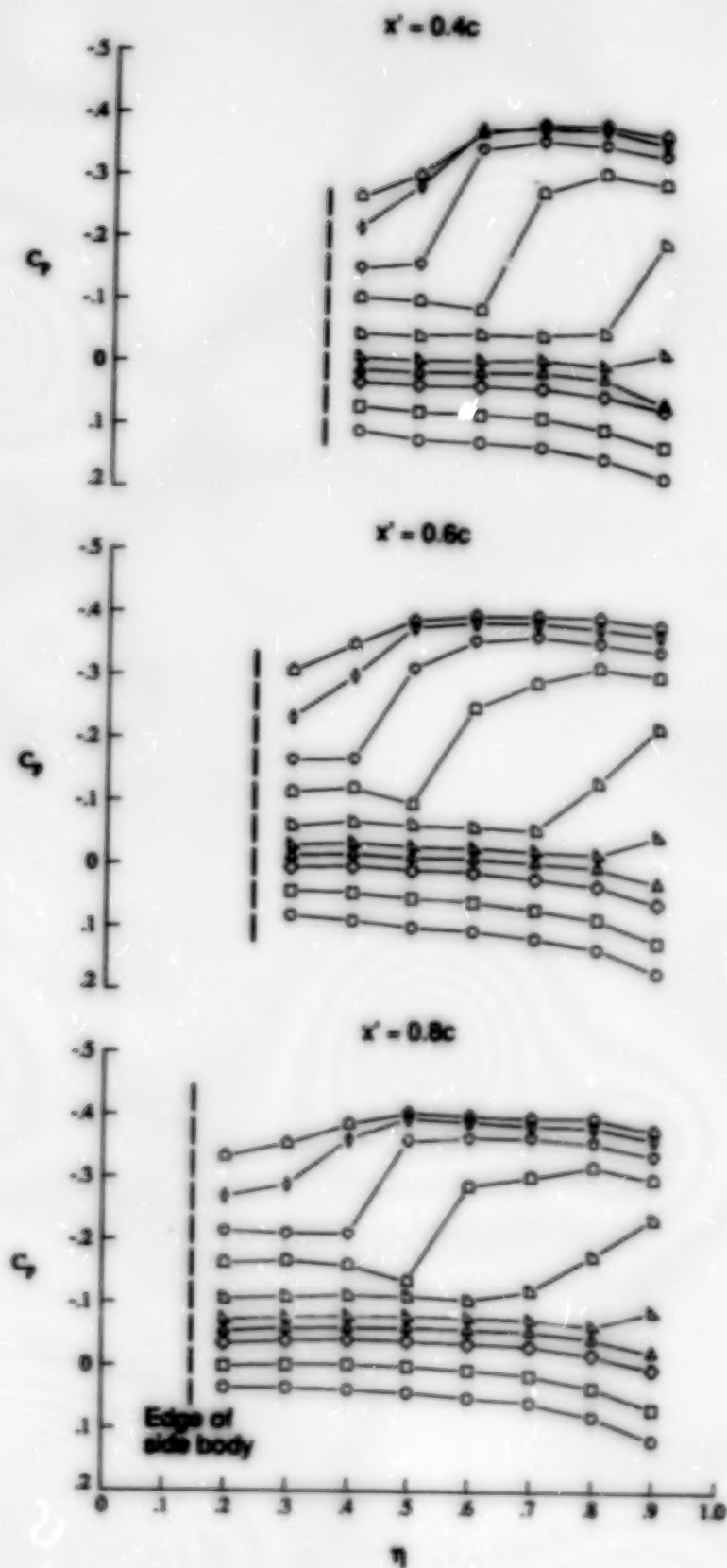


α , deg

○	-3.81
□	-1.87
◇	0.16
△	1.17
△	2.17
○	4.17
○	8.15
○	12.19
○	16.13
○	20.17

(a) $M = 1.60$.

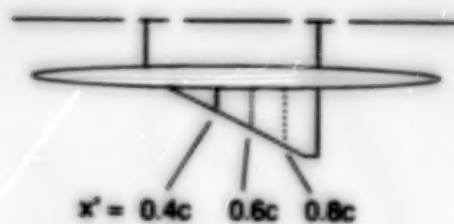
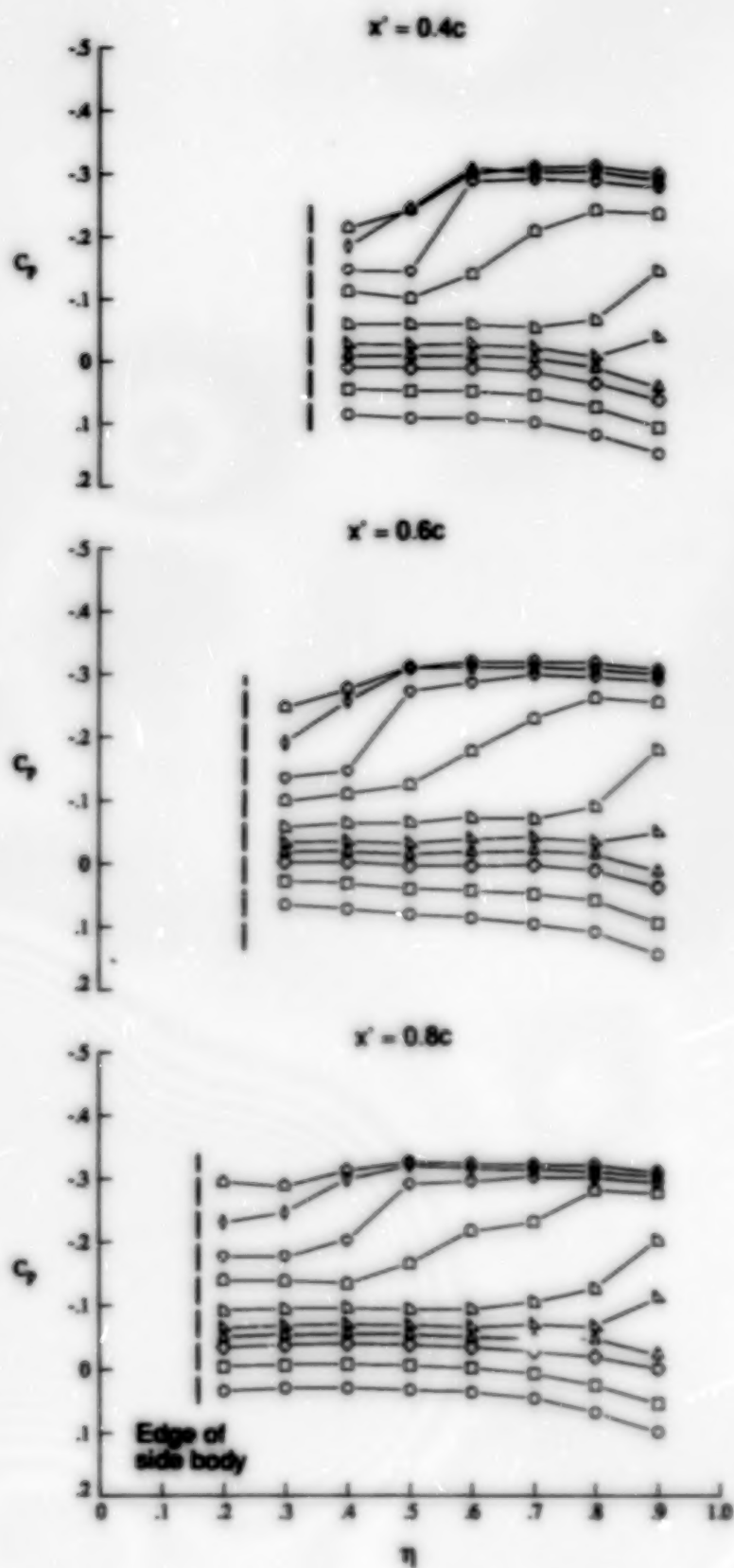
Figure 50. Effect of angle of attack on surface pressure coefficient distributions over delta outboard wing of unswept/delta configuration at $x' = 0.4c$, $0.6c$, and $0.8c$ for $M = 1.60$, 1.80 , 2.00 , and 2.16 .



α , deg
-3.92
-1.93
0.00
1.13
2.10
4.07
8.10
12.07
16.11
20.00

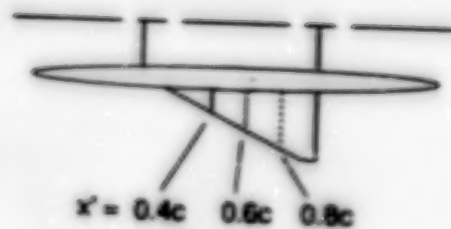
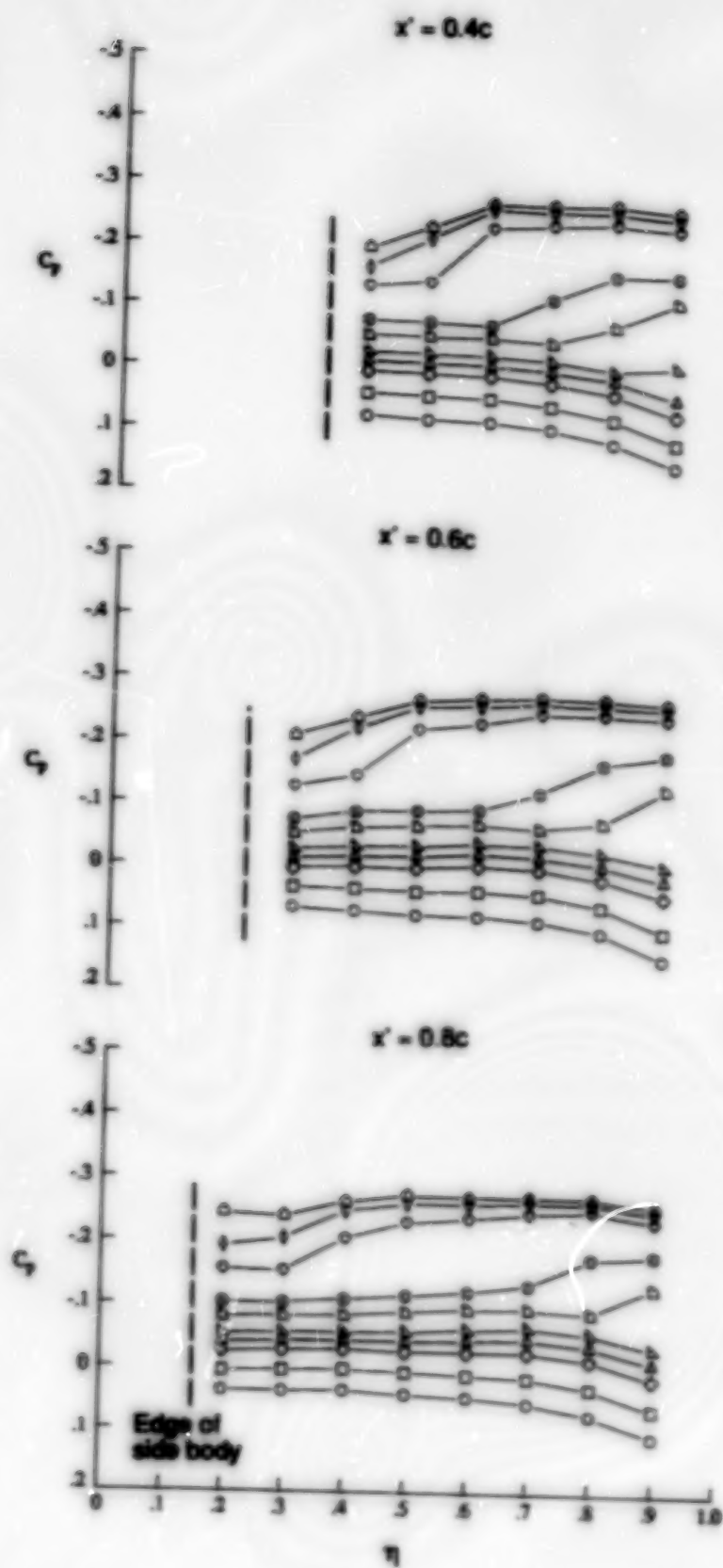
(b) $M = 1.80$.

Figure 50. Continued.



(c) $M = 2.00$.

Figure 50. Continued.



α , deg	
-4.08	○
-2.12	□
-0.10	○
0.90	△
1.89	▽
3.93	◇
5.95	⊙
11.95	⊗
15.96	⊕
19.96	⊖

(d) $M = 2.16$.

Figure 50. Concluded.

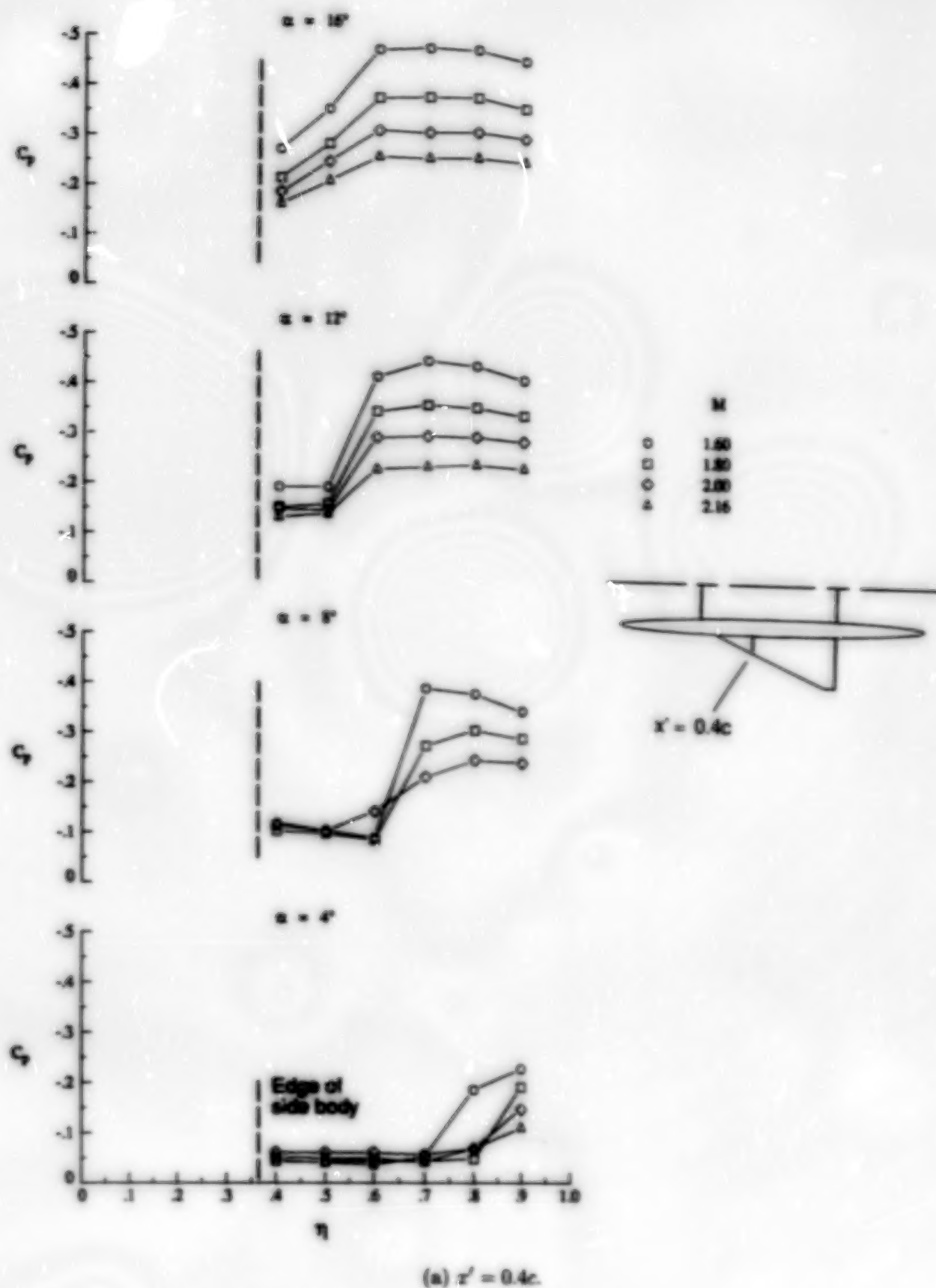
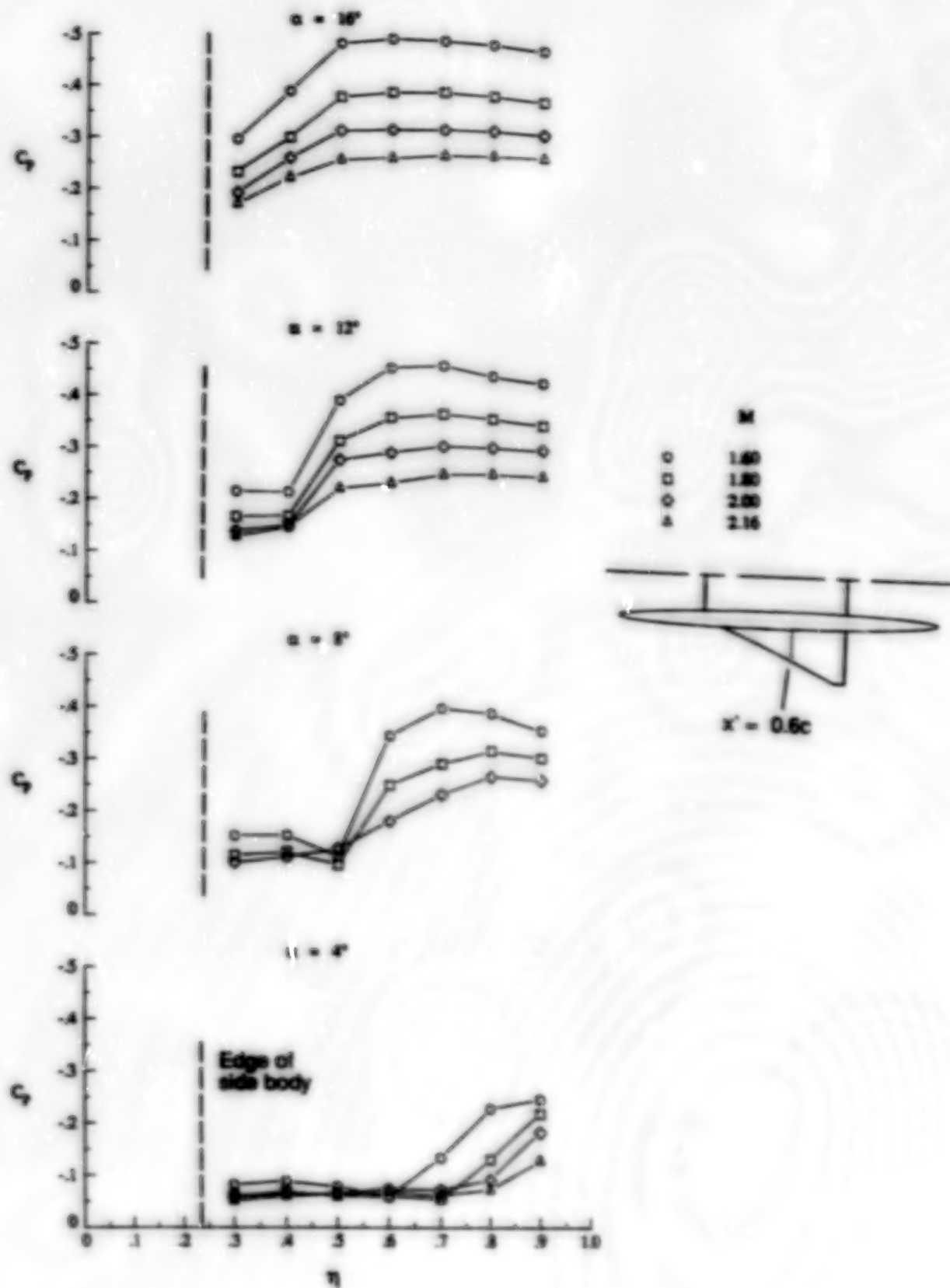
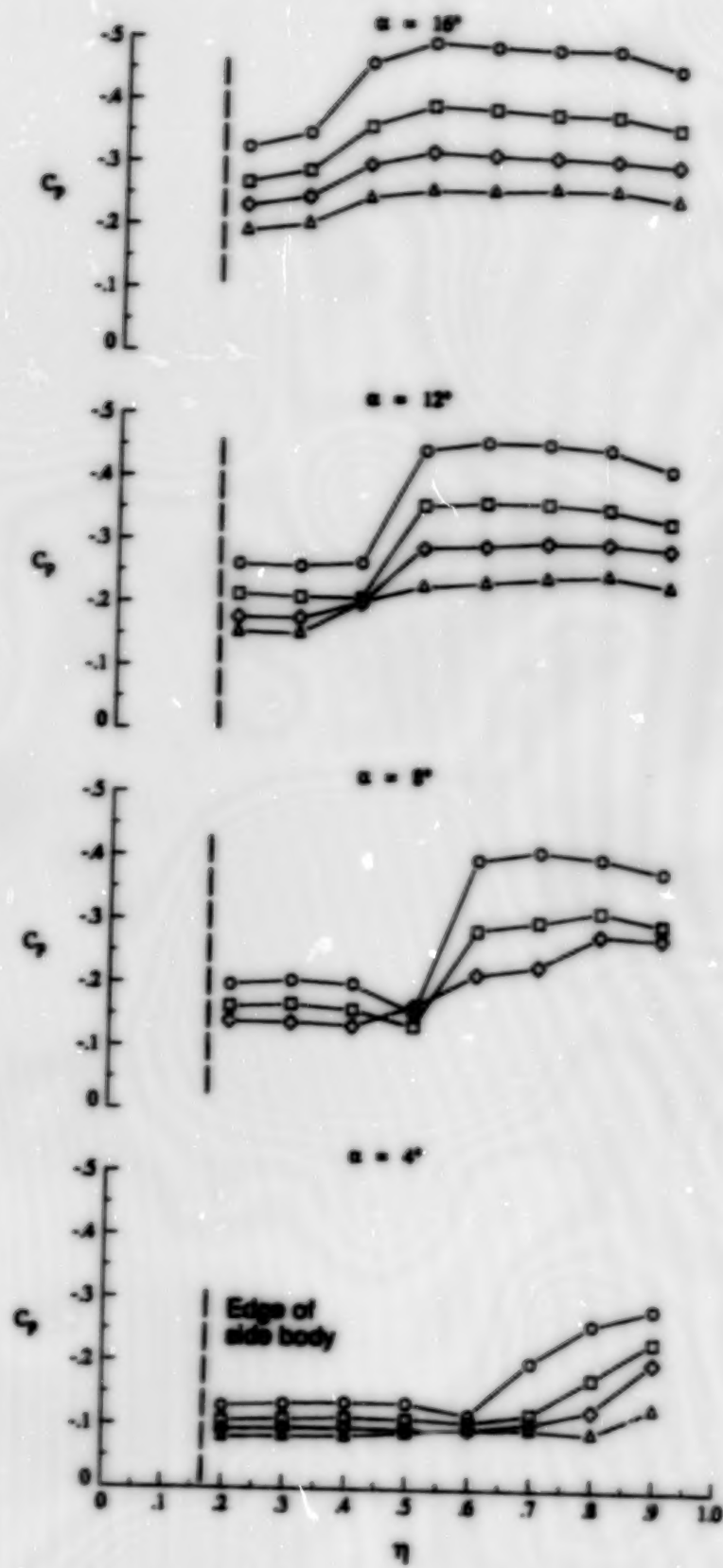


Figure 51. Effect of Mach number on surface pressure coefficient distributions over delta outboard wing of unswept/delta configuration at $x' = 0.4c$, $0.6c$, and $0.8c$ for $\alpha = 4^\circ$, 8° , 12° , and 16° .

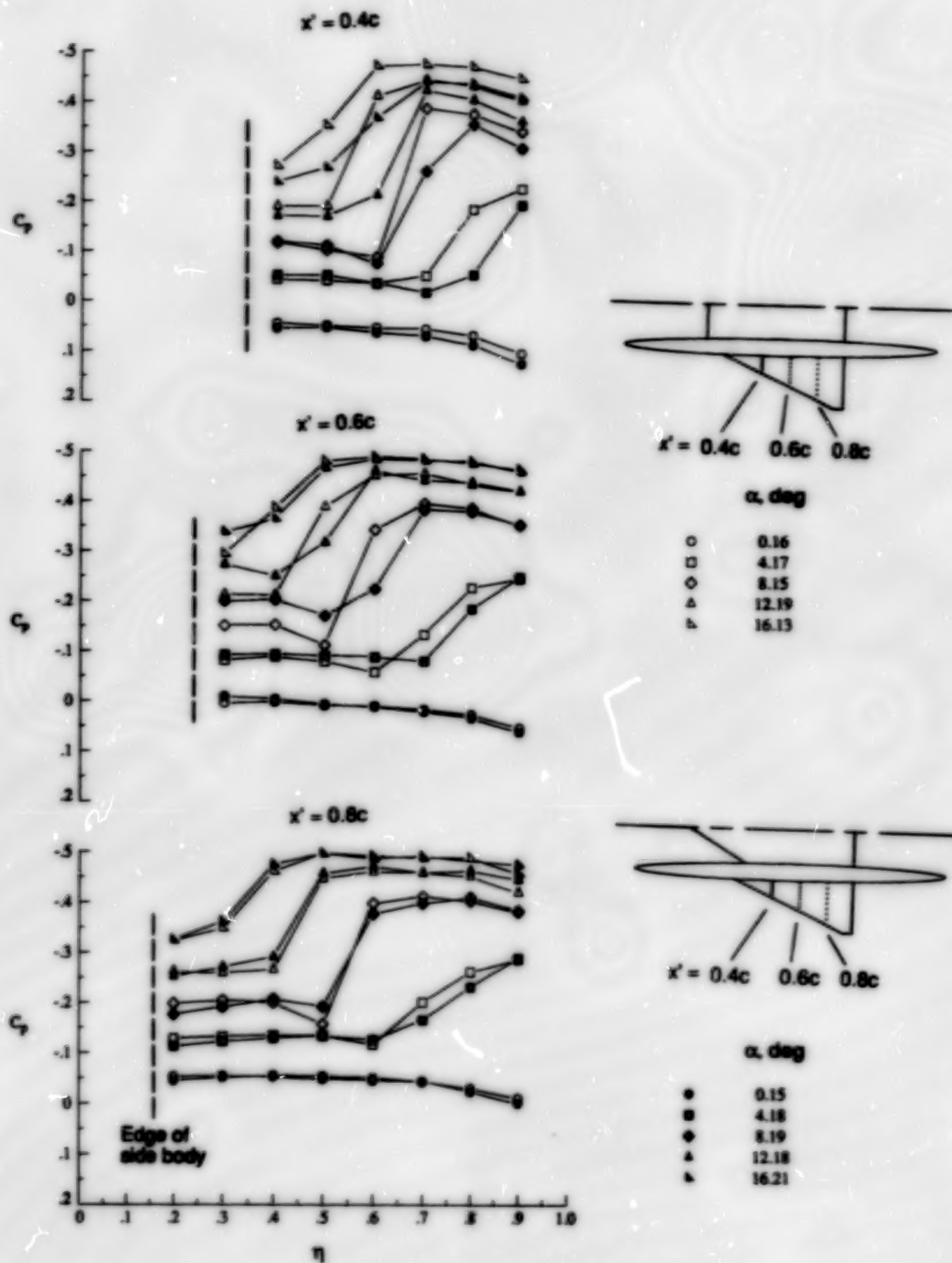


(b) $x' = 0.6c$.

Figure 51. Continued.

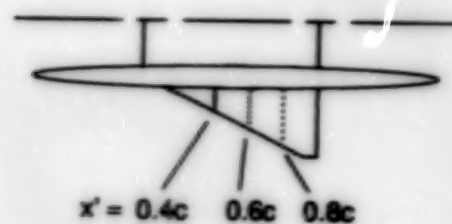
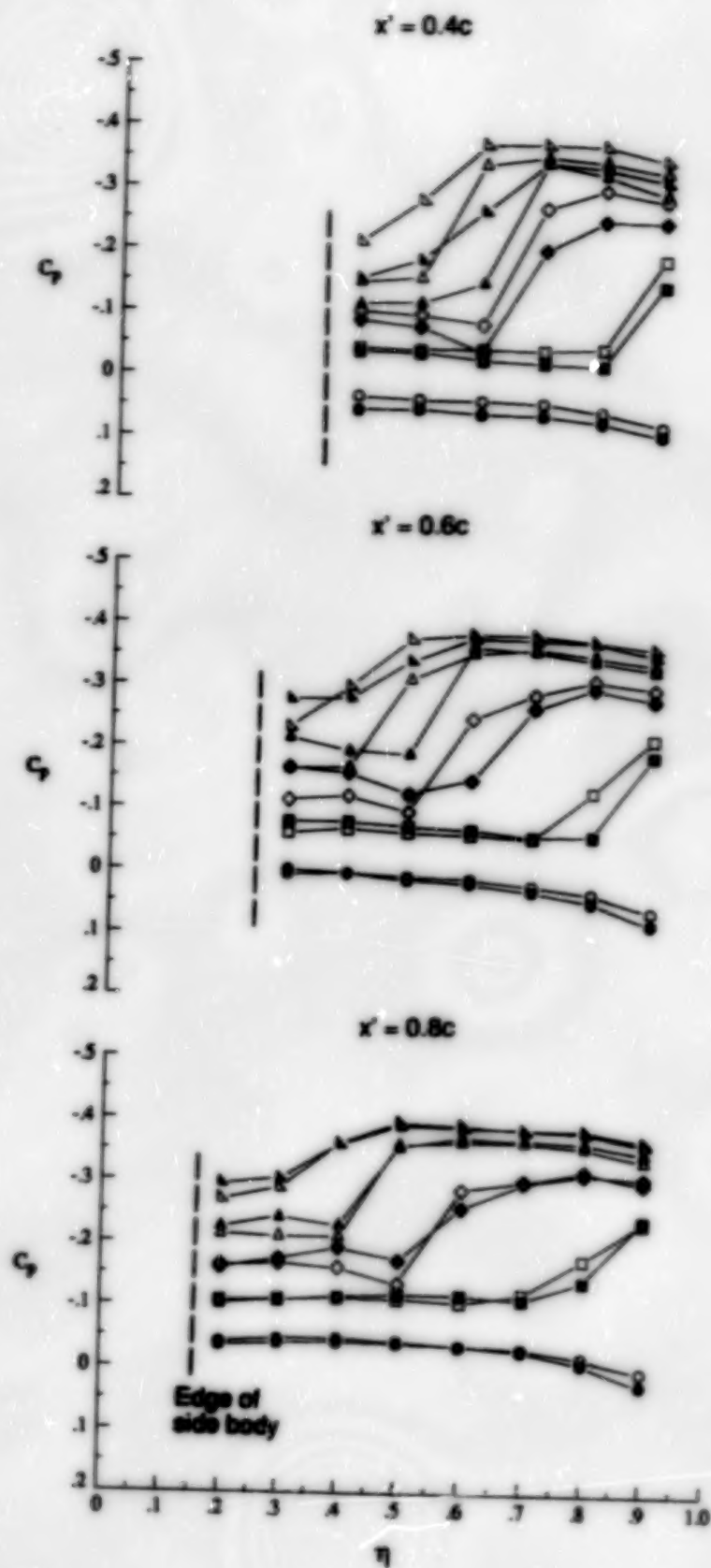


(c) $x' = 0.8c$.
Figure 51. Concluded.



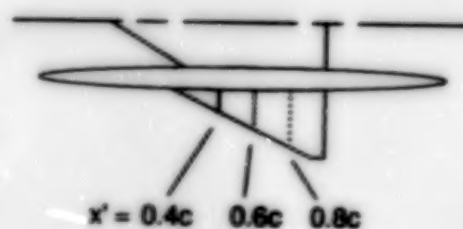
(a) $M = 1.60$.

Figure 52. Effect of inboard wing planform shape on surface pressure coefficient distributions over delta outboard wing at $x' = 0.4c$, $0.6c$, and $0.8c$ for $M = 1.60$, 1.80 , 2.00 , and 2.16 .



α , deg

○	0.09
□	4.07
◇	8.10
△	12.07
▽	16.11

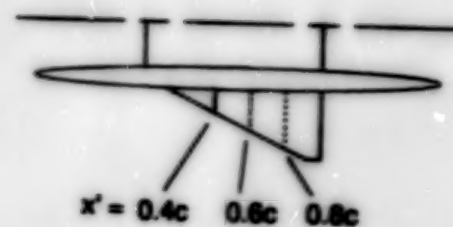
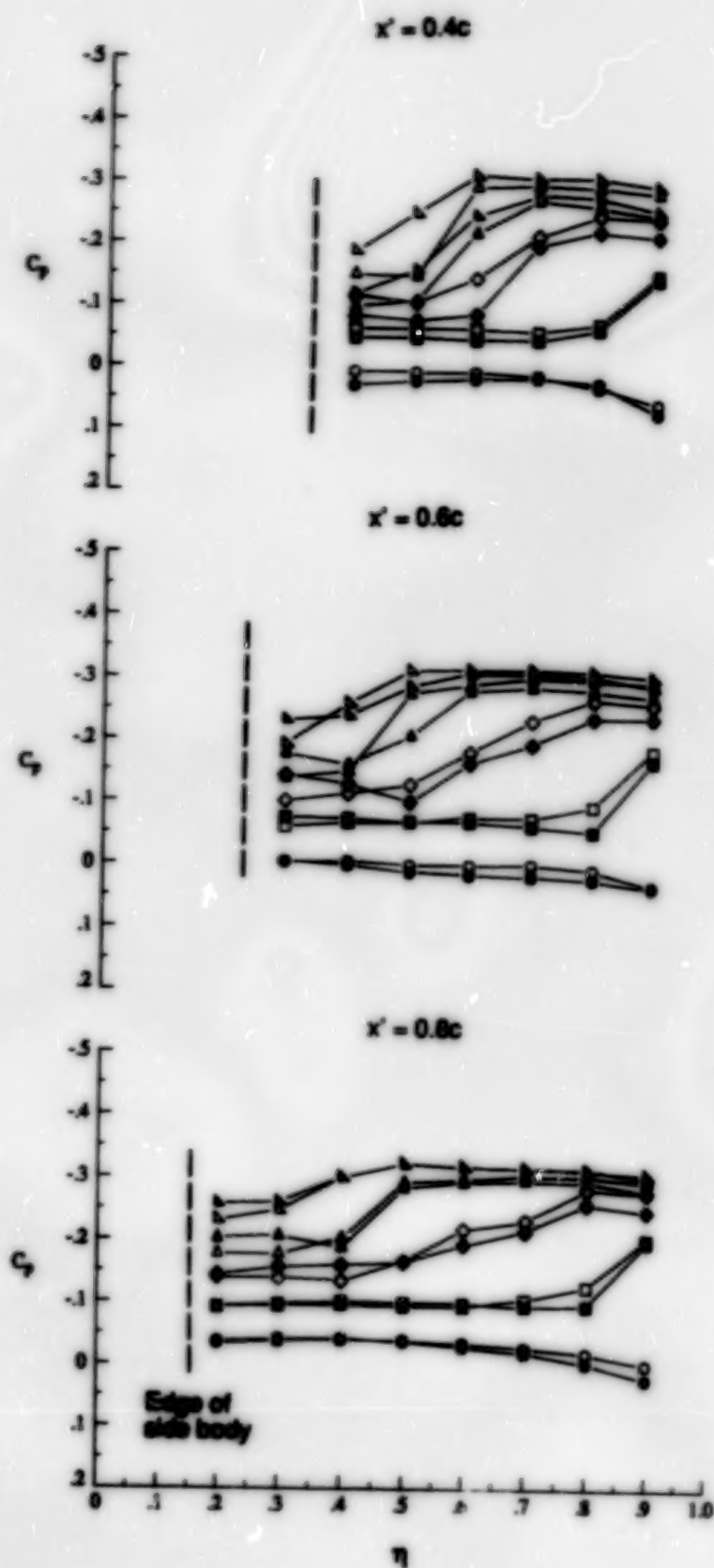


α , deg

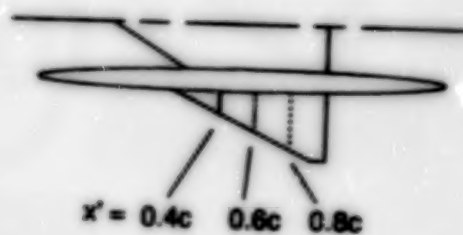
●	0.04
■	4.06
◆	8.05
▲	12.11
▼	16.05

(b) $M = 1.80$.

Figure 52. Continued.



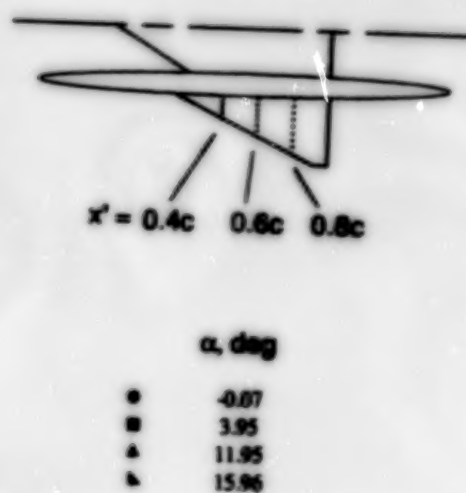
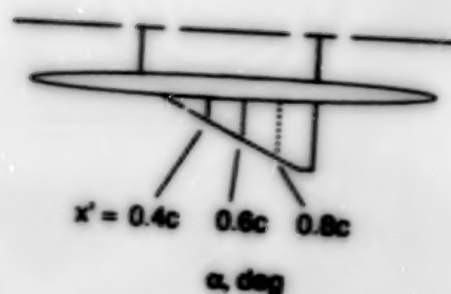
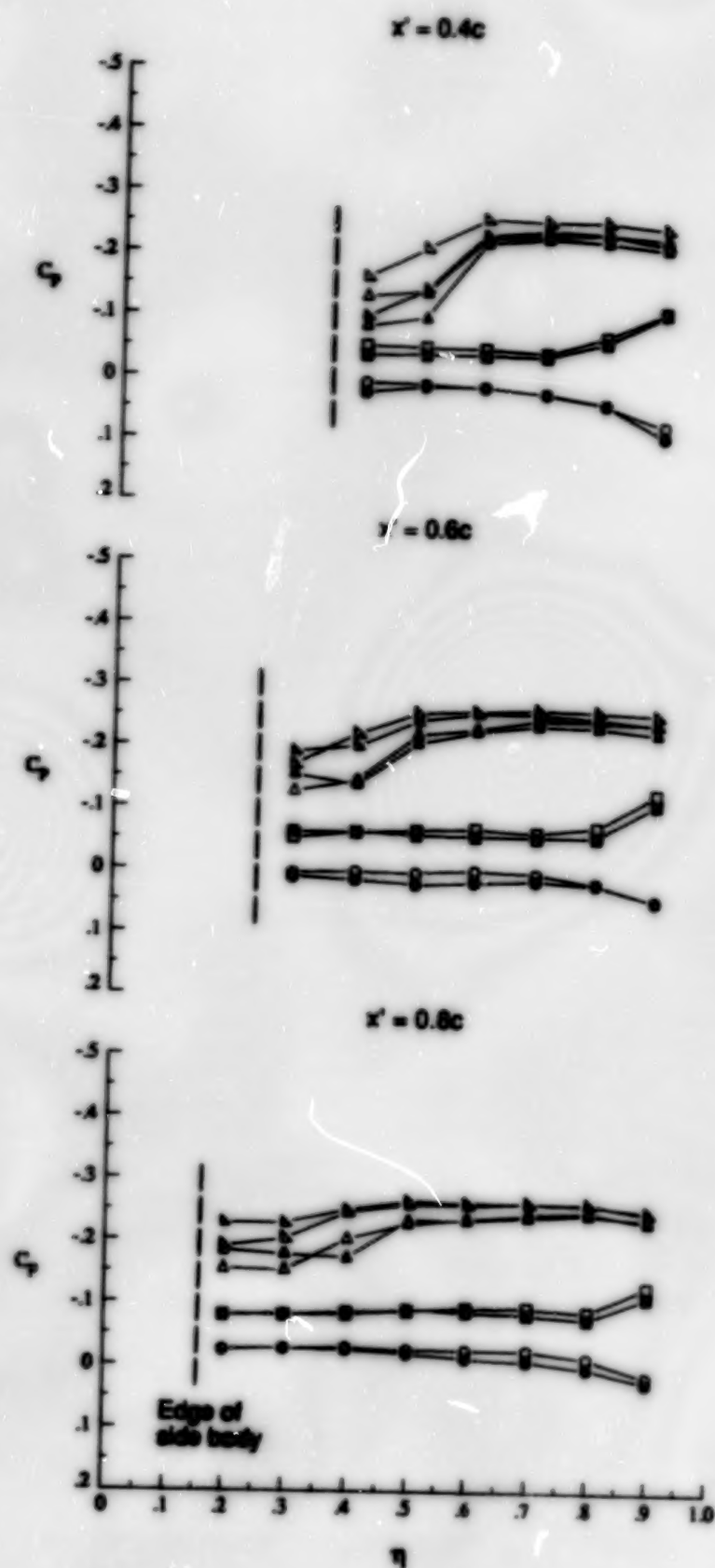
α , deg	
○	0.25
□	4.29
◇	8.33
△	12.39
△	16.35



α , deg	
●	0.25
■	4.23
◆	8.23
▲	12.25
▲	16.27

(c) $M = 2.00$.

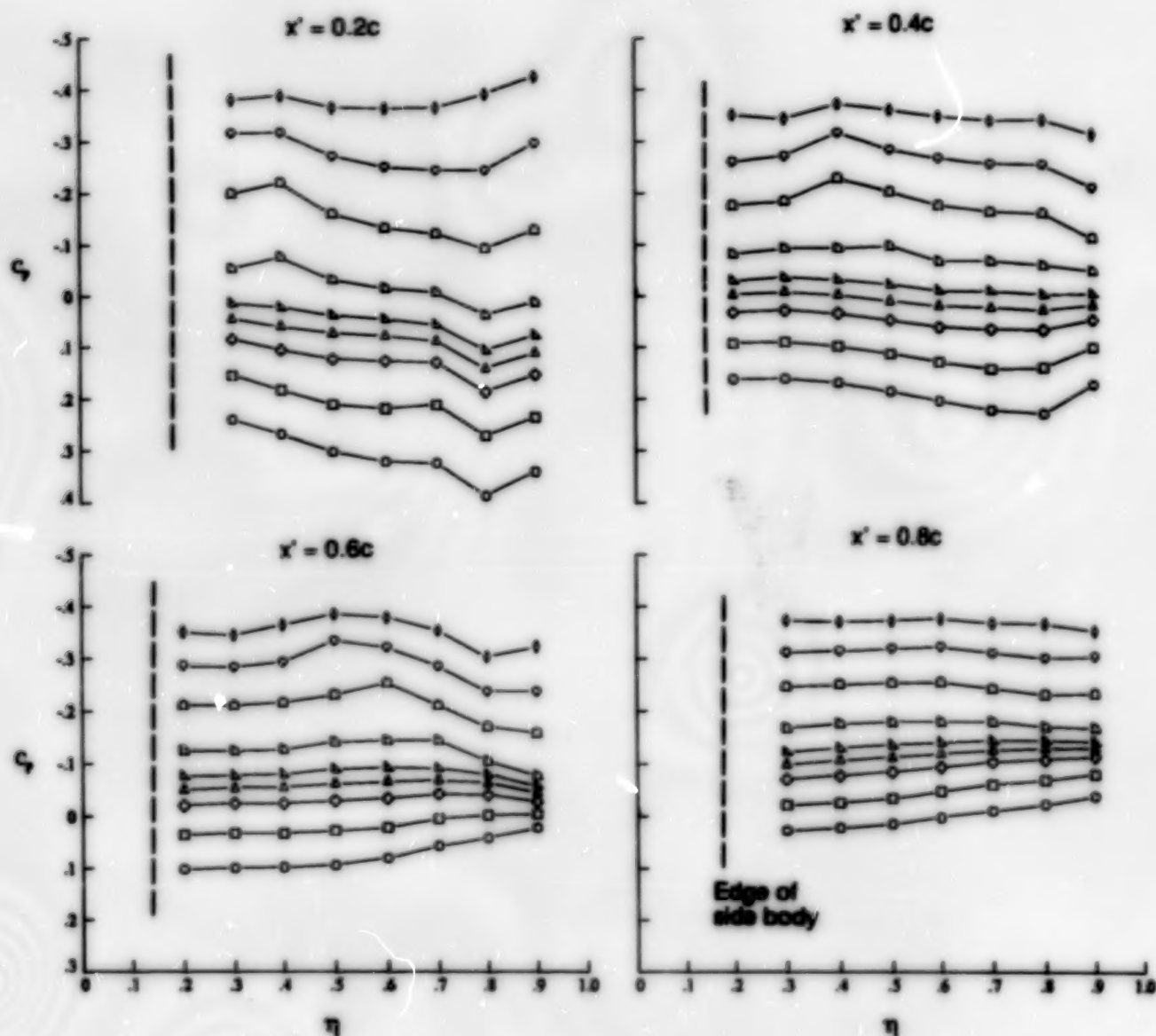
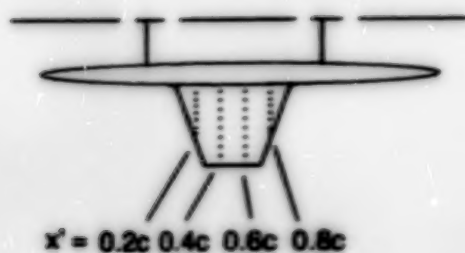
Figure 52. Continued.



(d) $M = 2.16$.

Figure 52. Concluded.

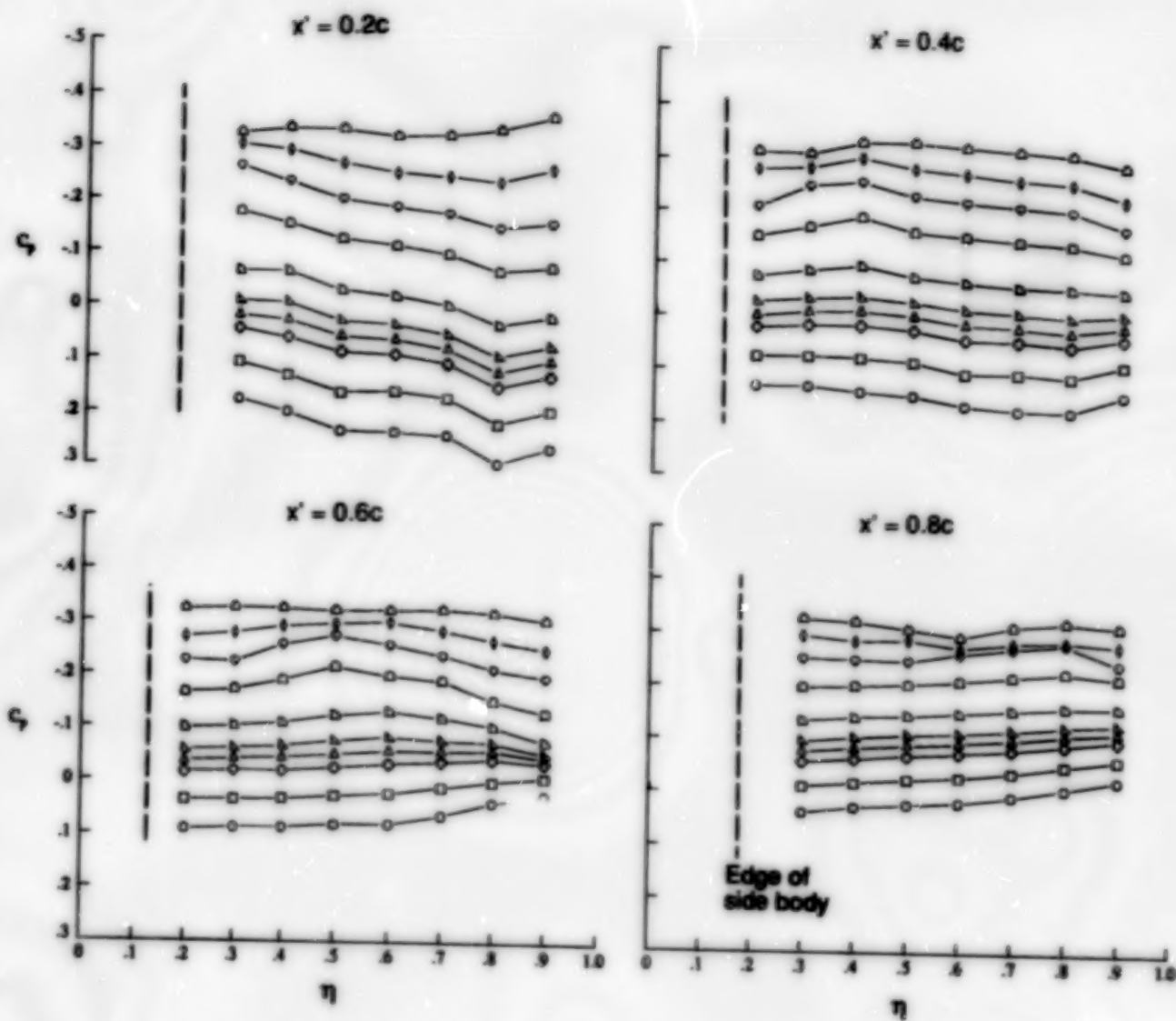
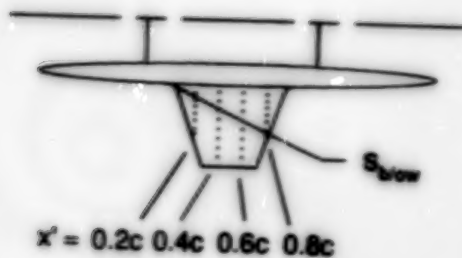
α , deg	
○	-3.83
□	-1.81
△	0.17
△	1.21
△	2.19
○	4.20
○	8.22
○	12.18
+	16.17



(a) $M = 1.60$.

Figure 53. Effect of angle of attack on surface pressure coefficient distributions over small-trapezoidal outboard wing of unswept/small-trapezoidal configuration at $x' = 0.2c, 0.4c, 0.6c$, and $0.8c$ for $M = 1.60, 1.80, 2.00$, and 2.16 .

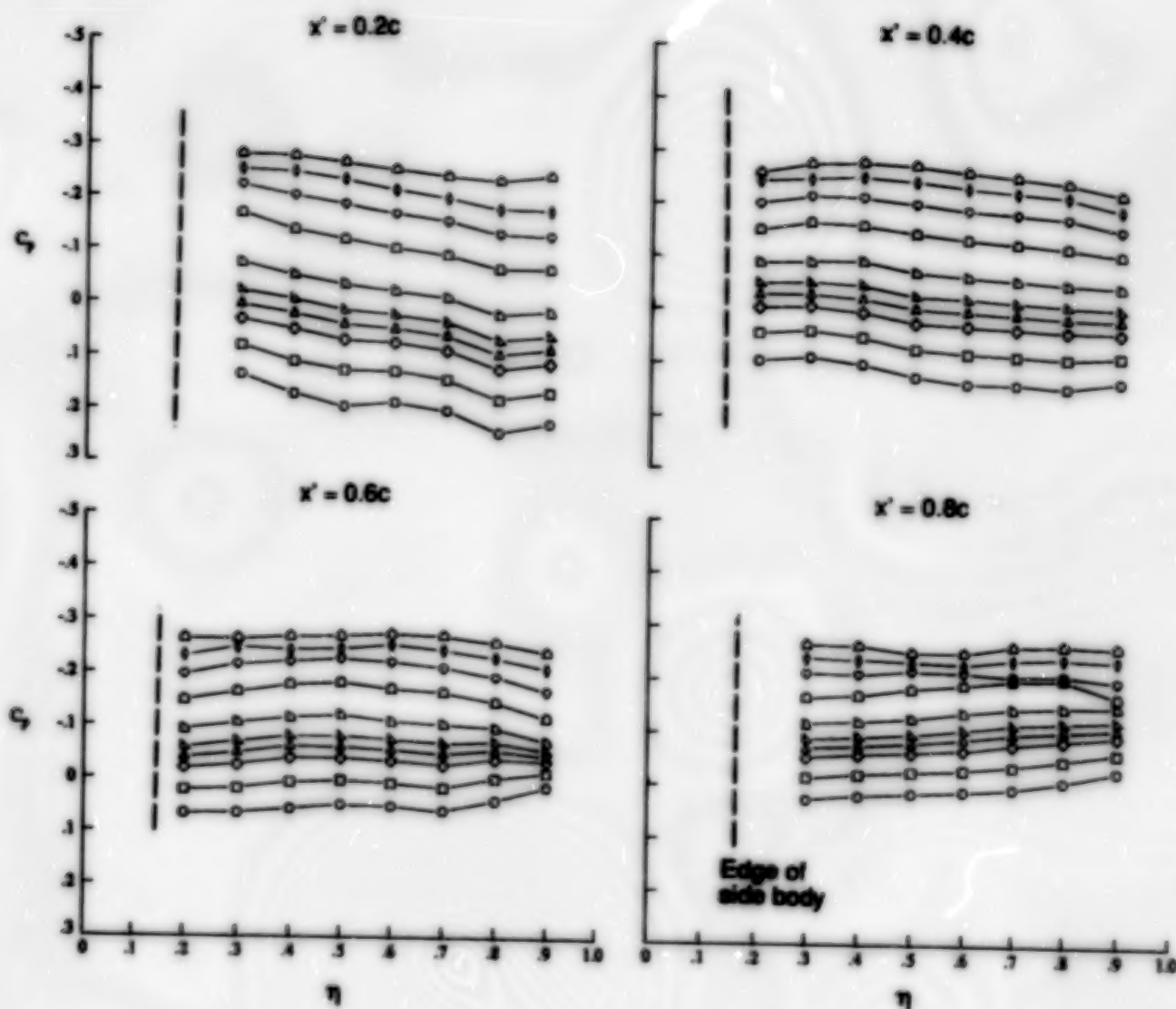
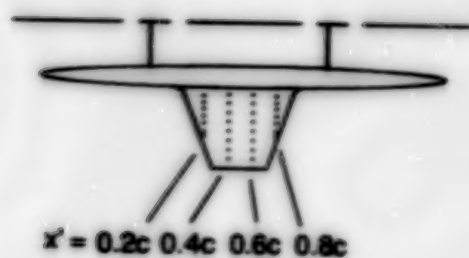
α , deg
-3.90
-1.88
0.15
1.09
2.07
4.13
8.16
12.13
16.07
20.06



(b) $M = 1.80$.

Figure 53. Continued.

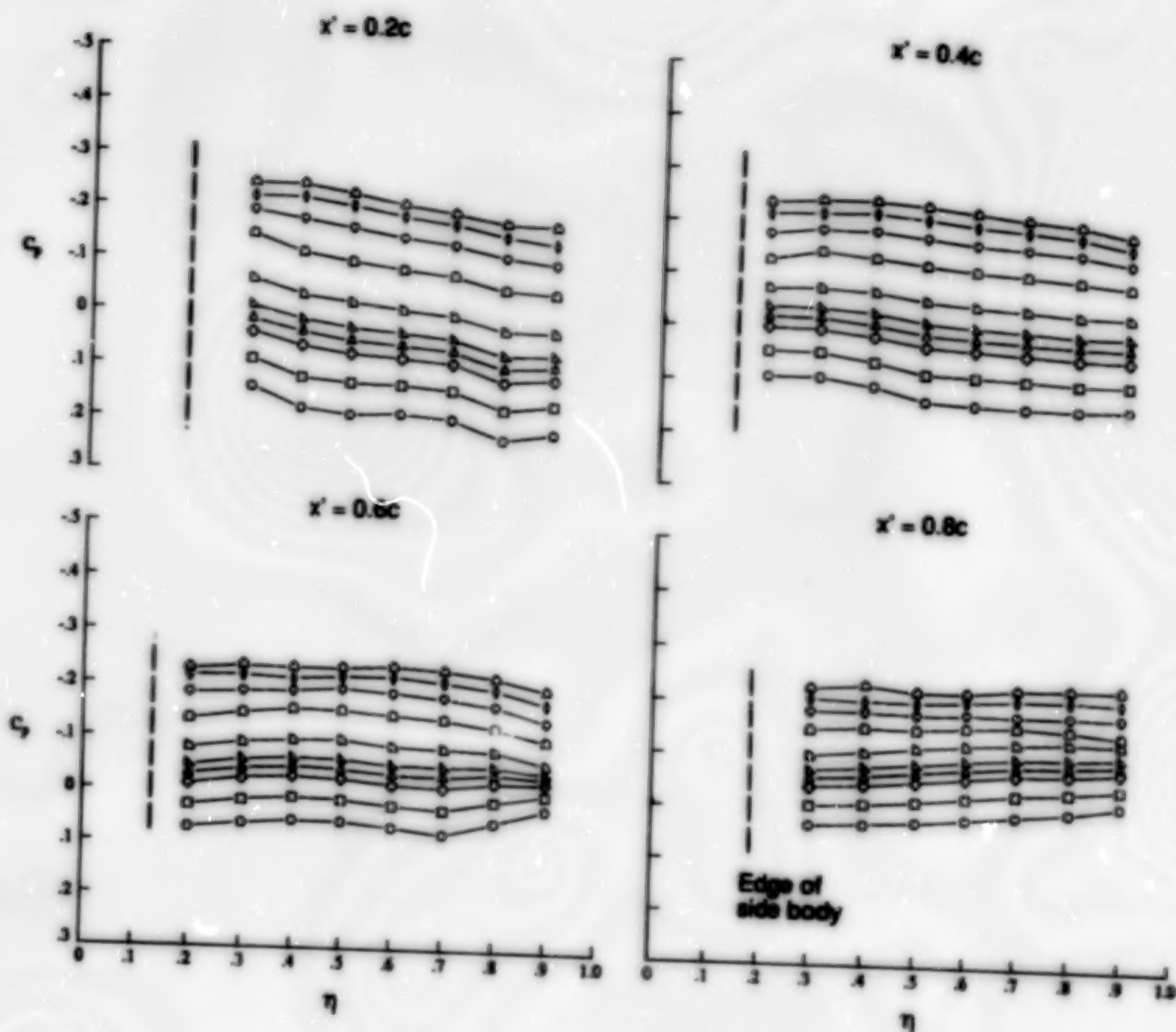
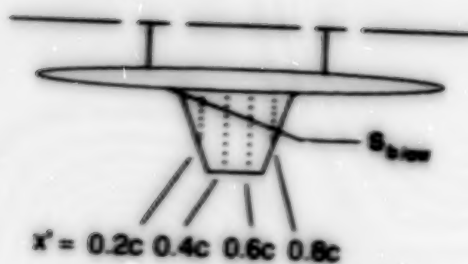
α , deg	
-3.76	○
-1.72	□
0.24	◇
1.25	△
2.27	▽
4.25	◇
8.28	○
12.29	○
16.26	○
20.31	○



(c) $M = 2.00$.

Figure 53. Continued.

α , deg	
0	-4.17
1	-2.18
2	-0.15
3	0.83
4	1.81
5	2.83
6	3.89
7	4.87
8	5.85
9	6.88

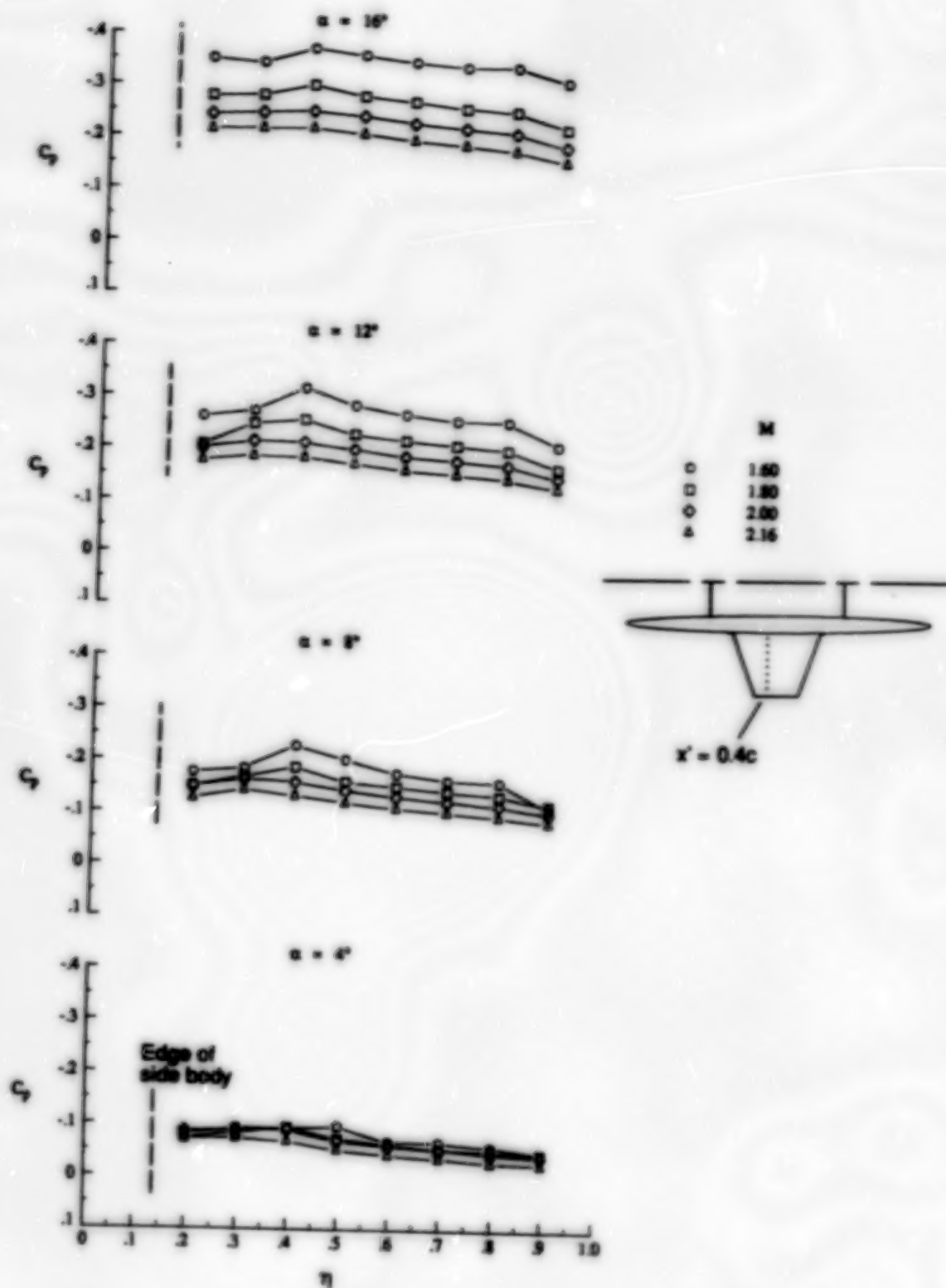


(d) $M = 2.16$.

Figure 53. Concluded.

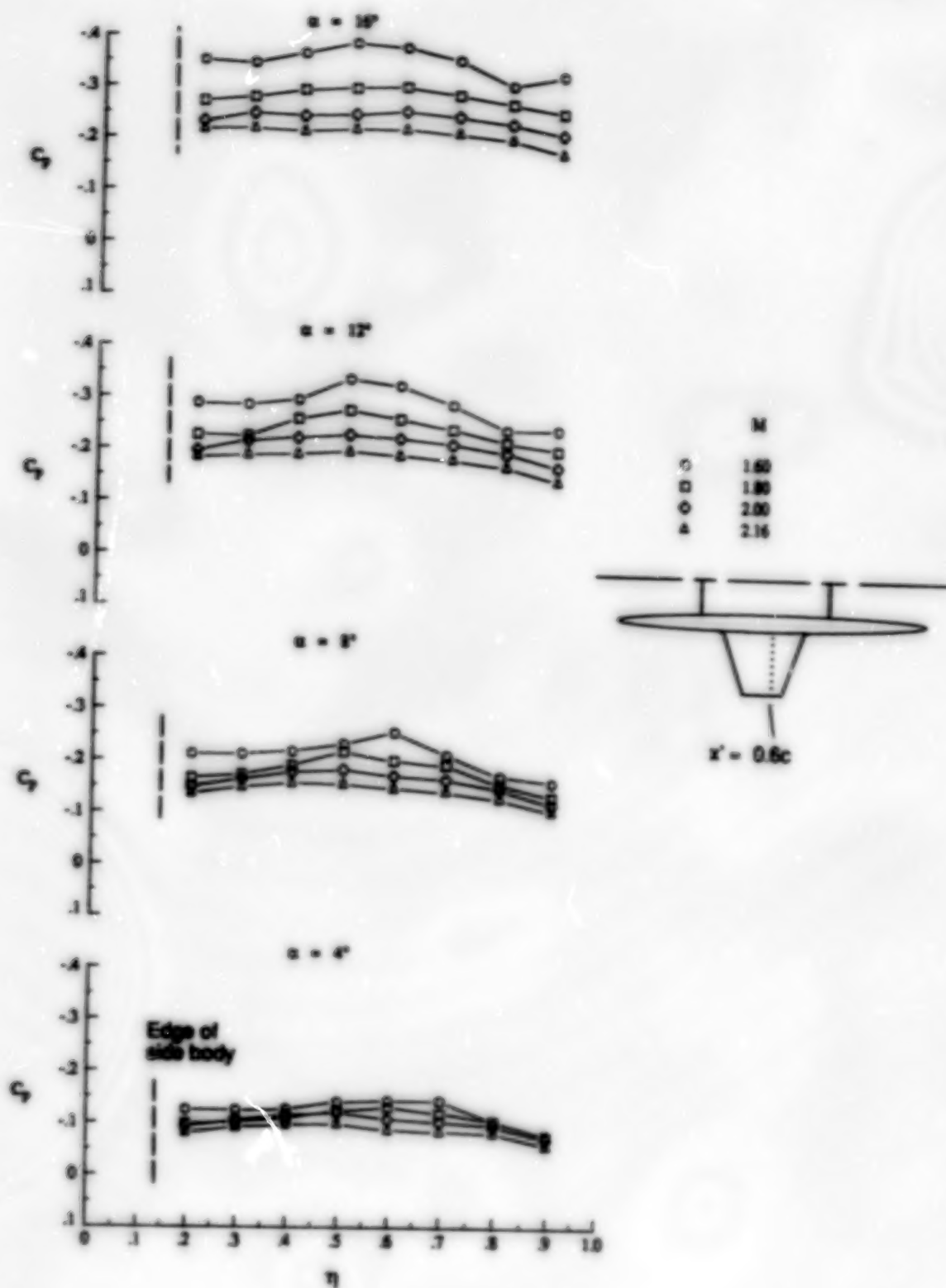


Figure 54. Effect of Mach number on surface pressure coefficient distributions over small-trapezoidal outboard wing of unswept/small-trapezoidal configuration at $x' = 0.2c$, $0.4c$, $0.6c$, and $0.8c$ for $\alpha = 4^\circ$, 8° , 12° , and 16° .



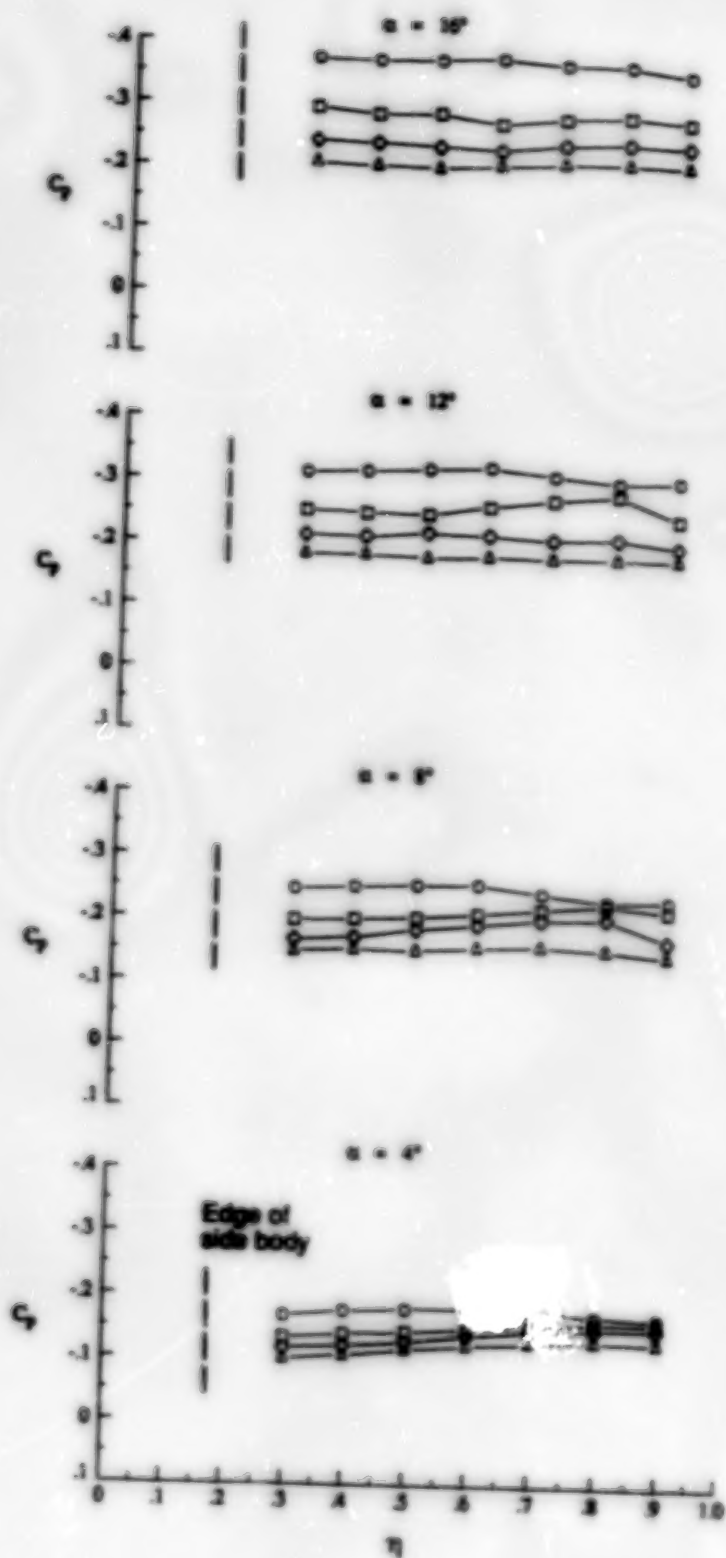
(b) $x' = 0.4c$.

Figure 54. Continued.



(c) $x' = 0.6c$.

Figure 54. Continued.



(d) $x' = 0.8c$.

Figure 54. Concluded.

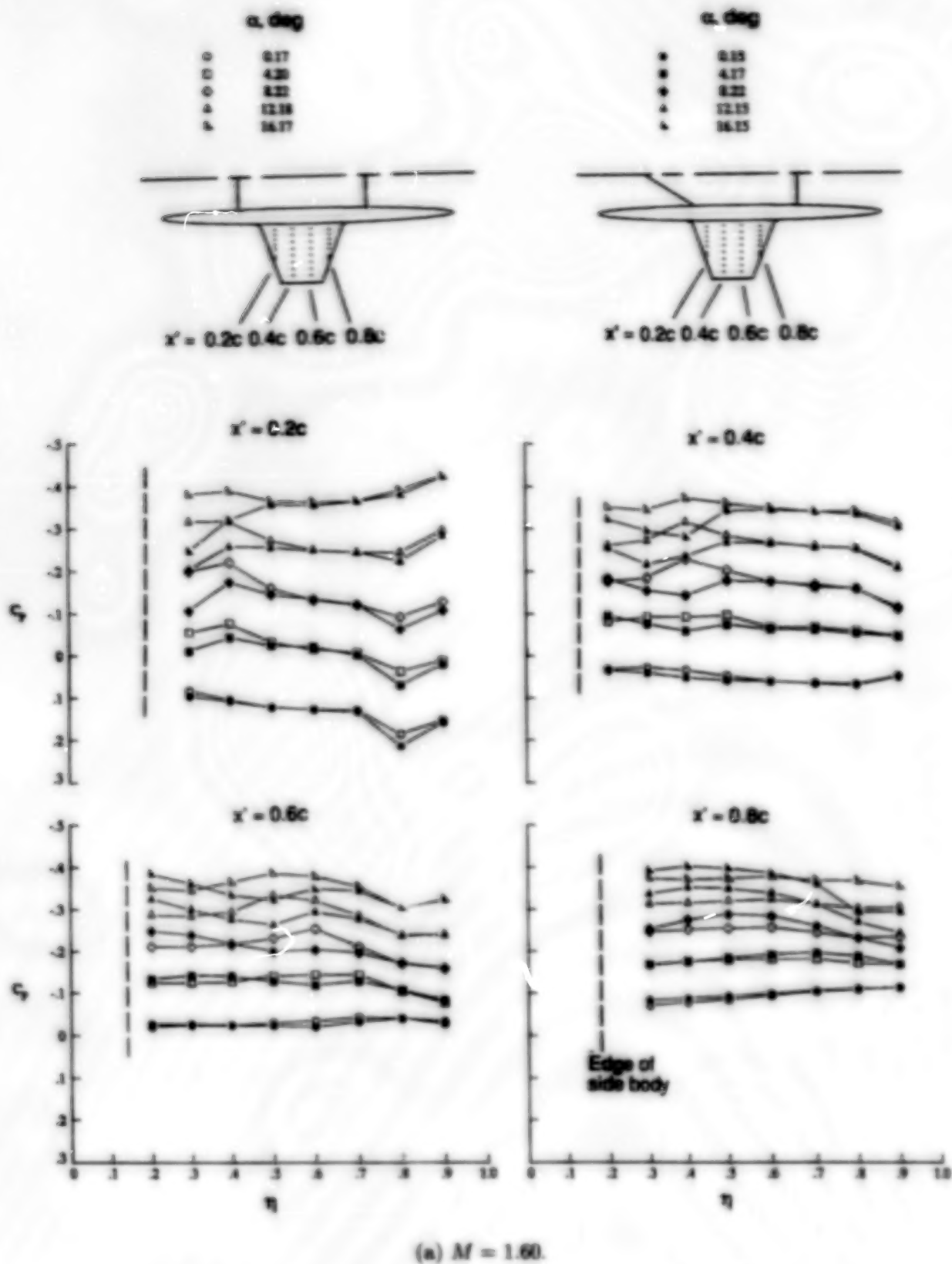
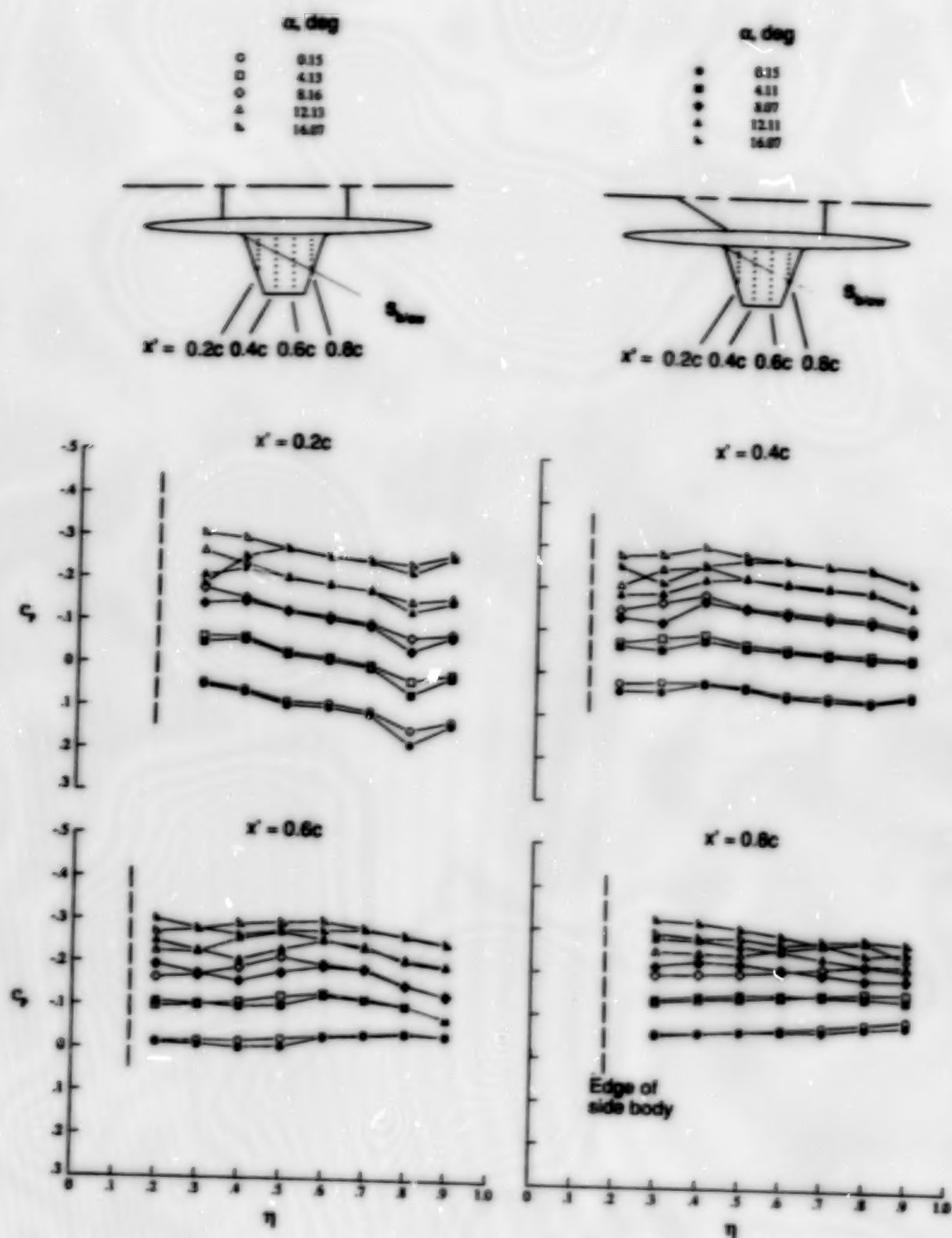
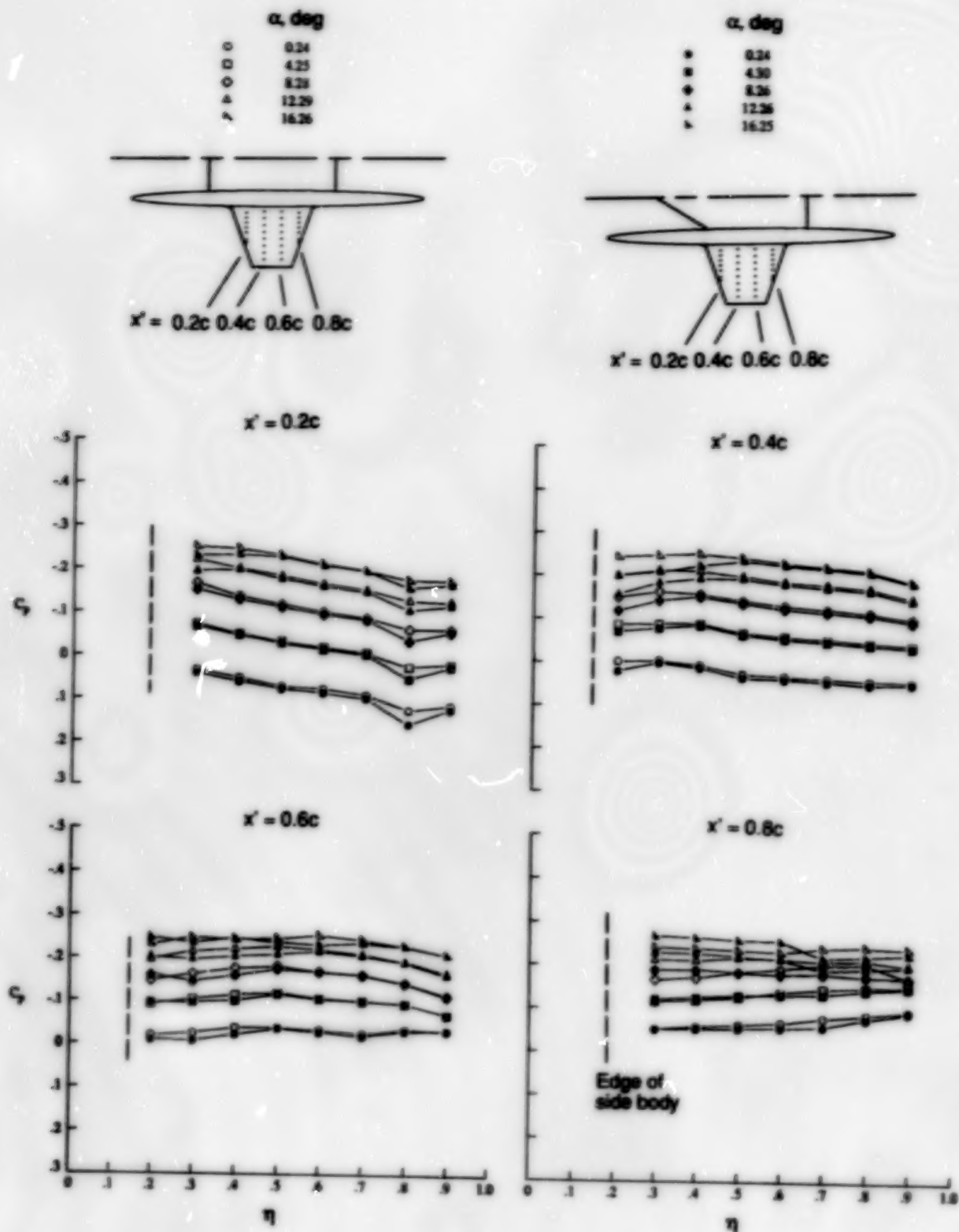


Figure 55. Effect of inboard wing planform shape on surface pressure coefficient distributions over small-trapezoidal outboard wing of unswept/small-trapezoidal configuration at $x' = 0.2c$, $0.4c$, $0.6c$, and $0.8c$ for $M = 1.60$, 1.80 , 2.00 , and 2.16 .



(b) $M = 1.80$.

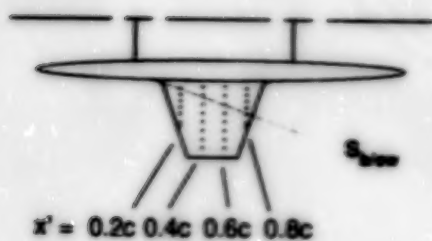
Figure 55. Continued.



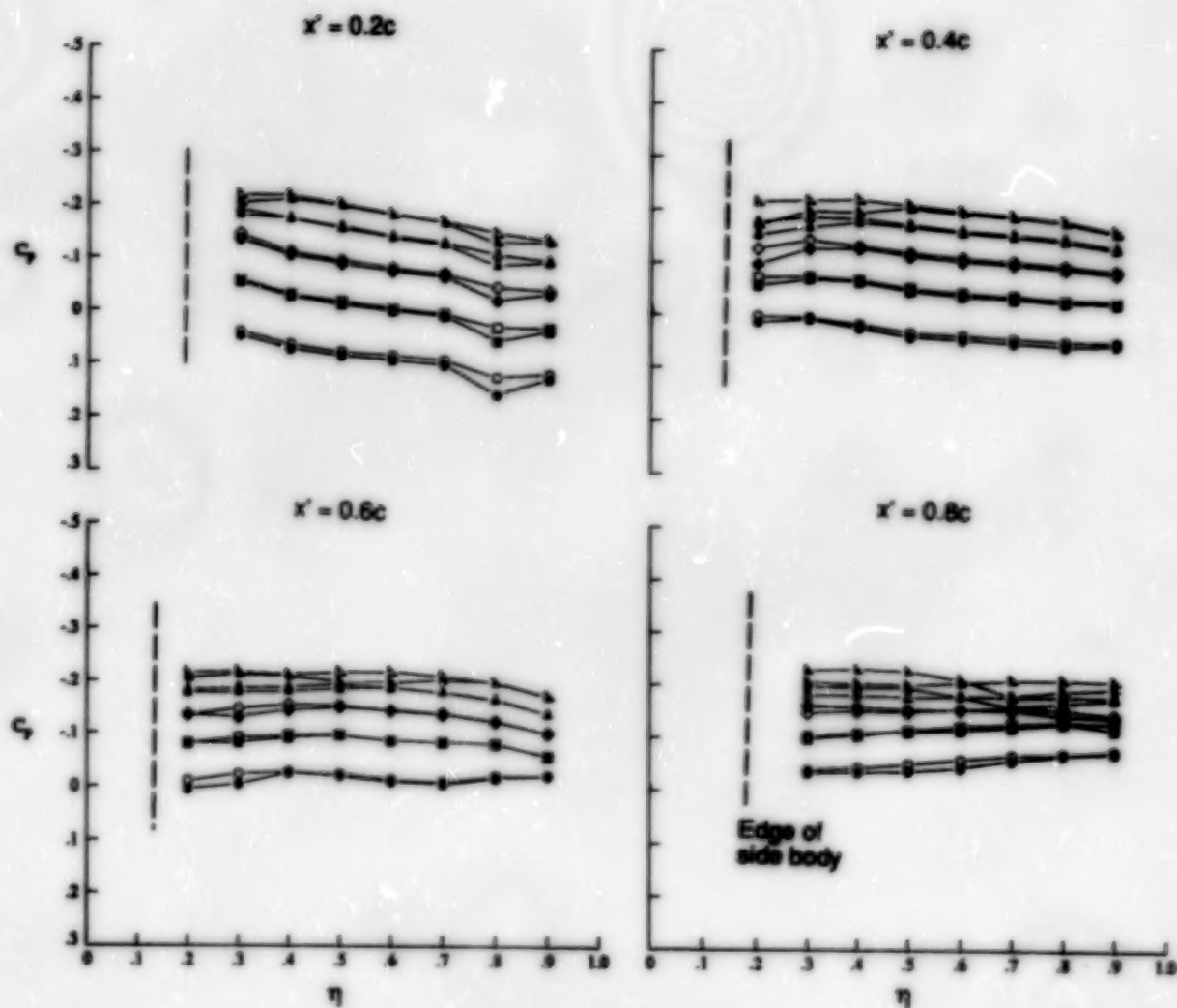
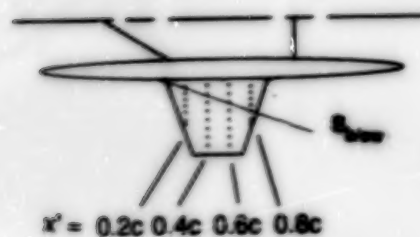
(c) $M = 2.00$.

Figure 55. Continued.

	α , deg
○	-0.15
□	3.83
△	7.89
△	11.87
△	15.85



	α , deg
●	-0.12
■	3.94
●	7.90
△	11.95
△	15.91



(d) $M = 2.16$.

Figure 55. Concluded.

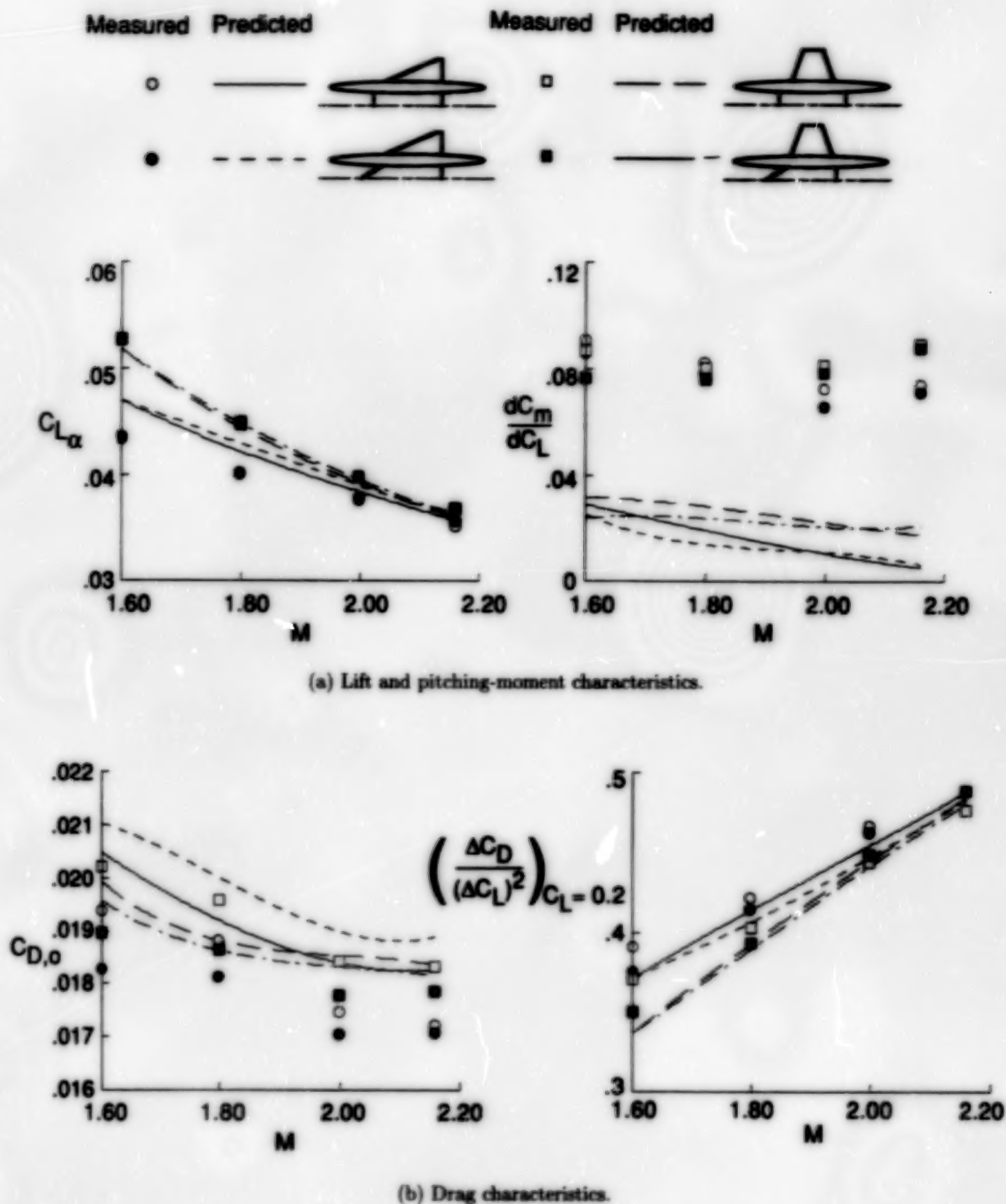
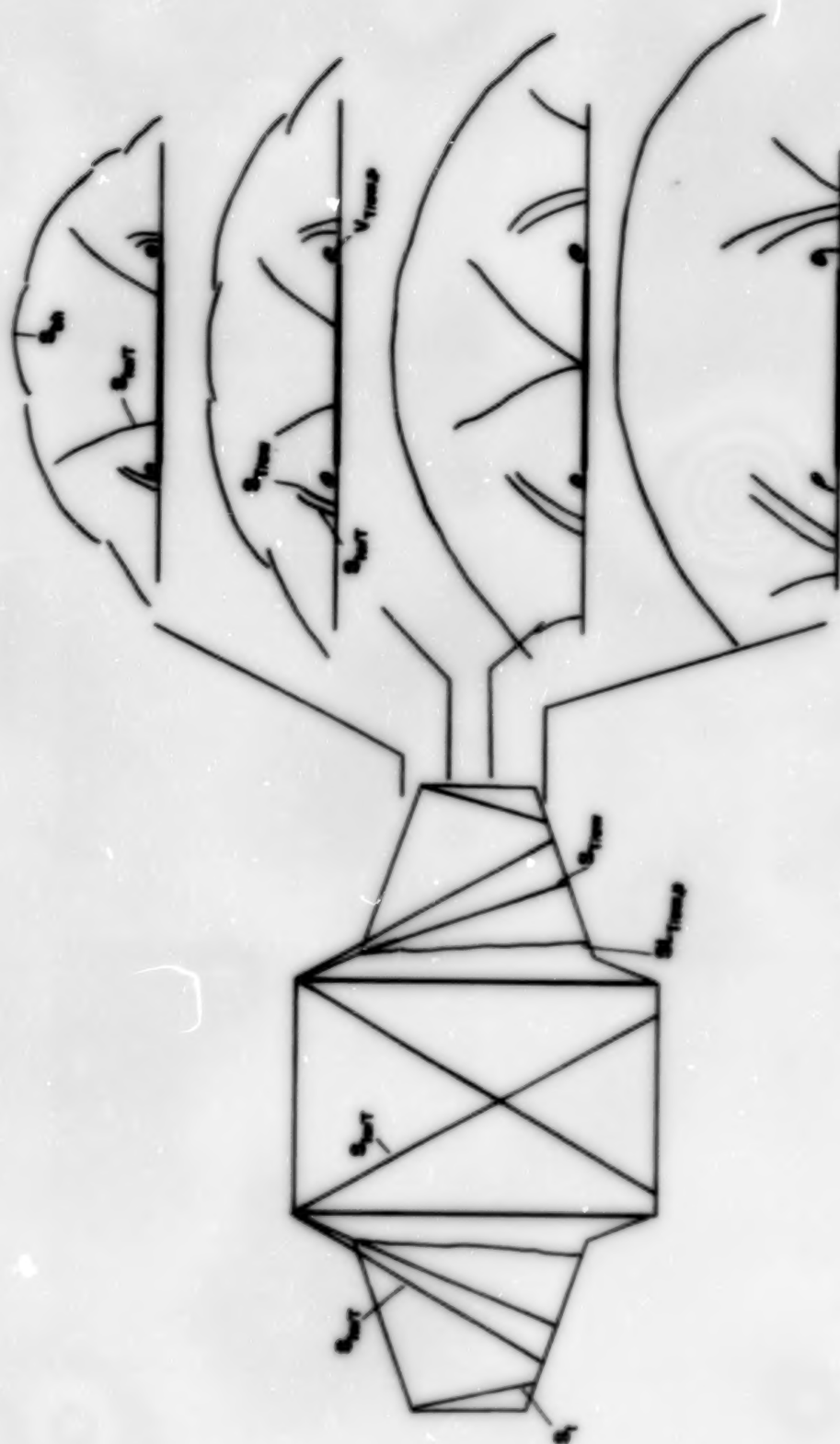


Figure 56. Predicted and measured effects of inboard planform shape and Mach number on longitudinal aerodynamic characteristics for delta and small-trapezoidal outboard multibody configurations.



Top view, $\alpha = 8^\circ$
(See oil-flow photographs in fig 58.)

Spanwise cross-section cuts; $\alpha = 16^\circ$
(See vapor-screen photographs in figs. 59 to 61.)

Figure 57. Flow pattern over the unswept/small-trapezoidal wing-alone configuration for $M = 2.16$.

ORIGINAL PAGE
BLACK AND WHITE PHOTOGRAPH

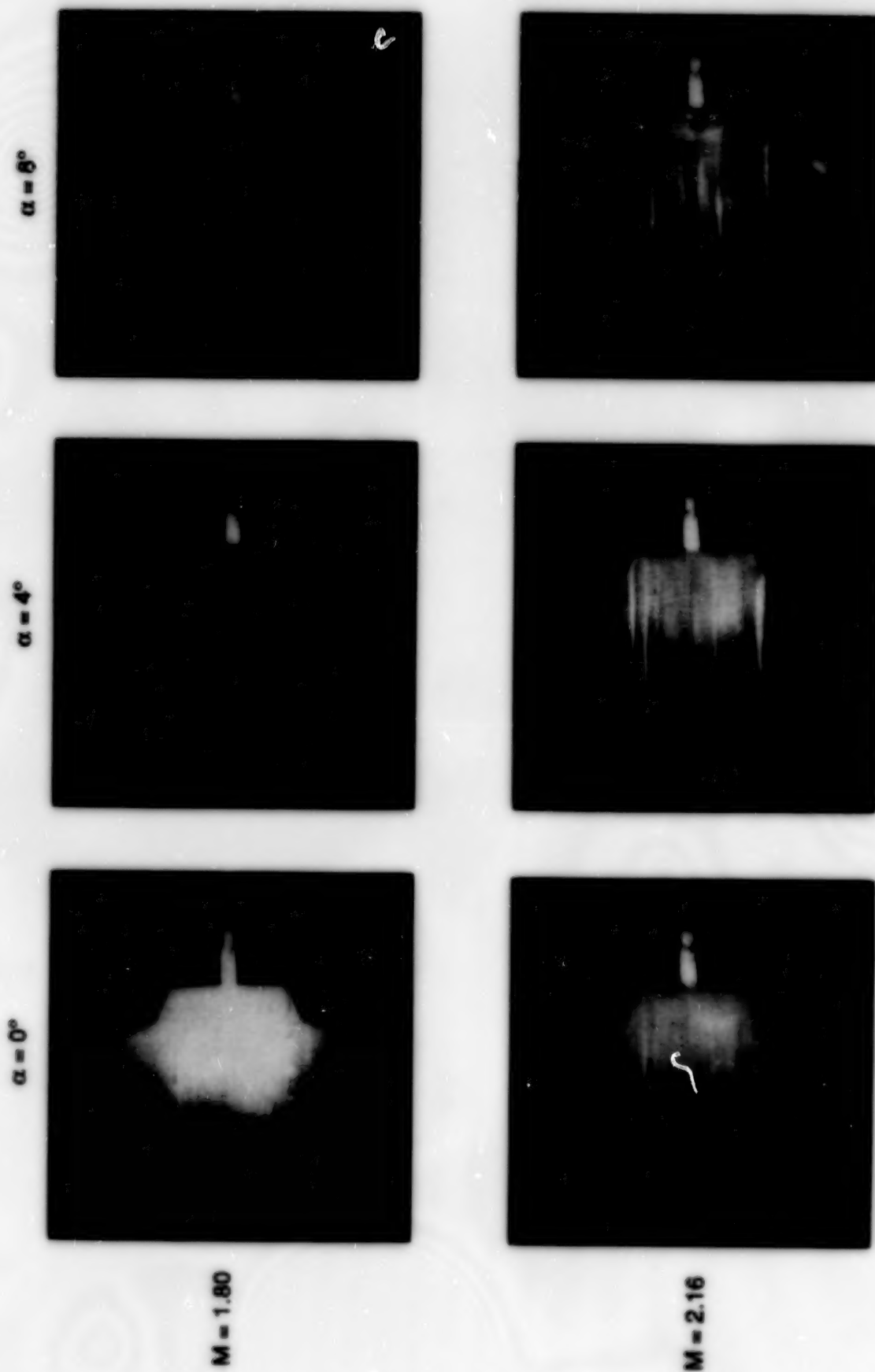
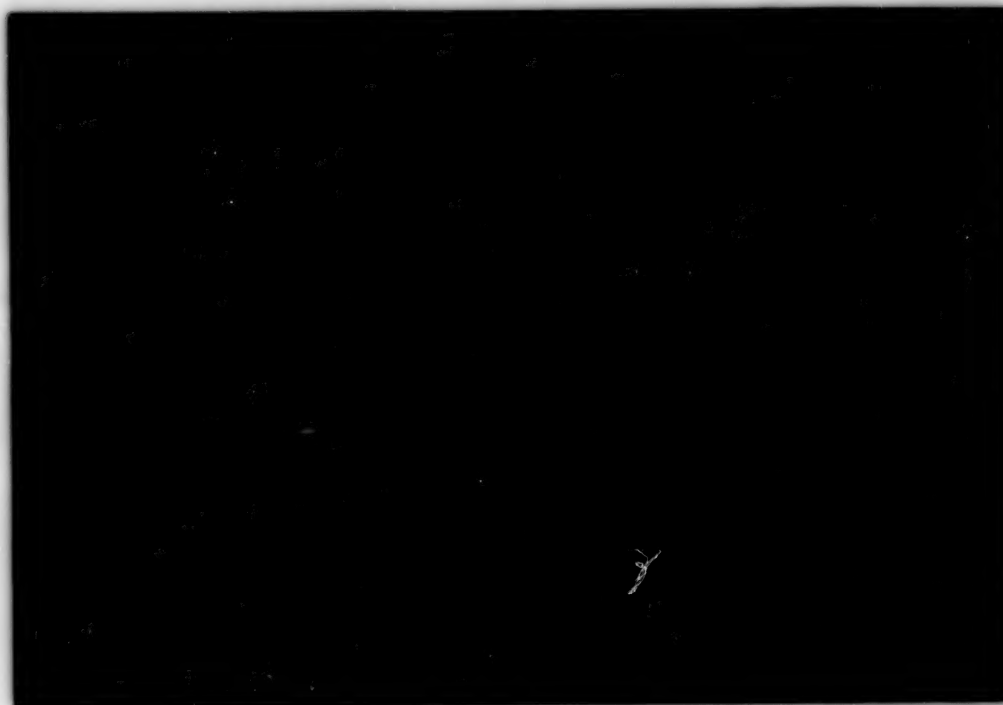


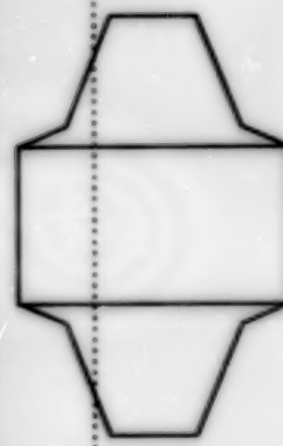
Figure 58. Oil-flow photographs for upper surface of unswept/small-trapezoidal wing-alone configuration at $\alpha = 0^\circ$, 4° , and 8° and $M = 1.80$ and 2.16 .

ORIGINAL PAGE
BLACK AND WHITE PHOTOGRAPH

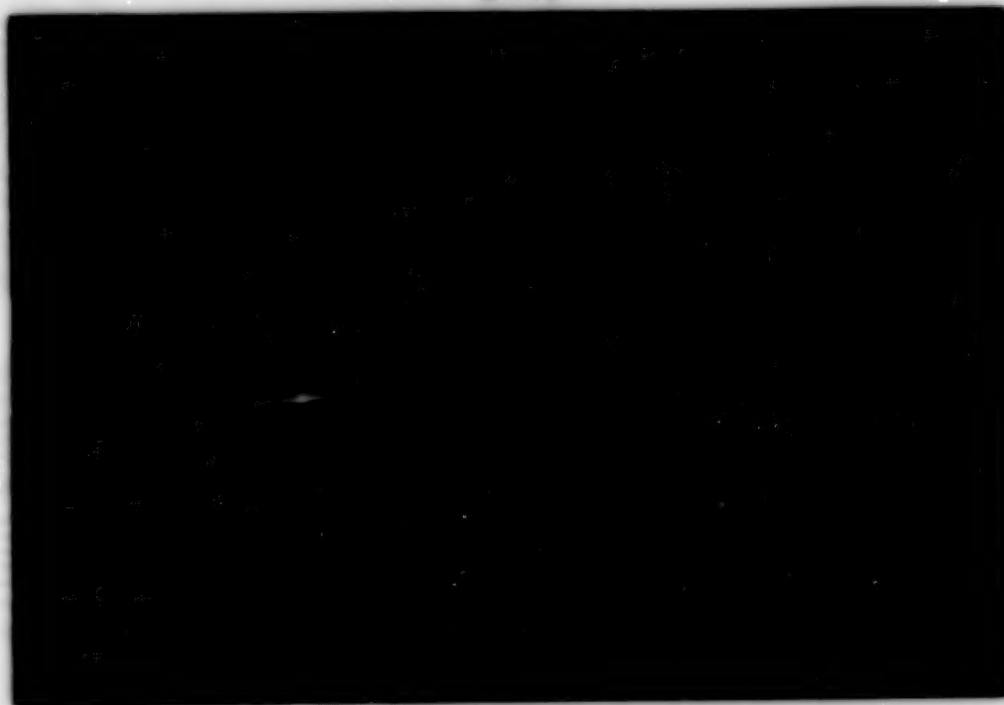
$\alpha = 8^\circ$



$x' = 3.80$ in.



$\alpha = 16^\circ$



(a) $M = 1.60$.

Figure 59. Vapor-screen photographs at $x' = 3.80$ in. for unswept/small-trapezoidal wing-alone configuration for various angles of attack and Mach numbers.

ORIGINAL PAGE
BLACK AND WHITE PHOTOGRAPH

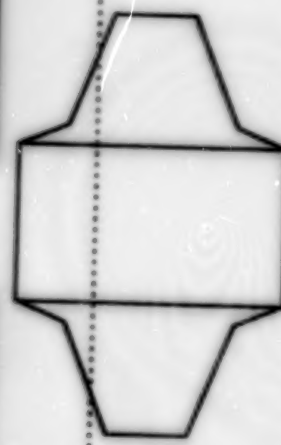
$\alpha = 4^\circ$



$\alpha = 8^\circ$



$x' = 3.80 \text{ in.}$

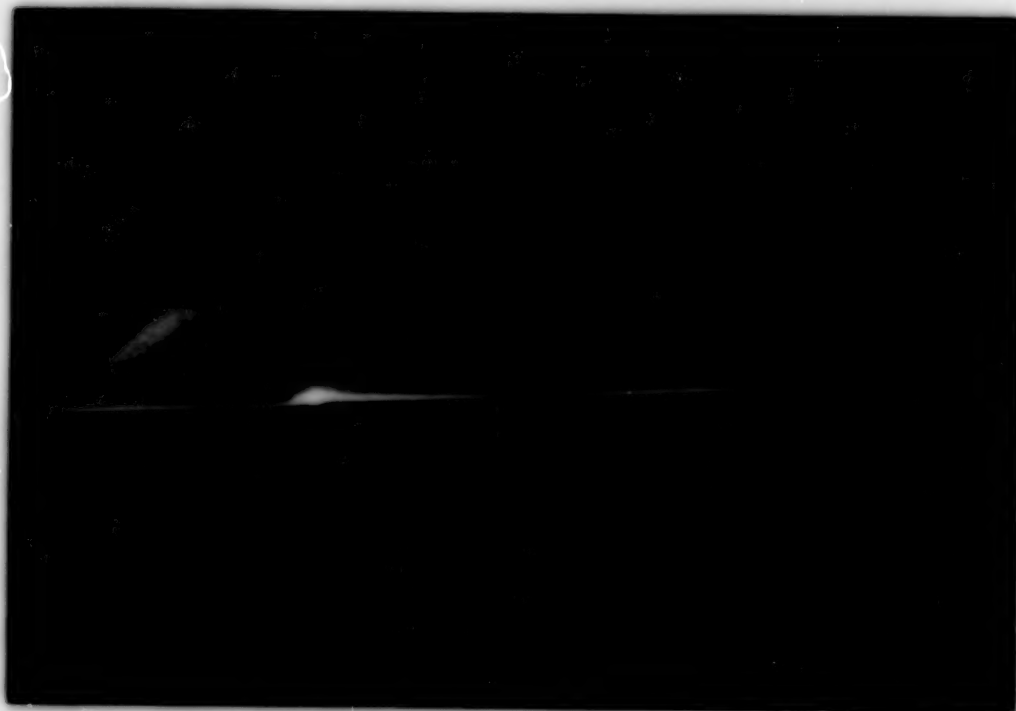


(b) $M = 1.80$.

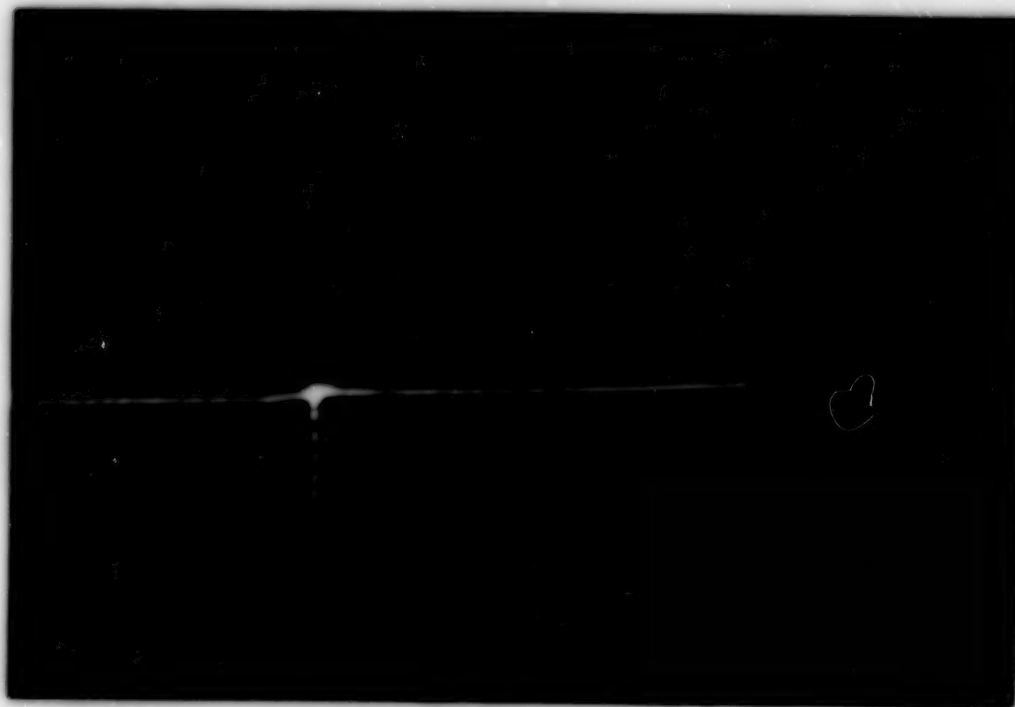
Figure 59. Continued.

ORIGINAL PAGE
BLACK AND WHITE PHOTOGRAPH

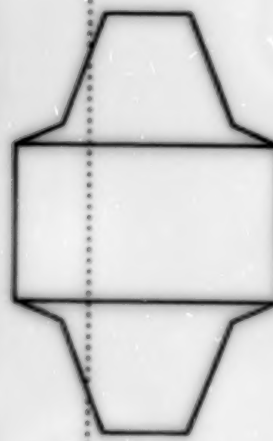
$\alpha = 12^\circ$



$\alpha = 16^\circ$



$x' = 3.80$ in.



(b) Concluded.

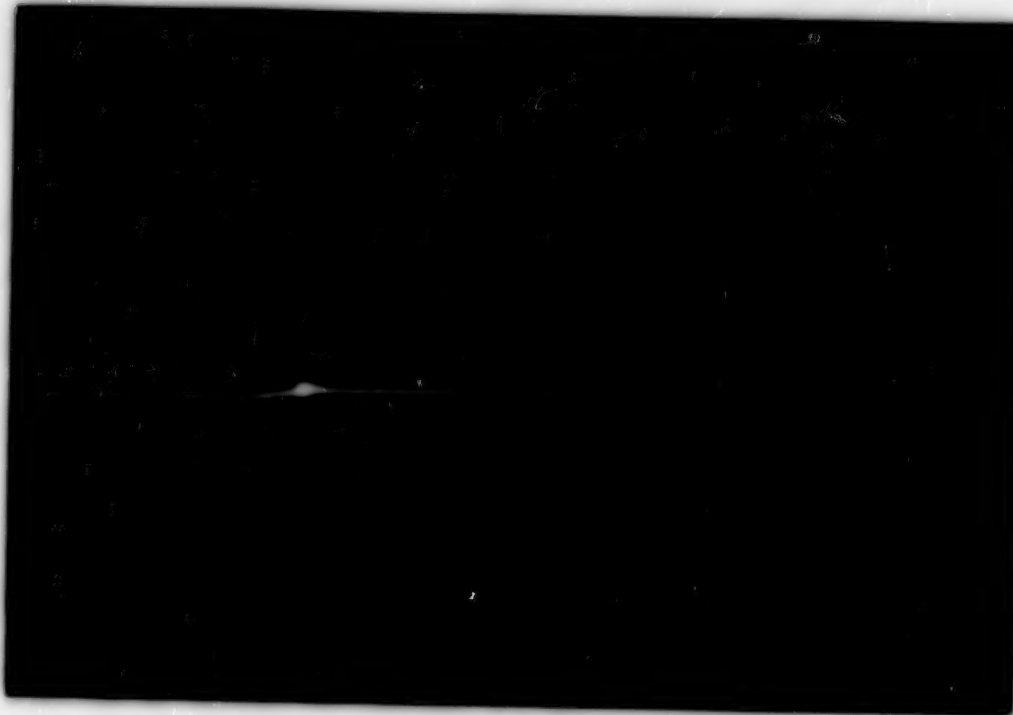
Figure 59. Continued.

ORIGINAL PAGE
BLACK AND WHITE PHOTOGRAPH

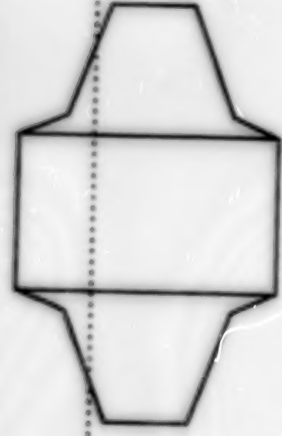
$\alpha = 8^\circ$



$\alpha = 16^\circ$



$x' = 3.80 \text{ in.}$



(c) $M = 2.00$.

Figure 59. Continued.

ORIGINAL PAGE
BLACK AND WHITE PHOTOGRAPH

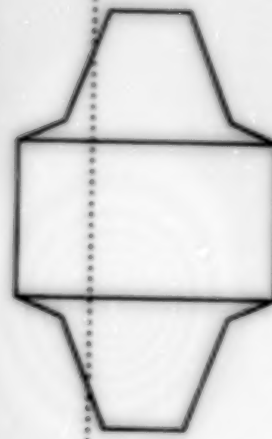
$$\alpha = 4^\circ$$



$$\alpha = 8^\circ$$



$$x' = 3.80 \text{ in.}$$



(d) $M = 2.16$.

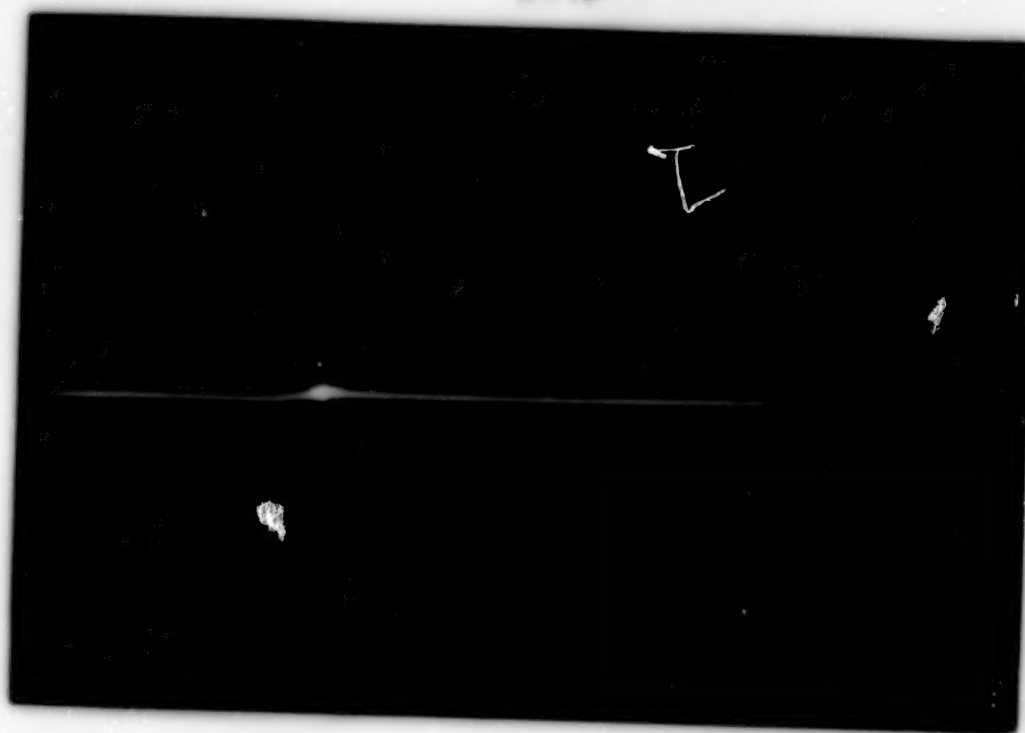
Figure 59. Continued.

ORIGINAL PAGE
BLACK AND WHITE PHOTOGRAPH

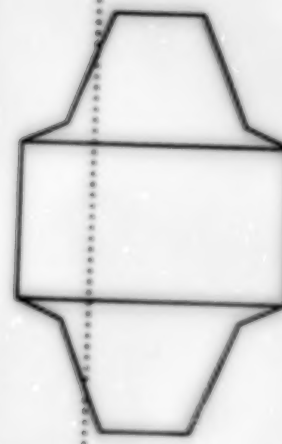
$\alpha = 12^\circ$



$\alpha = 16^\circ$



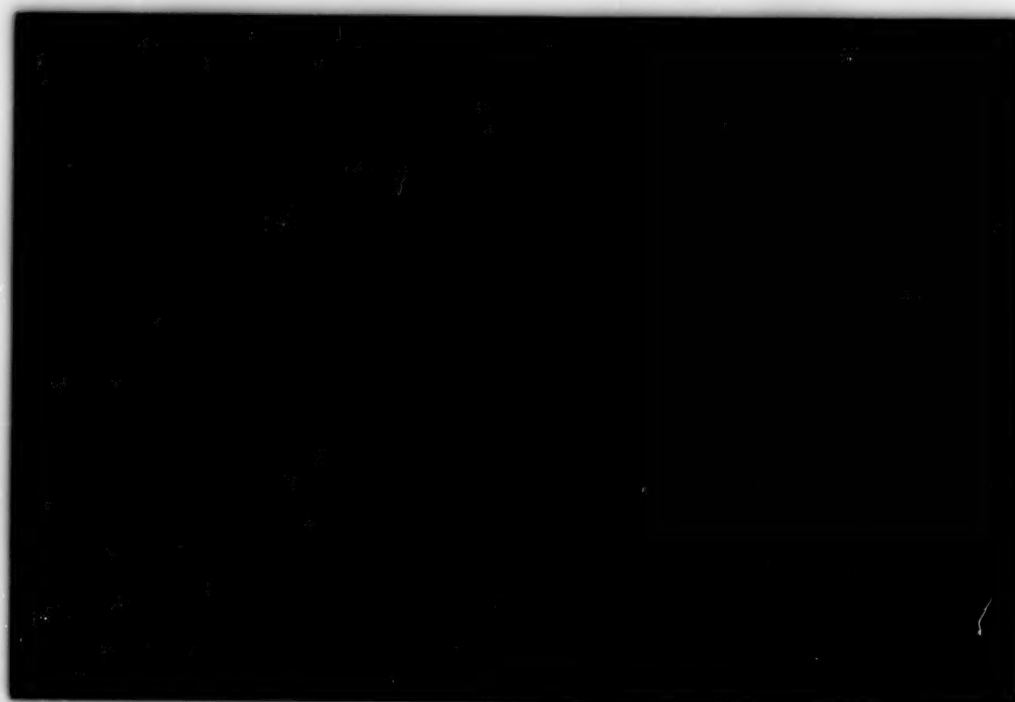
$x' = 3.80 \text{ in.}$



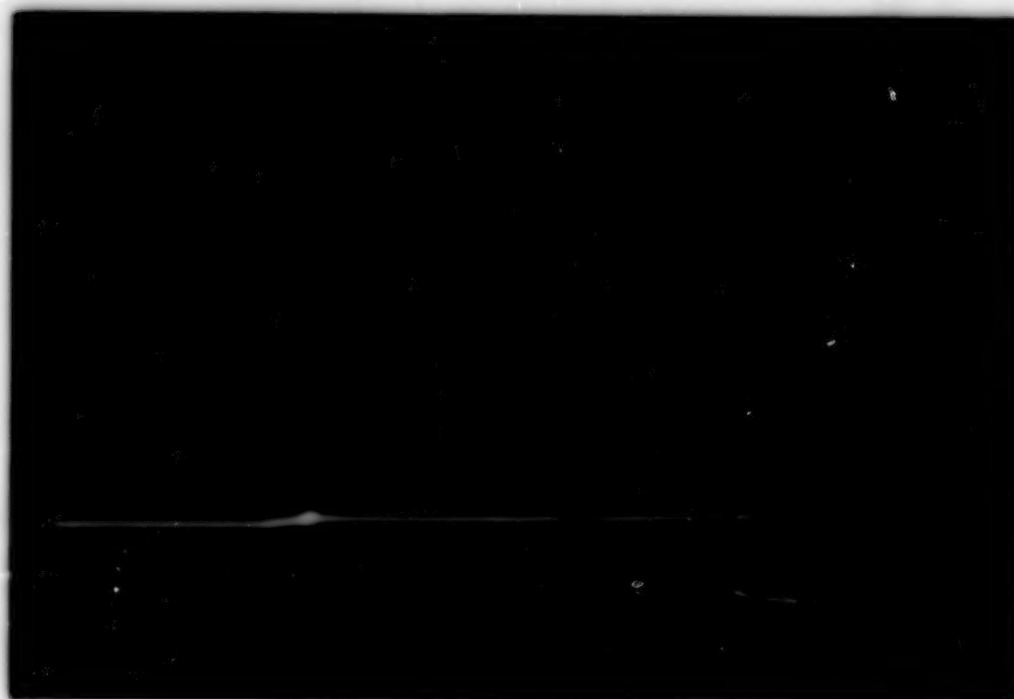
(d) Concluded.

Figure 59. Concluded.

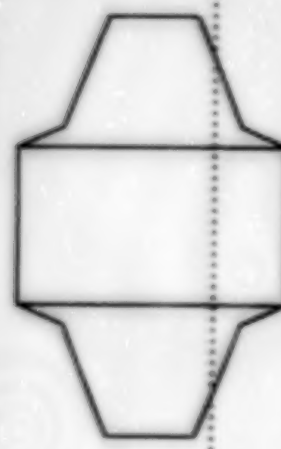
$\alpha = 8^\circ$



$\alpha = 16^\circ$



$x' = 9.20$ in.

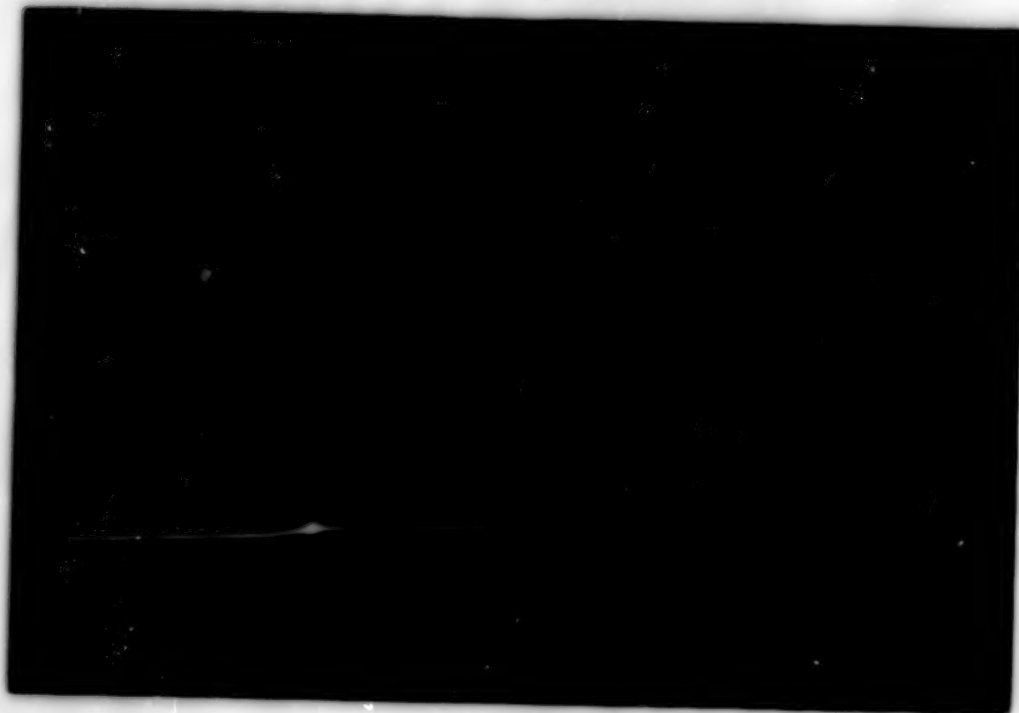


(a) $M = 1.60$.

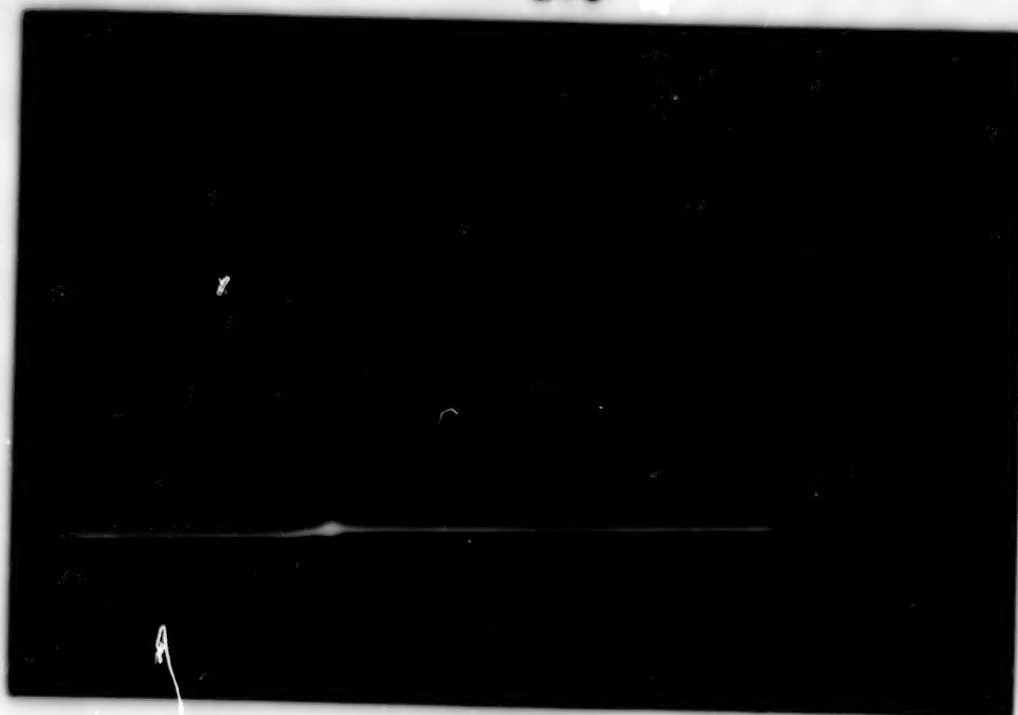
Figure 60. Vapor-screen photographs at $x' = 9.20$ in. for unswept/small-trapezoidal wing-alone configuration for various angles of attack and Mach numbers.

ORIGINAL PAGE
BLACK AND WHITE PHOTOGRAPH

$\alpha = 4^\circ$



$\alpha = 5^\circ$



$x' = 9.20 \text{ in.}$

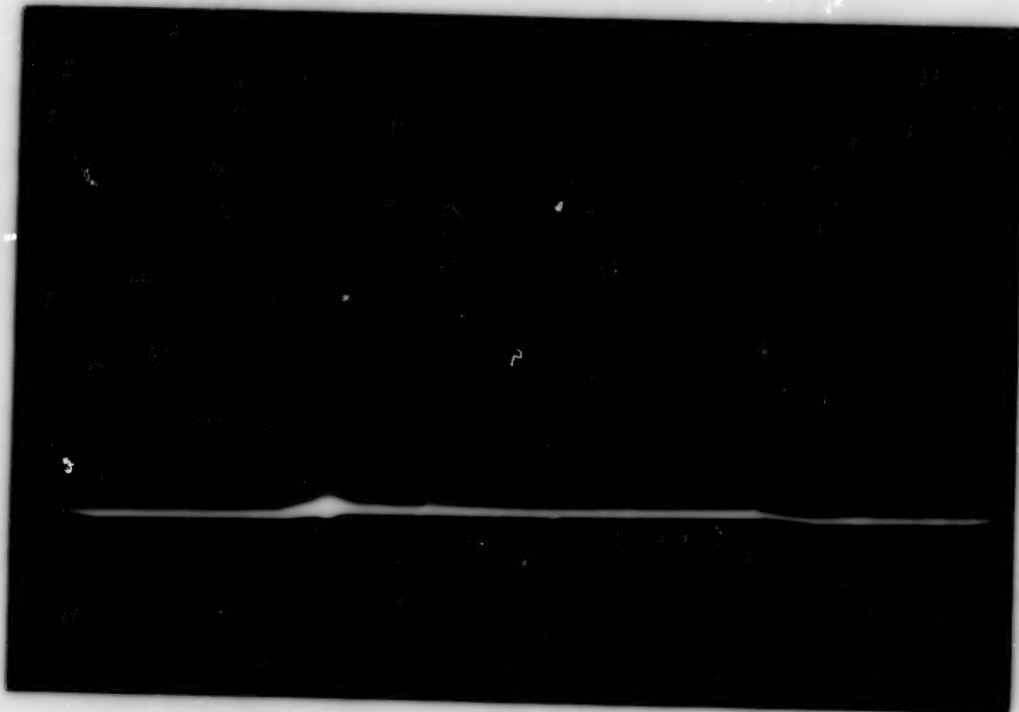


(b) $M = 1.80$.

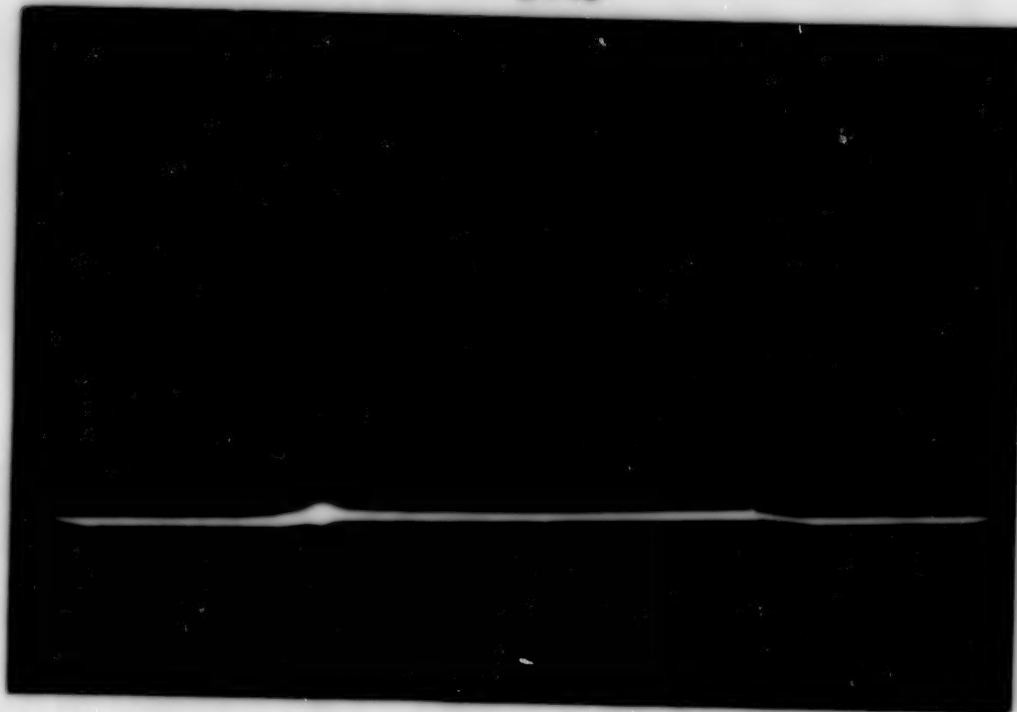
Figure 60. Continued.

ORIGINAL PAGE
BLACK AND WHITE PHOTOGRAPH

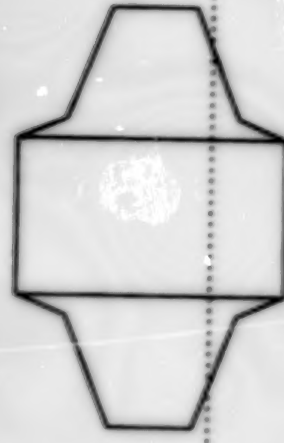
$\alpha = 12^\circ$



$\alpha = 16^\circ$



$x' = 9.20 \text{ in.}$



(b) Concluded.

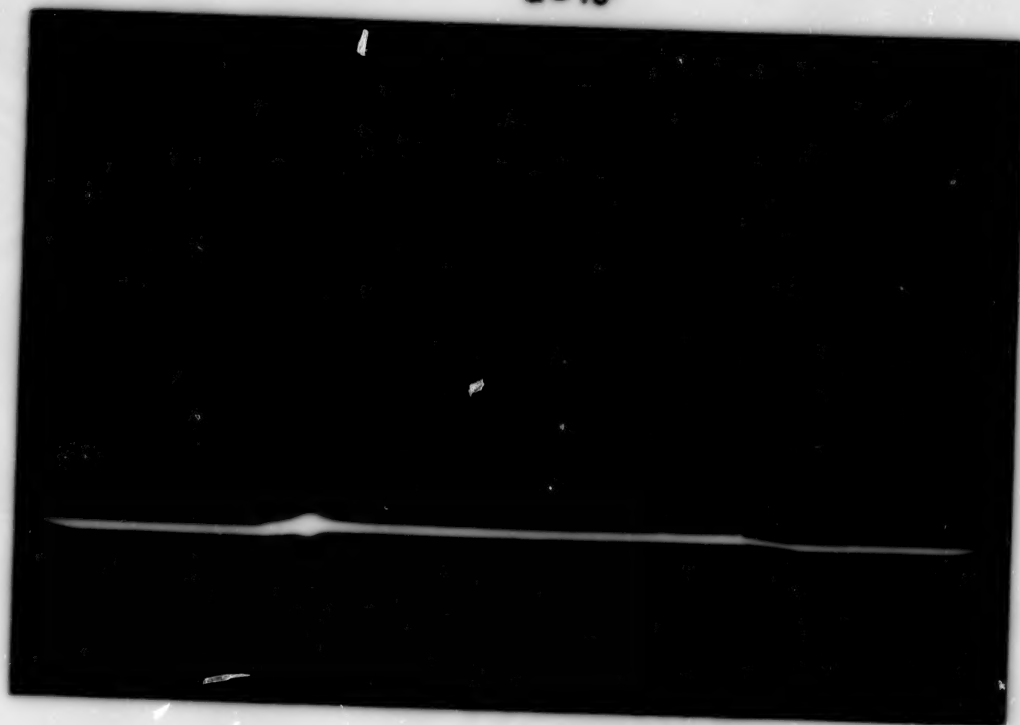
Figure 60. Continued.

ORIGINAL F-35
BLACK AND WHITE PHOTOGRAPH

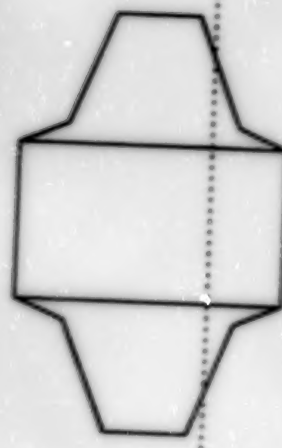
$\alpha = 8^\circ$



$\alpha = 16^\circ$



$x' = 9.20 \text{ in.}$

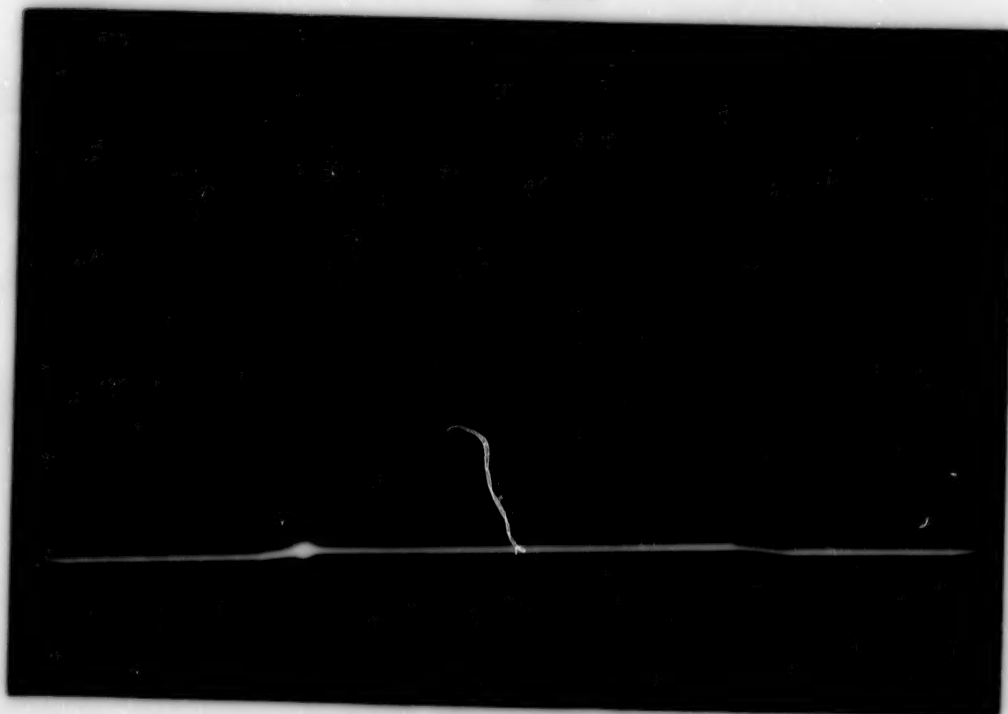


(c) $M = 2.00$.

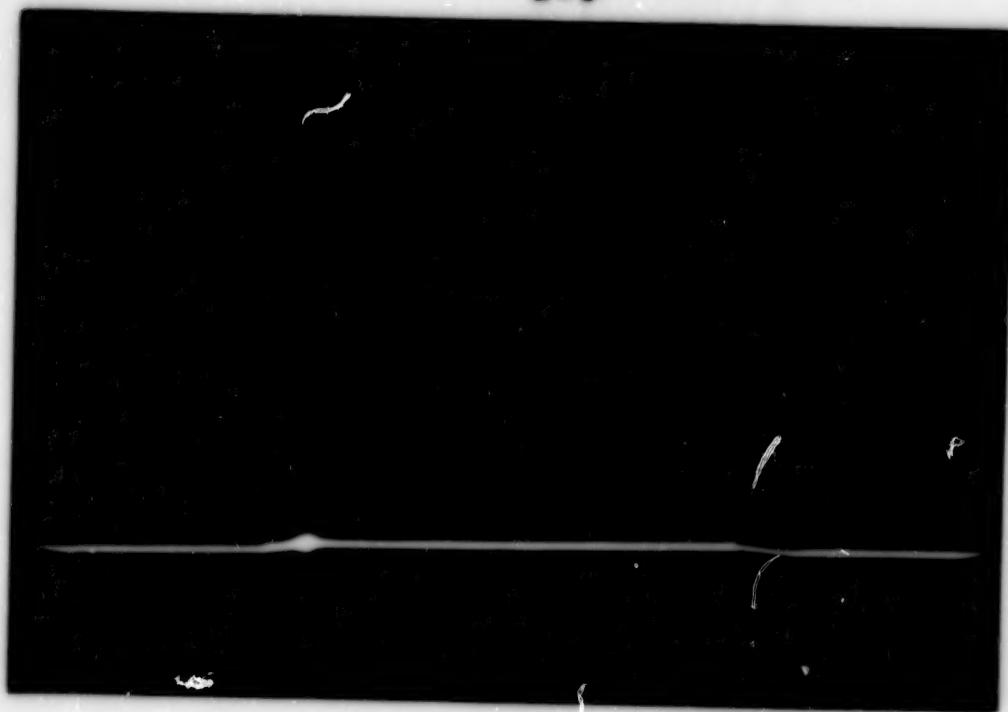
Figure 60. Continued.

ORIGINAL PAGE
BLACK AND WHITE PHOTOGRAPH

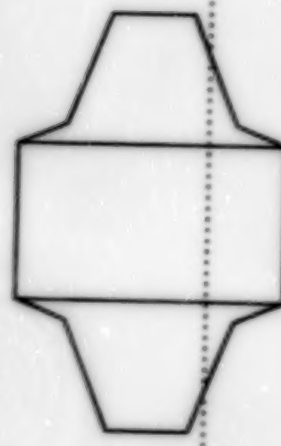
$\alpha = 4^\circ$



$\alpha = 8^\circ$



$x' = 9.20$ in.

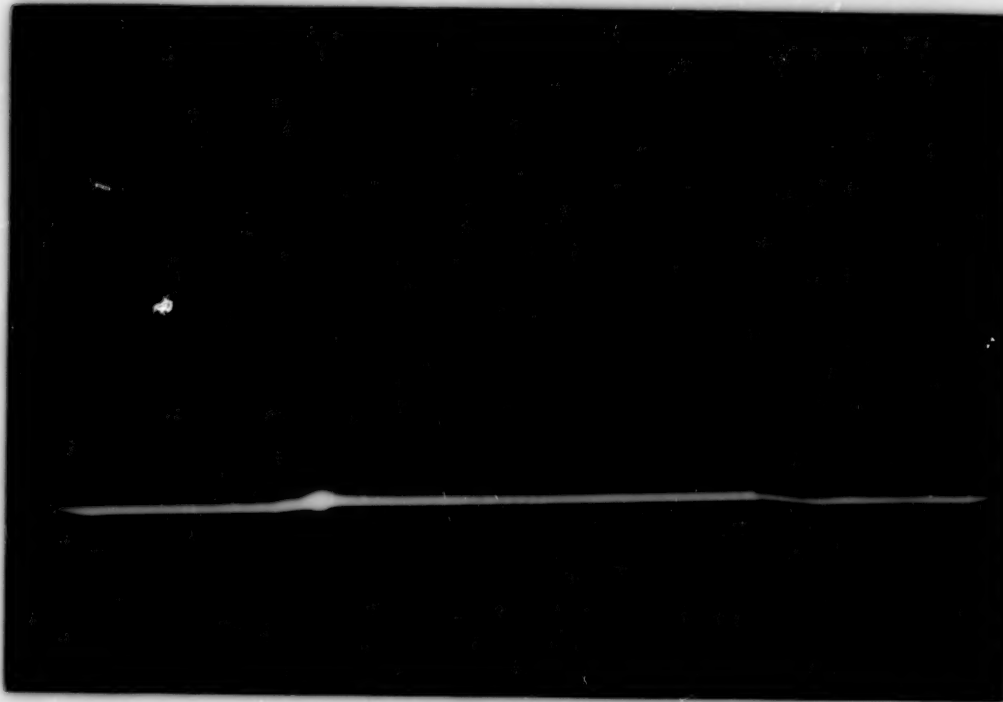


(d) $M = 2.16$.

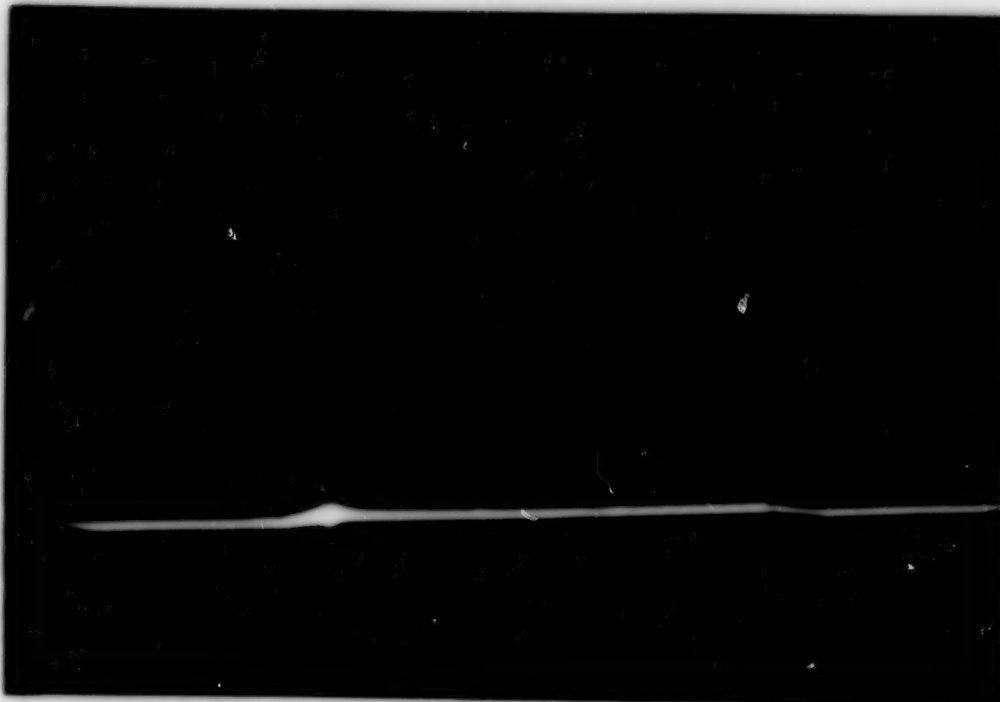
Figure 60. Continued.

ORIGINAL PAGE
BLACK AND WHITE PHOTOGRAPH

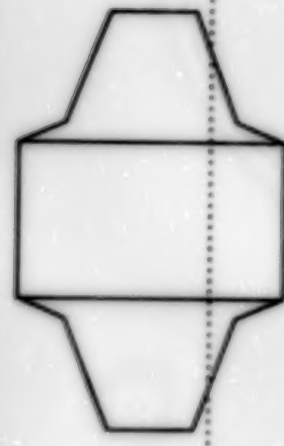
$\alpha = 12^\circ$



$\alpha = 16^\circ$



$x' = 9.20 \text{ in.}$

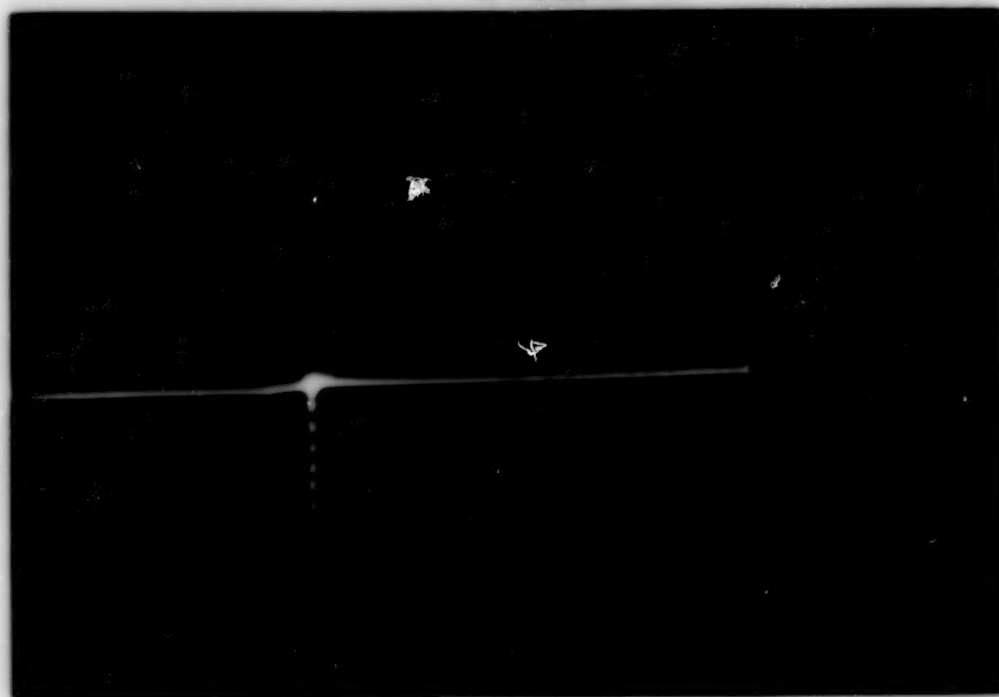


(d) Concluded.

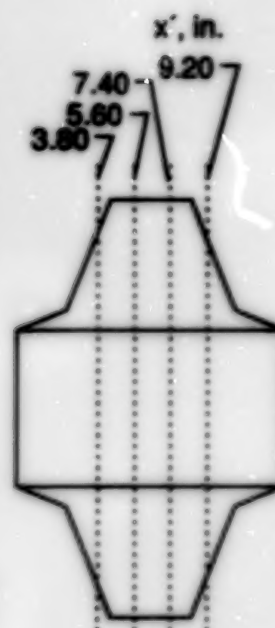
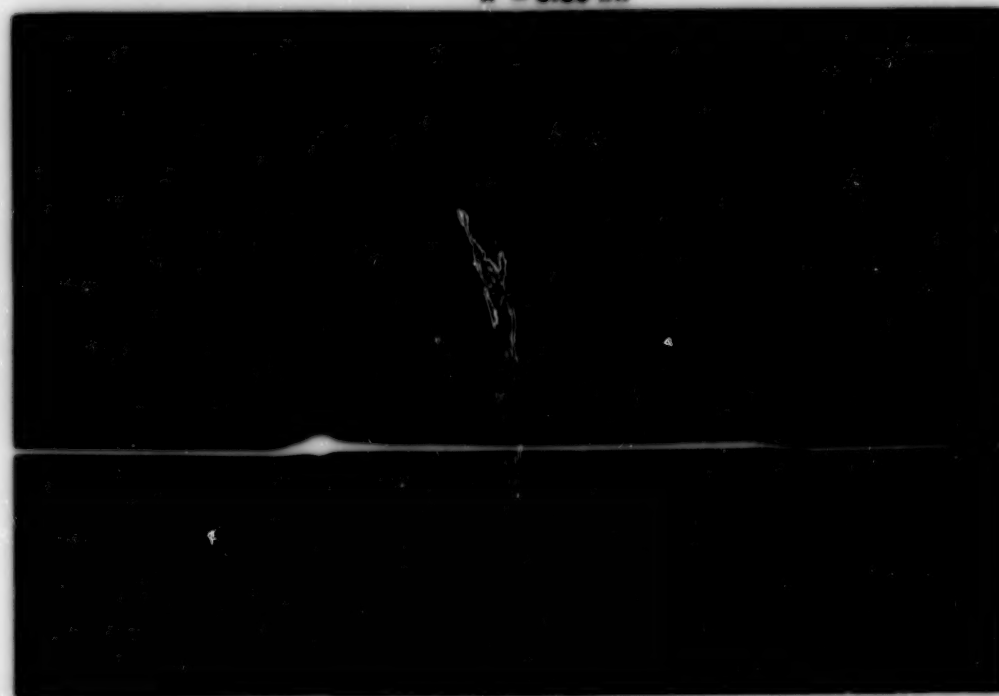
Figure 60. Concluded.

ORIGINAL PAGE
BLACK AND WHITE PHOTOGRAPH

$x' = 3.20$ in.



$x' = 5.60$ in.

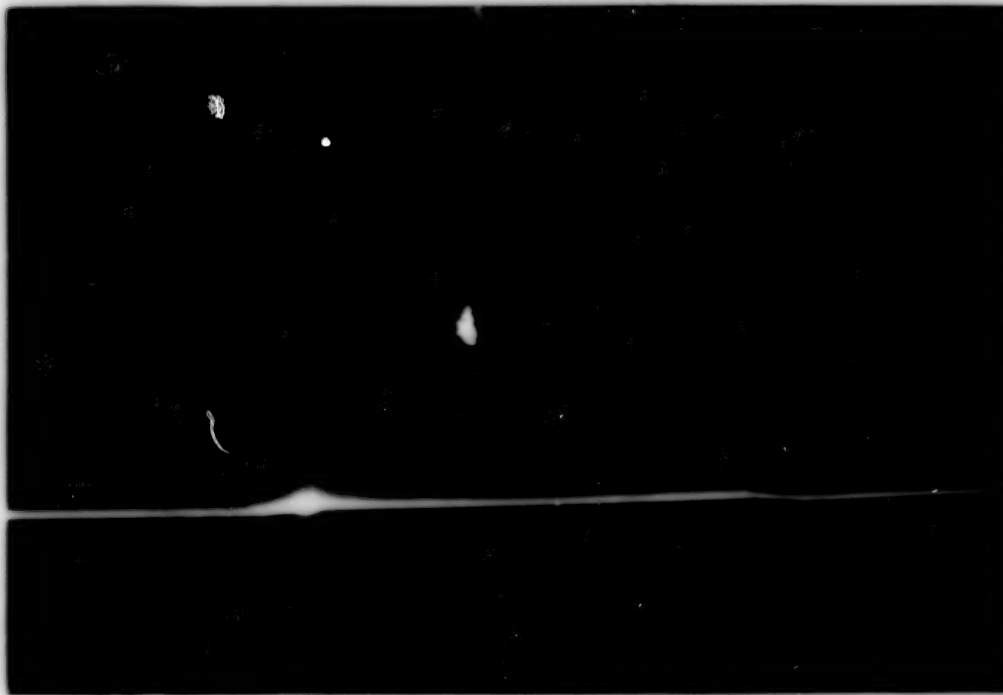


(a) $M = 1.80$.

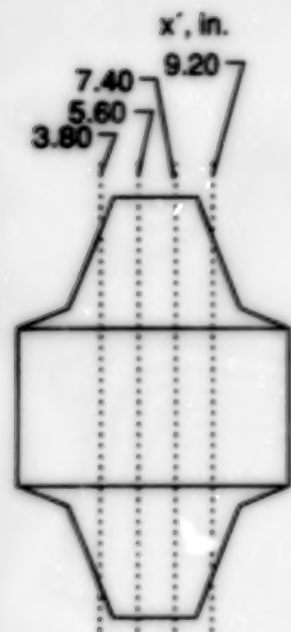
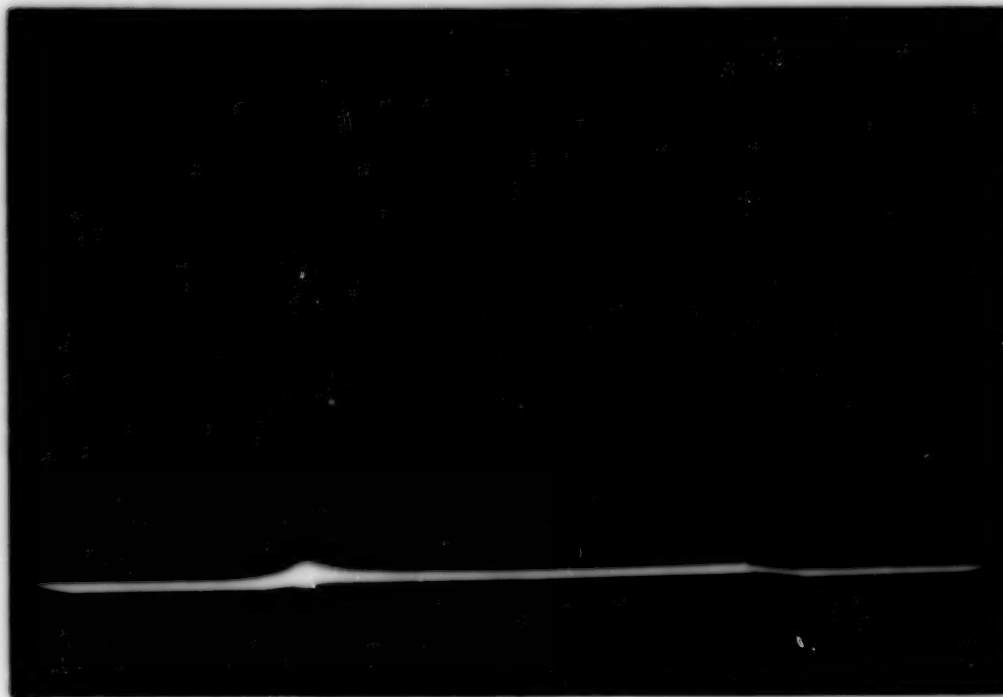
Figure 61. Vapor-screen photographs for unswept/small-trapezoidal wing-alone configuration at four longitudinal locations for $\alpha = 16^\circ$ and $M = 1.80$ and 2.16.

ORIGINAL PAGE
BLACK AND WHITE PHOTOGRAPH

$x' = 7.40$ in.



$x' = 9.20$ in.

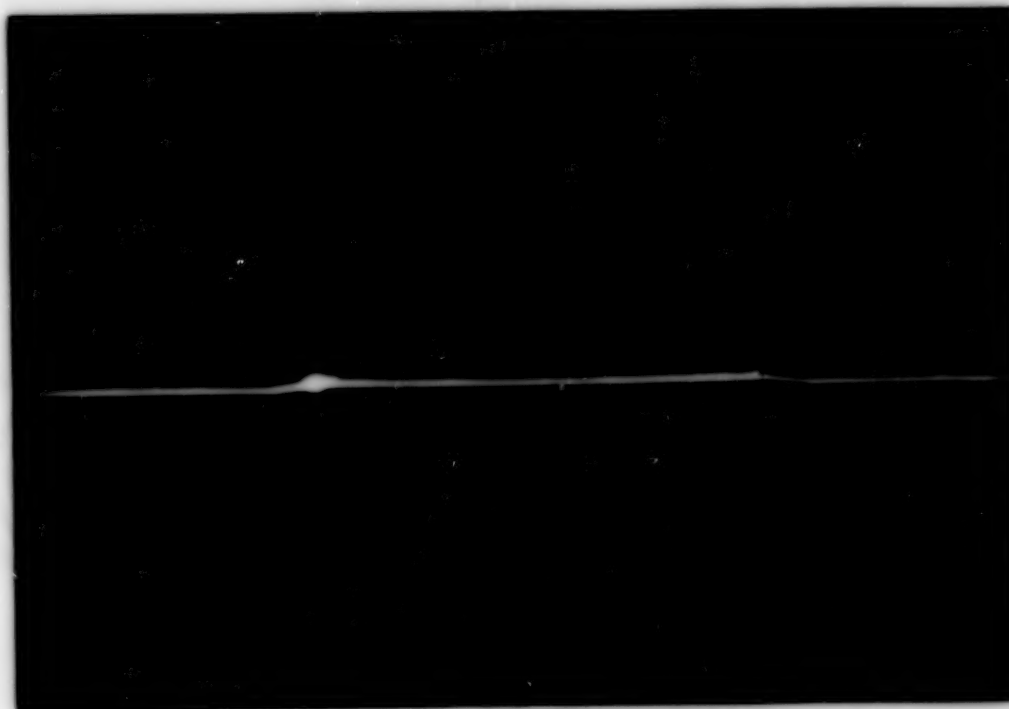


(a) Concluded.

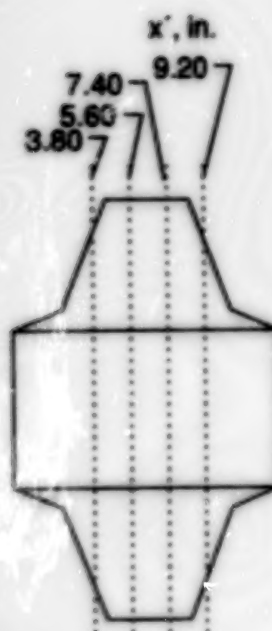
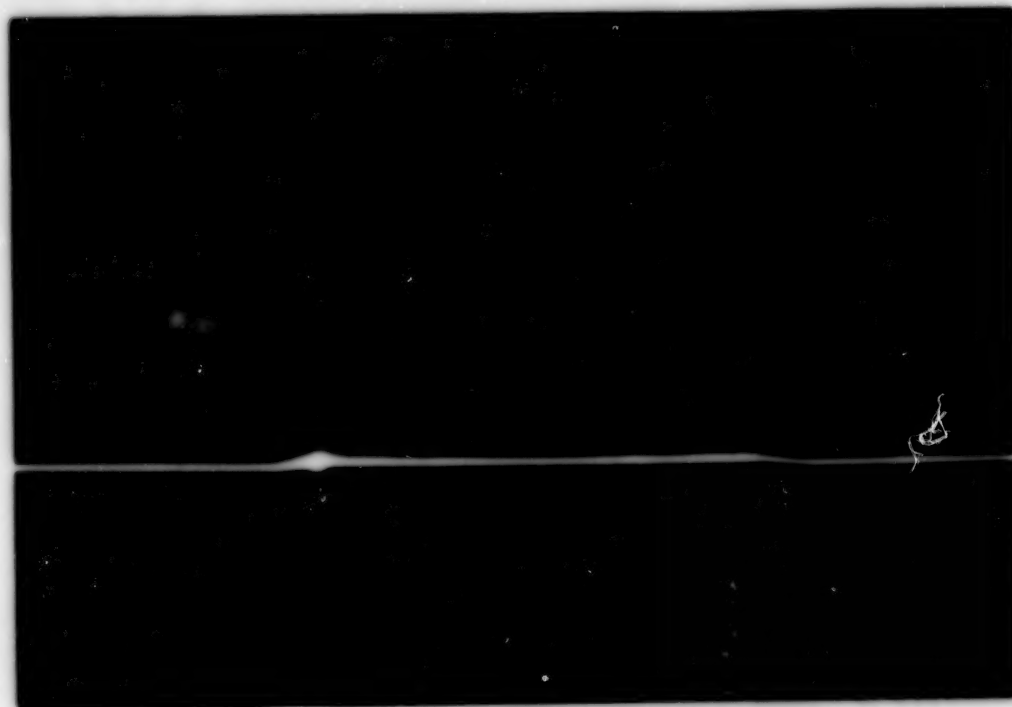
Figure 61. Continued.

ORIGINAL PAGE
BLACK AND WHITE PHOTOGRAPH

$x' = 3.20$ in.



$x' = 5.60$ in.

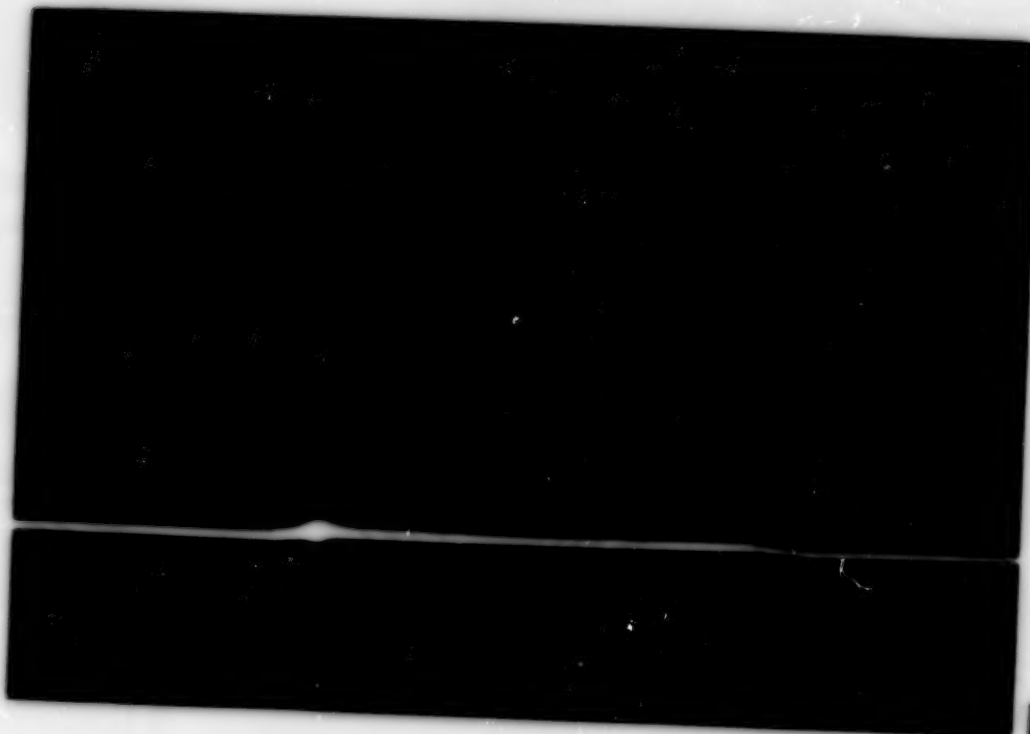


(b) $M = 2.16$.

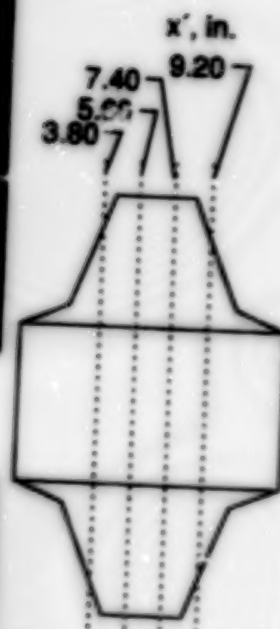
Figure 61. Continued.

ORIGINAL PAGE
BLACK AND WHITE PHOTOGRAPH

$x' = 7.40$ in.

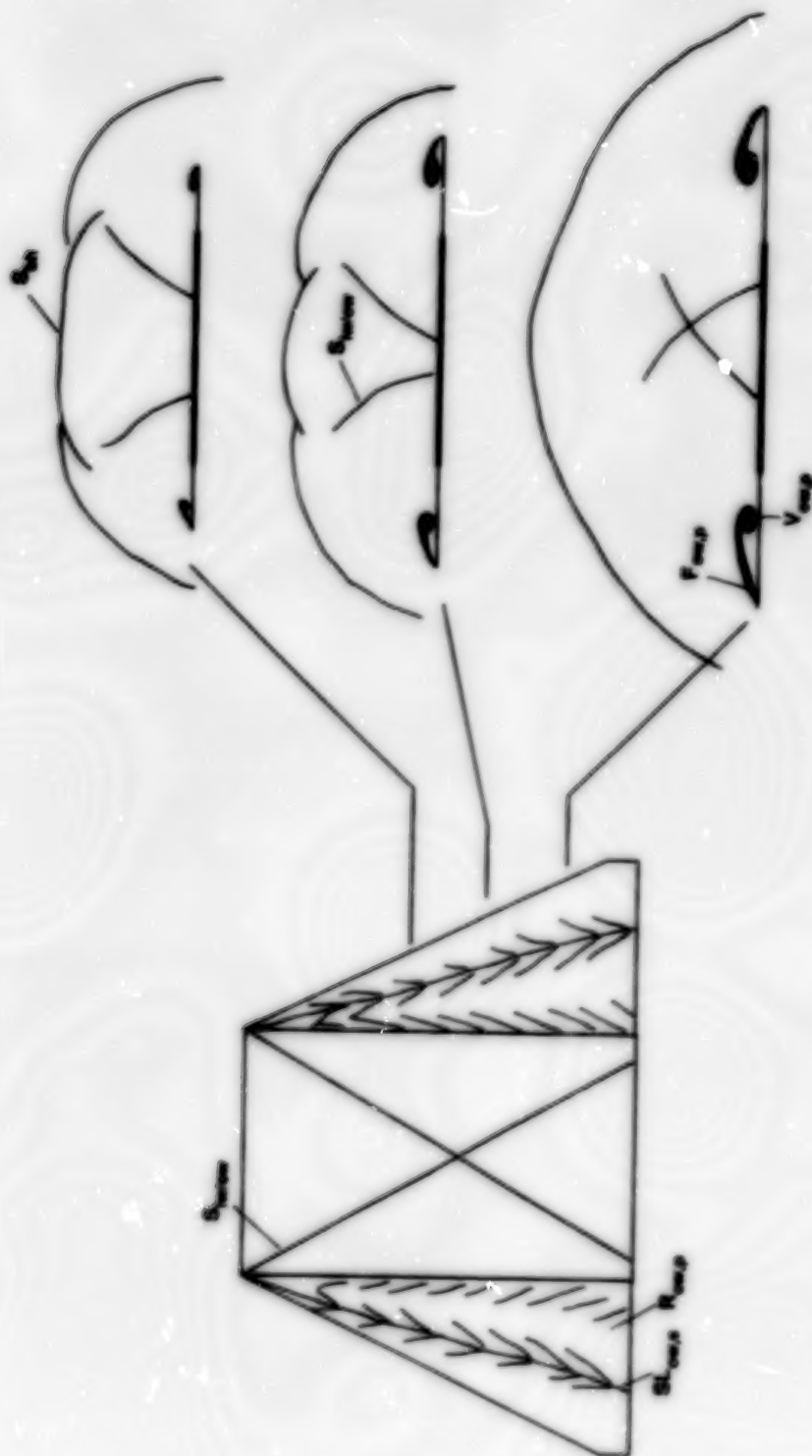


$x' = 9.20$ in.



(b) Concluded.

Figure 61. Concluded.



Top view, $\alpha = 8^\circ$
(See oil-flow photographs in fig 63.)

Spanwise cross-section cuts: $\alpha = 16^\circ$
(See vapor-screen photographs in figs. 64 to 65.)

Figure 62. Flow pattern over unswept/delta wing-alone configuration for $M = 2.16$.

ORIGINAL PAGE
BLACK AND WHITE PHOTOGRAPH

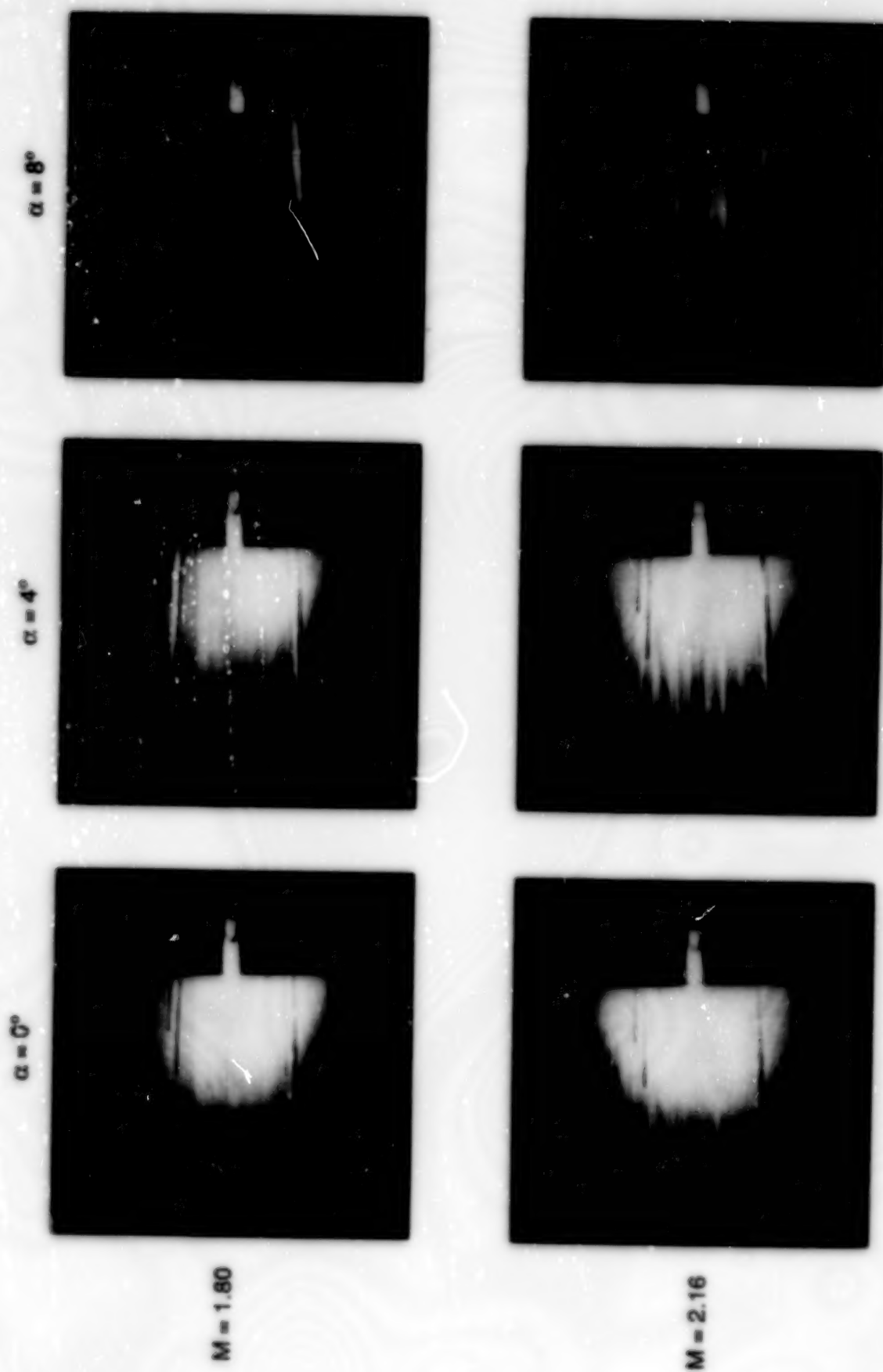


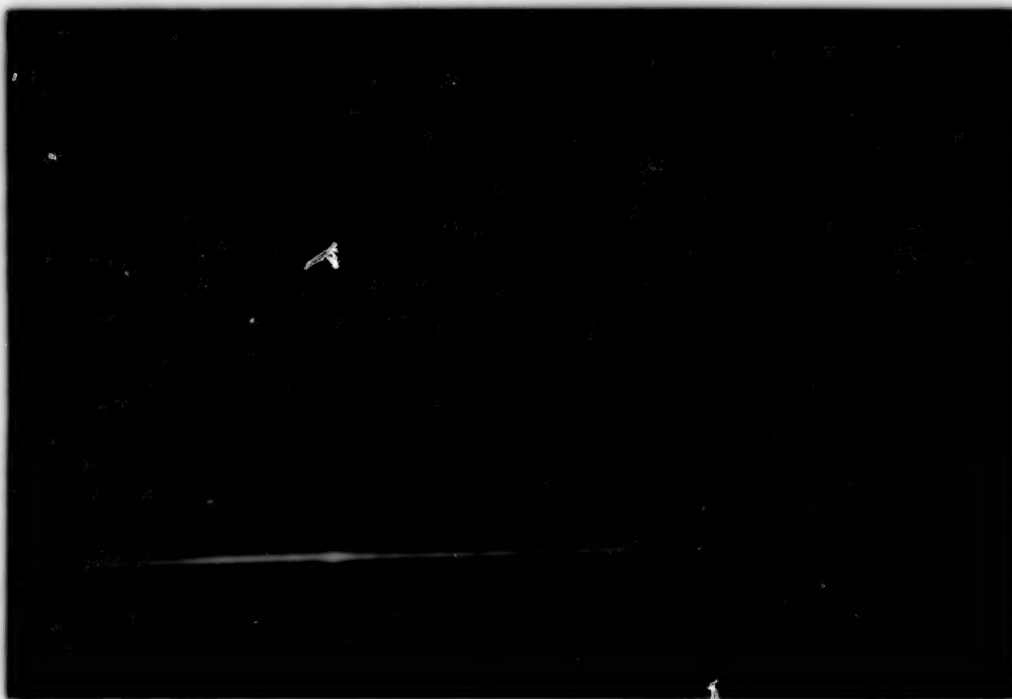
Figure 63. Oil-flow photographs for upper surface of unswept/delta wing-alone configuration at $\alpha = 0^\circ, 4^\circ$, and 8° and $M = 1.80$ and 2.16 .

ORIGINAL PAGE
BLACK AND WHITE PHOTOGRAPH

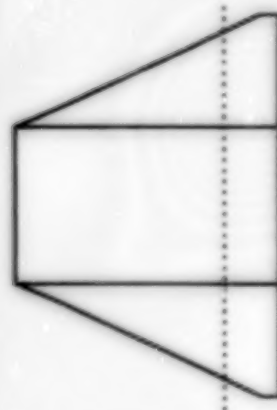
$\alpha = 4^\circ$



$\alpha = 8^\circ$



$x' = 10.4$ in.

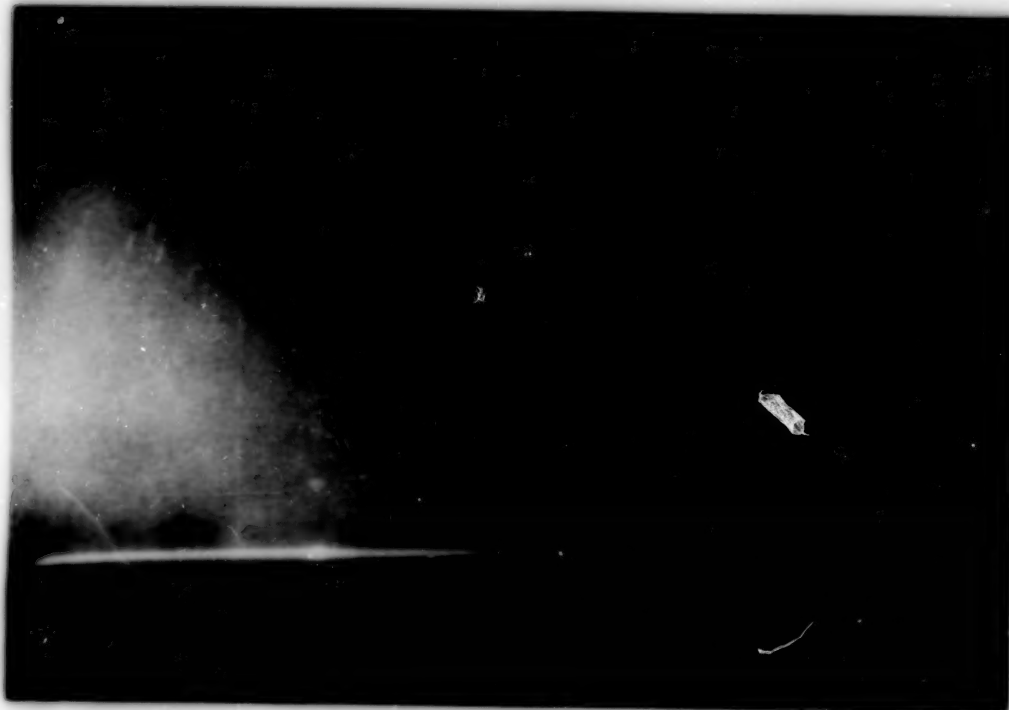


(a) $M = 1.60$.

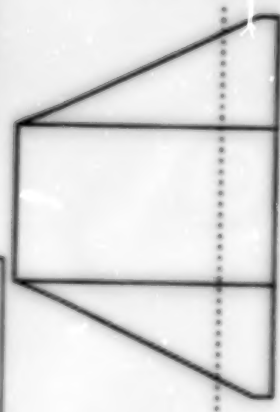
Figure 64. Vapor-screen photographs at $x' = 10.4$ in. for unswept/delta wing-alone configuration for various angles of attack and Mach numbers.

ORIGINAL PAGE
BLACK AND WHITE PHOTOGRAPH

$\alpha = 12^\circ$



$x' = 10.4 \text{ in.}$



$\alpha = 16^\circ$



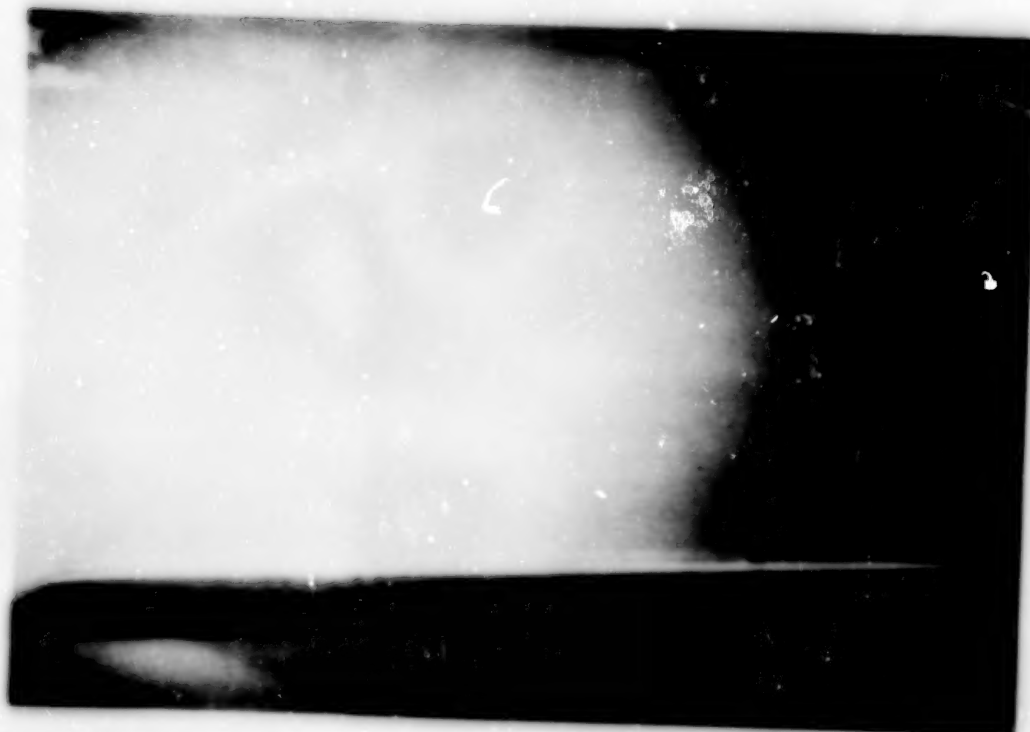
Not available

(a) Concluded.

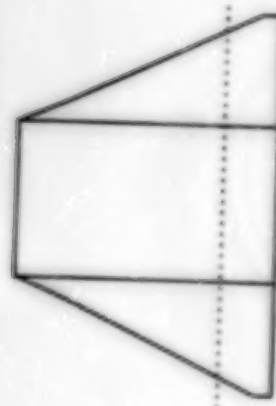
Figure 64. Continued.

ORIGINAL WHITE
BLACK AND WHITE PHOTOGRAPH

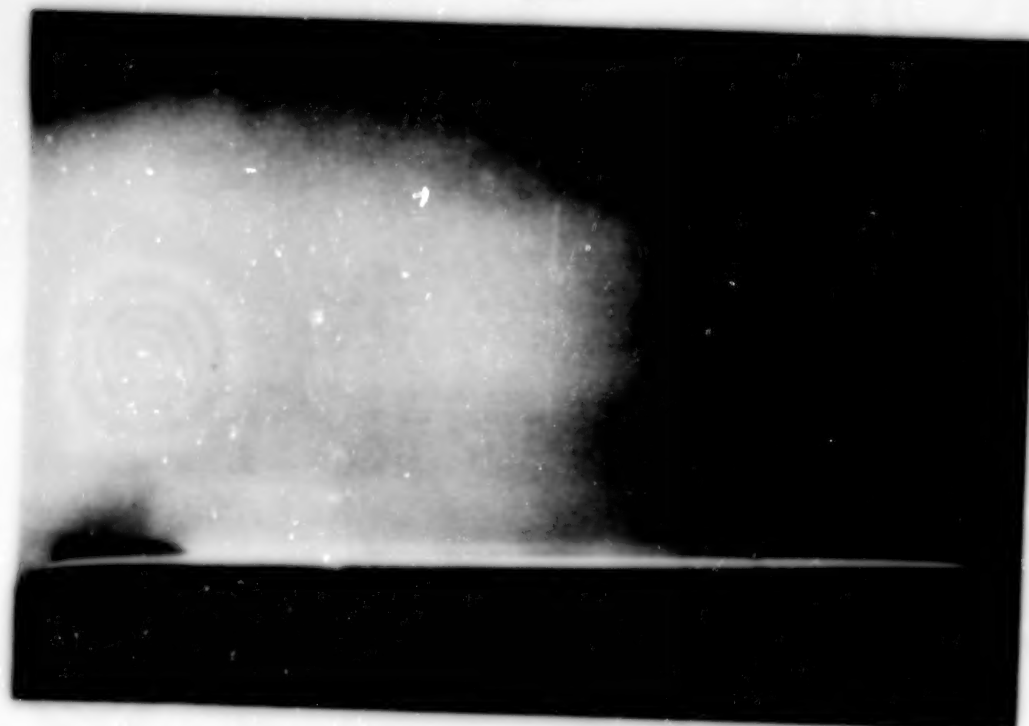
$\alpha = 4^\circ$



$x' = 10.4 \text{ in.}$



$\alpha = 8^\circ$

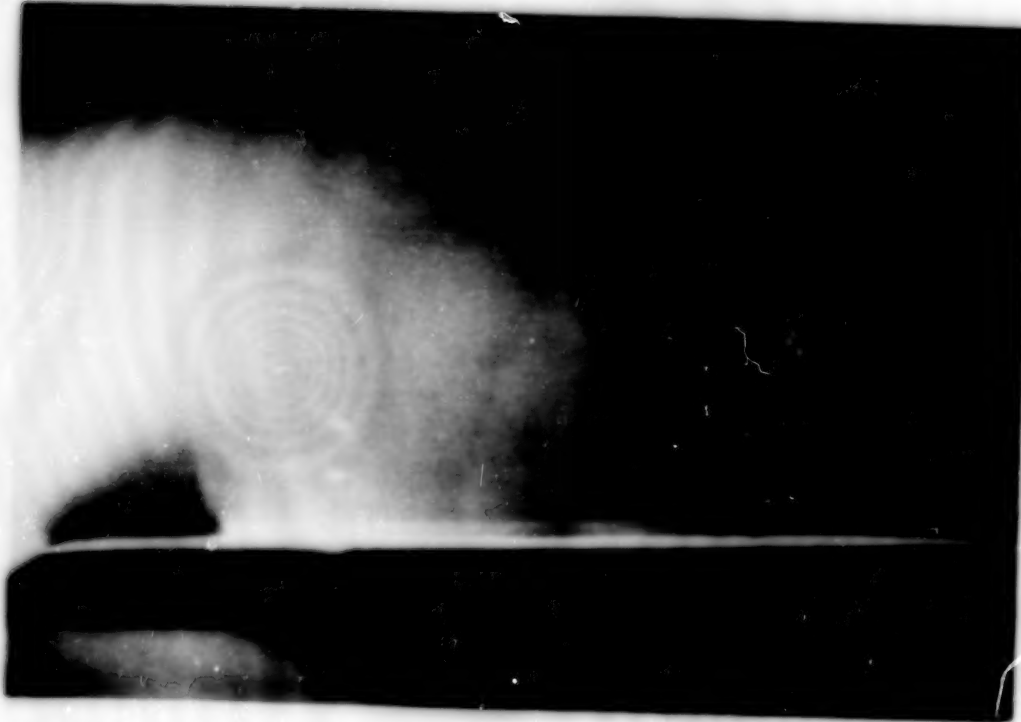


(b) $M = 1.80$.

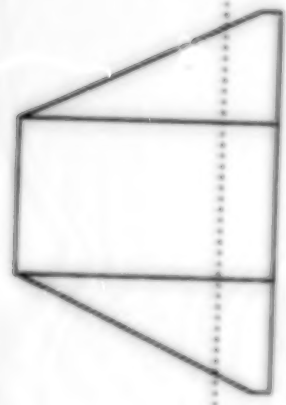
Figure 64. Continued.

ORIGINAL PAGE
BLACK AND WHITE PHOTOGRAPH

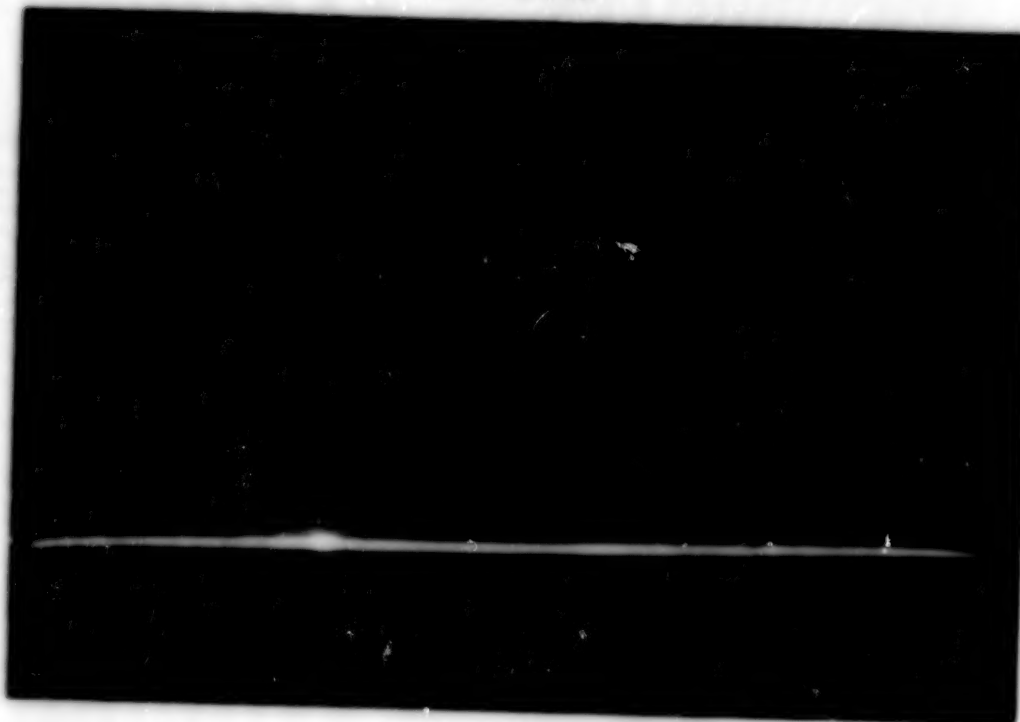
$\alpha = 12^\circ$



$x' = 10.4 \text{ in.}$



$\alpha = 16^\circ$

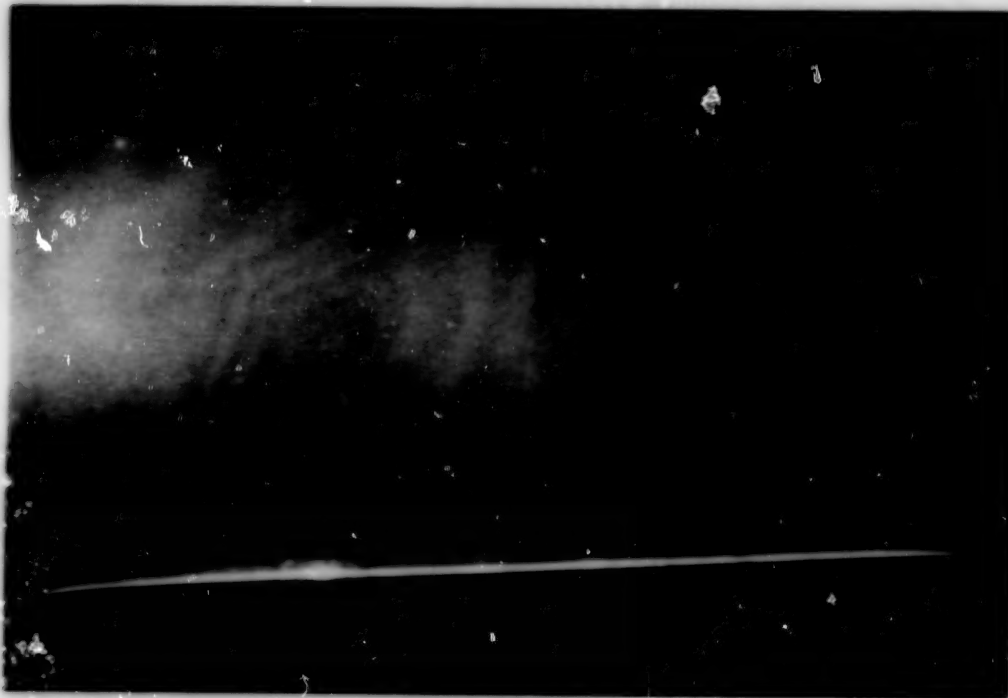


(b) Concluded.

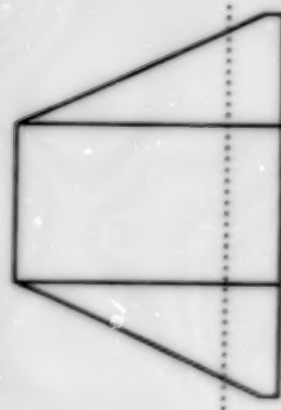
Figure 64. Continued.

ORIGINAL PAGE
BLACK AND WHITE PHOTOGRAPH

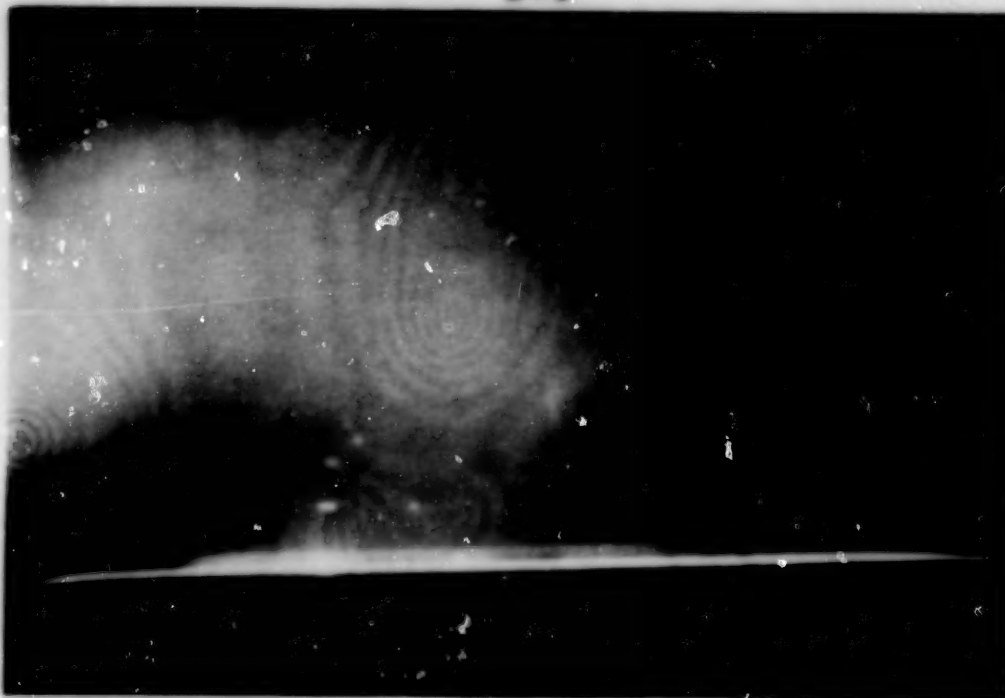
$\alpha = 6^\circ$



$x' = 10.4 \text{ in.}$



$\alpha = 8^\circ$

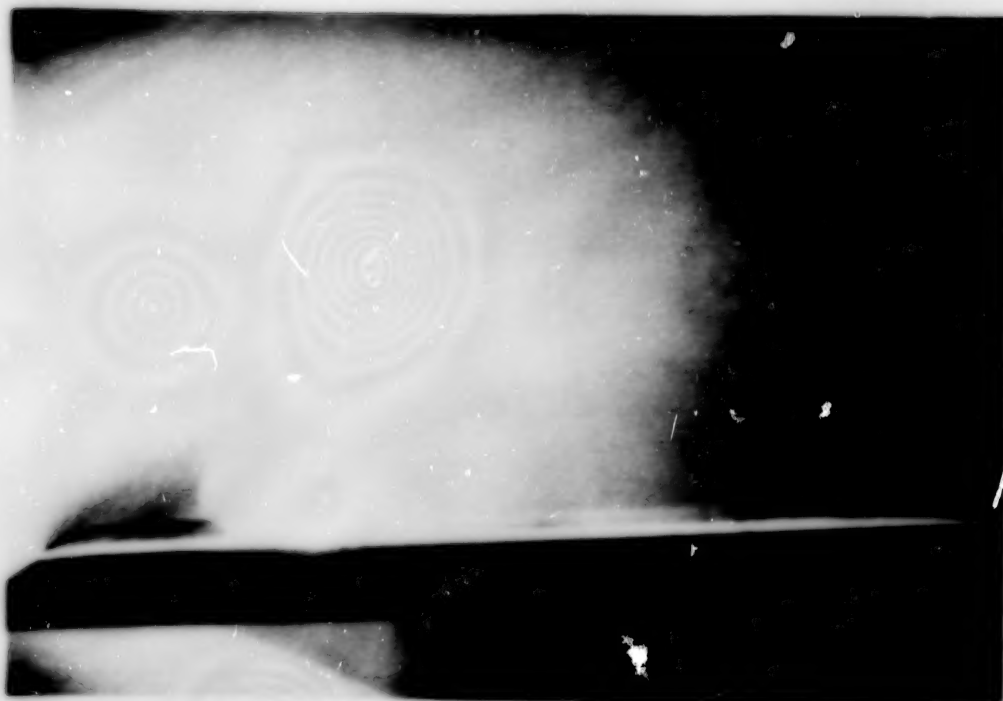


(c) $M = 2.00$.

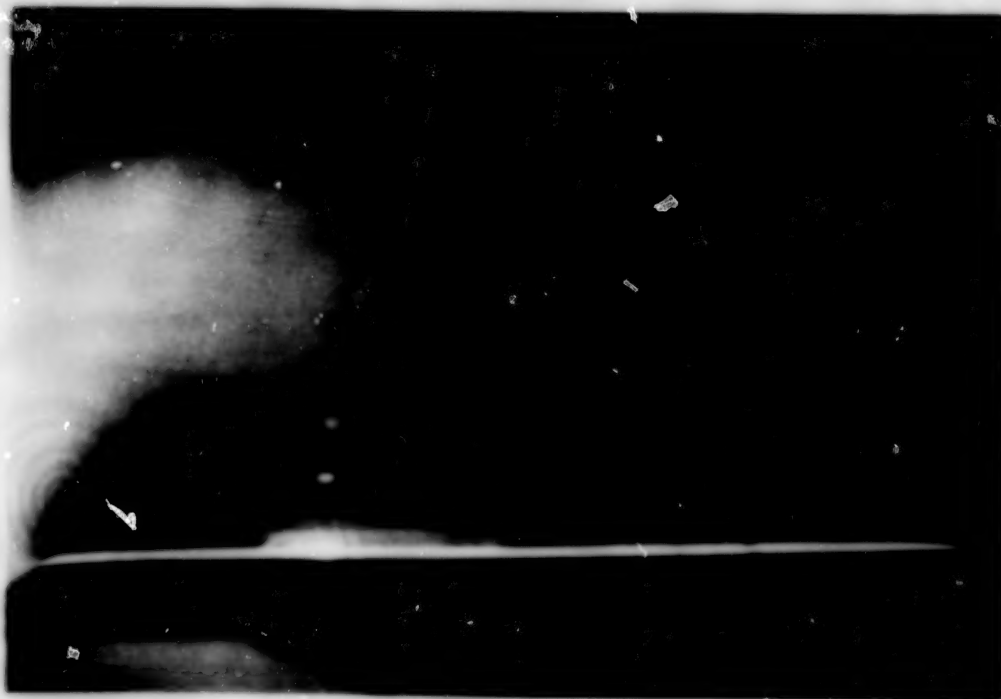
Figure 64. Continued.

ORIGINAL PAGE
BLACK AND WHITE PHOTOGRAPH

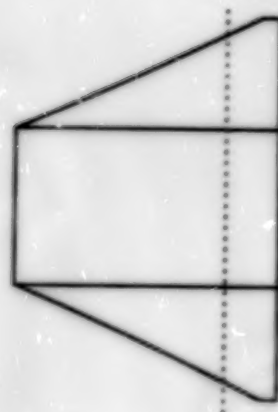
$\alpha = 12^\circ$



$\alpha = 16^\circ$



$x' = 10.4 \text{ in.}$



(c) Concluded.

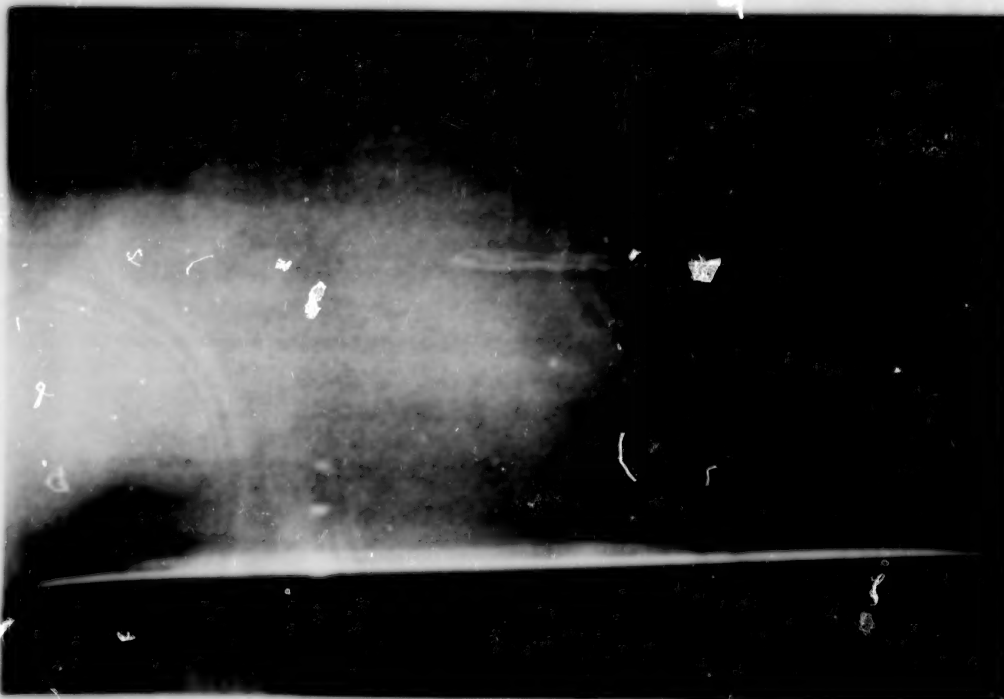
Figure 64. Continued.

ORIGINAL PAGE
BLACK AND WHITE PHOTOGRAPH

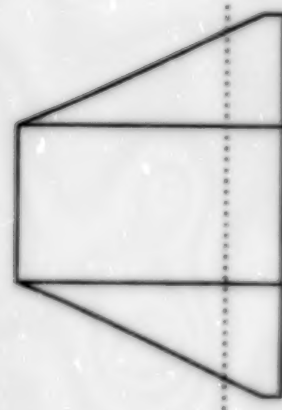
$\alpha = 4^\circ$



$\alpha = 8^\circ$



$x' = 10.4$ in.

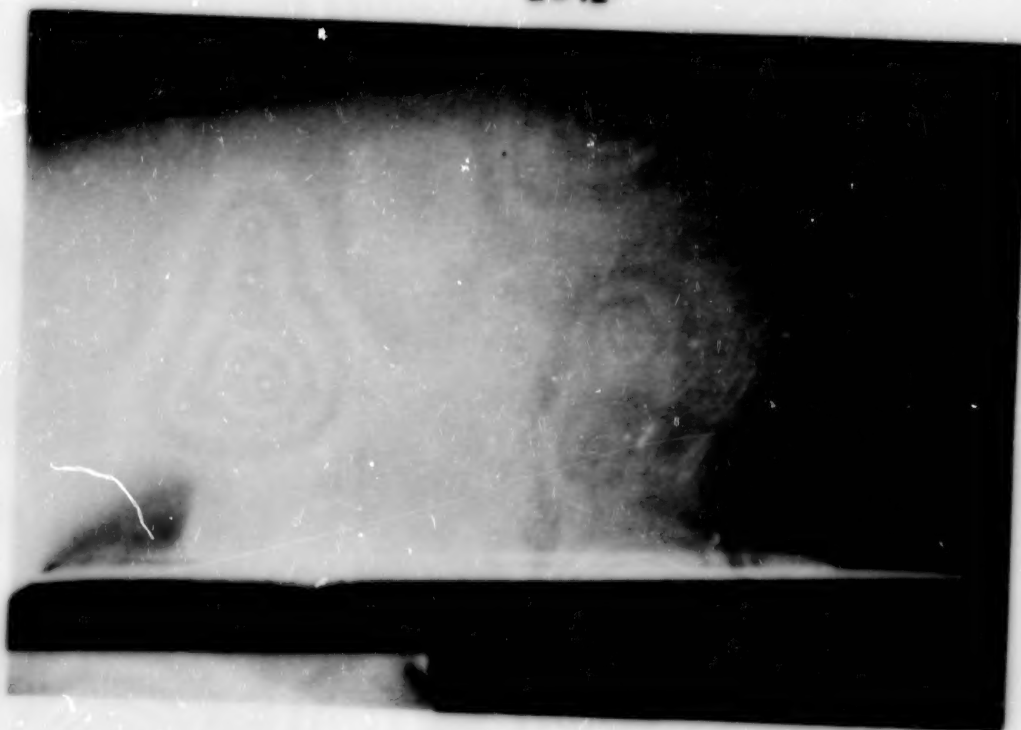


(d) $M = 2.16$.

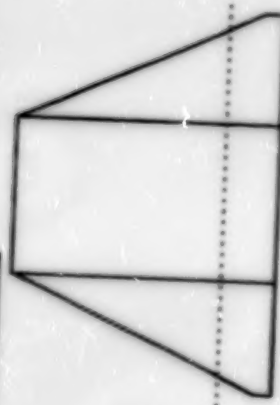
Figure 64. Continued.

ORIGINAL PAGE
BLACK AND WHITE PHOTOGRAPH

$\alpha = 12^\circ$



$x' = 10.4 \text{ in.}$



$\alpha = 16^\circ$



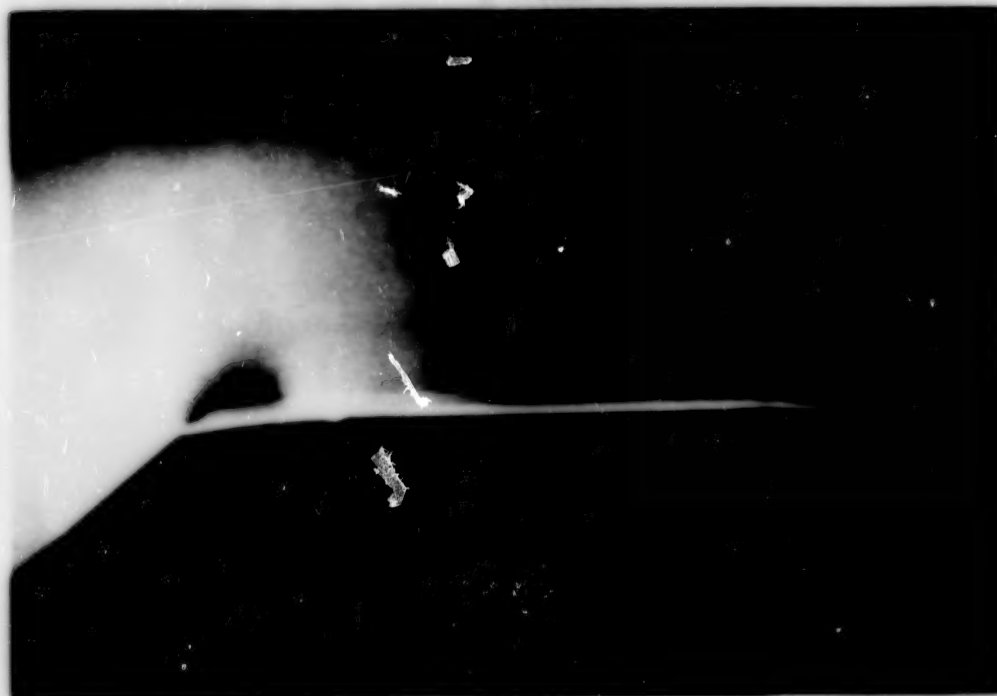
Not available

(d) Concluded.

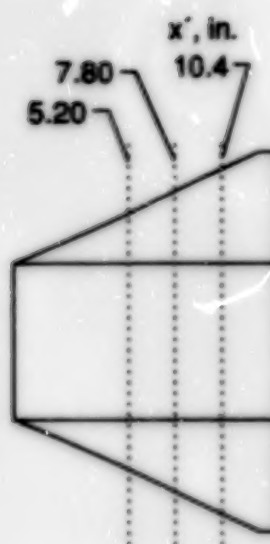
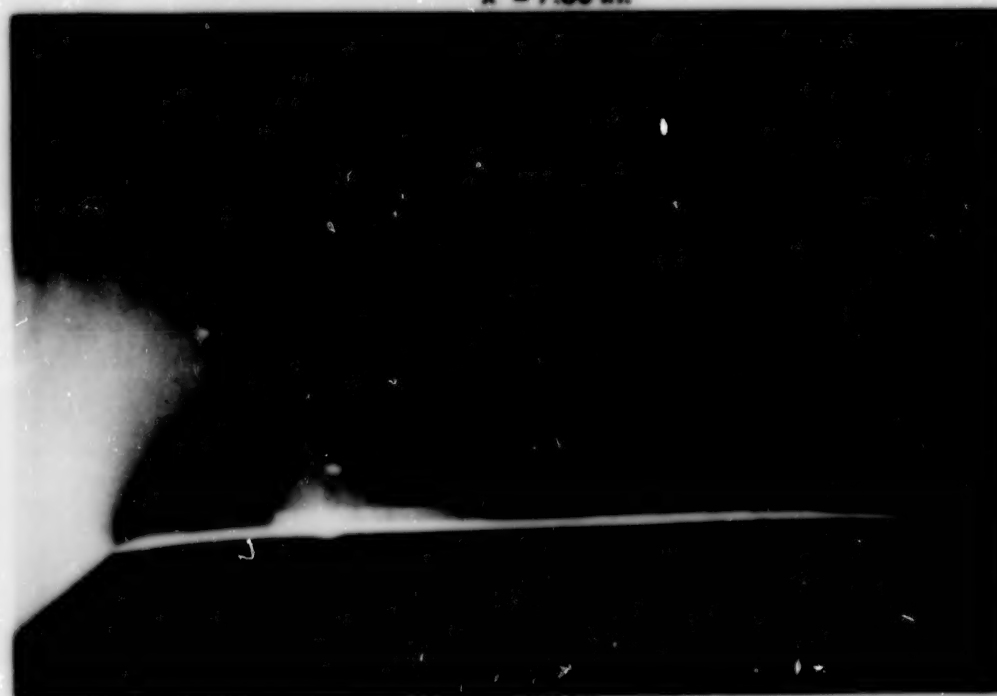
Figure 64. Concluded.

ORIGINAL PAGE
BLACK AND WHITE PHOTOGRAPH

$x' = 5.20$ in.



$x' = 7.80$ in.

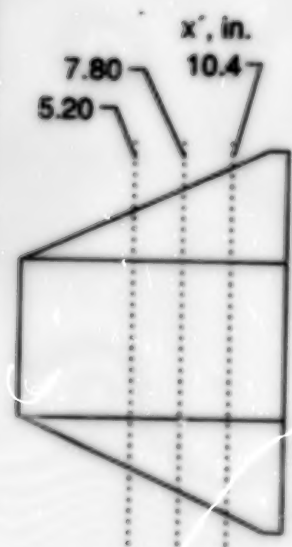


(a) $M = 1.80$.

Figure 65. Vapor-screen photographs for unswept/delta wing-alone configuration at three longitudinal locations for $\alpha = 16^\circ$ and $M = 1.80$ and 2.16.

ORIGINAL PAGE
BLACK AND WHITE PHOTOGRAPH

$x' = 10.4$ in.



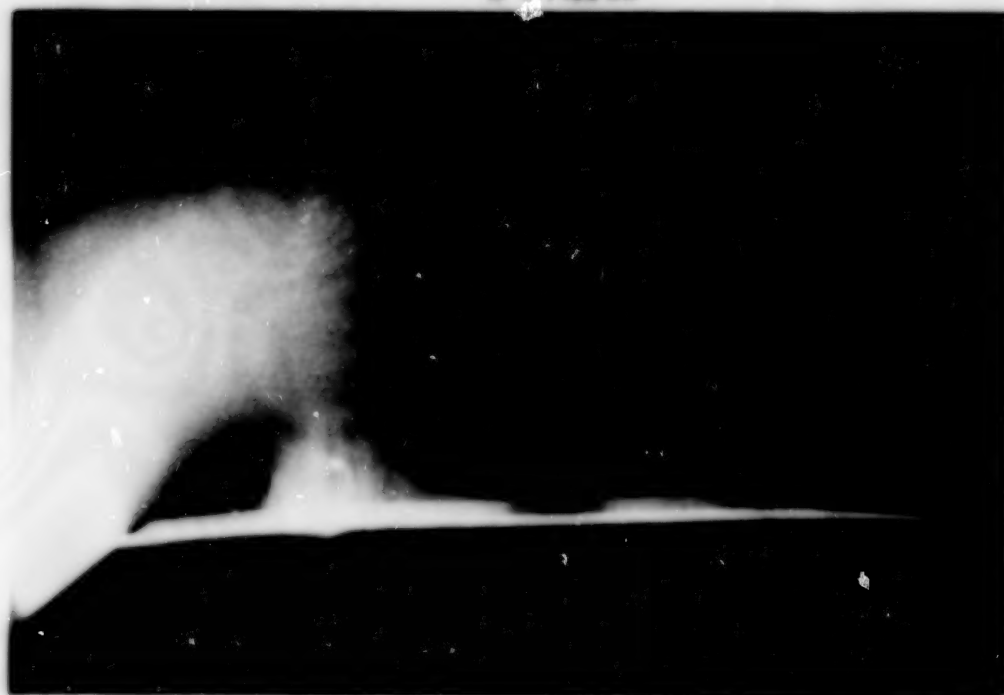
(a) Concluded.

Figure 65. Continued.

ORIGINAL PAGE
BLACK AND WHITE PHOTOGRAPH
 $x' = 5.20$ in.

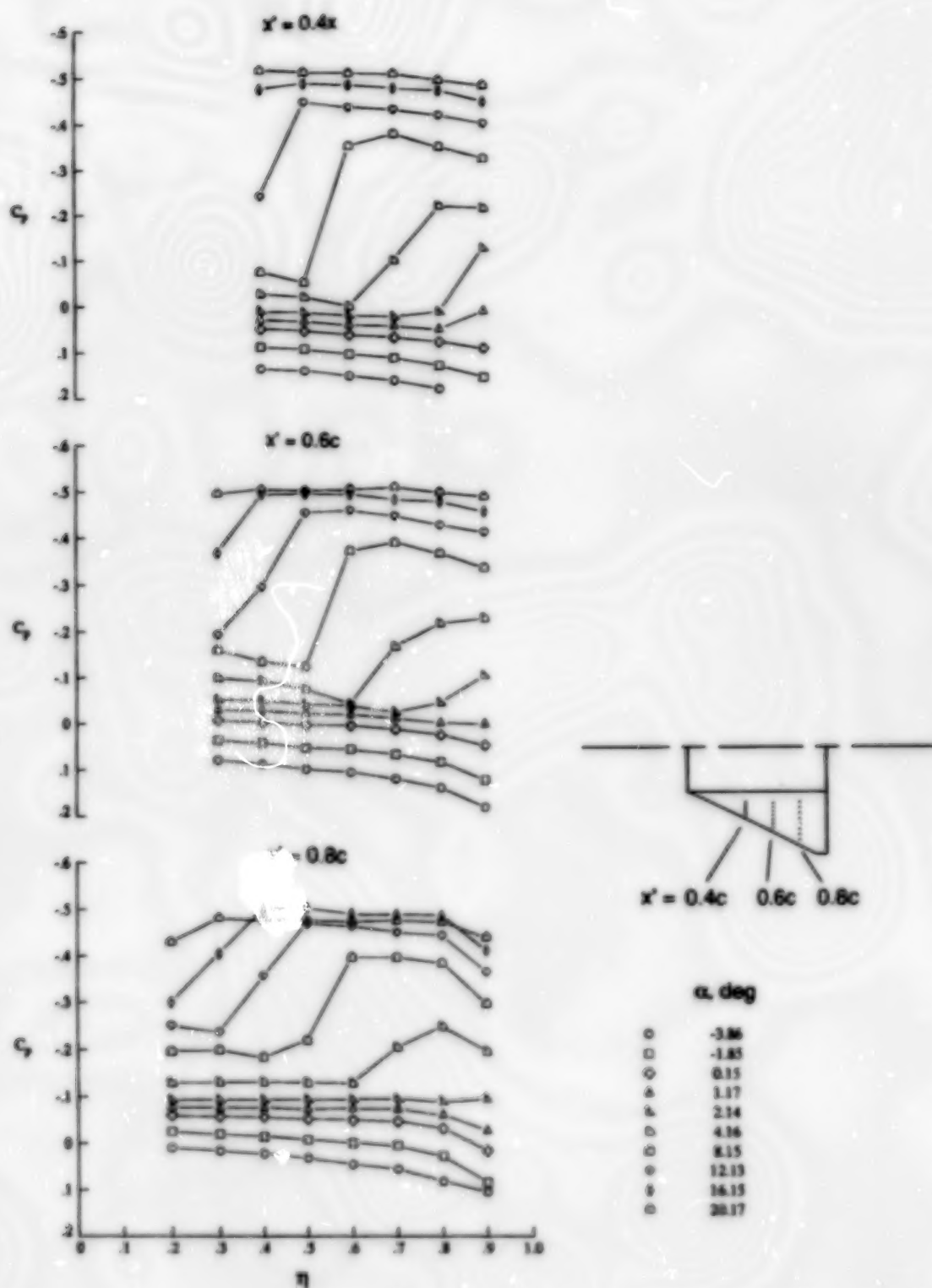


$x' = 7.80$ in.



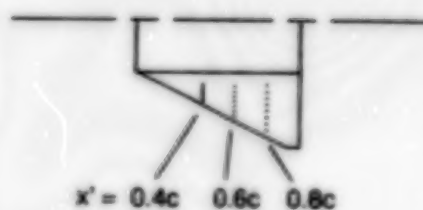
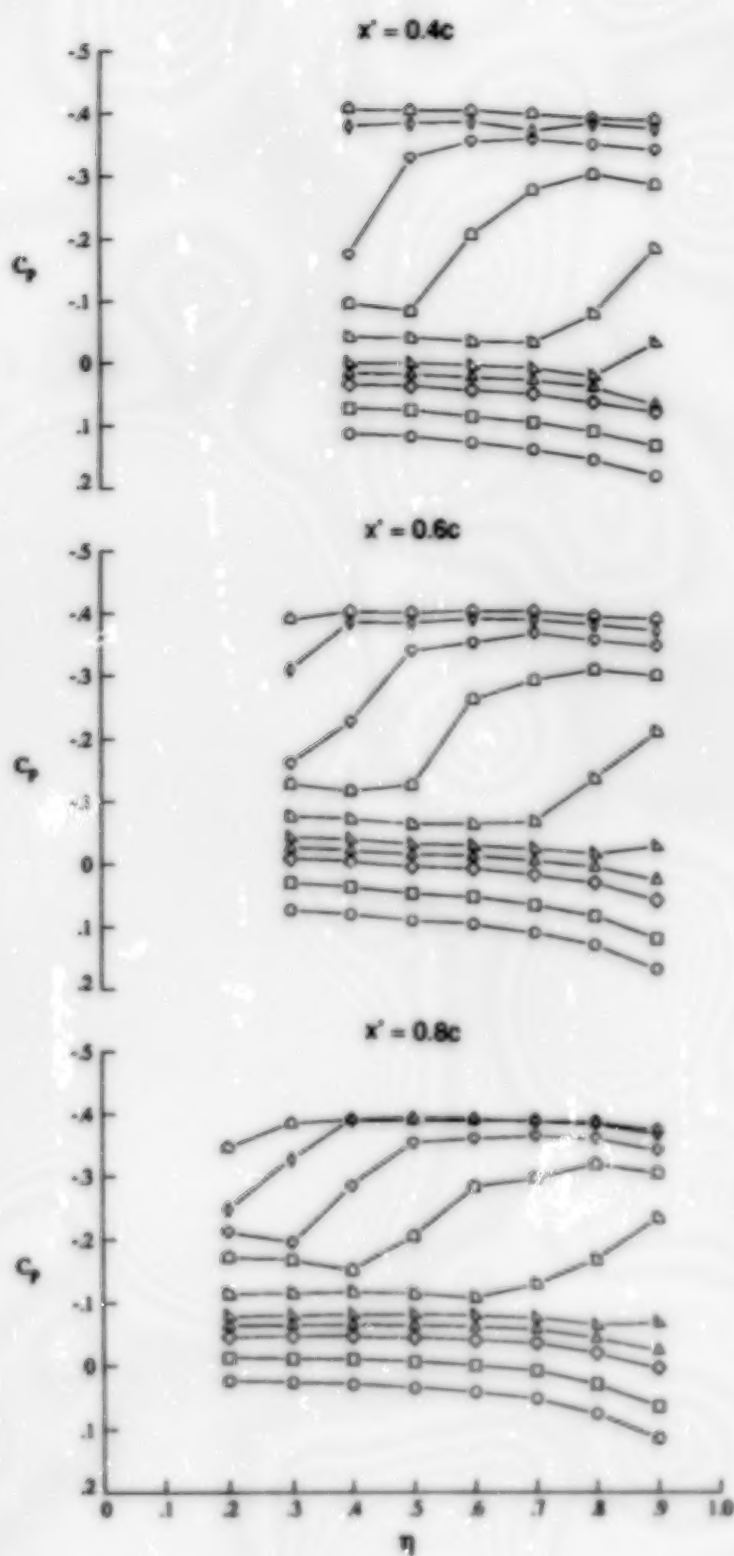
(b) $M = 2.16$.

Figure 65. Concluded.



(a) $M = 1.60$.

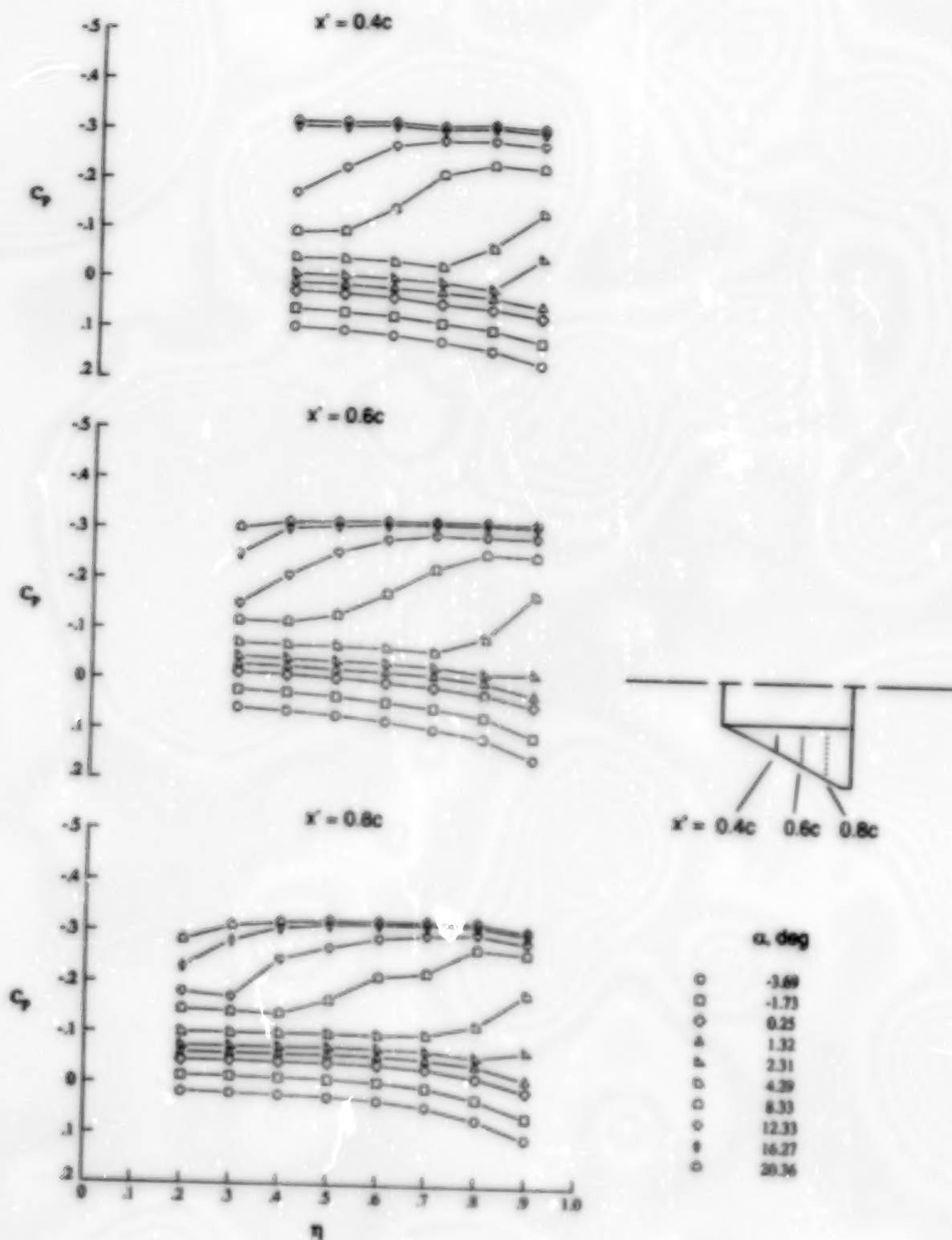
Figure 66. Effect of angle of attack on surface pressure coefficient distributions over delta outboard wing of unswept/delta wing-alone configuration at $x' = 0.4c, 0.6c$, and $0.8c$ for $M = 1.60, 1.80, 2.00$, and 2.16 .



α , deg
○ -3.95
□ -1.93
○ 0.06
△ 1.09
△ 2.06
○ 4.10
○ 8.15
○ 12.06
○ 16.11
○ 20.11

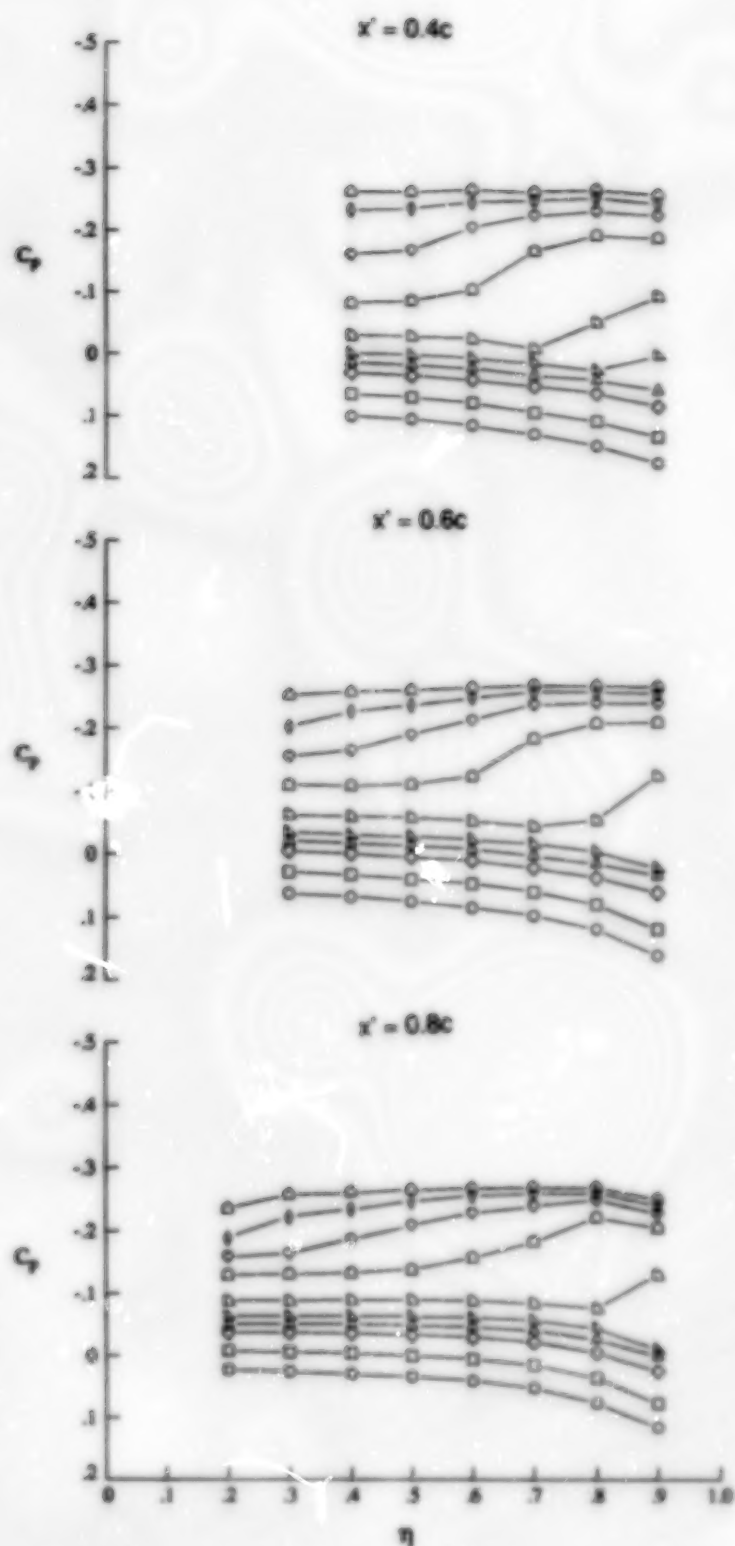
(b) $M = 1.80$.

Figure 36. Continued.



(c) $M = 2.00$.

Figure 66. Continued.



α , deg	
○	-4.11
□	-2.15
◇	-0.15
△	0.92
×	1.90
●	3.91
○	7.96
○	11.90
○	15.89
○	19.92

(d) $M = 2.16$.

Figure 66. Concluded.

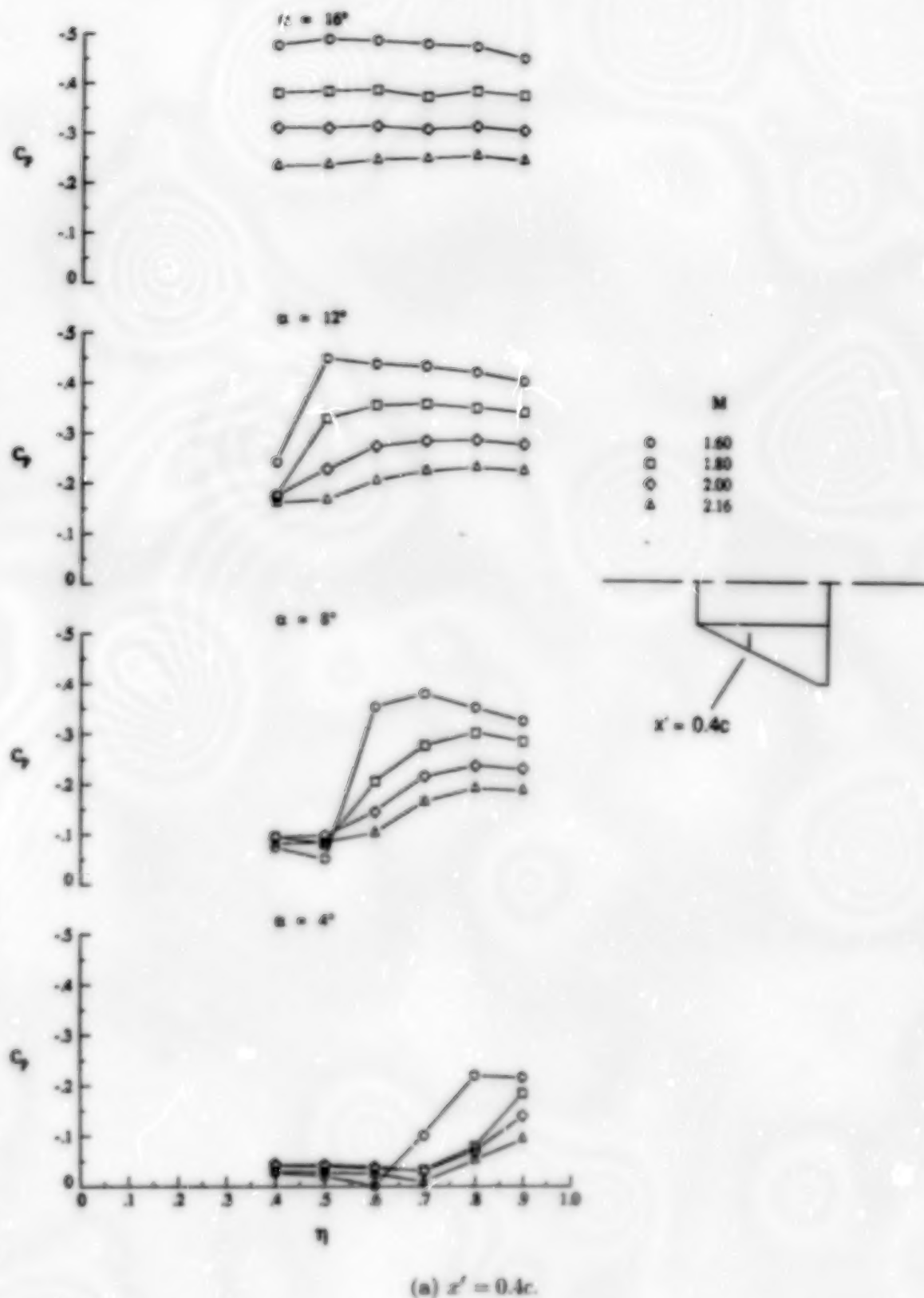
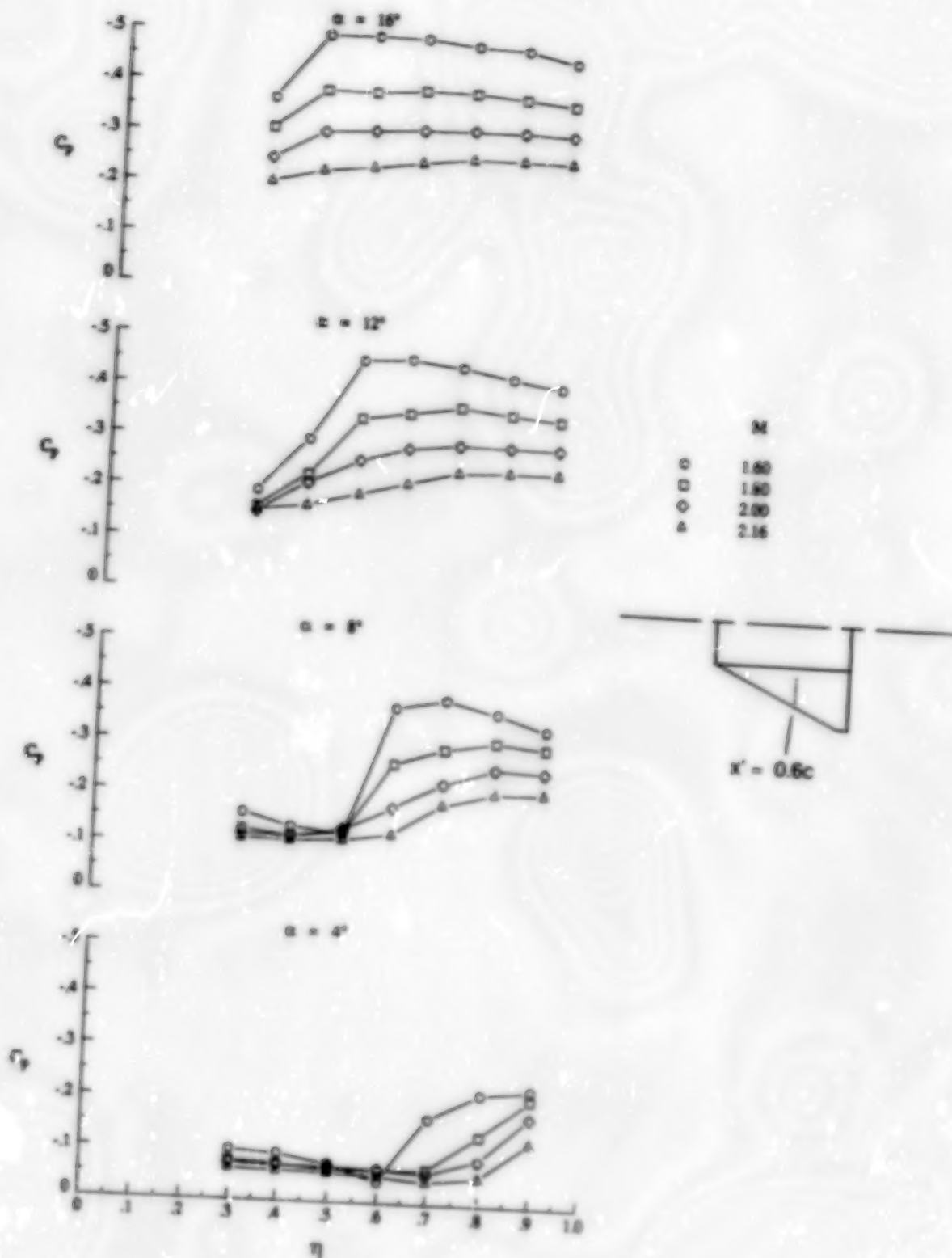
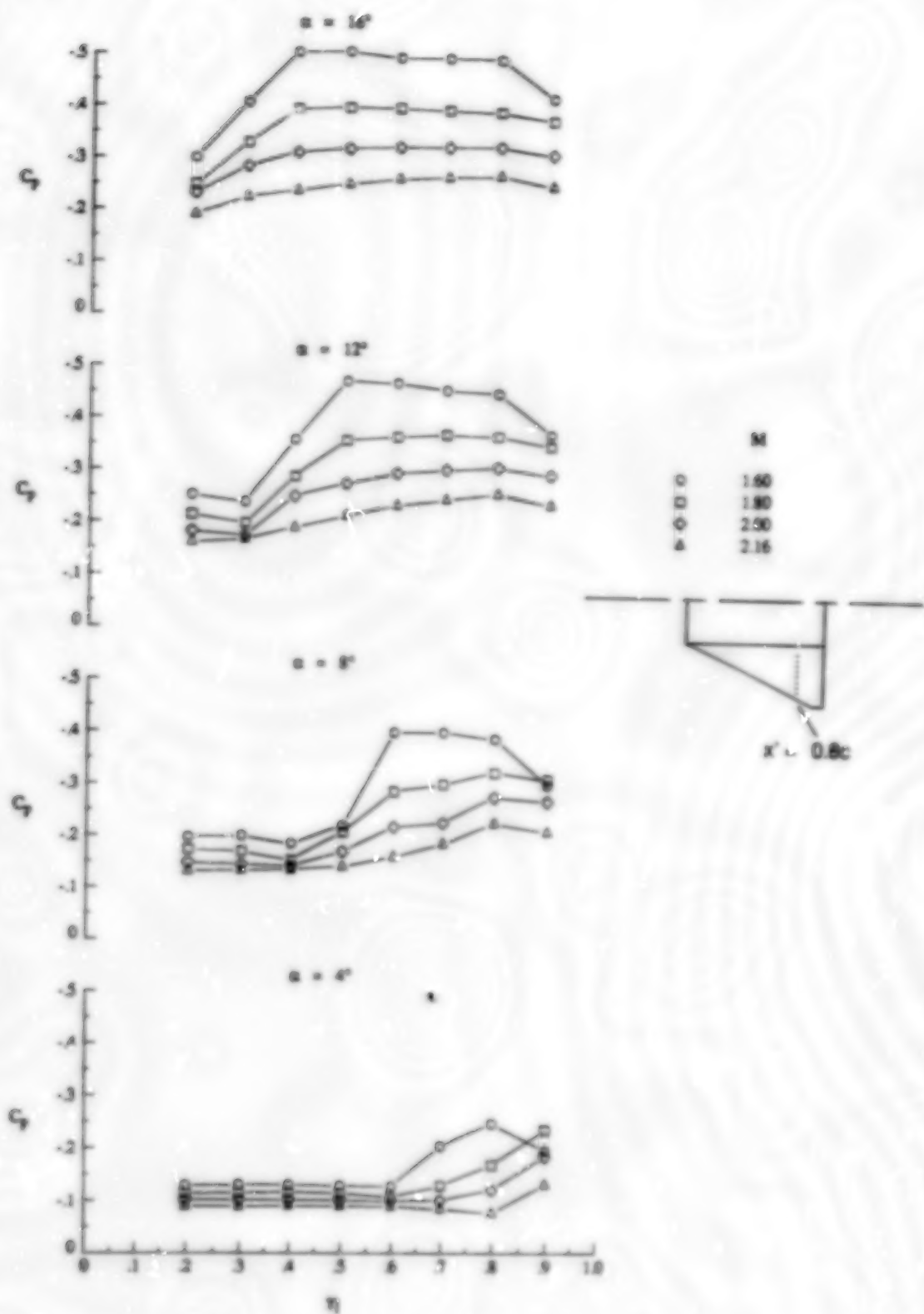


Figure 67. Effect of Mach number on surface pressure coefficient distributions over delta outboard wing of unswept/delta wing-alone configuration at $x' = 0.4c$, $0.6c$, and $0.8c$ for $\alpha = 4^\circ$, 8° , 12° , and 16° .



(b) $x' = 0.6c$.

Figure 67. Continued.



(c) $x' = 0.8c$.

Figure 67. Concluded.